Forschungszentrum Jülich
*in der Helmholtz-Gemeinschaft*

50 Jahre / Zukunft

# Josephson Tunnel Junctions with Ferromagnetic Interlayer

Martin Weides

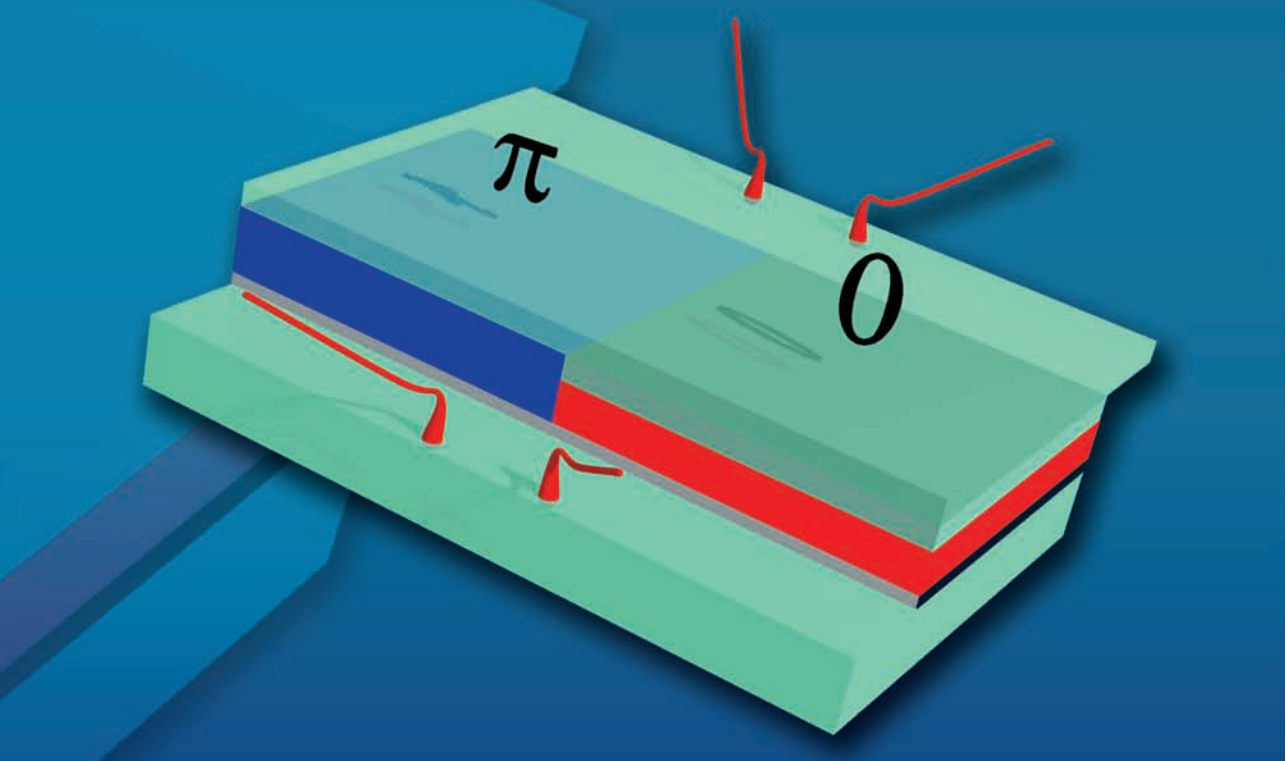


**Informationstechnik**
**Information Technology**

Schriften des Forschungszentrums Jülich
Reihe Informationstechnik / Information Technology Band / Volume 13

Forschungszentrum Jülich GmbH
Institut für Festkörperforschung (IFF)
Elektronische Materialien (IFF-6)

# Josephson Tunnel Junctions with Ferromagnetic Interlayer

Martin Weides

Schriften des Forschungszentrums Jülich
Reihe Informationstechnik / Information Technology Band / Volume 13

ISSN 1433-5514 ISBN 978-3-89336-472-5

Bibliographic information published by the Deutsche Nationalbibliothek.
The Deutsche Nationalbibliothek lists this publication in the Deutsche Nationalbibliografie; detailed bibliographic data are available in the Internet at http://dnb.d-nb.de.

| | |
|---|---|
| Publisher and Distributor: | Forschungszentrum Jülich GmbH<br>Zentralbibliothek, Verlag<br>D-52425 Jülich<br>Telefon (02461) 61-5368 · Telefax (02461) 61-6103<br>e-mail: zb-publikation@fz-juelich.de<br>Internet: http://www.fz-juelich.de/zb |
| Cover Design: | Grafische Medien, Forschungszentrum Jülich GmbH |
| Printer: | Grafische Medien, Forschungszentrum Jülich GmbH |
| Copyright: | Forschungszentrum Jülich 2007 |

Schriften des Forschungszentrums Jülich
Reihe Informationstechnik / Information Technology Band / Volume 13

D 38 (Diss., Köln, Univ., 2006)

ISSN 1433-5514
ISBN 978-3-89336-472-5

The complete volume is freely available on the Internet on the Jülicher Open Access Server (JUWEL) at http://www.fz-juelich.de/zb/juwel

# Zusammenfassung

Supraleitung und Ferromagnetismus sind gut bekannte physikalische Eigenschaften fester Körper, die intensiv untersucht wurden und aufgrund ihrer unterschiedlichen Spin-Ordnungen für lange Zeit als gegensätzliche Phänomene galten. Es wurde gezeigt, dass die Kombination von Supraleitung und Ferromagnetismus zu einer vielfältigen und interessanten Physik führt. Ein besonderes Beispiel, die Phasenoszillationen des supraleitenden Ordnungsparameters innerhalb des Ferromagneten, spielt eine besondere Rolle für die in dieser Arbeit untersuchten Kontakte.

In dieser Promotionsarbeit präsentiere ich Josephson-Kontakte mit einer dünnen $Al_2O_3$ Tunnelbarriere und einer ferromagnetischen Zwischenschicht, d.h. Supraleiter-Isolator-Ferromagnet-Supraleiter (SIFS) Schichten. Die Herstellung der Kontakte wurde hinsichtlich der Isolierung der Elektroden und der Homogenität des Stromtransportes optimiert. Die Kontakte waren entweder im 0 oder $\pi$ gekoppelten Grundzustand, abhängig von der Dicke der ferromagnetischen Schicht und der Temperatur. Der Einfluss der ferromagnetischen Schichtdicke auf die Transporteigenschaften und die Kopplung (0, $\pi$) der SIFS-Tunnelkontakte wurde untersucht.

Des Weiteren habe ich einen so genannten 0-$\pi$ Josephson-Kontakt durch eine gestufte ferromagnetische Zwischenschicht mit wohl definierten Dicken hergestellt. Bei einer bestimmten Temperatur ist dieser 0-$\pi$ Kontakt vollkommen symmetrisch. In diesem Fall entsteht im Grundzustand ein supraleitender Stromwirbel mit einem Magnetfluss von der Größe eines fraktionierten magnetischen Flußquants $\Phi_0$. Solche Systeme erlauben die Untersuchung der Physik fraktionierter Magnetflüsse und zugleich die Konstruktion von verschiedenen elektronischen Schaltungen.

Die hier vorgestellten SIFS Kontakte haben eine exponentiell verschwindene Dämpfung bei $T \to 0$. Die im Rahmen dieser Arbeit entwickelte SIFS Technologie kann zur Herstellung von klassischen und Quanten-Bausteinen wie Oszillatoren, Speicherzellen und Qubits eingesetzt werden.

# Abstract

Superconductivity and ferromagnetism are well-known physical properties of solid states that have been widely studied and long thought about as antagonistic phenomena due to difference in spin ordering. It turns out that the combination of both superconductor and ferromagnet leads to a very rich and interesting physics. One particular example, the phase oscillations of the superconducting order parameter inside the ferromagnet, will play a major role for the devices discussed in this work.

In this thesis, I present Josephson junctions with a thin $Al_2O_3$ tunnel barrier and a ferromagnetic interlayer, i.e. superconductor-insulator-ferromagnet-superconductor (SIFS) stacks. The fabrication of junctions was optimized regarding the insulation of electrodes and the homogeneity of the current transport. The junctions were either in the 0 or $\pi$ coupled ground state, depending on the thickness of the ferromagnetic layer and on temperature. The influence of ferromagnetic layer thickness on the transport properties and the coupling (0, $\pi$) of SIFS tunnel junctions was studied.

Furthermore, using a stepped ferromagnetic layer with well-chosen thicknesses, I obtained the so-called 0-$\pi$ Josephson junction. At a certain temperature this 0-$\pi$ junction can be made perfectly symmetric. In this case the ground state corresponds to a vortex of supercurrent creating a magnetic flux which is a fraction of the magnetic flux quantum $\Phi_0$. Such structures allow to study the physics of fractional vortices and to build various electronic circuits based on them.

The SIFS junctions presented here have an exponentially vanishing damping at $T \to 0$. The SIFS technology developed within the framework of this work may be used to construct classical and quantum devices such as oscillators, memory cells and qubits.

# Contents

# Acknowledgements

This thesis was done in collaboration with a considerable number of people, who all contributed in different ways.

I thank my supervisor *Priv.-Doz. Dr. Hermann Kohlstedt* for the inspiring collaboration with him, his unwavering enthusiasm and for giving me the freedom and resources from which I greatly benefitted.

A thank you to the head of our institute *Prof. Rainer Waser* for providing an excellent environment to perform this research. Both I thank for granting me the opportunity to attend a number of meetings, summer schools and conferences during the past years.

Thanks are also due to *Prof. J. Stutzki*, *Prof. G. Eilenberger* and *Priv.-Doz. Dr. Daniel Bürgler* for accepting the tasks of co-examiner, chairman of the board of examiners and assessor, respectively.

I have benefited a lot from the collaboration with *Dr. Edward Goldobin*. I want to thank him for stimulating this Ph.D. thesis and the inspiring discussions we had in the last three years, steering my research activities in the right direction. In addition his critical comments on my draft are acknowledged with gratitude.

I am indebted to *Prof. Valery Ryazanov* for the enjoyable time I had at the Laboratory of Superconductivity of the Institute of Solid State Physics, Russian Academy of Science in Chernogolovka. There I enjoyed fruitful discussions with *Vladimir Oboznov*.

Thanks are also due to *Prof. Reinhold Kleiner* and *Prof. Dieter Kölle*, both University of Tübingen, for the interest they showed in my thesis and their support of several projects.

I am grateful to *Dr. Dietmar Doenitz* from the Tübingen group for having the opportunity to perform *Low Temperature Scanning Electron Microscopy* experiments under a nice atmosphere and the fruitful discussions.

Special credit is also due to *Matthias Kemmler*, Tübingen group, who conducted several "very" low temperature experiments despite his own interesting research work.

I am obliged to *Prof. R. Gross* and *Dr. Achim Marx* for stimulating and to *Karl Madek* and *Sven Beutner* (Walther-Meissner-Institut, Garching) for

conducting microwave spectroscopy and macroscopic quantum tunneling measurements at "extremely" low temperatures and for the inspiring discussions we had.

I would like to thank *Prof. A. Buzdin* from Université Bordeaux for supporting me with the adequate formula for describing the charge transport in my junctions.

My special appreciation goes to *Dr. Karsten Tillmann* and *Doris Meertens* for providing the HRTEM measurement, to *Christina Schindler* for the SEM images and to *Andreas Gerber* for RBS measurements.

I also owe thanks to *Bernd Hermanns* for his help on technological issues and *Mona Nonn* for the fabrication of lithography masks.

I would like to thank all colleagues at Forschungszentrum Jülich, including my (alumni) office mates *Dr. Michael Fitsilis*, *Alexander Kaiser*, *Christian Nauenheim*, *Dr. Adrian Petraru*, *Jochen Puchalla*, *Serge Röhrig*, *Dr. Julio Rodriguez*, *Patrick Schützendorf* and *Dr. Simon Stein*. I am very thankful to our secretary *Maria Garcia* for her taking care of the administrative works.

Special thanks to the mechanical workshop headed by *K. Hirtz* and his colleagues.

Thanks are also due to *Janet Carter-Sigglow*, *Halit Anapa* and *Dr. Heiko Braak* for their careful reading of several Chapters of this thesis.

I acknowledge the financial support by the European Research Foundation within the framework of the PiShift programm and the Heraeus Foundation.

Finally, I would like to thank my family and especially my girlfriend *Bianca Fornoff* for having accompanied and supported me during the years as Ph.D. student.

# Introduction

Superconductivity and ferromagnetism are two opposing phenomena: a bulk superconductor expels a magnetic field, which in turn destroys the superconductivity. The reason is the unequal symmetry in time: Ferromagnetic order breaks the time-reversal symmetry, whereas conventional superconductivity relies on the pairing of time-reversed states.

Conventional superconductivity has been described microscopically in a classical work by J. Bardeen, L. Cooper and J. Schrieffer (BCS) [1]. According to this theory due to the electron interaction with the crystal lattice the electrons form *Cooper pairs*, consisting of electrons with opposite spins and momenta. The Cooper pair wave function $\Psi$ can be used as the *order parameter* of the system. The superconductivity is destroyed by a magnetic field via the orbital (interaction of the superconducting order parameter with the vector potential of the magnetic field) and the paramagnetic effect (magnetic exchange field tends to align the spins of Cooper pairs in the same direction). Therefore the coexistence of superconductivity and ferromagnetism in bulk materials is suppressed.

Surprisingly, the coexistence of superconductivity and ferromagnetism may be easily achieved in heterostructures of thin ferromagnetic (F) and superconducting (S) films, such as S/F, FSF or SFS multilayers. Inside the F-layer the superconducting order parameter is damped and spatially oscillating. This is the so-called anomalous proximity effect, which is analogous to the inhomogeneous superconductivity predicted by Fulde and Ferrell [2] and by Larkin and Ovchinnikov [3].

In a classical paper B. Josephson [4] predicted that the supercurrent through an SIS junction (I: non-magnetic insulating tunnel barrier) is given by $I = I_c \sin(\phi)$, where $\phi$ is the phase difference of the superconducting wave functions of the two electrodes and $I_c > 0$ is the maximum supercurrent that can pass through the junction. When no current ($I = 0$) is passed through the *Josephson junction* (JJ), the Josephson phase $\phi = 0$ corresponds to the energy minimum. The solution $\phi = \pi$ corresponds to the energy maximum and is unstable. This is the so-called 0 Josephson junction or 0 JJ.

If the F-layer thickness in an SFS stack is of the order of half the oscillation length, the amplitude of the order parameter may go through zero at the center of the F-layer. In that case, a state with the opposite sign of the order parameter, i.e. a shift of $\pi$, in the adjacent superconducting layer is provided. This is the so-called $\pi$ Josephson junction or $\pi$ JJ.

In an SFS or SIFS-type $\pi$ JJ the critical current is negative and the Josephson relation becomes: $I = -I_c \sin(\phi) = |I_c| \sin(\phi + \pi)$ [5, 6]. Such a $\pi$ JJ obviously has $\phi = \pi$ in the ground state and the solution $\phi = 0$ corresponds to the energy

maximum and is unstable. These novel types of Josephson junctions have been recently realized using SFS [7, 8] and SIFS [9] technologies. They may substantially improve the parameters of various classical and quantum electronic circuits [10–12].

Even more interesting things happen when the coupling of superconducting electrodes changes within a single Josephson junction, i.e. one half is a 0 JJ and the other half is a $\pi$ JJ. This is the so-called 0–$\pi$ junction. If the 0 and $\pi$ parts are symmetric (equal critical currents and lengths), the ground state of the system corresponds to a spontaneously formed vortex of supercurrent circulating around the 0–$\pi$ phase boundary. The ground state of the system is degenerated, as the spontaneously circulating currents may rotate clockwise or counter-clockwise. The circulating motion of Cooper pairs generates a magnetic field with the flux $|\Phi| \leq \Phi_0/2$ inside the junction. In case of a long one-dimensional junction, with junction length $L$ being much larger than the Josephson penetration depth $\lambda_J$, the vortex has the size $\sim \lambda_J$ and carries the flux $\Phi = \pm\Phi_0/2$, i.e. a semifluxon [13, 14]. For a shorter junction length the vortex does not fit into the junction and the flux inside the junction is reduced. The semifluxons have been actively studied both in theory and experiment during the past few years[15–20, and references herein] .

For the first time semifluxons were observed using $d$-wave superconductors at so-called tricrystal grain boundaries [21] and later in $YBa_2Cu_3O_7$–Nb ramp zigzags [22]. In these systems the phase shift of $\pi$ takes place inside the $d$-wave superconductor and not at the barrier.

Due to the advent of controlled coupling by proper chosen ferromagnetic thicknesses, 0–$\pi$ JJs have also recently been realized in low-$T_c$ SFS-like systems [23]. However there are still some disadvantages, such as the uncontrolled preparation of the 0–$\pi$ phase boundary and the indirect detection of the spontaneous flux in SFS junction by an adjacent SIS junction. Furthermore, this system is strongly dissipative due to the absence of a tunnel barrier.

In this thesis I present high quality 0 and $\pi$ Josephson tunnel junctions and the first *controllable* 0-$\pi$ *tunnel* JJ of SIFS type that are fabricated using a $Nb/Al_2O_3/Ni_{60}Cu_{40}/Nb$ heterostructure.

This thesis is organized as follows. In Chapter 1 a review of the theory of superconductivity relevant for the topics discussed in this thesis is given and the special case of two weakly coupled superconductors, i.e. a conventional Josephson junction (0 JJs), is discussed. Chapter 2 focuses on the physics of induced superconductivity in a ferromagnetic film. The coexistence of magnetism and superconductivity in one and the same material or their interaction in spatially separated materials leads to a number of interesting new phenomena. The peculiar property of $\pi$ JJs with inversion of the coupling in the ground state will be described. In Chapter 3 the concept of a junction with one half being 0 and the other half being $\pi$ coupled, i.e. the so-called 0–$\pi$ junction, is presented. Chapter 4 explains the technological aspects of sample fabrication. Special attention is paid to the interface properties of the multilayer heterostructures and the oxidation process. The formation of a uniform tunnel barrier is essential for low-dissipative junctions. Of further importance is the patterning of samples to obtain a low junction-to-junction variation of parameters. The formation of a step in the F-layer to fabricate a 0–$\pi$ junction will be described in detail. Chapter 5 concerns about the ferromagnetic material that was employed

as a phase-change interlayer. Chapter 6 contains a detailed report on the studies of 0 and $\pi$ coupled SIFS junctions. Results of extensive transport measurements are given. The last Chapter 7 is devoted to the spontaneous flux arising in 0–$\pi$ junctions. The determination and calculation of the intrinsic spontaneous magnetic flux in the junction are shown and the major results of this thesis are presented.

Some interesting experiments based on the SIFS junction were performed in cooperation with the University of Tübingen and the Walther-Meissner-Institut in Garching, respectively. Appendix A is dedicated to Low Temperature Scanning Electron Microscopy (LTSEM) experiments on Josephson tunnel junctions with ferromagnetic interlayer. Experiments were done on samples with different thicknesses of the F-layer and with various geometries of the junction area. The effect of an external magnetic field on the Josephson current is studied. Appendix B deals with the escape of the phase of a current-biased $\pi$ Josephson tunnel junction from the zero-voltage state by means of thermal activation or quantum tunneling as well as the presence of weak microwave radiation at temperatures down to 40 mK.

# Part I

# Theory

# Chapter 1

# Basic properties of Josephson junctions

In this Chapter I give a short review on superconductivity and a detailed study of the general properties of two coupled superconductors. Of special interest are Josephson junctions (JJs) with a dielectric tunnel barrier. The dynamics of charge carriers and of the electromagnetic fields in the Josephson junction are related to the phase difference $\phi$ of the wave functions $\Psi_{1,2}$ of each superconducting condensate. The static and dynamic properties of the Josephson junctions are discussed.

## 1.1 Superconductivity

The most striking property of a superconductor is the vanishing electrical resistance, when cooled below the transition temperature $T_c$, as discovered in 1911 by Heike Kamerlingh-Onnes [24]. This effect was later called *superconductivity*. Moreover its ideal diamagnetic behavior when placed in magnetic fields (Meissner effect) and the quantization of the magnetic flux through a hole in a superconductor are likewise staggering.

According to the microscopic theory by John Bardeen, Leon N. Cooper and John R. Schrieffer [25], developed in 1957 for so-called low-$T_c$ superconductors, on which I will focus on, the conduction electrons are interacting with phonons of the crystal lattice. If the temperature is below $T_c$ the interaction gives rise to an effective attraction between electrons and leads to the formation of the *Cooper pairs* - two electrons with opposite spins and momenta. Due to the anti-parallel combination of electron spins and momenta, the total spin of each pair vanishes. Therefore the Cooper pair has a bosonic character and below $T_c$ all Cooper pairs are condensed into a common electronic ground state of the superconductor. The single electron, or *quasiparticle*, is considered as an excitation. It has an energy at least by $\Delta$ higher than the ground state. The bosonic nature of the Cooper pair enables the description of the superconducting state by an effective macroscopic wave function

$$\Psi(\underline{r}) = \sqrt{n^{\mathrm{CP}}(\underline{r})}\, e^{i\Theta(\underline{r})}, \tag{1.1}$$

with an amplitude proportional to the Cooper pair density $n^{\mathrm{CP}}$ and their phase $\Theta$. The phenomenological theory of superconductivity given by V. Ginzburg and L.

Table 1.1: *Typical values for bulk* Nb *and* Al *from [29].*

| | $T_c$ [K] | $\lambda_L$ [nm] | $\xi_0$ [nm] | $\lambda_L/\xi_0$ | $2\Delta$ [meV] | $B_c$ [T] |
|---|---|---|---|---|---|---|
| niobium | 9.25 | 39 | 38 | 1.02 | 3.0 | 0.21 |
| aluminium | 1.17 | 16 | 1600 | 0.01 | 0.34 | 0.01 |

Landau [26], prior to the BCS theory, gives a very good description of the macroscopic properties at $T \leq T_c$ by using $\Psi$ as the *order parameter*. Two characteristic lengths are introduced: at the vicinity of a superconductor surface or near the interface to an ordinary conductor, the order parameter $\Psi$ varies from its bulk value over the *coherence length* $\xi_0$. The second characteristic length is the *London penetration depth* $\lambda_L$, which describes the fall-off of magnetic fields and screening currents inside a superconductor.

A remarkably interesting phenomena is the quantization of magnetic flux through a superconducting ring. The electromagnetic induction effect (Lenz rule) and the vanishing electrical resistance generate a persistent current whose magnetic flux is frozen. In analogy to atom physics where the wave function of the orbital electron has to contain an integral number of the wavelength, the enclosed magnetic flux in a superconductor can only assume integral multiples of the magnetic flux quantum [27, 28]:

$$\Phi_0 = \frac{h}{2e} = 2.07 \times 10^{-15} \text{ Wb}.$$

The table 1.1 gives an overview about the superconducting properties of niobium and aluminium, which are used to fabricate Josephson junctions for this thesis.[1]

## 1.2 The Josephson Relations

The state of the superconductor can be described by the macroscopic wave function $\Psi$, Eq.(1.1). When two superconductors are brought close together and are only separated by a thin insulating barrier, the wave functions penetrate through the barrier from both sides and couple with each other. The system energy is reduced due to the coupling. The time evolution of the wave functions of the superconductors $1, 2$ on each side of the barrier can be described by

$$i\hbar\frac{\partial\Psi_{1,2}}{\partial t} = E_{1,2}\Psi_{1,2} + K\Psi_{2,1},$$

with the eigenenergies of the superconductors $E_{1,2}$ and the coupling constant $K$ describing the wave functions interaction. It is assumed that a voltage is applied between both superconductors so that $e^*(V_2 - V_1) = E_2 - E_1 = e^*V$ with applied voltage $V$ and $e^* = 2e$ the charge carried by a Cooper pair. By changing the wave

[1] Note that the transition temperature of aluminium is below the standard measuring temperature of 4.2 K.

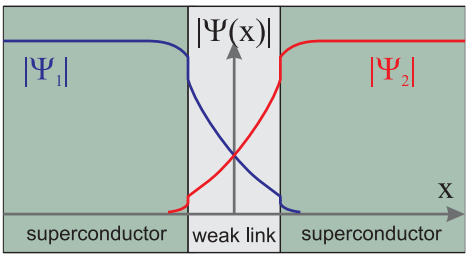


Figure 1.1: *Two superconductors are separated by a weak link, e.g. a tunnel barrier (SIS) or a normal metal (SNS). The proximity effect in the weak link leads to an overlap of the wave functions.*

functions to the more convenient form in terms of the pair densities

$$\Psi_{1,2} = \sqrt{n_{1,2}^{\mathrm{CP}}} e^{i\Theta_{1,2}},$$

the *gauge invariant phase difference* across the junction is introduced as

$$\phi = \Theta_2 - \Theta_1. \tag{1.2}$$

One obtains

$$\frac{\partial n_{1,2}^{\mathrm{CP}}}{\partial t} = \pm \frac{2}{\hbar} K \sqrt{n_1^{\mathrm{CP}} n_2^{\mathrm{CP}}} \sin\phi, \tag{1.3}$$

and

$$\frac{\partial \Theta_{1,2}}{\partial t} = -\frac{K}{\hbar} \sqrt{\frac{n_1^{\mathrm{CP}}}{n_2^{\mathrm{CP}}}} \cos\phi \pm \frac{eV}{\hbar}. \tag{1.4}$$

The rate of pair density change in one superconductor is opposite to that in the other. No change in total pair density is happening, as this would create a charge imbalance. Instead, this displays just a tendency to change the pair charge density due to the supercurrent flowing from one electrode to the other. Equation (1.3) can be written to obtain the *first Josephson relation* [4]

$$j_s = j_c \sin\phi, \tag{1.5}$$

where the critical current density $j_c$ is a constant. The free energy $E_J$ of the Josephson junction, the so-called *Josephson energy* is generally given by the integral

$$E_J(\phi) = \frac{\Phi_0}{2\pi} A \int_0^{\phi} j_c \sin(\phi)\, d\phi = \frac{\Phi_0}{2\pi} I_c (1 - \cos\phi), \tag{1.6}$$

where $I_c = A \cdot j_c$ is the critical current and $A$ the junction area. In case that the phase difference $\phi$ between both superconductors is zero, the energy gain from coupling is maximal, and is reduced as $\phi \to \pi/2$ and the current density $j$ raises to its maximum $j_c$. For larger currents the Josephson junction switches into the voltage state. The

motion of the phase $\phi$ can be calculated from equation (1.4) using Eq.(1.2) to obtain the *second Josephson relation*:

$$\frac{\partial \phi}{\partial t} = \frac{2e}{\hbar} V = \frac{2\pi}{\Phi_0} V. \tag{1.7}$$

Thus, if the applied voltage is constant, I get for the phase $\phi = \phi_0 + \omega_J t$, where

$$\omega_J = \frac{2\pi}{\Phi_0}\mathrm{V} = \frac{2\mathrm{e}}{\hbar}\mathrm{V} \quad \text{with} \quad \frac{1}{\Phi_0} = 483.6\ \frac{\mathrm{MHz}}{\mu\mathrm{V}}. \tag{1.8}$$

Using the first Josephson relation (1.5)

$$j_s = j_c \sin(\omega_J t + \phi_0).$$

The time average of the evolution of phase can be monitored by measuring the dc voltage across the junction and using the second Josephson relation (1.7)

$$\langle V \rangle = \left\langle \frac{\partial \phi}{\partial t} \right\rangle \frac{\Phi_0}{2\pi}.$$

Under an applied dc voltage across the weak link the current through the barrier is an ac current with the *Josephson frequency* $\omega_J \propto \mathrm{V}$.

### 1.2.1 Types of Josephson junctions

A Josephson junction is formed by two superconductors separated by a thin insulator (SIS type), so that the Cooper pairs can tunnel through it. The Josephson effect was first observed in such so-called *Josephson tunnel junctions* (SIS) [30]. Besides tunnel junctions, a weak link between two superconductors can be formed in many other ways, such as superconductor-normal metal-superconductor (SNS) sandwiches, thin film bridges, point contacts [31], grain boundary junctions or others [32]. For the work presented here SIS, SINS and SIFS-like Josephson junctions were investigated, with F being the ferromagnetic layer (see Chapter 2 for details).

## 1.3 Tunneling of Cooper pairs and quasiparticles

I want to focus on the current transport through an SIS-type Josephson tunnel junction. The different tunneling regimes for the current-biased junctions are plotted in the I-V characteristic (IVC) in Fig. 1.2(a) and the energy scheme in Fig. 1.2(b).
• A: Starting from zero current, the zero voltage current branch corresponds to the tunneling of the Cooper pairs, as described by the dc Josephson relation (1.5).
• B: When reaching the critical value $I_c$ the lossless current transport breaks down and the system jumps into a voltage state that corresponds to the double gap energy $2\Delta/e$. The gap energy expresses the binding energy of the Cooper pairs. For the voltages $V = 2\Delta/e$ the tunneling current is dominated by quasiparticles, i.e. single electrons, as the peaks in the densities of states of both superconductors are overlapping.

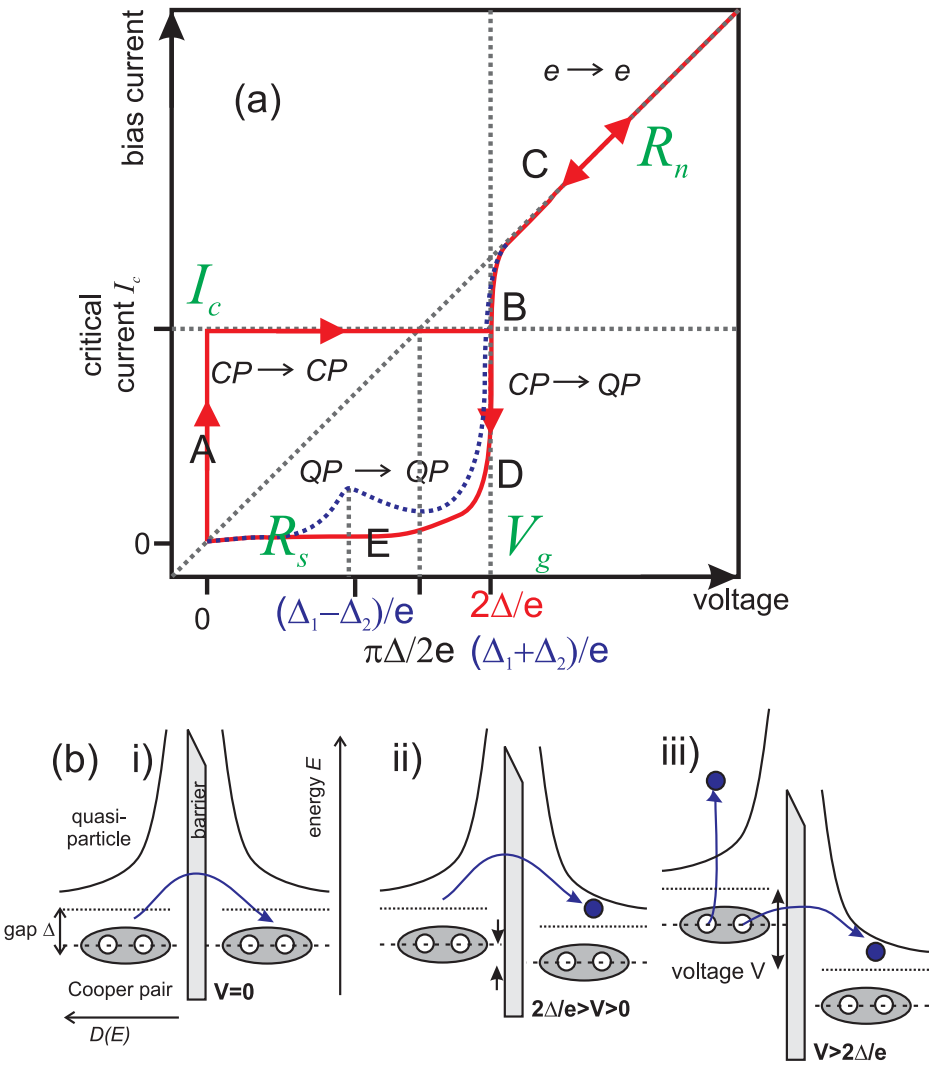


Figure 1.2: *(a) I-V characteristic of Josephson tunnel junctions (SIS: red, $S_1IS_2$: blue) with different tunneling regimes. Indicated by $I_c$ is critical current, $V_g$ gap voltage, $R_n$ normal resistance and $R_s$ subgap-resistance; (b) Bose representation of electron density states of superconductor i) Cooper pair tunneling ($CP \rightarrow CP$), ii) quasiparticle tunneling ($QP \rightarrow QP$) and iii) Cooper pair dissociation and tunneling into quasiparticle states ($CP \rightarrow QP$).*

• C: A further increase of the bias current merely displays Ohm's law at $V > 2\Delta/e$ with normal resistance $R_n$ and direct tunneling of single electrons.
• D: When the bias current is decreased a hysteretic behavior is observed. The tunneling current remains to be carried by quasiparticles and for zero temperature the

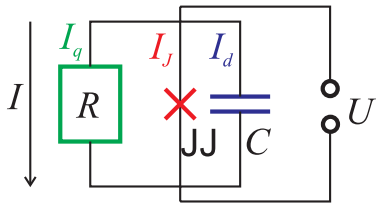


Figure 1.3: *Equivalent circuit in the RCSJ model. R and C denote the shunt resistor and capacitor, respectively. The ideal Josephson junction is depicted by the cross.*

current should decrease to zero before the systems jumps into the zero voltage state again.
• E: For finite temperatures a sub-gap quasiparticle current is observed due to the temperature induced breaking of Cooper pairs. In case of $\Delta_1 \neq \Delta_2$ a peak in the IVC appears at $V = \mid (\Delta_1 - \Delta_2)/2 \mid$. More details can be found in Fig. 1.2.

### 1.3.1 Resistively and Capacitively Shunted Junction model

W. C. Stewart [33] and D. E. McCumber [34] introduced a simple model of equivalent circuits for Josephson junctions to describe the I-V characteristic of a Josephson junction for bias currents below and above the critical current $I_c$. The model is called *Resistively and Capacitively Shunted Junction* (RCSJ) model. According to the Kirchhoff circuit law equations, the total current flowing through such a system is the sum of the currents in each of the three paths, i.e. the Josephson-current $I_J$, the quasiparticle current $I_q$ and the displacement current $I_d$ (cf. Fig. 1.3). Assuming that the resistance $R$ is voltage independent $I_q = V/R$, only valid for small tunnel currents, the total current $I$ can be expressed as

$$I = I_J + I_q + I_d = I_c \sin\phi + \frac{V}{R} + C\dot{V},$$

with condensator $C = I_d/\dot{V}$ carrying the displacement current and ohmic shunt resistance $R$ for the normal electron current. The voltage $V_c = I_c R$ is the *characteristic voltage* of the Josephson junction. Inserting the second Josephson relation (1.7), yields a differential equation for phase difference $\phi$

$$0 = \underbrace{-I + I_c \sin\phi}_{\partial U/\partial\phi} + \frac{1}{R}\frac{\Phi_0}{2\pi}\dot{\phi} + C\frac{\Phi_0}{2\pi}\ddot{\phi}. \tag{1.9}$$

Normalizing the time to the inverse of the plasma frequency $t = \omega_{p0}^{-1}\tau$, I obtain from Eq.(1.9) the equation of motion for the phase difference

$$0 = -\gamma + \sin\phi + \frac{1}{\sqrt{\beta_c}}\dot{\phi} + \ddot{\phi}. \tag{1.10}$$

The plasma frequency is given by

$$\omega_{p0} = \sqrt{\frac{2\pi I_c}{\Phi_0 C}} \tag{1.11}$$

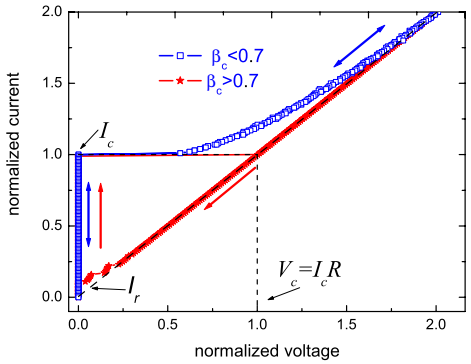


Figure 1.4: *I-V characteristic for over- (blue) and underdamped (red) current-biased junctions. Calculated using* StkJJ *simulator [35].*

and the bias current $I$ through a Josephson junction is normalized to the critical current $I_c$ and called $\gamma$. Eq.(1.10) is a nonlinear second order differential equation and identical to that describing a driven and damped pendulum. The dimensionless, material dependent parameter

$$\beta_c = \frac{2\pi I_c R^2 C}{\Phi_0}$$

is called *Stewart-McCumber* parameter. It is the inverse square root of the dimensionless damping coefficient $\alpha = 1/\sqrt{\beta_c}$ and describes the damping of the plasma oscillations in the junction.

Junctions with dielectric barriers such as $Al_2O_3$ have usually a high $RC$ product and therefore a high $\beta_c$ and low damping coefficient $\alpha$. In the I-V characteristic, shown in Fig. 1.4, this manifests as a large hysteresis, when one measures in the current-biased mode. Junctions with a metallic interlayer instead of a tunnel barrier, i.e. SNS-type junctions, usually have $\beta_c$ below 0.7 and are overdamped (see Fig. 1.4). In the low damping limit ($\beta_c \gg 1$), the Josephson junction can be still in the voltage state for bias currents $I < I_c$ and switches back to the zero-voltage state at the return current $I_r$. For strongly underdamped junctions $\beta_c$ can be calculated from measured $I_c$ and $I_r$ as

$$\beta_c \overset{\beta_c \gg 1}{\approx} \left[\frac{4}{\pi}\frac{I_c}{I_r}\right]^2 . \tag{1.12}$$

The SIFS-type junctions, which are subject of this thesis, have some intermediate values of $\beta_c$, that strongly depend on the thickness of the F-layer and the temperature (see Chap. 6.4).

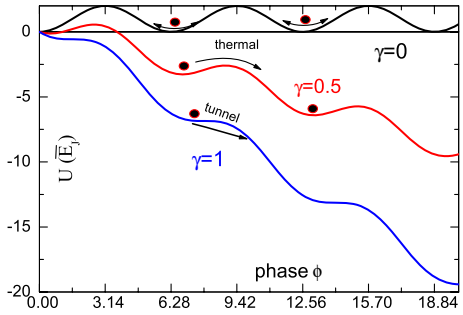


Figure 1.5: *"Tilted washboard" potential for different bias currents $\gamma = I/I_c$. The phase particle is indicated by a circle.*

### 1.3.2 Temperature dependence of $j_c$ in SIS and SNS junctions

The temperature dependence of the maximum supercurrent density, the so-called critical current density $j_c$, through an SIS junction was calculated from microscopic theory by Ambegaokar and Baratoff [36, 37] as

$$j_c(T) = \frac{\pi}{2}\frac{\Delta(T)}{e\rho_0}\tanh\frac{\Delta(T)}{2k_BT},$$

where $\Delta(T)$ is the temperature dependent energy gap of the (identical) superconductors, $k_B$ is the Boltzmann constant and $\rho_0$ is the specific resistance per unit area. For SNS junctions the temperature dependence of the critical current density is [25]

$$j_c(T) = \frac{3\pi}{2e}\frac{\Delta(T)}{\rho_0^2 k_B T}\frac{d_N/\xi_N}{\sinh\left(d_N/\xi_N\right)},$$

with $\xi_N$ the characteristic coherence length of the Cooper pair density inside the normal metal N and $d_N$ its thickness. Note that in both cases (SIS and SNS-type junctions) the critical current density $j_c(T)$ increases for decreasing temperature.

### 1.3.3 Washboard potential

The potential energy $U$ of the system can be derived by considering the Eq.(1.9) as the second Newtons law $ma = F$, and formally defining $U$ as $F = -\partial U/\partial\phi$. In this case $U$ has the form:

$$U(\gamma,\phi) = -\bar{E}_J\left(\gamma + \cos\phi - 1\right), \tag{1.13}$$

with Josephson energy $\bar{E}_J = \frac{I_c\Phi_0}{2\pi}$.

The dynamics of the Josephson phase is equivalent [33, 34] to that of a particle of mass $m = C\left(\frac{\Phi_0}{2\pi}\right)^2$ with velocity $\dot{\phi}$ proportional to the voltage and coordinate $\phi$ moving in the tilted washboard potential $U$, see Eq.(1.13). Depending on the current bias $\gamma$ and the damping $\alpha$, the phase $\phi$ can be constant, oscillate with small

amplitude, rotate over $\pi$, $2\pi$ et cetera. In case of small phase oscillations, the average voltage is zero, whereas if the phase rotates, a dc-voltage drop appears across the junction.
For currents $\gamma < 1$, the particle is in the so-called *locked state*, where it is trapped in a local minimum and may oscillate with the plasma frequency

$$\omega_p(\gamma) = \omega_{p0} \left(1 - \gamma^2\right)^{1/4},$$

where $\omega_{p0}$ is the oscillation frequency of the particle when the potential is not tilted.

The damping is given by a dimensionless damping parameter $\alpha = 1/Q = 1/\sqrt{\beta_c}$, where $Q = \omega_p RC$ is the quality factor. A current $\gamma$ through the Josephson junction tilts the potential and the slope depends on the bias current $\gamma$. Therefore, the potential barrier height, which separates two local minima, decreases with increasing $\gamma$, see Fig. 1.5.

When the bias current is ramped from $\gamma = 0$ up to 1, the junction is in the zero voltage state in the absence of thermal and quantum fluctuations.

At finite temperature, the Josephson phase may switch or *escape* from a shallow minimum into a finite voltage state even for $\gamma < 1$. Two escape mechanisms are present. Due to the thermal energy, the particle escapes from the well over the barrier, which is the so-called *classical* or *thermal escape*. It was introduced by Kramers [38] and later extended by Büttiker *et al.* [39] for the case of an underdamped Josephson junction. Including quantum mechanics, the so-called *quantum escape* or *macroscopic quantum tunneling* (MQT) [40] can take place. The particle in Fig. 1.5 has a finite probability to tunnel through the potential well even for $\gamma < 1$.

Another quantum phenomena is the existence of quantized energy levels in the washboard potential (1.13), which can be probed spectroscopically by exciting the phase from the ground state to higher energy levels. This is similar to the quantized energy states of a harmonic oscillator. The microwave induced population of the higher energy levels can be observed in the distribution of switching current $I_{sw}$ of the Josephson junctions (cf. Ref. [41, 42]).

## 1.4 Josephson junction in magnetic field

The aim of this Section is to derive the influence of an in-plane magnetic field on the supercurrent through the junction (see Fig. 1.6). For the sake of simplicity the magnetic field of the bias current is neglected. The effective magnetic thickness $\Lambda$ of the junction for the magnetic field penetration, caused by screening currents, is defined by the London penetration depth $\lambda_L$ and the thicknesses of the superconducting electrodes $t_1$ and $t_2$. The quantity $\Lambda$ is given by [43]:

$$\Lambda = d_I + \lambda_L \tanh\left(\frac{t_1}{2\lambda_L}\right) + \lambda_L \tanh\left(\frac{t_2}{2\lambda_L}\right).$$

In case of thick superconducting electrodes ($t_1, t_2 \gg \lambda_L$) this reduces to $\Lambda = d_I + 2\lambda_L$.

The characteristic length scale for spatial variation of $\phi(x)$ is the *Josephson penetration depth* $\lambda_J$. This length indicates how far a magnetic field can penetrate into

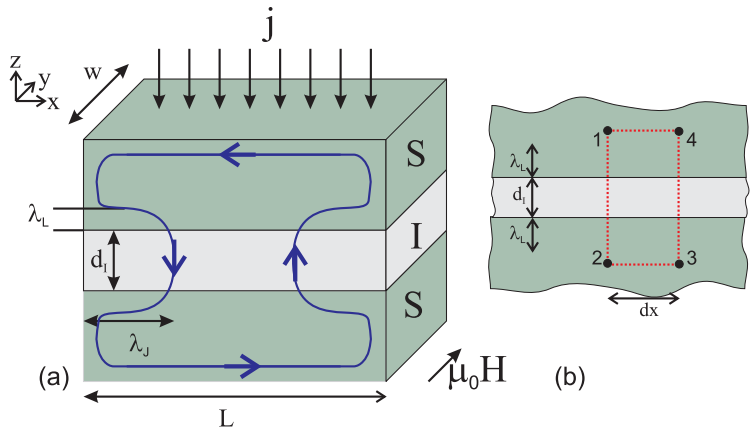


Figure 1.6: *i) Distribution of the screening currents for a Josephson tunnel junction in magnetic field H, ii) closed integration path across tunnel barrier.*

an extended Josephson junction of length $L \gg \lambda_J$. The Josephson penetration depth is defined as:

$$\lambda_J = \sqrt{\frac{\Phi_0}{2\pi\mu_0 d' j_c}}. \tag{1.14}$$

The quantity $d'$ is given by

$$d' = d_I + \lambda_L \coth\left(\frac{t_1}{\lambda_L}\right) + \lambda_L \coth\left(\frac{t_2}{\lambda_L}\right),$$

and reduces to $d' = d_I + 2\lambda_L$ if $t_1, t_2 \gg \lambda_L$.

As one can see from the Eq.(1.14) $\lambda_J$ is inversely proportional to the square root of critical current density $j_c$. Therefore the normalized length $\ell = L/\lambda_J$ can be varied by changing $j_c$. If either the junction length $L$ or width $w$ is much larger than $\lambda_J$ the so-called *long Josephson junction* (LJJ) is obtained. Usually one studies one-dimensional LJJs, i.e. $L \geq \lambda_J$ and $w \leq \lambda_J$, see Section 1.4.1.

The magnetic field $\overrightarrow{H}$ parallel to the layers is related to the gauge invariant phase difference $\phi$, Eq.(1.2), as

$$\phi = \Theta_2 - \Theta_1 + \frac{2\pi}{\Phi_0}\int \overrightarrow{A}\,\overrightarrow{dl},$$

where $\overrightarrow{A}$ is the electromagnetic vector potential. The phase difference for two different points separated by $dx$ at coordinate $x$ is then (Fig. 1.6)

$$\phi(x+dx) - \phi(x) = \frac{2\pi}{\Phi_0}\left[\int_1^2 \overrightarrow{A}(x+dx) - \int_3^4 \overrightarrow{A}(x)\right].$$

The enclosed flux in the path $\overline{1234}$ (Fig. 1.6(b)) is calculated as

$$\delta\Phi = \int_S \mu_0 \overrightarrow{H}\overrightarrow{dS} = \oint \overrightarrow{A}\,\overrightarrow{dl} = \int_1^2 \overrightarrow{A}\,\overrightarrow{dl} + \underbrace{\int_2^3 \overrightarrow{A}\,\overrightarrow{dl}}_{0} + \int_3^4 \overrightarrow{A}\,\overrightarrow{dl} + \underbrace{\int_4^1 \overrightarrow{A}\,\overrightarrow{dl}}_{0}. \tag{1.15}$$

The second and fourth term in Eq.(1.15) are vanishing when the horizontal parts of the integration path are considerably deeper from the barrier in the superconductor than $\lambda_L$.[2] Taking the enclosed magnetic flux $\Phi$ into account one gets for a differentially small section $dx$ of the junction

$$\frac{\phi(x+dx)-\phi(x)}{dx} = \phi_x = \delta\Phi = \frac{2\pi}{\Phi_0}\Lambda\mu_0 H,$$

where $\mu_0$ is the vacuum permeability and $\Lambda\mu_0 H$ is the magnetic flux per unit length. Therefore, the magnetic field induces a gradient of the phase difference, i.e. the Josephson phase $\phi$, across the Josephson junction. Assuming that $L \leq \lambda_J$, the magnetic field penetrates uniformly. Then one can integrate to arrive to

$$\phi = \frac{2\pi}{\Phi_0}\Lambda\mu_0 H x + \phi_0,$$

and the current density as

$$j(x) = j_c \sin\left(\phi(x)\right) = j_c \sin\left(\frac{2\pi}{\Phi_0}\Lambda\mu_0 H x + \phi_0\right).$$

The local supercurrent density is sinusoidally oscillating along the junction. The total supercurrent is given by $I_c(H,\phi_0) = \int j(x)dx$. The maximum supercurrent for a given field is calculated by maximizing $I_c(H,\phi_0)$ with respect to $\phi_0$:

$$I_c(H) = \int_L j_c(x) \sin\left(\frac{2\pi}{\Phi_0}\Lambda\mu_0 H x + \phi_0\right) dx = I_c \left|\frac{\sin \pi\frac{\Phi}{\Phi_0}}{\pi\frac{\Phi}{\Phi_0}}\right|, \tag{1.16}$$

assuming at the last equal sign:

- homogenous critical current density $j_c$
- rectangular junction with junction length $L$ and $I_c = L^2 j_c$
- $\Phi = \mu_0 H \Lambda L$ is the flux induced by $H$ on the total JJ cross section

This results holds only for short Josephson junctions (SJJ) ($L \leq \lambda_J$) and if the self fields of the bias current are neglectable. The sinc-type critical current diffraction pattern is often referred to as *Fraunhofer pattern* (Fig. 1.7) in analogy to the diffraction of light through a slit.

### 1.4.1 Sine-Gordon-model

I want to derive the general differential equation for a long Josephson junction. In this model, the junction is described by a parallel connection of small RCSJ-like JJs interconnected by a parallel connection of an inductance and a resistance. Superconducting screening currents and penetrating magnetic field from outside the interface are required to investigate the local current density $j(x)$. The external bias current density $j_e$ and the magnetic field $H(x)$ are added. The external current $I_e$ is

[2] The case of thin electrodes $\approx \lambda_L$ is treated by Weihnacht [43].

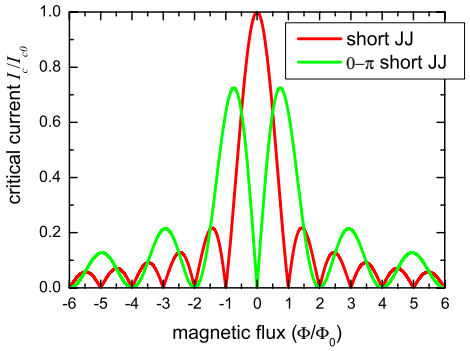


Figure 1.7: *$I_c(H)/I_c(0)$ pattern of a short JJ (red line) and a short 0–$\pi$ JJ (green line), discussed in Chap. 3.*

injected in each JJ and the external magnetic flux $\Phi$ threading each junction cell is taken into account. The wave equation is derived considering the flux quantization and the inductive current $I_d^n$

$$\phi_{n+1} - \phi_n = \frac{2\pi}{\Phi_0}\left(\Phi - \mu_0 d' I_d^n dx\right)$$

where the magnetic flux through each junction loop n can be expressed as $\Phi = \mu_0 \Lambda H dx$. After some calculations based on the Kirchhoff law and the subsequent transformation to the continuous limit (see for example [14]) one gets for the spatial variation of $\phi$ due to external magnetic fields

$$\frac{\Lambda}{d'}\frac{\partial H(x)}{\partial x} - j_c \lambda_J^2 \frac{\partial^2 \phi}{\partial x^2} = j_e - j, \tag{1.17}$$

where $j$ the current density through the Josephson barrier. Rewriting the Eq.(1.9) in terms of the local current densities yields:

$$j(x) = j_c \sin\phi + \frac{\Phi_0}{2\pi\rho_0}\dot{\phi} + \overline{C}\frac{\Phi_0}{2\pi}\ddot{\phi}, \tag{1.18}$$

with specific resistance $\rho_0$. Here $C^* = \epsilon\epsilon_0/d_I$ is the capacitance per unit area and $d_I$ is the insulator thickness. Equation (1.17) can then be expressed using Eq.(1.18)

$$\lambda_J^2 \frac{\partial^2 \phi}{\partial x^2} - \frac{1}{\omega_{p0}^2}\frac{\partial^2 \phi}{\partial t^2} - \sin\phi = \frac{1}{\omega_c}\frac{\partial \phi}{\partial t} - \frac{j_e}{j_c} + \frac{2\pi\mu_0\Lambda\lambda_J^2}{\Phi_0}\frac{\partial H}{\partial x} \tag{1.19}$$

as partial differential equation in one dimension and time with the *Josephson plasma frequency* $\omega_{p0}$, cf. Eq.(1.11), and the *characteristic frequency* $\omega_c = 2\pi j_c \rho_0/\Phi_0$. Equation (1.19) is the *perturbed sine-Gordon equation* [31] which describes the long Josephson junction as a non-linear system with the boundary conditions given by the junction geometry and the externally applied magnetic field. For theoretical investigation of the system standard normalized units are used, i.e. the coordinate is normalized

to the Josephson penetration depth $\lambda_J$ and the time to the inverse plasma frequency $\omega_{p0}^{-1}$. After such normalization the Eq.(1.19) becomes

$$\phi_{xx} - \phi_{tt} - \sin\phi = \alpha\phi_t - \gamma + h_x(x), \tag{1.20}$$

with the dimensionless damping coefficient $\alpha$ the normalized bias current density $\gamma$ and $h(x) = \mu_0 H(x) 2\pi\Lambda\lambda_J/\Phi_0$. There are no analytical solutions of Eq.(1.20) for the general case.

## 1.5 Excitation in long Josephson junctions

In long Josephson junctions ($L \gg \lambda_J$) exists many linear and non-linear electromagnetic excitations. They can be analyzed theoretically by considering the junction as a non-linear waveguide described by the sine-Gordon equation (1.20) [44].

The analogy between the dynamical equation describing a short Josephson junction and that describing a simple plane pendulum subjected to damping $\sim \alpha$ and an applied mechanical torque $\sim \gamma$ is well known and is widely utilized, see [45, 46]. In extension of this analogy to the case of long Josephson junctions an elastic coupling between adjacent pendula described via $\phi_{xx}$ is added, see Eq.(1.20).

In a long Josephson junction are three types of fundamental excitations: *plasma oscillations*, *breathers* and *fluxons*[47].

• *Plasma oscillations* stem from oscillatory motions of a single pendulum. In the simplest case all the pendula in a chain oscillate in phase. The motion is equivalent to the eigen oscillations of a single pendulum. Less trivial are the running or standing plasma waves $\phi \propto \sin(kx - \omega t)$ with dispersion relation $\omega = \sqrt{1 + k^2}$, which have a gap in the spectrum of allowed frequencies from 0 to $\omega_{p0}$. The velocity of electromagnetic waves in the barrier is given by

$$\bar{c}_0 = \lambda_J \omega_{p0} = c\sqrt{\frac{d_I}{\epsilon d'}},$$

reflecting the fact that electric fields exist only across the barrier thickness $d_I$, whereas magnetic fields exist throughout the magnetic field penetration $d'$. $\bar{c}_0$ is called *Swihart velocity* [48], which is typically equal to a few percent of the speed of light $c$ in vacuum.

• *Breather oscillations* are unstable with respect to the perturbation terms and therefore they decay after some transient time. They can be interpreted as a bound state of a fluxon-antifluxon pair.

• The *fluxon* stems from rotary or *over the top* motions of a single pendulum. A single fluxon is just a $2\pi$ twist in the pendulum chain. The fluxons are highly robust objects. They emerge due to topological reasons, therefore they are called topological solitons. Mathematically, the fluxon corresponds to a $2\pi$ kink of the phase $\phi(x)$, see Fig. 1.8. For the analytical solution of the unperturbed sine-Gordon equation (1.20) (r.h.s. is zero) the function

$$\phi(x,t) = 4\arctan\left[\exp\left(-\frac{x - X(t)}{\sqrt{1 - u^2(t)}}\right)\right]$$

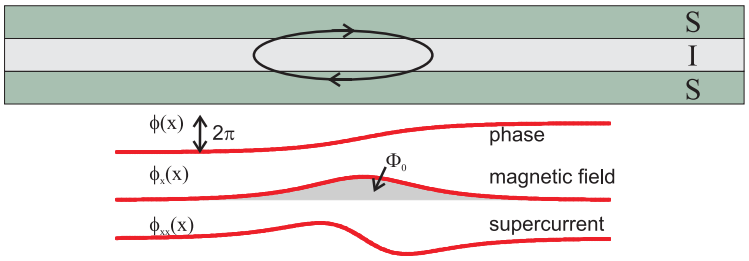


Figure 1.8: *Appearance of a fluxon in a long Josephson junction (top) as a $2\pi$-kink in the phase difference $\phi(x)$ and as a solitary wave with the magnetic field proportional to $\phi_x(x)$ and supercurrent $\phi_{xx}(x)$.*

is chosen, which is the well-known single soliton solution (traveling wave) to the sine-Gordon equation with $X(t) = ut$ and constant $u$ with $|u| \leq \bar{c}_0$. The magnetic field associated with the phase change of a fluxon is given by $\phi_x(x)$ and its total flux is the magnetic flux quantum $\Phi_0$. This magnetic flux is generated by a circulating supercurrent $j(x) = \sin(\phi(x))$, often called Josephson vortex, located between the superconducting films separated by the weak link, as depicted in Fig. 1.8. A sketch of phase, magnetic field and supercurrent associated with a fluxon can be found in the Fig. 3.1, too.
The fluxon behaves very much like a relativistic particle with respect to the limiting velocity $\bar{c}_0$, carrying a magnetic flux equal to $\pm\Phi_0$. It interacts with the environment of the junction, such as an externally applied magnetic field and injected currents.
The 0–$\pi$ LJJ system, where a $\pi$ kink of phase takes place, is described in Chapter 3.

### 1.5.1 Zero Field steps (ZFS)

Applying a bias current $0 < \gamma < 1$ through the junction in the absence of a magnetic field causes a uniform phase $\phi = \arcsin\gamma$. After introducing a fluxon into the junction it will be pushed to one end of the junction via the Lorentz force, caused by the bias current $\gamma$. If the fluxon arrives to one end of the junction with enough kinetic energy the pendulum chain will continue to wind op. The end pendulum will undergo a rotation of $2\pi + 2\pi = 4\pi$ and the resulting *antifluxon* will be pushed towards the other junction end. This leads to a dynamic steady state, with the fluxon bouncing back and forth along the junction. In the mechanical model the angular velocity corresponds to a voltage $\sim \dot{\phi}$ in the junction and a state with $\langle\dot{\phi}\rangle \neq 0$ manifests as steps in the current-voltage characteristic when tracing out the Stewart-McCumber branch. At sufficiently slow rotation velocity the pendulum chain can spontaneously develop a dynamic instability that results in one or more fluxons trapped in the LJJ, and *zero field steps* (ZFS) appear in I-V characteristic when increasing the bias current again. The asymptotic voltage of these steps is given by

$$V_{\mathrm{n,ZFS}} = \frac{n \cdot \Phi_0 \cdot \bar{c}_0}{L}, \tag{1.21}$$

where $n$ is the number of fluxons in the junction and $L$ is the junction length [49]. At a bias current $\gamma < 1$ the systems switches back to the quasiparticle curve shown in Fig. 1.2(a).

In presence of damping some energy is lost during the reflection at each edge. If the kinetic energy is not sufficient enough to survive the reflection the junction phase relaxes after short breather-like transient oscillations into the static equilibrium: $\phi = 0$.

### 1.5.2 Fiske steps

By switching on an external magnetic field $H$ in-plane and perpendicular to the LJJ axis, the reflection of fluxons becomes energetically adverse. The external field adds energy to fluxons reflected at one boundary, but subtracts energy on the opposite side. This breaks the symmetry and leads to an unidirectional fluxon motion for sufficient high magnetic fields. Fluxons are nucleated at one end and decay at the opposite end of the junction. The energy released in the decay process may propagate as decaying oscillation with velocity close to the Swihart velocity $\bar{c}_0$ to the other end of the junction. If the effective length of the junction $\ell = L/\lambda_J$ is of the order of the coherence length of the oscillations or shorter, then the electromagnetic wave reaches the opposite edge of the junction. After the reflection it interferes with itself and forms a standing wave. The frequency of oscillations of the Josephson phase $\phi$ in the standing wave is defined by the length of junction, the Swihart velocity of the electromagnetic waves and mode number n. The pumping of energy into the standing electromagnetic wave, when the fluxon leaves the junction, takes place in phase with the wave. This gives rise to resonances, so-called *Fiske steps*, in the IVC [50] with asymptotic voltage

$$V_{\mathrm{n,FS}} = \frac{n \cdot \Phi_0 \cdot \bar{c}_0}{2 \cdot L},$$

which is just half of the spacing for ZFSs.

## 1.6 Shapiro steps

An interesting effect is that the Josephson phase $\phi$ can be become phase-locked to an externally applied alternating current, i.e. a microwave with the frequency $\omega_{rf}$. This happens if the Josephson frequency $\omega_J$ is nearly similar to an integral multiple of the microwave frequency, i.e. $\omega_J = n \cdot \omega_{\mathrm{rf}}$. The phase changes synchronously to the external frequency ($\frac{\partial \phi}{\partial t} = \omega_{\mathrm{rf}}$). After Eq.(1.7) this corresponds to a voltage of

$$V_s = \frac{\Phi_0}{2\pi}\omega_{rf}.$$

The phase-locking can be observed as the appearance of a current step, the so-called *Shapiro step*, at multiples of the voltage $V_s$ in the IVC [51]. The maximum critical current depends on the microwave power and is described by the Bessel function $J_0(A)$. Here $A$ is the amplitude of the microwave.

# Chapter 2

# JJs with ferromagnetic barrier

In the preceding Chapter the simple case of a Josephson junction with a non-magnetic barrier (SIS and SNS type) was considered. In this Chapter the physics of Josephson junctions with a ferromagnetic interlayer is reviewed.

Superconductivity, which causes ideal diamagnetism (at least in low $T_c$ superconductors) and ferromagnetism were long though as contradicting phenomena, as the magnetic field can destroy conventional superconductivity by exchange mechanism. Microscopically they are two competing phenomena: while ferromagnetism forces the spins to be aligned in parallel, the singlet superconductivity prefers antiparallel spin orientation of the electrons in Cooper pairs. Actually, interesting physics can be studied when the two phenomena are combined in superconducting ferromagnets, ferromagnetic superconductors or as follows, in heterostructures of thin magnetic and superconducting layers [52].

## 2.1 The $\pi$ state

As pointed out in Chapter 1, the current-phase relation $I_s(\phi)$ and the energy $E_J$ of the conventional Josephson junction Eq.(1.6) are given by

$$I_s(\phi) = \frac{2\pi}{\Phi_0}\frac{\partial E_J}{\partial \phi} = I_c \sin(\phi) \qquad E_J(\phi) = \frac{\Phi_0 I_c}{2\pi}(1-\cos\phi),$$

where $\phi$ is the phase difference of the macroscopic superconducting wave functions $\Psi_{1,2}$ (order-parameters of each electrode) across the junction.

In the standard situation $I_c$ is positive and the minimum of the Josephson energy is at $\phi = 0$. However, in 1977 Bulaevskii *et al.* [5] calculated the supercurrent through a barrier with magnetic impurities and predicted the possibility of a negative supercurrent, $I_c < 0$. As a result the solution for $-I_c \sin(\phi) = 0$ with $\phi = 0$ is unstable and corresponds to the maximum energy, while $\phi = \pi$ will be stable and corresponds to the ground state. Such JJs are called $\pi$ junctions, opposite to conventional 0 junctions with positive $I_c$. In case of a $\pi$ Josephson junction, the first Josephson relation and consequently the energy-phase relation are modified to

$$I_s(\phi) = I_c \sin(\phi+\pi) = -I_c \sin(\phi) \qquad E_J = \frac{\Phi_0 I_c}{2\pi}\left[1-\cos(\phi+\pi)\right] = \bar{E}_J(1+\cos\phi).$$

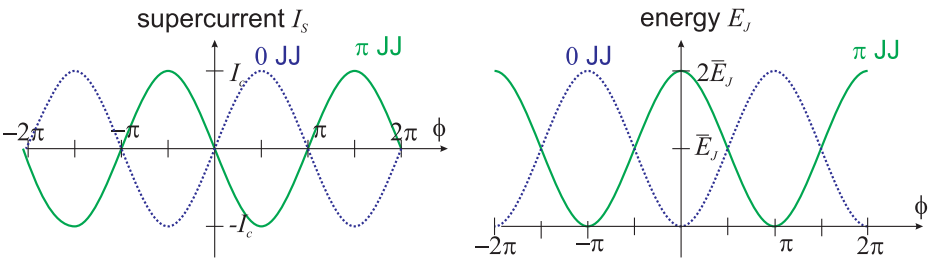


Figure 2.1: *Current-phase relation $I_s(\phi)$ at $T = 0$ and the corresponding energy-phase $E_J(\phi)$ relation for 0 and $\pi$ JJs.*

The measured critical current in a single junction is always positive and is equal to $|I_c|$. It is impossible to distinguish 0 JJs from $\pi$ JJs if one just measures the IVC of a single Josephson junction. In Fig. 2.1 the Josephson energy $E_J(\phi)$ and supercurrent $I_s(\phi)$ are plotted for 0 and $\pi$ JJs. In general, the phase of the Josephson junction can be expressed by $\phi(x,t)+\bar{\theta}(x)$, where $\bar{\theta}(x) = 0, \pi$ is the order parameter related component of phase. The physical reason for the sign inversion of the order parameter inside a ferromagnet is given in Sec. 2.2.

### 2.1.1 Proximity effect in F-layer

In this Section the basic physics of the superconducting proximity effect in magnetic metals is explained. The Curie temperature $T_C$ of the ferromagnetic metal is supposed to be much larger than the superconducting transition temperature $T_c$.

In a bilayer between a superconductor S and a normal metal N the Cooper pair density from S decays in N over a certain distance $\xi_N$, which is called the *coherence length*. Thus, superconducting properties are induced in the N-layer. This is the so-called *proximity effect*. Simultaneously, the superconductivity is weakened in the superconductor (*inverse proximity effect*) [53]. The supercurrent flow in SNS stacks is understood phenomenologically in terms of the proximity effect: the Cooper pairs diffuse from both superconductors into the normal metal over the characteristic length $\xi_N$. If the normal metal is not to thick compared to this coherence length, a supercurrent can flow.

In S/F bilayers the Cooper pair density $n^{\mathrm{CP}}$ not only decays over the distance $\xi_{F1}$, but acquires a spatially dependent phase inside the ferromagnet. It oscillates with the characteristic oscillation period $\xi_{F2}$. The schematic behavior of the superconducting order parameter at S/N and S/F interfaces is depicted in Fig. 2.2. The oscillation of $n^{\mathrm{CP}}$ depends on the exchange field $E_{\mathrm{ex}}$ and results in spatial oscillations of the $T_c$ in S/F bilayers and multilayers [54] as well as of the critical current density $I_c$ in SFS trilayers, and is explained later in this Chapter, cf. Fig. 2.7(a)-(d).

### 2.1.2 Fulde-Ferrell-Larkin-Ovchinnikov (FFLO) state

The physical picture of the proximity effect in S/F bilayers is also referred to as *induced Fulde-Ferrel-Larkin-Ovchinnikov* (FFLO) state [2, 3]. In the FFLO state of

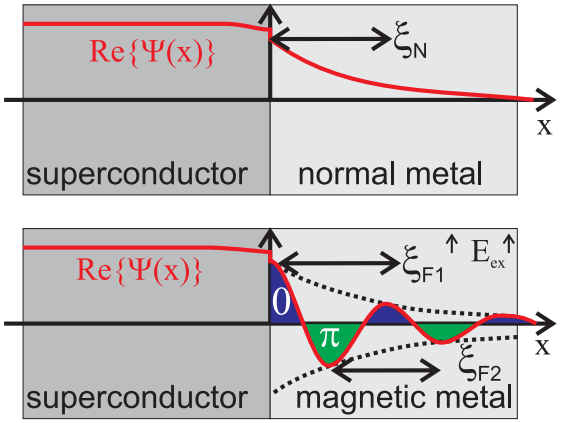


Figure 2.2: *Schematic behavior of the superconducting order parameter in S/N and S/F bilayers. In the absence of a potential barrier at the interface the order parameter varies continuously.*

a ferromagnetic superconductor the superconducting order parameter $\Psi$ is generated in the presence of an exchange field. Energetically a spherically symmetric distribution of the electrons is less favorable than the distribution extended along one of the directions perpendicular to the exchange field, due to the Zeeman splitting of the electron levels. It turns out that Cooper pairs with a non-zero center of mass momenta appear, and a spatially inhomogeneous distribution function $n^{\mathrm{CP}}$ develops. However, as electron pairing and phase coherence occurs together, the FFLO state occupies a small part of the phase diagram and is fragile to atomic disorder. Instead, in S/F or SFS hybrid structures only the phase coherence is required for the propagation of the superconducting correlations in the F-layer. It is more robust in this artificial heterostructures as the electron pairing takes place inside the S-layer.

## 2.2 Microscopic origin of $\pi$ shift

In this Section the physics of itinerant ferromagnetism is reviewed, as its unequal spin up and spin down density of states $D^{\uparrow\downarrow}$ lead to a finite center of mass momentum of the Cooper pairs and to the spatial oscillation of the superconducting order parameter inside the F-layer.

### 2.2.1 Itinerant magnets

The Pauli principle forbids two electrons of the same spin to be in the same state at the same time. The antisymmetry of the fermionic wave functions leads to vanishing amplitudes of the electron wave functions with same spin at the crossing point. As a consequence the Coulomb repulsion energy is reduced. If on the other hand two electrons with opposing spins are in the same state the repulsion energy increases. The electrostatic energy of the system depends on the relative orientation of the electron

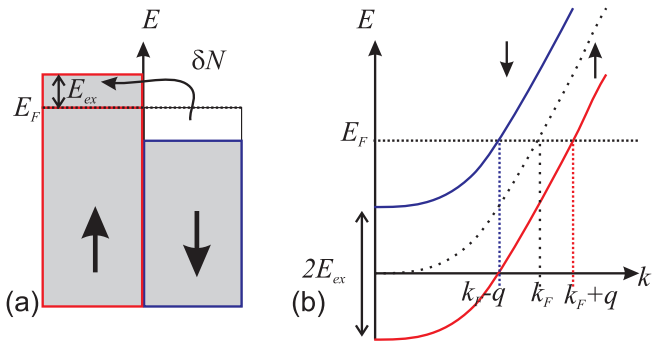


Figure 2.3: *(a) Stoner model describes the appearance of itinerant magnetism as electron with spins ↑ and ↓ have different density of states due to long-order correlations. (b) Fermi-wave vectors of both spins in metallic magnets.*

spins. The difference in energy is defined as the *exchange energy* $E_{\mathrm{ex}}$ and results from an attractive dipolar interaction between electrons with the same orientation of spins.

The origin of magnetism in $3d$ magnets, such as Co, Ni, Fe and their alloys like NiCu, was explained by Stoner by the model of *itinerant magnetism* based on the exchange interaction among electrons from the $3d$ band [55]. The magnetic ordering of the band electrons results in an increase of kinetic energy, but a decrease of the potential (exchange) energy. The total density of states $D^{\uparrow\downarrow}$ is divided into spin up and spin down densities, defined as

$$D^{\uparrow\downarrow} = D_0(E \mp E_{\mathrm{ex}}).$$

The Stoner criteria predicts correctly that some of the $3d$ transition metals have magnetic ordering if

$$\widetilde{I} D(E_F) > 1,$$

where $\widetilde{I}$ is the exchange integral for itinerant electrons.

In equilibrium the total energy of both electron gases with spin ↑ and ↓ is the same. The kinetic energy of the majority electrons at the Fermi level is bigger than the one of the minority electrons. The excess above $E_F$ is given by the exchange energy $E_{\mathrm{ex}}$, depicted in Fig. 2.3. The kinetic energy of both spin gases is given by

$$E_F^{\uparrow\downarrow} = E_F \pm E_{\mathrm{ex}},$$

and for the wave vectors at the Fermi level:

$$k_F^{\uparrow\downarrow} = k_F \pm q,$$

where $q$ is the shift of electron wave vectors at the Fermi level. Under the assumption that the exchange energy $E_{\mathrm{ex}}$ is smaller than the Fermi energy $E_F$ and the dispersion relation is parabolic, one can relate the difference of the wave vectors $k_F^{\uparrow\downarrow}$ at Fermi level to the exchange energy $E_{\mathrm{ex}}$ by

$$q = \frac{E_{\mathrm{ex}}}{\hbar v_F},$$

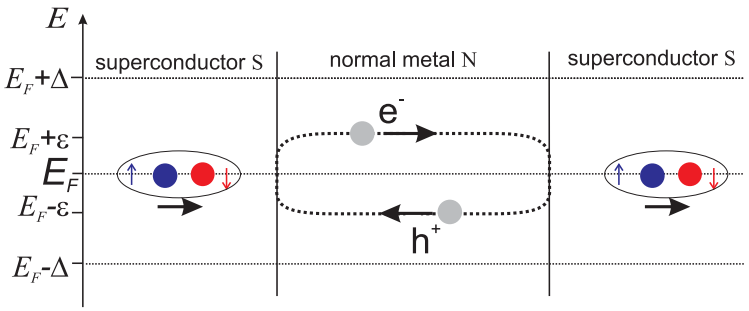


Figure 2.4: *SNS stack: transfer mechanism for Cooper pairs through N by Andreev reflections. Electron $e^-$ generates a hole $h^+$ at the N/S interface due to conservation of charge and momentum.*

where $v_F$ is the Fermi velocity in the ferromagnet.

### 2.2.2 Andreev bound states in SNS and SFS junctions

I want to focus on the Cooper pairs transport through SNS and SFS junctions. For simplicity the Cooper pair, which adiabatically crosses the S/N or S/F interface, has an electron momenta perpendicular to the interface. When the Cooper pairs enters the N-layer (F-layer), where it is not an eigenstate, it becomes an evanescent state and decays exponentially on the length scale of the normal metal coherence length $\xi_N = v_F/2\pi T$.

#### SNS junction

Microscopically the transfer of Cooper pairs through an SNS junction occurs via Andreev reflections at the two interfaces [56], creating discrete *Andreev bound states* (ABS). The spectrum of these levels is sensitive to the superconducting phase difference between the electrodes. An electron-like excitation $\epsilon$ in the metallic N-layer with energy lower than the superconducting energy gap $\Delta$, i.e. between $E_F$ and $E_F \pm \Delta$, is evanescent in the superconductor (since between $E_F$ and $E_F \pm \Delta$ no quasiparticle states exist) and propagates in the N-layers. It is reflected at the N/S interface as a hole and is then reflected back as an electron at the opposite S/N interface [57], as illustrated Fig. 2.4. During the reflection process a Cooper pair is condensed in the superconductor due to conservation of charge and momentum. The relative phase of the electron-hole pair changes by $\Delta\phi = 2 \cdot \delta k \cdot d_N$, where $d_N$ is the length (or thickness) of the normal metal and $\delta k = \epsilon/\hbar v_F$. A bound state appears at energy $\epsilon_n$ when this phase shift $\Delta\phi$ matches the phase difference at the two interfaces, modulo $2\pi$. Hence, the phase shift is given by

$$\Delta\phi = 2\frac{\epsilon_n}{\hbar v_F} d_N.$$

The constructive interference of the electron- and hole-like excitations gives rise to bound states, which carry the supercurrent.

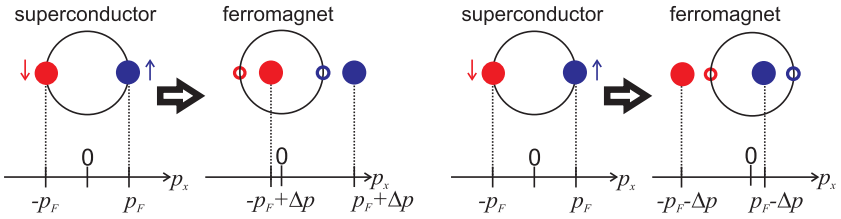


Figure 2.5: *SFS stack: Cooper pair going from superconductor to ferromagnet acquires a momentum* $\pm 2\Delta p = 2\hbar q = 2E_{\mathrm{ex}}/v_F$. *Adapted from [54].*

### SFS junction

The same mechanism accounts for the Josephson coupling through a ferromagnet (SFS JJs), although the spectrum of the ABS is modified by the spin splitting of the electron bands, as the Andreev reflections reverse the spin of the quasiparticles [58]. The spectral current density that describes the current density per bound state in the F-layer is a function of the exchange energy $E_{\mathrm{ex}}$, as shown in the next part.

The Pauli-shift of the conduction bands, see Fig. 2.3, in the ferromagnet *raises* the potential energy of the spin-down electron of the Cooper pair by the ferromagnetic exchange energy $E_{\mathrm{ex}}$ and *lowers* the potential energy of the spin up electron by the same amount. Conservation of energy forces the spin-up electron to rise its kinetic energy while the spin-down electron decreases its kinetic energy to balance the chance of the potential energy.
In detail: A Cooper pair entering the ferromagnet (Fig. 2.5(a)) may acquire a center of mass momentum $2q = 2\hbar\Delta p = 2E_{\mathrm{ex}}/v_F$ or $-2q$, as in Fig. 2.5(b). Fermionic antisymmetry requires to consider both cases. The *total momentum* of the Cooper pair in the F-layer is *non-zero*. The phase shift of the Andreev pairs contains the additional term $\pm 2qd_F$ due to the exchange energy. Therefore the expression for the phase shift is modified:

$$\Delta\phi = 2\frac{\epsilon_n \pm E_{\mathrm{ex}}}{\hbar v_F} d_F,$$

where $d_F$ is the length (or thickness) of the magnetic metal. The Cooper pair wave function in the singlet state ($\uparrow\downarrow - \downarrow\uparrow$) becomes [53]

$$\Psi(d_F) = \Psi_0 \left(e^{i(\phi+\Delta\phi)} + e^{i(\phi-\Delta\phi)}\right) \sim \cos\left(d_F/\xi_{F2}\right) e^{-d_F/\xi_{F1}},$$

with $\xi_{F1}$, $\xi_{F2}$ the characteristically coherence and oscillations lengths.

From this expression the singlet Cooper pair density is spatially oscillating in the F-region as the superconducting wave function oscillates in the ferromagnetic layer along the direction normal to the S/F interface. The oscillation length is given by $\xi_{F2}$. The phase of order parameter can be shifted by $\pi$ for a certain thickness $d_F$. Then, the minimum of the energy which corresponds to the ground state of SFS is obtained for $\phi = \pi$, i.e. a $\pi$ junction.

The dependence of the critical current on the F-layer thickness $I_c(d_F)$ and temperature $I_c(T)$ can be described by the general Ginzburg-Landau functional [25] with

the superconducting order parameter $\Psi$, as done by Buzdin and Ryazanov [59, and references herein]. The order parameter

$$\Psi \sim e^{-d_F/\xi_F} = e^{-d_F/\xi_{F1}} e^{-id_F/\xi_{F2}}$$

is a function of the complex coherence length $\xi_F^{-1} = \xi_{F1}^{-1} + i\xi_{F2}^{-1}$, where $d_F$ is the coordinate in the direction perpendicular to the interface. The Cooper pair distribution oscillates on a scale set by the material and temperature dependent parameter $\xi_{F2}$. This *ansatz* for the oscillations of order parameter will be used in the next Section.

## 2.3 Theory of $\pi$ junctions

I want to focus on SFS junctions with a conductive ferromagnetic barrier and later study the complex system of SIFS junctions with I-layer being a tunnel barrier.

The equations for the superconducting order parameter in the semiclassical approximation are based on the Eilenberger equations [60] in S/F bilayers and further simplified in the case of the strong elastic scattering (the diffusive approximation) by Usadel [61].

### Review of clean and diffusive limit

There is a quantitative difference between the coherence lengths in *clean* ($\ell/\xi_{F1} \gg 1$) and *diffusive* ($\ell/\xi_{F1} \ll 1$) ferromagnets, where $\ell$ is the *electron mean free path*. The diffusive limit implies that the mean free path is the second smallest spatial scale after the Fermi wavelength $k_F$. In the diffusive limit and at zero temperature the coherence length coincides exactly with the oscillation period ($\xi_{F1} = \xi_{F2}$) [6, 62], whereas in the ideal clean limit the coherence length $\xi_{F1}$ is formally infinite [63]. However it is limited by elastic impurity scattering [64] or spin-orbit scattering [54], but still exceeds the oscillation period $\xi_{F2}$. In presentence of magnetic scattering the system becomes even more complex, as we will see below.

Although the ground state with $\pi$ phase shift can be achieved in any SFS structure, in practice the spatial oscillations are easier to observe in cleaner systems due to the weaker damping, but the short oscillations length might be of the same order of magnitude as the layer roughness. Diffusive diluted ferromagnetic alloys like NiCu and PdNi have a smaller exchange energy and therefore a longer oscillation period, but usually a shorter coherence length as the *clean* ferromagnets Co, Fe or Ni. To avoid roughness effects, the first experiments were performed on SFS junctions in the diffusive limit.

The following overview on $\pi$ coupled junctions is based on a recent review of Buzdin [53].[1] The $I_c(d_F)$ dependence is affected by the interface transparency (SFS-/SIFS-type junction), the electron mean free path $\ell$ (clean/diffusive limit) and the spin-flip and spin-orbit scattering time.

[1] Note that all calculation presented here are only strictly valid near $T_c$.

### 2.3.1 Josephson effect in the SFS/SIFS sandwich

Up to now the majority of experimental work on $\pi$ coupled junctions has been done in SFS-type junctions [7, 8, 65–67]. I want to review these high transparency junctions before discussing the SIFS-type junctions.

#### High transparency (SFS) junctions without magnetic scattering

In the *clean* limit and in the absence of magnetic scattering the critical current through an SFS junction is [63]:

$$I_c R(d_F) = \frac{\pi \Delta^2}{4e} \frac{\left|\sin(\frac{d_F}{\xi_F})\right|}{\frac{d_F}{\xi_F}}, \tag{2.1}$$

with $\xi_F \equiv \xi_{F2} = 4E_{\rm ex}/v_F$, whereas in the *diffusive* limit it is [6]:

$$I_c R(d_F) \propto 2\frac{d_F}{\xi_F} \left| \frac{\cos\frac{d_F}{\xi_F}\sinh\frac{d_F}{\xi_F} + \sin\frac{d_F}{\xi_F}\cosh\frac{d_F}{\xi_F}}{\cosh\frac{2d_F}{\xi_F} - \cos\frac{2d_F}{\xi_F}} \right|, \tag{2.2}$$

with $\xi_F \equiv \xi_{F2} = \sqrt{\hbar D/E_{\rm ex}}$, diffusion coefficient of the ferromagnet $D$, normal resistance $R_n = d_F\rho_F/A$, specific resistance of the F-layer $\rho_F$ and the junction area $A$. In the clean limit $I_c(d_F)$ decays $\propto 1/d_F$ whereas in diffusive limit it decays exponentially $\propto e^{-d_F/\xi_F}$.
Fig. 2.6 depicts $I_c(d_F)$ of SFS JJs given by the two Eqs.(2.1, 2.2) for $I_c R(d_F)$. Note that in clean and diffusive limit $\xi_F$, $\xi_{F1}$ and $\xi_{F2}$ may differ substantially.

#### SFS junction with magnetic scattering in F-layer

The influence of magnetic scattering on the order parameter has to be included for the diffusive limit, as it changes the $I_c(d_F)$ dependences [54]. Two types of electron scattering sources exist: spin-orbit and spin-flip scattering. Both lead to a decrease of the coherence length $\xi_{F1}$ and an increase of the oscillations length $\xi_{F2}$.
• In the presence of the *spin-orbit scattering* the spin singlet Cooper pair changes by spin-flip scattering to a spin-triplet and the pairs with net momentum $q$ mix up with pairs having momentum $-q$. Therefore, such a Cooper pair *sees* an exchange field which changes its sign along the $x$-direction. The average exchange field $E_{\rm ex}$ experienced by the pair is decreased. The decay to a spin triplet state is a pair breaking effect, giving the pairs a finite lifetime, which is determined by the exchange field. The spin-orbit scattering is strong in metals with large $Z$, thus it can be neglected for NiCu alloys used in this work.
• *Spin-flip scattering* is inherent to ferromagnetic layers because of magnetic impurities like clusters, spin-waves or non-stoichiometric lattices. Spin-flip scattering arises in weak ferromagnetic alloys such as $Ni_xCu_{x-1}$, because their vicinity to the disappearance of ferromagnetism makes them prone to large magnetic disorder. Although using a weak alloy as F-layer has the advantage that they can be made thick enough to avoid roughness effects. In SFS JJs based on diluted ferromagnetic alloys this is the mayor source for magnetic scattering.

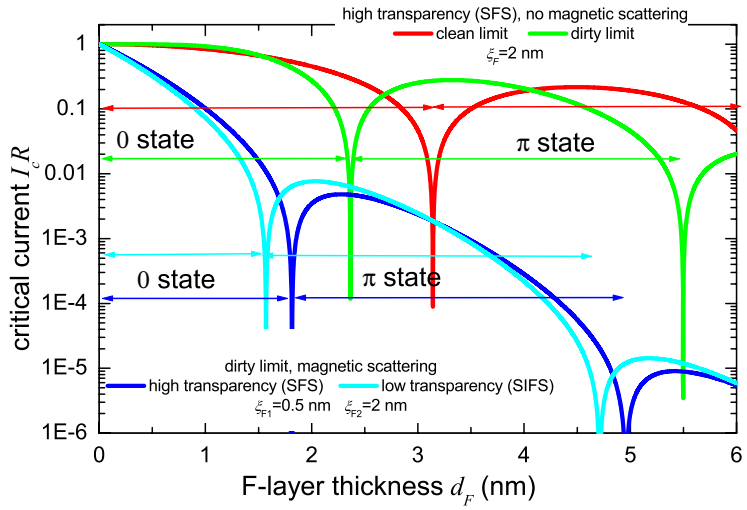


Figure 2.6: *$I_cR$ dependence on the F-layer thickness ($d_F$) for Eqs.(2.1, 2.2, 2.3, 2.4). Note that $\xi_F$, $\xi_{F1}$ and $\xi_{F2}$ depend on electron mean free path and the kind of scattering. They differ in quantity for all four cases.*

For the complete theoretical analysis one needs to take thermal energy contributions for the pair-breaking processes into account. This is done by introducing a complex wave vector $k = (k_1 + ik_2)$ with

$$k_{1,2} = \frac{1}{\xi_F}\sqrt{\sqrt{1+\alpha^2} \pm \alpha},$$

where $\alpha = 1/\tau_s E_{\rm ex}$ and $\xi_F = \sqrt{\hbar D/E_{\rm ex}}$ is the oscillation length without spin-flip scattering. Since the F-layer is a diluted alloy, the timescale of the inelastic magnetic scattering $\tau_s$ is important. The coherence length $\xi_{F1} = 1/k_1$ may be substantially smaller than the oscillating length $\xi_{F2} = 1/k_2$. In the absence of magnetic scattering ($\tau_s \to \infty$), the coherence and oscillation wave vectors are the same: $k_1 = k_2$ [68].

In the limits of $E_{\rm ex} \gg T_c$, short coherence length $\xi_{F1} < d_F$ and non-spin active interfaces, cf. Ref. [69], one obtains the following analytical expression for the *high* transparent SFS system, where the interfaces transparency parameters $\gamma_{B1}$ of S/F and $\gamma_{B2}$ of F/S are zero:

$$I_cR(d_F) \propto \left|\cos\frac{d_F}{\xi_{F2}} + \frac{\xi_{F1}}{\xi_{F2}}\sin\frac{d_F}{\xi_{F2}}\right| e^{\frac{-d_F}{\xi_{F1}}}. \tag{2.3}$$

This equation is valid for the SFS junctions with NiCuF-layers from Ryazanov *et al.* [7, 65], where the transition from 0 to $\pi$ ground state was observed for the first time.

**SIFS junctions with magnetic scattering**

The tunnel barrier, necessary for low transparent SIFS junctions, is difficult to realize due to the appearance of microshorts in the barrier if the interface roughness is comparable to the tunnel barrier thickness. SIFS-type Josephson junctions have been implemented in 2002 by Kontos *et al.* [9] using a very thick $Al_2O_3$ tunnel barrier and later on samples with a much thinner tunnel barrier fabricated for this thesis.[2]

If just the F/S part of the ferromagnetic barrier is transparent ($\gamma_{B2} = 0$) and the other S/I/F part, treated like a single interface, has a *low* transparency parameter $\gamma_{B1}$ the critical current can be expressed as [72]:

$$I_c R(d_F) \propto \frac{1}{\gamma_{B1}} e^{\frac{-d_F}{\xi_{F1}}} \left| \cos \frac{d_F}{\xi_{F2}} \right|. \tag{2.4}$$

When neglecting the F/S contribution $\gamma_{B2} \equiv 0$ ($\gamma_{B2} \ll \gamma_{B1}$) one can estimate the total transparency of the junction $\gamma_{B1} = \gamma_B = R/A\rho_F\xi^*$, where $R$ is total resistance, $A$ the junction area, $\rho_F$ is $F$-layer resistivity and $\xi^* = \sqrt{\hbar D/2\pi k_B T_c}$.

Equation (2.4) is valid for SIFS JJs based on NiCu alloys, which were used for this thesis. The temperature dependence of the critical current $I_c(T)$ requires much more calculations [53, 68].

The $I_c R(d_F)$ dependences for the four cases treated above (clean/diffuse SFS-JJs and diffusive high/low transparent SIFS JJs with magnetic scattering) are shown in Fig. 2.6. For the low transparency SIFS JJs the first maximum occurs at lower thickness than for high transparency SFS junctions. This is due to the effect of the insulating layer on the Andreev amplitude at the F/S interface.
Note that the $I_c R(d_F)$ dependences were derived under the assumption that $\xi_{F2} =$ const. In principle $\xi_{F2}$ is a weak function of the temperature, thus the critical crossover thickness $d_F^{0\text{-}\pi}$ between the 0 and $\pi$ phase, where $I_c R(d_F^{0\text{-}\pi}) = 0$, is temperature dependent. $d_F^{0\text{-}\pi}$ decreases as $T$ drops and the 0 to $\pi$ crossover may be observed by measuring the $I_c(T)$ dependence of a JJ with $d_F$ near $d_F^{0\text{-}\pi}$.

### 2.3.2 Spontaneous supercurrent in $\pi$ coupled loop

Bulaevskii *et al.* [5] predicted that a $\pi$ coupled junction incorporated into a long superconducting ring (e.g. a rf-SQUID with $\pi$ junction or a dc-SQUID with 0 JJ and $\pi$ JJ) may generate a spontaneous supercurrent in the ring. The corresponding magnetic flux depends on the inductance of the ring and the length of loop and may be as large as half a flux quantum $\Phi_0$. It is caused by the phase difference over the $\pi$ junction in the ground state. This phase difference generates a circulating supercurrent in the ring which short-circuits the junction. In case of a small loop the flux may be absent and the junction is still in the 0 state, as this increases the energy of the JJ, but still reduces the total energy of the system. In case of a long loop the magnetic field can be $\pm\Phi_0/2$, depending on the direction of circulation of the supercurrent (clockwise or counter-clockwise). The spontaneous flux can be detected either by superconducting quantum interference device (SQUID) magnetometry in a rf-SQUID configuration [73], or by a micro-Hall sensor [74].

[2] Recently, SIFS junctions were fabricated by Born *et al.* [70] and Latempa *et al.* [71], too.

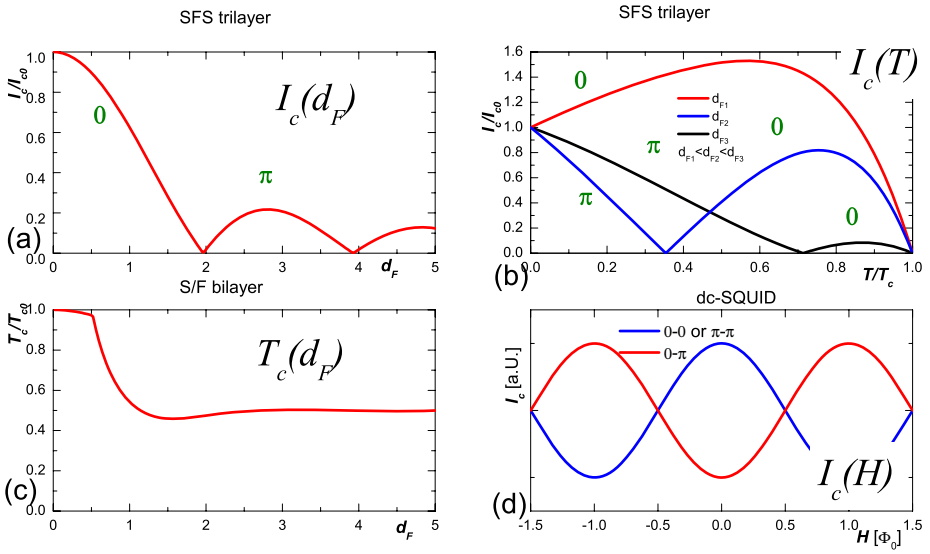


Figure 2.7: *Several detection techniques for π coupling: (a) Nonmonotonic F-layer thickness and (b) temperature dependences of the normalized critical current $I_c/I_{c0}$. (c) Critical temperature $T_c/T_{c0}$ dependence on the F-layer thickness $d_F$ for SF bilayers, (d) $I_c(H)$ of dc-SQUID.*

#### π junction in superconducting ring

The magnetic field dependence of $I_c$ in a superconducting loop with an odd number of identically coupled junctions allows one to determine the kind of coupling (0 or π) of these junctions, see Fig. 2.7(d). This has been exploited by Ryazanov *et al.* [75], who used a triangular SFS arrays to observe a temperature-induced change of coupling from 0 to π. Similar phase sensitive experiment was done by using a dc SQUID with just one of the two junctions being π coupled [76].

The junctions consisting of 0 and π coupled parts in *one* long Josephson junction, so-called 0–π LJJs, exhibit an *intrinsic* magnetic flux of $\Phi_0/2$, too. The 0–π LJJ is an analog of a 0–π SQUID with long rather than point-like JJs and loop size $\to 0$. For clarity I refer only to fractional vortices in these types as *semifluxons*. They are considered in detail in Chapter 3.

### 2.3.3 Critical temperature $T_c$ of SF multilayers

Prior to the first unambiguous experimental demonstrations of the T-induced 0–π transition via $I_c(T)$ [7] in 2000, several experiments were done on S/F multilayers. If the F-layer thickness is smaller than $\xi_{F2}$, the pair wave function in the F-layer changes just a little and is similar to the superconducting order parameter in the adjacent superconductor. This corresponds to the 0 phase. If $d_F \approx \xi_{F2}/2$ the Cooper pair wave function may change the sign inside each F-layer. This corresponds to a

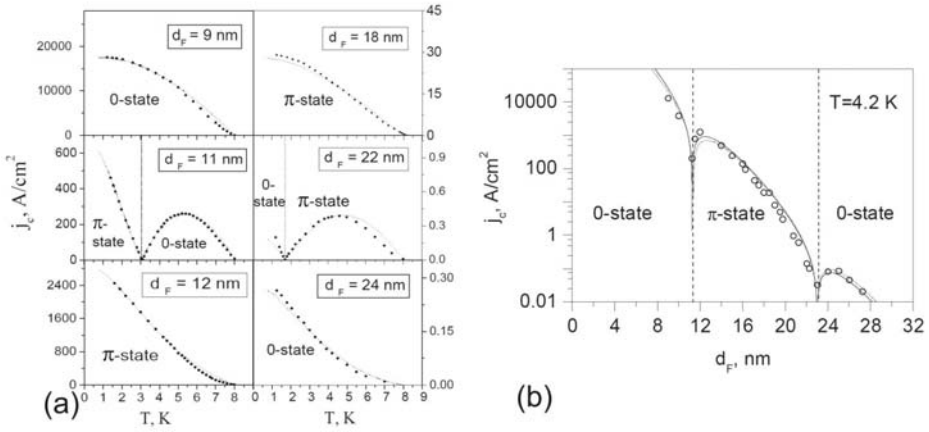


Figure 2.8: *(a) Temperature dependence of the critical current density $j_c(T)$ for SFS junctions with $Ni_{53}Cu_{47}$ for various $d_F$. The cusp at $T = 3$ K for $d_F = 11$ nm indicates a temperature induced crossover from 0 to $\pi$ state and the one at $T = 1.7$ K for $d_F = 22$ nm a crossover from $\pi$ to $2\pi = 0$ state. (b) $j_c(d_F)$ dependence for SFS junctions at* 4.2 K. *Data from Ref. [68].*

difference of $\pi$ of the superconducting order parameter between adjacent S-layers. Increasing the thickness of the F-layer may provoke subsequent transitions from uniform 0–0–0–0... to 0–$\pi$–2$\pi$–3$\pi$... superconducting order parameter phases. The Josephson phase will be 0–0–0... or $\pi$–$\pi$–$\pi$... This results in a nonmonotonic dependence of the critical temperature $T_c$ on $d_F$.
S/F bilayers cannot exhibit transitions between 0 and $\pi$ coupling but nevertheless show a nonmonotonic dependence of $T_c$ on $d_F$. A common feature, shown in Fig. 2.7(c), is the dip and saturation of $T_c$ with increasing $d_F$, because the superconductivity is suppressed in an adjacent diffusive ferromagnet with thickness $d_F \gg \xi_{F2}$. The dip is a self-interference effect of the spatially oscillating order parameter. In a recent work by Zdravkov *et al.* [77] a pronounced re-entrant superconducting transition temperature $T_c$ for $Nb/Ni_xCu_{1-x}$ bilayers was reported. A review about S/F bilayers was given by Fominov *et al.* [78].

## 2.4 Experiments with SFS/SIFS Josephson junctions

**Temperature induced 0 to $\pi$ crossover**

The oscillation length $\xi_{F2}$ is temperature dependent, and drops for decreasing temperature, as pointed out in Section 2.3.1. This temperature dependence is the origin of the anomalous dependence of the critical current $I_c$ on temperate for JJs with $d_F$ near the crossover thickness $d_F^{0-\pi}$, cf. Fig. 2.7(b). Ryazanov and coworkers [7, 68, 75, 79] observed the first phase crossover in SFS JJs by $I_c(T)$ measurements.

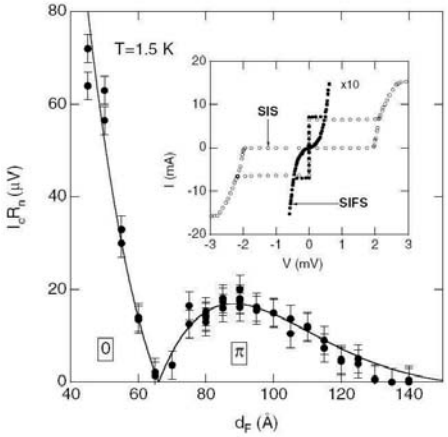


Figure 2.9: *Dependence of the Josephson coupling $I_cR$ on F-layer thickness $d_F$ for SIFS junctions with F=$Pd_{88}Ni_{12}$. The minimum at $d_F = 65$Å indicates the transition from 0 to $\pi$ coupling. The inset shows typical IVCs of SIFS (full circles) and SIS junctions (empty circles). Data from Ref. [9].*

They have realized an inversion of coupling by using the diluted ferromagnet $Ni_{52}Cu_{48}$ ($T_C$ about 20–30 K and $d_F \approx 22$ nm). The weakness of the exchange field $E_{ex}$ allowed them to drive the phase crossover by temperature at zero magnetic field [7], see Fig. 2.8(a). Five years later systematic studies [68] of $I_c(d_F)$ in JJs based on $Ni_{53}Cu_{47}$ have revealed that the 0 to $\pi$ transition occurs at $d_F = 11$ nm, and the transition from $\pi$ to $2\pi$, i.e. 0, takes place at $d_F = 22$–23 nm. A very strong variation of $I_c(d_F)$ over six orders of magnitude was observed in the thickness interval 8–28 nm, which is related to the strong effect of magnetic scattering, see Fig. 2.8(b).

A similar experiment on the $I_c(T)$ dependence was done later by Sellier *et al.* [65] using $Ni_{48}Cu_{52}$ as an F-layer. It should be noted that their alloy showed no sign of magnetic hysteresis, but only an enhanced magnetic moment at low temperatures, unlike the hysteretic NiCu alloys from Ryazanov *et al.* [7]. The crossover thickness is determined as $d_F^{0-\pi} = 18$ nm. The thicker NiCu layer for the crossover is supported by theoretical indications that even a paramagnetic interlayer or ferromagnetic impurities in the barrier can lead to $\pi$ coupling [5]. Sellier [65] noted the presence of magnetic scattering and demonstrated that it strengthens a decrease of $I_c(d_F)$ and, at the same time, increases the spatial period of $I_c(d_F)$ oscillations. This was confirmed by recent measurements of the local density of states (DOS) on the upper surface of a $Ni_{48}Cu_{52}$ film for various thicknesses using a very low temperature scanning tunneling microscope [80].

### F-layer thickness induced 0 to $\pi$ crossover

Kontos *et al.* [9] observed for the first time oscillations of the critical current as a function of the F-layer thickness in SIFS JJs based on Nb/Al-$Al_2O_3$/$Pd_{88}Ni_{12}$/Nb

heterostructures. This $I_c(d_F)$ is shown in Fig. 2.9. The correct theory for $I_c(d_F)$ can be found in [81]. The I-layer was rather tick and the specific resistance of the barrier was high ($\rho_0 \sim 3\,\mathrm{m\Omega cm^2}$). The critical current density $j_c$ in the $\pi$ state was below $7\,\mathrm{mA/cm^2}$. The Josephson coupling $V_c = I_cR$ at 1.5 K can be estimated from the data and is of the order of 20 $\mu$V, i.e. 50 times lower than that measured on SIS junctions without a PdNi interlayer. The very low critical current densities in the $\pi$ coupled state demanded very large junction areas ($1\,\mathrm{mm^2}$) and led to a very large Josephson penetration depth $\lambda_J = 3.7$ mm.
In this thesis I report on $\pi$ JJs having much higher $j_c$ and $I_cR$ values (see Chap. 6). In the $\pi$ state a critical current density $j_c \approx 5\,\mathrm{A/cm^2}$ was reached at $T = 2.1\,\mathrm{K}$, resulting in $I_cR \approx 400$ $\mu$V and $\lambda_J \approx 160$ $\mu$m.

Oscillations of $I_c(d_F)$ were also reported by Blum *et al.* [82] using a strong ferromagnet as barrier in Nb/Cu/Ni/Cu/Nb structures and Bell *et al.* [66] using an epitaxial bottom electrode and ferromagnetic barrier by in Nb/$Fe_{20}Ni_{80}$/Nb JJs. Although the data scattering in both cases is large. Multiple 0 to $\pi$ transition were reported in a recent publication by Born and coworkers [70]. They used SIFS JJs based on Nb/Al-$Al_2O_3$/$Ni_3Al$/Nb heterostructures. $Ni_3Al$ provides an F-layer with very weak decay of Cooper pairs, i.e. clean limit. The inversion of coupling in JJs with strong ferromagnetic barriers of Co, Ni and $Ni_{80}Fe_{20}$ was recently observed by Robinson *et al.* [83].

## 2.5 Advantages of $\pi$ coupled SIFS junctions

The SIFS junction exhibits considerable advantages over the SFS junction. At the S/I/F interface the wave-like properties of the Cooper pairs give rise to a finite tunneling probability, i.e. an exponential dependence of the Josephson current on the barrier thickness. Cooper pairs and quasi-particle tunneling probabilities are strongly reduced, resulting in a lower supercurrent $I_c$ and higher resistance $R$ as in comparison with the entire metallic SFS junctions. SIFS junctions offer the freedom to tune the essential electric parameters, such as $j_c$, over a wide range and still keep high $I_cR$ products. In addition, niobium based tunnel junctions are usually underdamped ($\beta_c \gg 1$), which is desired for applications where low dissipation is required, e.g. superconducting qubits [84].

The low junction resistance in SFS junctions ($\sim 10\,\mu\Omega$) demands sophisticated methods for voltage measurements like a superconducting quantum interference device (SQUID) voltmeter or a lock-in amplifier, whereas for SIFS junctions a room temperature voltage amplifier can be used.

SFS or SIFS $\pi$ junctions have been proposed as potential logic elements in quantum computing circuits. For the *quiet* flux qubit [12, 84] based on active $\pi$ JJs, which is self-biased and well decoupled from the environment, one needs to use high quality $\pi$ JJs with i) high resistance to avoid decoherence and ii) reasonably high critical current density $j_c$. High $j_c$ is required to have the Josephson energy $E_J \propto I_c = j_c \cdot A \gg k_BT$ for junction areas $A$ of a few square microns or below and to keep the Josephson plasma frequency $\omega_p \propto \sqrt{j_c}$, which plays the role of an attempt frequency in the quantum tunneling problem, on the level of a few GHz. Similar requirements are applicable for $\pi$ junction circuits working in the classical domain, e.g.

for *rapid single flux quantum* (RSFQ) logics [11, 85], where an important parameter, which defines the speed of the operation, is the product of the critical current $I_c$ and the resistance $R$.

## 2.6 Higher harmonics: $\sin 2\phi$ component

Generally speaking, the current-phase relation $I_s(\phi)$ has to be periodic in $\phi$, so the second or even higher harmonics are possible:

$$I_s(\phi) = \frac{2e}{\hbar}\frac{\partial E_J}{\partial \phi} = I_1 \sin(\phi) + I_2 \sin(2\phi) + \dots . \tag{2.5}$$

Until now the higher harmonics were neglected ($I_2 = 0$), but indeed they appear in Josephson junctions formed by point contacts or nonequilibrium normal metals [86, 87]. In SFS or SIFS junctions the amplitude of the first harmonic $I_1$ is proportional to $e^{-d_F/\xi_F}$ and the second harmonic contribution $I_2$ is proportional to $e^{-2d_F/\xi_F}$. Usually $I_2$ is much smaller than $I_1$ and can be neglected [88, 89]. However, for $d_F$ and $T$ in the vicinity of the 0–$\pi$ crossover the first harmonic vanishes and the contribution of the second harmonic becomes important.

Up to now I am aware of two experiments on SFS junctions with controversial results.

First, Sellier *et al.* [90] observed half-integer Shapiro steps (ref. Sec. 1.6) at the 0 to $\pi$ transition in SFS JJ with $d_F = 17$ nm. They attributed these fractional steps to the doubling of the Josephson frequency due to the $\sin 2\phi$ component in the current-phase relation (CPR). At the temperature driven 0 to $\pi$ crossover the $I_c$ was non-zero.

Second, the measurements by Frolov *et al.* [73] on a SFS junction with $Ni_{53}Cu_{47}$ as the F-layer provided no evidence for the appearance of the second harmonic in the CPR at the 0–$\pi$ transition point. However, these measurements have been performed on a junction with the F-layer thickness about 22 nm, i.e. near the second minimum on the $I_c(d_F)$ dependence, where the $\pi$ to $= 0$ transition occurs and $I_2$ exponential lower than at the first crossover point [89]. The much higher critical current near the first minimum at $d_F \approx 11$ nm may be better suited for the detection of the second harmonic.

Note that F-layer thickness inhomogeneities resulting in non-uniform $j_c(x, y)$ could give an alternative explanation of the experimental result of Sellier *et al.* [90]. More details can be found in a recent publication [91] on a simultaneous coupled 0–$\pi$ JJ with a stepped F-layer, described in Chap. 3.6.

# Chapter 3

# Fractional vortices in 0–$\pi$ JJs

The appearance of a spontaneous supercurrent, so-called Josephson vortex at the boundary between a 0 and a $\pi$ coupled long Josephson junction, i.e. a 0–$\pi$ LJJ, was predicted by Bulaevskii *et al.* in 1978 [92]. This supercurrent carries a fractional flux of half-integer flux quantum $\Phi_0/2$ and is called *semifluxon* (SF). In this Chapter a theoretical analysis based on the perturbed sine-Gordon equation is given and various systems showing such 0–$\pi$ phase boundaries are discussed.

## 3.1 Sine-Gordon equation including 0–$\pi$ phase boundaries

The difference between conventional 0 or $\pi$ Josephson junction and the 0–$\pi$ (or 0–$\pi$–0,...) junction examined here is the presence of boundary points in the phase with steps of $\pi$ along the junction axis.

The first calculation of the free energy for a long 0–$\pi$ Josephson junction was done in 1995 by Xu *et al.* [13] and two years later corrected and extended for junctions of intermediate length by Kirtley *et al.* [15]. They calculated the difference in the free energy of a 0–$\pi$ junction with spontaneous fractional flux and a 0–$\pi$ junction in the flat phase state, i.e. with no flux. In the following I summarize an alternative calculation given later by Goldobin *et al.* [14].

In comparison with the usual normalized perturbed sine-Gordon equation (1.20), the equation for the dynamics of the Josephson phase in 0–$\pi$ junctions contains the additional term

$$\bar{\theta}_{xx}(x) = \pi \sum_k \sigma_k \delta_x(x - x_k).$$

which describes the boundary points with $\pm\pi$ phase jumps at $x_k$. It is convenient to present the phase $\phi(x)$ as a sum of the magnetic component $\mu(x)$ and the order parameter related component $\bar{\theta}(x) = 0, \pi$

$$\phi(x,t) = \mu(x,t) + \bar{\theta}(x). \tag{3.1}$$

Therefore the Eq.(1.20) with the phase given by Eq.(3.1) can be simplified by rewriting it only for the *magnetic* component $\mu(x)$

$$\mu_{xx} - \mu_{tt} - \sin(\mu) \underbrace{\cos(\bar{\theta})}_{\pm 1} = \alpha\mu_t - \gamma(x) + h_x(x). \tag{3.2}$$

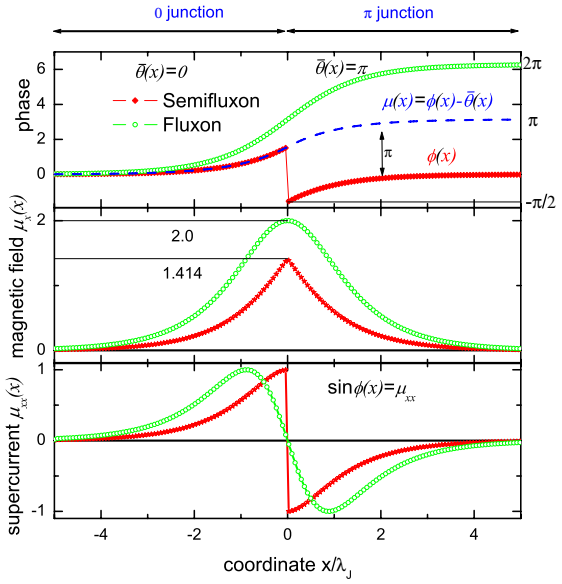


Figure 3.1: *Comparison of semifluxon and fluxon shapes. Top: total phase $\phi(x)$ and magnetic component $\mu(x)$, middle: magnetic-field profile $\mu_x(x)$, bottom: supercurrent profile* $\sin(\phi) = \mu_{xx}(x)$ *[14].*

It should be stressed that this is the usual perturbed sine-Gordon equation as discussed in Chapter 1 with just the sign of $\sin(\mu)$ changing at each 0–$\pi$ phase boundary. This model is valid for both d-wave based and SFS/SIFS-type JJs. The phase $\mu$ (continuous) is a real value in SFS/SIFS-type JJs, while $\phi$ is the phase in d-wave JJs.

## 3.2 Integer and semi-integer fluxons

Solving Eq.(3.2) for the static case without the perturbation terms, i.e. $\mu_{xx}^{\mp} = \pm \sin \mu$, yields the *semifluxon shape* in terms of the magnetic phase $\mu(x)$ as

$$\mu(x) = -4\mathrm{sgn}(x) \arctan\left(\tan(\pi/8)e^{-|x|}\right),$$

For comparison, the total phase of a fluxon with center at $x = 0$ is given by Eq.(1.5):

$$\phi(x,t) = 4 \arctan\left(e^{x}\right).$$

The derivative of $\mu(x)$ is equal to the *magnetic field* at a given point of the junction [14]:

$$\mu_x(x) = \frac{2}{\cosh(|x| - \ln\tan(\pi/8))} \quad . \tag{3.3}$$

The field in the center of the semifluxon is $\mu_x(0) = \sqrt{2} = 1.414$ and the total area under $\mu_x$ is $\pi$, i.e. $\Phi_0/2$ in absolute values, whereas the field in the center of a fluxon

is equal to 2 and the total area is $2\pi$ ($\Phi_0$). The *supercurrent density* is calculated as

$$\sin(\mu+\bar{\theta}) = \pm\sin(\mu) = \mu_{xx} = -2\mathrm{sgn}(x)\frac{\sinh(|x| - \ln\tan(\pi/8))}{\cosh^2(|x| - \ln\tan(\pi/8))}.$$

Fig. 3.1 gives an overview of the functions $\phi(x)$, $\mu(x)$, $\mu_x(x)$ (magnetic field), and $\mu_{xx}(x) = \sin(\phi(x))$ (supercurrent) of a semifluxon and a fluxon. Note that all is in normalized units.
The semifluxons are pinned at the 0–π phase boundary, carry half a quantum of the magnetic flux and have a sharp maximum that looks like a cusp with an exponential tail, whereas the fluxons are moving objects carrying one quantum of the magnetic flux.

The semifluxon is generated by Josephson currents in the absence of a driving bias current $\gamma$ and an external field $h$. It can be directly detected by measuring $I_c(H)$ in a LJJ [15], by scanning superconducting quantum interference device (SQUID) microscopy[1] or by low temperature scanning electron microscopy (LTSEM) [94].

## 3.3 Short and long 0–π JJs

The presence of a semifluxon or a fluxon in a LJJ generates a finite magnetic field $\mu_x(x) \neq 0$ even at a distance of $3\lambda_J$ or larger from the 0–π phase boundary in the center, as shown in Fig. 3.1. Until now the LJJ limit was considered, where the phase of the semifluxon extends completely inside the junction and the magnetic flux trapped in the LJJ is equal to half a flux quantum (semifluxon). If $L \approx \lambda_J$ the solution (3.3) for the magnetic field, depicted in Fig. 3.1 and 3.2(a) by the dashed line, is not valid, as the boundary conditions $\phi_x(\pm L/2) = 0$ are not satisfied anymore. The flux in shorter JJs is smaller than $|\Phi_0/2|$, so in the case of the SJJ limit I will refer to the spontaneous flux as *fractional* vortex instead of semifluxon.

To construct the solution for a fractional vortex in a 0–π JJs of finite length $\ell = L/\lambda_J$, mirror images (i.e. anti-semifluxons) are situated outside to the left and the right of the junction at a distance of $L/2$ from each edge. For the complete solution one needs to introduce an infinite chain of mirror images with alternating polarities [95]. The final magnetic field profile $\mu_x(x)$ is shown at the top of Fig. 3.2(a) by the thick solid line.

### 3.3.1 Energy of symmetric and asymmetric 0–π JJs

Kirtley *et al.* calculated the free energy of 0–π JJs for various lengths of 0 and π parts [15]. The bottom part of Fig. 3.2 addresses the generation of spontaneous flux in 0–π junctions as a function of the reduced length $L/\lambda_J$ and the degree of asymmetry $L_\pi/L = 1 - L_0/L$, where $L_0, L_\pi$ are the lengths of 0 and π parts, so that $L = L_0 + L_\pi$. Fig. 3.2(b) depicts the ratio of free energies $F_v/F_0$ of the state with some spontaneous flux normalized to the state with no flux. The dashed line is the incorrect result of Xu *et al.* [13] for junctions of intermediate length $L/\lambda_J$. Contrary to their results the state of the *symmetric* 0–π junction ($L_0/L = L_\pi/L = 0.5$) with

[1] if junction is in the LJJ limit [22, 93], like the sample depicted in Fig. 3.5.

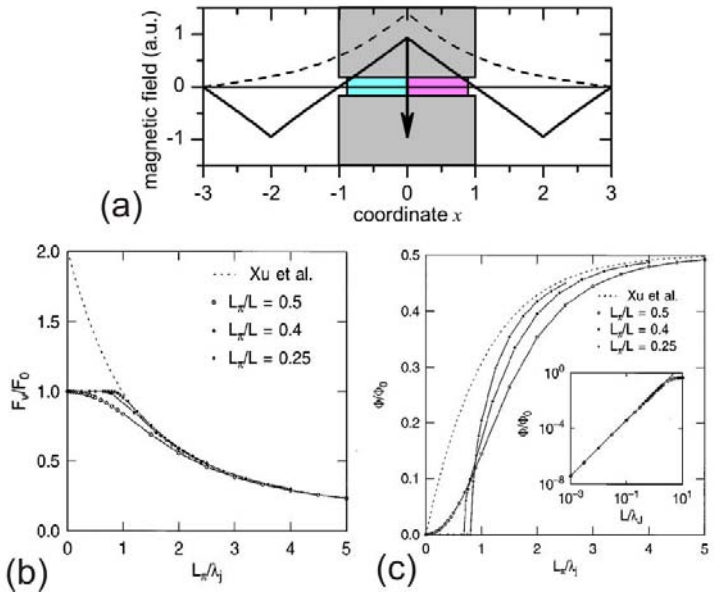


Figure 3.2: *(a) Sketch of the fractional vortex in a symmetric 0–π JJ and two mirror images outside the junction. Dashed line: magnetic field of semifluxon in an infinite LJJ, Solid line: magnetic field of the fractional vortex in a JJ of $\ell = L/\lambda_J = 2$. Arrow indicates the 0–π phase boundary created by external current injectors. Published in Ref. [95]. (b) Ratio of the free energy for the solution with spontaneous flux $F_v$ to that with no flux $F_0$ and (c) spontaneous total flux $\Phi/\Phi_0$ for a 0–π junction as function of the length of the π part $L_\pi/\lambda_J$ and for different asymmetries $L_\pi/L_0$. The inset shows $\Phi/\Phi_0$ for a symmetric ($L_\pi = L_0$) junction on a log-log scale. Data from Ref. [15].*

spontaneous flux has lower energy than the state without flux. Thus, the symmetric 0–π junctions should *always* have some selfgenerated flux. Although, as we seen from Fig. 3.2(c) the spontaneous flux vanishes as $L \to 0$.

For example, a symmetric 0–π JJ of the total length $\lambda_J$ has a spontaneous magnetic flux $\Phi = \Phi_0/8\pi \approx 0.04\Phi_0$ (for calculation see next Section). A symmetric 0–π JJ of the length $8\lambda_J$ has a spontaneous flux of some $2 - 3\%$ below $\Phi_0/2$.

### 3.3.2 Spontaneous flux in short 0–π JJs

Fig. 3.2(c) depicts the spontaneous flux $\Phi$ versus $L_\pi/\lambda_J$ for various asymmetries $L_\pi/L$. The inset shows the spontaneous flux $\Phi$ for a symmetric short junction. In the SJJ limit the phase of junction $\mu_x(x)$ deviates just a little from the average value of 0, and the spontaneously generated magnetic field $\mu_x(x)$ increases linearly towards the center of the junction, starting at zero at the edges (Fig. 3.2(a)). For these short junctions with length $\ell$ the spontaneous flux $\Phi$ is calculated by a simple geometrical

argument. The spontaneous flux of *symmetric* SJJs is determined by the area below its magnetic field, described by $\bar{\mu}_x(x) = \mu_x(x) - \mu_x(\ell/2)$. $\bar{\mu}_x(x)$ is vanishing at the junction border.

$$\frac{\Phi(\ell)}{\Phi_0} = \int_{-\ell/2}^{+\ell/2} \bar{\mu}_x(x)dx = \int_{-\ell/2}^{+\ell/2} \mu_x(x)dx - \ell \cdot \mu_x\left(\frac{\ell}{2}\right) \overset{\ell<1}{\approx} \frac{\ell}{8\pi} ,$$

as plotted by the straight line in the inset of Fig. 3.2(c).
For *asymmetric* SJJs the state with no flux $\Phi = 0$ has the lowest free energy. There is no spontaneously generated flux up to a critical value of $L_\pi/\lambda_J \approx 1$. The amplitude of the spontaneously generated flux approaches $\Phi_0/2$ as $L_\pi/\lambda_J$ gets larger.

Until now all it was assumed that $j_c(\pi) = -j_c(0)$ and the 0–$\pi$ JJ is asymmetric in length. In principle the ratio of asymmetry $\delta$ is given by the *product* of the current density $j_c$ times the junction length $L$, i.e.

$$1 - 2\delta = \frac{|j_c(\pi)| \times L_\pi}{|j_c(0)| \times L_0}.$$

### 3.3.3 0–$\pi$ JJ in magnetic field

The magnetic diffraction pattern $I_c^{0\text{-}\pi}(H)$ for 0–$\pi$ junctions differs from the corresponding patterns for conventional 0 or $\pi$ coupled Josephson junctions. For simplicity I want to concentrate on the two limits $L \leq \lambda_J$ and $L \gg \lambda_J$.

• $L \leq \lambda_J$: In a short 0–$\pi$ JJ the sign difference between the supercurrents flowing through the 0 junction and $\pi$ junction causes a reduction of $I_c$ at zero magnetic field. The analytical form for a symmetric 0–$\pi$ JJ with equal absolute $j_c(0)$ and $j_c(\pi)$ and $I_c = A \cdot j_c$, junction area $A$, is

$$I_c^{0\text{-}\pi}(H) = I_c \left| \frac{\sin^2 \pi \frac{\Phi}{2\Phi_0}}{\pi \frac{\Phi}{2\Phi_0}} \right|, \tag{3.4}$$

as given by Wollman *et al.* [96] and Xu *et al.* [13]. The $I_c^{0\text{-}\pi}(H)$ of the short Josephson junctions (SJJs) is given by equation (1.16). The magnetic diffraction pattern of the short 0 and the 0–$\pi$ JJs are compared in Fig. 1.7 and for various junction length in Fig. 3.3 (a,b) (for inline geometry[2]).

• $L \gg \lambda_J$: The $I_c^{0\text{-}\pi}(H)$ for short and long 0–$\pi$ junctions are different, due to the spontaneous complete formation of a semifluxon in the latter one. The effect of increasing $L$ on the magnetic diffraction pattern of a 0 junction (shown as 0–0 junction in Fig. 3.3(a)) in inline geometry is to reduce both the height of the central peak and amplitude of the successive oscillations for increasing magnetic field $H$. Instead, for the 0–$\pi$ junction, the increase of junction length $L$ leads to a reduced depth of the central minimum at $H = 0$. However, even for $L/\lambda_J = 10$, the critical current initially increases with the external magnetic field up to $\Phi/\Phi_0 \approx 0.5$. If $L/\lambda_J \to \infty$ the curves for the 0 and 0–$\pi$ junction still differ, as the $I_c(H)$ of 0–$\pi$ junction has always a plateau-like $I_c(H)$ pattern for small magnetic fields, due to the complete formation of the semifluxon at the center of junction [13, 15].

[2]Note that in this thesis the junctions are patterned in overlap geometry, where the current is uniformly distributed and the critical current $I_c$ increases uniformly with the junction length $L$.

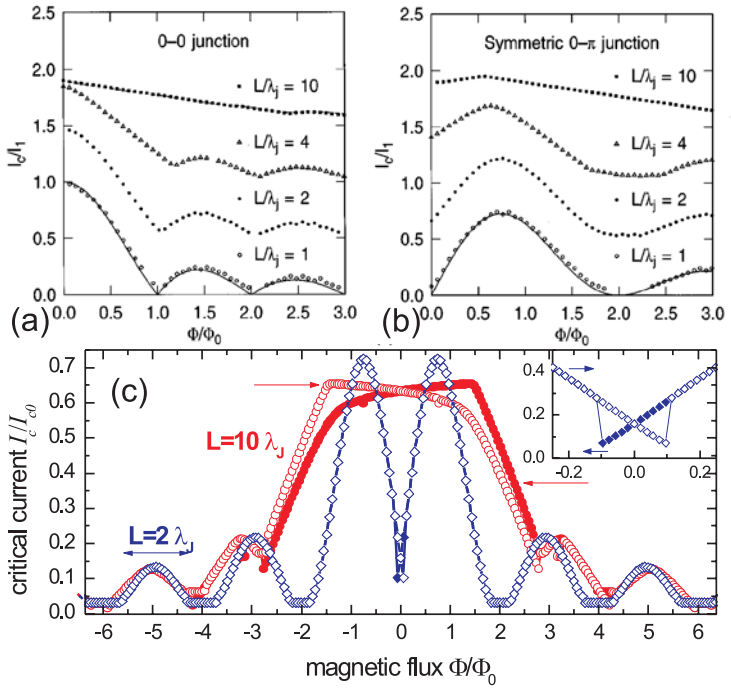


Figure 3.3: $I_c(H)/I_{c0}$ *for a series of junction lengths* $L/\lambda_J$. *(a) 0–0 junction and (b) symmetric 0–π junction in inline geometry. Solid curve is the analytical result in the short junction* $L \ll \lambda_J$ *limit. Curves have been offset vertically by* 0.5. *Data from Ref. [15]. (c)* $I_c^{0-\pi}(H)$ *of symmetric 0–π short* ($L = 2\lambda_J$) *and long JJ* ($L = 10\lambda_J$), *simulated with* StkJJ *[35]. Magnetic field polarizes the fractional vortex and the diffraction pattern depends on magnetic history. Degree of polarization shift depends on the amplitude of the fractional vortex.*

For a complete discussion the effect of polarity of the fractional flux on the $I_c^{0-\pi}(H)$ pattern should be included. This can be done using the StkJJ simulator [35]. In Fig. 3.3(c) the magnetic diffraction pattern for a symmetric 0–π JJ in short ($L = 2\lambda_J$) and ($L = 10\lambda_J$) long limit are plotted. For $L = 2\lambda_J$ the diffraction pattern, apart from the region near $H = 0$ (depicted on the inset), is still symmetric, whereas for LJJs ($L = 10\lambda_J$) it becomes asymmetric. Its final form depends on the magnetic history, as the magnetic field may flip the semifluxon when penetrating inside the Josephson junction.

## 3.4 Bias current and semi-integer fluxons

What happens if a uniform dc bias current is applied to a 0–π LJJ? The current acts like a driving (Lorenz-) force which tries to push the pinned SF in a certain

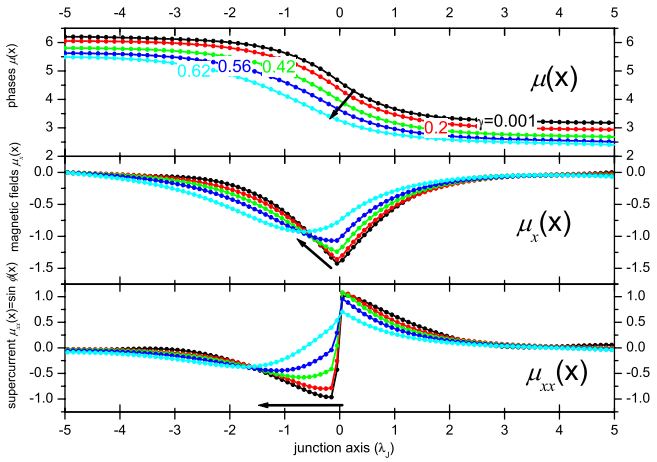


Figure 3.4: *Bias current $\gamma$ deforms magnetic phase $\mu(x)$, magnetic field $\mu_x(x)$ and supercurrent $\sin(\mu(x)+\bar{\theta})$ of the symmetric 0–$\pi$ junction of length $10\lambda_J$ containing a negative SF. Arrows indicate the direction of a change. For $\gamma \geq 2/\pi \approx 0.635$ the JJ is in voltage state and the SF flips between PSF and NSF state. Simulated with* StkJJ *[35].*

direction, depending on the polarities of the SF and of the bias current. In Fig. 3.4 the phase $\mu$, magnetic field $\mu_x$and supercurrent profile in a long 0–$\pi$ JJ with a negative semifluxon (NSF) are shown under various bias currents $\gamma$.

A bias current from 0 up to $2/\pi$ cannot move the SF, but just change its shape. The junction switches into the voltage state at $\gamma = 2/\pi \approx 0.635$ [17]. Now the junction is in the voltage state (not shown in Fig. 3.4). The negative semifluxon (NSF) becomes unstable and splits into a negative fluxon (=antifluxon) and a positive semifluxon (PSF), so that the total flux is conserved. The antifluxon moves away to the left under the action of the driving force $\gamma$. The PSF is still pinned but pushed to the right by the same driving force and consequently splits into a fluxon and a NSF. The fluxon moves away to the right. Thus, after emission of an antifluxon and fluxon, the system returns to the initial state with one trapped NSF and the whole switching process repeats, i.e. a SF of any polarity in a resistively biased LJJ emits two trains of fluxons: fluxons to the right and antifluxons to the left [17, 97, 98].

Finally, it should be mentioned that in the case of a asymmetric JJ with flat phase in the ground state $\mu_x(x) = 0$ a bias current or magnetic field may provoke the appearance of some fractional flux [17].

### 3.4.1 Semi-integer Zero Field steps

In a short 0–$\pi$ JJ the hopping of spontaneous flux under a driving bias current can take place, too. The centered SF and its mirror images (i.e. pinned NSF-PSF-NSF system) change the polarity at the same time. The PSF exchanges its position with one of the images (NSF), so that a NSF is in the center and a virtual fluxon $\Phi_0$ is

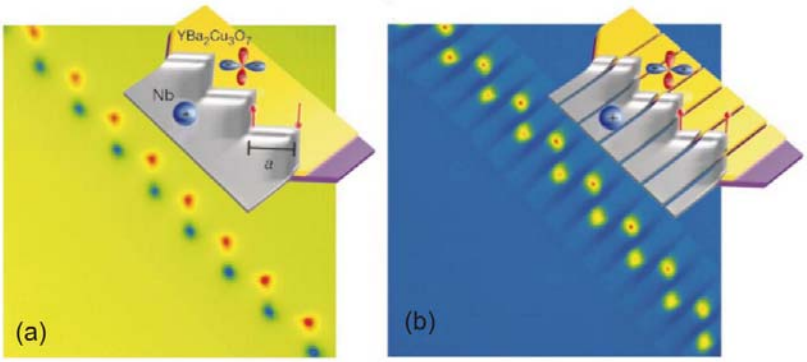


Figure 3.5: *SFs in connected (a) and unconnected (b)* $YBa_2Cu_3O_7$-Au − Nb *zigzag structures with facet length* $a = 40\ \mu$m, *imaged by scanning SQUID micrographs. The inset show geometries of the structures. (a) AFM-ordered, yellow/red and blue dots: semifluxons with opposite polarity, zero background flux: green, (b) FM-ordered, all semifluxons have same polarity (yellow/red), zero background flux is blue. Data from Ref. [22].*

transferred through the edge of the junction. Now the system is equivalent to PSF-NSF-PSF and the process repeats again, thus transferring another virtual fluxon. The net transferred flux results in a finite voltage across the junction as the phase of junction is changing with time. This process is very similar to the dynamics which takes place in a LJJ biased at the zero-field step (ZFS) (see Sec. 1.5.1). The total flux transferred per *reflection* is $2\pi$ and is twice smaller than for conventional ZFS. The velocity of the virtual fluxon does not exceed the Swihart velocity, so semi-integer ZFSs [16] can be observed in the experiment, as done by Goldobin and coworkers [95] in a 0–$\pi$ junction created with current injectors.

## 3.5 Realization of 0–$\pi$ junctions

0–$\pi$ Josephson junctions with a spontaneous flux in the ground state can be realized using various technologies. The presence of a spontaneous flux has been demonstrated experimentally in $YBa_2Cu_3O_7$-Nb ramp zigzags [22], in long Josephson 0–$\pi$ junctions fabricated using conventional Nb/Al-$Al_2O_3$/Nb technology with a pair of current injectors [95] and in the so-called tricrystal grain-boundary LJJs [93, 99, 100]. In this Section I want to focus on the first two systems[3] before the 0–$\pi$ JJ based on SFS/SIFS technology will be explained.

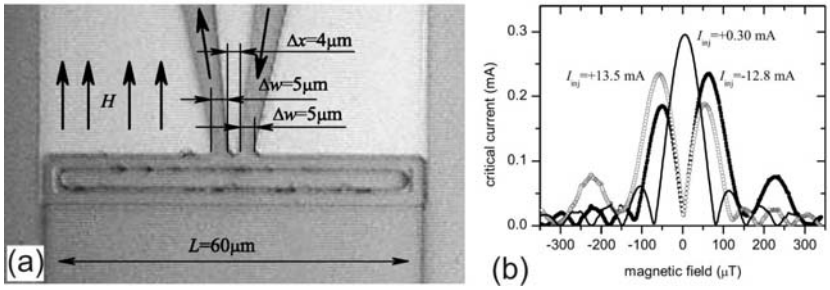


Figure 3.6: *(a) Optical microscope picture of a LJJ with two current injectors. Junction width of the LJJ is* $w = 5\ \mu$m, $\lambda_J = 30\ \mu$m *and* $j_c = 100$ A/cm$^2$. *The fractional flux is formed between the current injectors. (b)* $I_c(H)$ *dependence for* 0–0 *and* $+\pi$–0 *and* $-\pi$–0 *states of the junction. Data from Ref. [95].*

### 3.5.1 $YBa_2Cu_3O_7 - Nb$ ramp zigzags

By fabricating a ramp JJ in two directions different by 90° and along the a and b axis between an anisotropic superconductor such as $YBa_2Cu_3O_7$ and a metallic superconductor, e.g. Nb, 0 and $\pi$ JJs can be realized in one multilayer [22]. The $d_{x^2-y^2}$ wave order parameter symmetry in $YBa_2Cu_3O_7$ and the $s$-wave order parameter symmetry in Nb establish a phase shift of $\pi$ along one axis. From the top, these junctions look like zigzags with $\pi$ jumps of the Josephson phase at the corners. The SFs are formed at the corners of the zigzag. Disadvantages are i) the rather large damping (SNS like junction), ii) the fixed geometry due to $d_{x^2-y^2}$ wave order parameter symmetry and iii) the very different $T_c$'s of the superconducting electrodes, complicating the heating to the normal state to get rid of parasitically trapped flux. In the scanning SQUID microscopy image presented in Fig. 3.5, a spontaneously induced magnetic flux is clearly seen at every corner of the zigzag structure. The length of each facet ($\gg \lambda_J$) are well within the LJJ limit, thus the spontaneous flux at each corner is equal to $\Phi_0/2$. The observed SFs may be arranged antiferromagnetically, Fig. 3.5(a), or ferromagnetically, Fig. 3.5(b). For example, in the latter case there is no superconducting connection between the separate flux-generating 0–$\pi$ corner junctions and just individual, uncoupled vortices of 0–$\pi$ LJJs, aligned by a weak magnetic background signal, are present.

### 3.5.2 Artificial 0–$\kappa$ junctions

Using a pair of current injectors attached to one electrode of the LJJ, see Fig. 3.6(a), one can create an arbitrary phase boundary $\kappa$, not just $\pi$, of the Josephson phase $\phi(x)$ near the injector points [95, 101, 102]. Ideally, the injectors should have vanishing width and distance between them and carry an infinite large current. In reality, instead of a jump by $\kappa$, a rapid increase of the phase from $\phi$ to $\phi + \kappa$ over a small,

[3]Twin boundaries in d-wave superconductors usually appear as a parasitic effect during the film growth, but can be controlled to some extend.

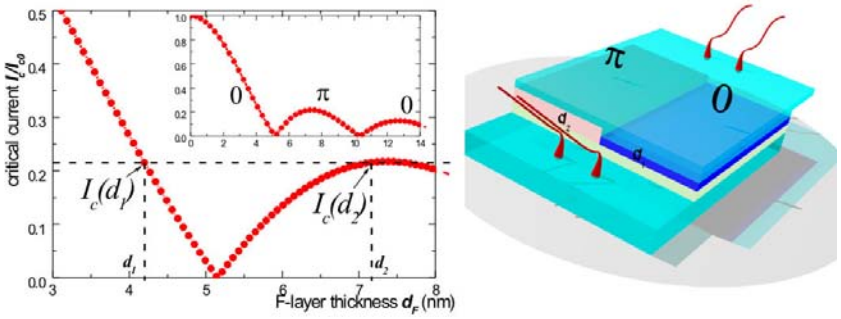


Figure 3.7: *Symmetric SIFS junctions with a step in the F-layer such that* $I_c(d_1) = -I_c(d_2)$ *and* $d_1(d_2)$ *being the F-layer thicknesses for* 0 *(*$\pi$*) coupling of the superconducting electrodes. Right: schematic layout of* 0–$\pi$ *JJ based on SFS/SIFS technology.*

but finite distance takes places. Physically this means that by passing a certain current from emitter to collector through the piece of the top electrode, the phase $\phi$ is twisted by $\kappa$ over the small distance $2\Delta w + \Delta x$ between the injector points (cf. Fig. 3.6(a)). This means a magnetic flux equal to $\Phi_0\kappa/2\pi$ is injected in this region. In Ref. [95] the artificial phase twisting region is about 10% of $\lambda_J$ when using optical photolithography. The large injector current $\sim$ 13 mA, its magnetic self-field and the finite distance and width of the injectors are disadvantages of this system. The magnetic diffraction pattern with and without the injector current is depicted in Fig. 3.6(b). The artificial 0–$\pi$ LJJ with $L \approx 2\lambda_J$ has a strongly developed minimum at $H = 0$.

### 3.5.3 SFS/SIFS Josephson junctions

As described in Chapter 2 the $\pi$ coupled SFS (SIFS) junctions are characterized by an intrinsic phase-shift of $\pi$ in the current-phase relation or, in other words, a negative critical current. By a proper chosen F-layer thickness $d_F$ the phase can be set to 0 or $\pi$ (Fig. 3.7) and the amplitude of the critical current densities $j_c(0)$ and $j_c(\pi)$ can be controlled to some degree. The advantage of this system is that it can be prepared in a multilayer geometry (thus allowing topological freedom of design) and it can be easily combined with the well-developed Nb/Al-$Al_2O_3$/Nb technology.

The starting point is the comparison of IVC and $I_c(H)$ for the reference 0 and $\pi$ JJs to estimate the important parameters such as the critical current $I_c$, the Josephson penetration depth $\lambda_J$ and the ratio of asymmetry $\delta$.
The fabrication of 0 and $\pi$ JJs on the same chip based on SFS/SIFS technology, e.g. in a dc-SQUID with 0 and $\pi$ junctions was reported [76]. However, for 0–$\pi$ junctions one needs 0 and $\pi$ coupling in *one* junction, setting high demands on the fabrication process.

Thus, the two[4] exclusive experimental works on the fabrication of 0–$\pi$ JJs based on SFS technology [23, 91] do *not* give information about $j_c(0)$ and $j_c(\pi)$. Hence,

[4]Beside the sample presented in Chapter 7.

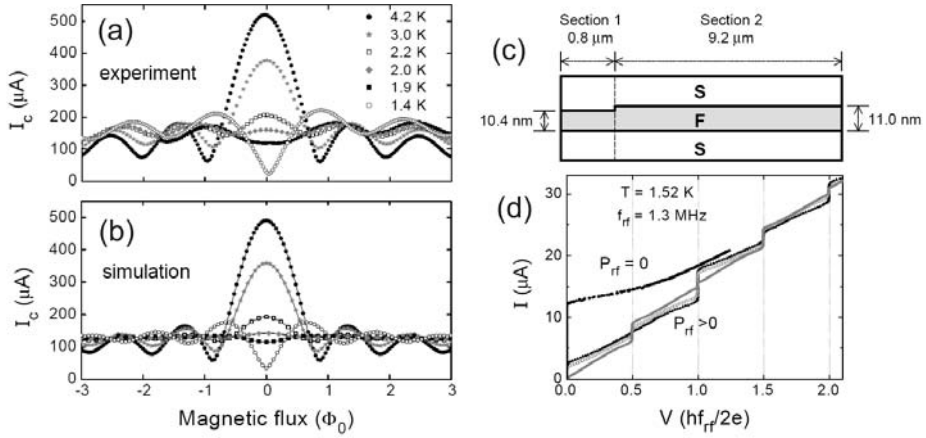


Figure 3.8: *(a) $I_c(H,T)$ pattern of SFS junction showing deviations at low temperatures, (b) simulated diffraction pattern using the deduced ferromagnetic barrier profile, (c) stepped F-layer deduced from $I_c(H)$ measurements, (d) IVC showing rf-induced Shapiro steps both at the usual voltages $V_s = \frac{hf_{rf}}{2e}$ and at half-integer values at $V_s/2$ near 0 to π transition. Data from Ref. [91].*

the Josephson penetration depth $\lambda_J$ cannot be calculated for these samples and the ratio of asymmetry $\delta$ is unknown.

The ideal 0–π JJ would have equal $|j_c(0)| = |j_c(\pi)|$ and 0–π phase boundary in its center to have the symmetric situation. Furthermore the junctions should be underdamped (SIFS structure) since low dissipation is necessary for the study of dynamics and have high $j_c$ (and hence small $\lambda_J \propto \sqrt{j_c}$) to reach the LJJ limit and to keep high $V_c = I_c R$ products. The SIFS based 0–π junctions fabricated in this thesis do fulfill these requirements, as shown in Chapter 7.

## 3.6 Current status of 0–π SFS/SIFS junctions

**Spontaneous current in 0–π JJ**

Recently, Frolov, Ryazanov and coworkers [91] reported on a spontaneous flux and half-integer Shapiro steps in SFS 0–π Josephson junctions. From the magnetic diffraction pattern, shown in Fig. 3.8(a,b), they deduced a stepped F-layer, Fig. 3.8(c), which was caused by inhomogeneities during the fabrication. By applying a microwave current and tracing the IVC they observed Shapiro steps, cf. Sec. 1.6, near the finite minimum of the $I_c(T)$ curve, see Fig. 3.8(d).

They suggested that this JJ with an non-intended step in the F-layer resembles a 0–π dc-SQUID, where the phase-lock of the spontaneous circulating current to the driving frequency can create integer and half-integer Shapiro steps [103].

The $\sin(2\phi)$ component is always present in case of the 0–π SQUIDs. It is not related to the existence of some fractional flux in such a 0–π junction, which depends

on the asymmetry $\delta$ of the junction. To reliably verify the presence of a microscopic $\sin(2\phi)$ component in an SFS junction with uniform F-layer thickness,[5] the simultaneous observation of half-integer Shapiro steps and period doubling in the current-phase relation is required, as the half-integer Shapiro steps can be caused by a 0–$\pi$ phase boundary due to unwanted roughness of the ferromagnetic layer.

As pointed out earlier in this Chapter the flux created at 0–$\pi$ JJ depends on the ratio of asymmetry and total junction length. The highly transparent SFS junction of Ref. [91] has a critical current density[6] of $j_c \approx 500$ A/cm$^2$ and $\lambda_J \approx 17$ $\mu$m, setting the $10 \times 10$ $\mu$m$^2$ junction to the SJJ limit and the strong asymmetry of the 0–$\pi$ step should prevent the spontaneous formation of magnetic flux in ground state (see Sec. 3.3.1).

**Semifluxons in 0–$\pi$ JJ as classical spins**

A publication by Della Rocca *et al.* [23] verifies that the spontaneous flux appearing in ferromagnetic 0–$\pi$ Josephson junctions behaves as a classical spin. From theoretically point of view this was clear, as the semifluxon has two degenerated ground states. They realized a 0–$\pi$ junction using SFS technology. The SFS-type 0–$\pi$ *source* junction is placed above a SIS-type *detector* junction. The step in F-layer was again achieved by uncontrolled roughness in the F-layer in the encircled part of Fig. 3.9(a). The $I_c(H)$ dependence of the source junction ($Nb^2$/PdNi/Nb–Al) was not measured directly because of the extremely small characteristic voltage $V_c$. Instead, the presence of the spontaneous fractional flux was detected by a miscellaneous SIS detector junction ($Nb^1$/Al-$Al_2O_3$/$Nb^2$) inductively coupled with the SFS JJ.

By varying $d_F$ they fabricated samples with $d_F$(PdNi) = 40 Å and 100 Å, where $d_F = 100$ Å corresponds to the $\pi$ coupled ground state. The top Nb–Al electrode had a superconducting transition temperature below 4.2 K. The $I_c(H)$ of the detector was first measured at 4.2 K, when the structure is SIS–SFN like and the spontaneous flux is absent. Below 2.0 K the top electrode becomes superconducting (SIS–SFS structure) and in case of a 0–$\pi$ source junction ($d_F = 100$ Å) the $I_c(H)$ of the detector junction shifts, as can be seen at the bottom part of Fig. 3.9(b).

The 0–$\pi$ JJ induced a shift in the magnetic diffraction pattern of the detector by approx. half a semifluxon ($\simeq \Phi_0/4$). The spontaneous flux pinned in the 0–$\pi$ JJ depends much on the ratio of asymmetry, which is unknown in this experiment, too. Maybe even multiple 0–$\pi$ steps are present in the F-layer. As these high transparent SFS junctions have probably a very small $\lambda_J$ the junction could be in the LJJ limit and the spontaneous flux might be approaching $\Phi_0/2$.

The magnetic remanence of the PdNi film lifts the degeneracy of the ground state and polarizes the supercurrent. As consequence, the sign of the shift in $I_c(H)$ is always the same below the Curie temperature ($T_C = 100$ K), indicating the same spontaneous current polarization. The authors showed by the equal distribution of positive and negative shifts by $\simeq \Phi_0/4$ of the $I_c(H)$ of detector junction in zero field cooling from room temperature ($T > T_C$), as depicted in Fig. 3.9(c) and the exact

[5] claimed by Sellier *et al.* [90], see Sec. 2.6.

[6] Magnetic scattering in the F-layer and the trilayer fabrication with breaking of vacuum result in this *moderate* $j_c$.

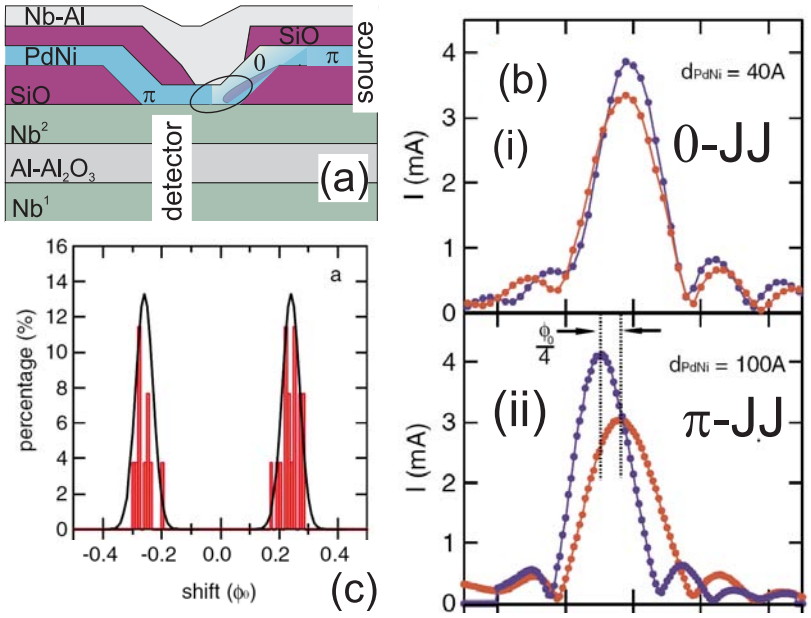


Figure 3.9: *(a) Semifluxon (source) is* $Nb^2$/PdNi/Nb-Al *stack with* $T_c = 3.6$ K. *Detector (*$Nb^1$/Al-$Al_2O_3$/$Nb^2$*) is coupled to source by common electrode (*$Nb^2$*). The loop indicates the location of SF. 0 coupling is set by holes in* PdNi *layer. (b)* $I_c(H)$ *of the detector for sources with* $d_F(\mathrm{PdNi}) = 40, 100$ Å *corresponding to i) 0 coupling and ii) π coupling. Red: measurements taken at* $T = 4.2$ K *(SIS–SFN) and blue:* $T < 2.0$ K *(SIS–SFS). Shift of* $I_c(H)$ *about* $\Phi_0/4$ *appears in (ii) case, where a 0–π JJ is realized, (c) Amplitude histograms of the spontaneous shift for 26 different cooldowns of different samples from* $T > T_C$ *and Gaussian fits. The Gaussians have mean values of* $+0.24\Phi_0$ *and* $-0.26\Phi_0$. *Data from Ref. [23].*

flux compensation upon field cooling, that these 0–π junctions behave as classical spins.

# Part II

# Experimental results

# Chapter 4

# Sample preparation

The fabrication of Josephson tunnel junctions with a ferromagnetic interlayer (SIFS stack), exhibiting a uniform transparency for Cooper pairs through the insulating and ferromagnetic double layers was challenging. To measure the tunnel current the superconducting electrodes on the bottom and the top of the I/F layers had to be contacted. The simple deposition of a multilayer stack was not sufficient. The device had to be patterned by thin film techniques in a crossbar geometry.

This Chapter describes the deposition method of multilayer films with a focus on the tunnel barrier formation and the lithographic patterning of samples. For the production of Josephson tunnel junctions a combined deposition and patterning process was utilized, which included sputter deposition, ion-beam etching, anodic oxidation and optical lithography. Individual process steps were modified in part to fulfill the particular requirements of SIFS junctions in the 0 and $\pi$ coupled regime. To ensure a high yield of functional junctions, the standard SNEAP patterning process [104, 105] for Nb/Al-$Al_2O_3$/Nb (SIS) junctions was modified and optimized for the SIFS-type junctions.

The fabrication of SIFS JJs with *symmetric* 0–$\pi$ coupling was a task with many obstacles. The sophisticated patterning process for obtaining a step of a few tenth of nanometer height in the ferromagnetic layer (F-layer) is treated in the last part of this Chapter.

The structural and electrical characterizations of the junctions are described in Chapter 6 (SIFS junction with a uniform F-layer) and Chapter 7 (SIFS junction with a stepped F-layer).

## 4.1 Sputter deposition

The fabrication of multilayers was performed in situ by a computer-controlled Leybold Univex 450B magnetron sputtering system (Fig. 4.1).

The deposition of thin films by a plasma was originally discovered in 1852 by *Sir Grove* and 1858 by *Plücker*. The term *sputtering* was first used in the 1920s by I. Langmuir and K. H. Kingdon and is derived from the Latin *sputare* (to emit salviva with noise). It is used for the erosion of a solid state surface (the target) by an energetic particle bombardment in the limit of small particle flux [106].

In an electric field between substrate and target the positive charged ions are

accelerated towards a negative charged target. By momentum transfer to the target atoms these ions generate non charged atoms with kinetic energies of about 10 eV, which move isotropic in space and are deposited in part on the substrate. A noble gas like argon is used as process gas at a pressure of several $10^{-3}$ mbar. Due to the natural radioactivity the gas atoms are partly ionized and the free electrons are accelerated towards the anode. Thereby more ions and electrons are produced in a cascade manner. The lower limit for the ionization voltage depends on gas, geometry of the set-up and the target material. Since the recombination of the gas ions and electrons takes place inside the plasma a discharge glow is visible.

To enhance the sputter rate *magnetron-sputtering* is used, where the stray fields of permanent magnets are focusing the plasma in a ring-formed area near the target. This increases the charge carrier density and leads to higher sputter rates. The distance between target and substrate is about 6 cm in the employed system. A rotary arm places the sample below the target. A computer controlled shutter between target and sample allows precise pre-sputtering and deposition timing. Typical power for metals is about 150 W for a 4 inch target (1.9 W/cm$^2$), yielding deposition rates of 1 nm/s. To decrease the deposition rates and to ensure a highly uniform grows of films the sample can be rotated under the target (down sputter method).

## 4.2 Multilayer deposition

Thermally oxidized 4-inch Si wafer served as substrates. The wafers were clamped onto a water cooled Cu-block.
First of all, the 120 nm Nb bottom electrode and the 5 nm thick Al layer were deposited.
Second, the aluminium was oxidized at room temperature for 30 min in a separate chamber at an oxygen partial pressure ranging from 0.001 to 50 mbar, depending on the desired critical current density $j_c$ of the superconducting tunnel junctions.

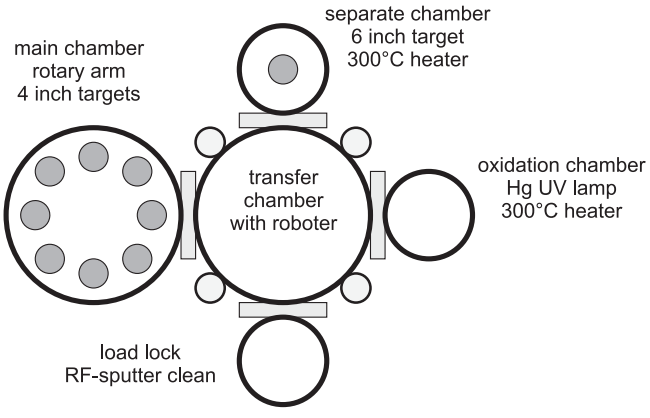


Figure 4.1: *Layout of Leybold Magnetron sputter machine Univex 450B.*

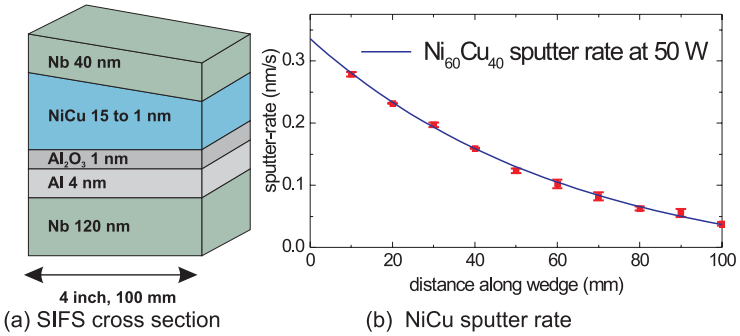


Figure 4.2: *(a) SIFS stack with* wedge*-shaped F-layer and (b) decreasing of* NiCu*-sputter rates across a 4 inch wafer off-placed underneath the target.*

Third, for the SIFS junctions the ferromagnet (i.e. a NiCu alloy) was deposited. For realization of the *wedge* shaped NiCu-layer, see Fig. 4.2(a), the substrate and sputter target were shifted about half the substrate length. This enabled the preparation of SIFS junctions with increasing F-layer thicknesses along the direction of the shift to avoid the inevitable run-to-run variations. The sputter-rates for NiCu along the gradient were determined by thickness measurements on reference samples using a Dektak profiler. In this way I prepared SIFS stacks with the F-layer thickness ranging between 1 and 15 nm, see Fig. 4.2(b).[1]
At the end a 40 nm Nb cap layer was deposited.
SINFS-type multilayer stacks with a normal metal N, i.e. Cu, were prepared, too.

The radius of neutral Ni and Cu atoms is about 0.15 nm. The polycrystalline structure of the NiCu film and the inherent interlayer roughness of room-temperature sputtered films prevent the exact estimation of the layer thickness. In addition, my experimental results suggested that a continuously variable-thickness model was more suitable for the junctions than a monolayers-thickness model. The mean F-layer thickness of the Josephson junction was calculated from its location on the shifted substrate and the sputter rates, shown in Fig. 4.2(b).

Nb and NiCu were statically deposited, while Al and Cu were deposited during

[1]The estimated variation of the F-layer over a length of 100 $\mu$m was less than 0.02 nm, i.e. it could be neglected.

Table 4.1: *Deposition parameters for SIS, SIFS and SINFS stacks.*

| metal | Ar pressure $[10^{-3}$ mbar] | power density [W/cm$^2$] | rate [nm/s] | deposition type |
|---|---|---|---|---|
| Nb | 7.0 | 5 | 2.0 | static |
| Al | 7.0 | 1.9 | 0.05 | rotation |
| NiCu | 4.2 | 0.6 | $\leq 0.34$ | shifted from target |
| Cu | 4.2 | 1.9 | 0.1 | rotation |

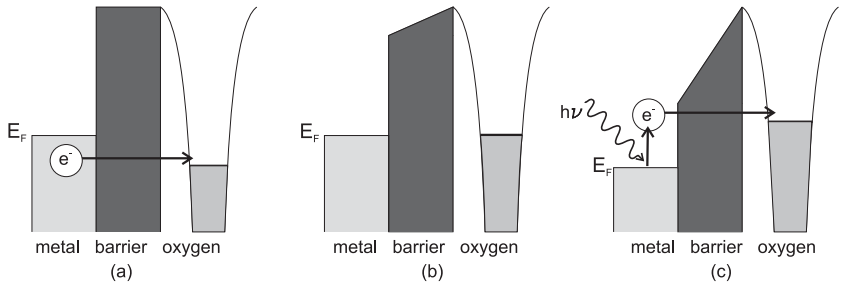


Figure 4.3: *Energy scheme for oxidation of metals. (a) electron transfer through barrier, (b) after ion transfer, asymmetric barrier, (c) UV-enhanced oxidation.*

sample rotation and at much lower deposition rates to obtain very homogeneous and uniform films. Details of the deposition process are depicted in table 4.1.

## 4.3 Oxidation process of tunnel barrier

The quality of a tunnel junction depends very much on the properties of the tunnel barrier. The tunneling probability is exponentially dependent on the barrier thickness. The inhomogeneity of the tunneling current scales with the interface roughness of the barrier. The chemical structure of the aluminium oxide and impurity atoms in the barrier influence the electronic properties such as the conservation of electron spin during tunneling.
As a result of the wetting of Al on Nb [107–109] the Nb/Al-$Al_2O_3$/Nb trilayer stack is the standard choice for the fabrication of Josephson tunnel junctions. After a few monolayers of Al on Nb a closed Al layer is formed. The oxidation of aluminium is self-limited and the $Al_2O_3$ layer is 30% thicker than before oxidation. Detailed studies on metal oxidation were performed by Cabrera and Mott [110, 111] and are shortly summarized for the case of aluminium.

The first Al monolayer oxidizes immediately in high vacuum due to the remaining oxygen in the residual gas. The lowest unoccupied orbital of the oxygen is energetically lower than the Fermi-energy of aluminium. After adsorption of oxygen on the $Al_2O_3$ surface, electrons are tunneling into the oxide-gas interface. This leads to a surface charge and thus to an electric field between the Al metal and the upper most oxide-layer. Subsequently positive Al-ions migrate toward the oxygen layer and form a new $Al_2O_3$. The maximum thickness of the $Al_2O_3$ barrier is determined by the potential difference between the Fermi-level of Al and the lowest unoccupied orbital level of the adsorbed oxygen, which depends on the partial oxygen pressure.

To form a thick $Al_2O_3$ barrier, of particular importance for junctions with very low critical current densities, an ultraviolet light (UV) assisted oxidation process [112, 113] was used. As UV source a mercury lamp with emission lines at 254 nm and 185 nm was employed. By this irradiation the molecular oxygen is transformed into highly reactive atomic oxygen and ozone. At 100 mbar the absorption length is larger than 30 cm, whereas the distance between lamp and substrate is less than

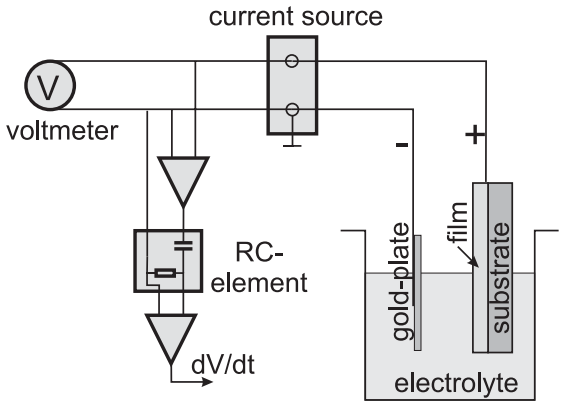


Figure 4.4: *Set-up for anodic oxidation of* Nb *and* Al*, used for i) the structural analysis of* Nb/Al-$Al_2O_3$/Nb *and ii) the formation of* $Nb_2O_5$ *for the junction insulation.*

10 cm. The photoelectric effect increases the energy of the aluminium-electrons (i.e. the electric field over the aluminium-oxide) and the final $Al_2O_3$ thickness is enhanced.

## 4.4 Anodic oxidation process

Anodization is an electrolytic process in which a metal, in this case niobium and aluminium, serves as the anode in a liquid electrolyte. The anodization was performed at room temperature using the standard anodization techniques [114] (see Fig. 4.4). The electrolyte is a mixture of 156 g ammonium pentaborate, 1120 ml ethylene glycol and 760 ml $H_2O$ [104]. The partially submerged Nb was used as anode and a gold-covered metal serves as cathode. The electric contact was made outside the electrolyte to the anode. By protecting parts of the niobium electrode with photoresist only a well-defined area was oxidized. When a constant current passed through the Nb or Al film in the electrolytic solution, the surface of the metal was converted to its oxide form. The oxidation front progressed from the electrolyte towards the metal. The final oxide thickness was determined by the maximum built-up voltage. About 0.88 nm of Nb was consumed and about 2.3 nm of $Nb_2O_5$ was produced for each volt applied across the anodization cell. The partial derivative of the voltage drop with time $dV/dt$ over the substrate depended on the metals, if the anodization current density was kept constant.

The anodic oxidation was used twice for the preparation of Nb based junctions: to monitor the sharpness of the Nb-Al and $Al_2O_3$-Nb interfaces (see Section 6.1.1) and to form niobium oxides for the tunnel junction insulation. Anodization processes of this type have been extensively used in the past for the fabrication of Nb based Josephson junctions [104, 105, 115–117].

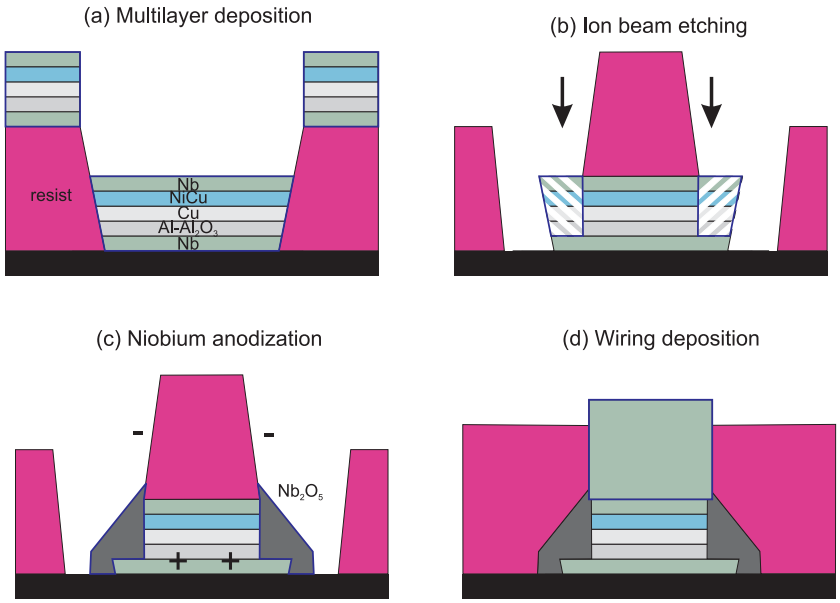


Figure 4.5: *(a) to (d) Three level photo mask procedure including ion-beam etching and Nb-anodization for junction insulation.*

## 4.5 Patterning

In general, tunnel junctions are patterned using optical lithography and Ar ion-beam milling. The standard procedure for the patterning of SFS or SIFS junctions [8, 9, 65, 79] is done by a three level photolithographic mask procedure, similar to Kroger *et al.* [104] and Gurvitch *et al.* [105]. The insulation of the junction is done by a self-aligned deposition of silicon-oxides after the etching.

For this thesis the patterning was modified to ensure a high yield of functional devices. A $Nb_2O_5$ insulator was formed by anodic oxidation of Nb after the ion-beam etching. The $Nb_2O_5$ exhibited a nearly defect free insulation between the superconducting electrodes, even for ferromagnetic interlayers of 15 nm thickness.

• With the first photolithographic process the bottom SIFS-layer areas were defined by a lift-off process. The situation after deposition of the SIFS sequence is shown in Fig. 4.5(a).

• After lift-off various kinds of the tunnel junctions were defined by applying the second photo mask step and followed by Ar ion-beam etching of the Nb, NiCu and Al layers. The etching was controlled by a secondary ion mass spectrometry (SIMS) and the procedure was stopped after the complete etching of the $Al_2O_3$ tunnel barrier, as shown in Fig. 4.5(b). During the etching the substrate was tilted by 70° and rotated to avoid etch fences at the edges of the mesas. The mass spectrum is plotted in Fig. 4.6. Note that the sensitivity of the spectrometer to Al allowed an accurate stop of etching just below the Al layer. The mesas were isolated by the SNEAP (Selective Niobium Etching and Anodization Process) [105], Fig. 4.5(c).

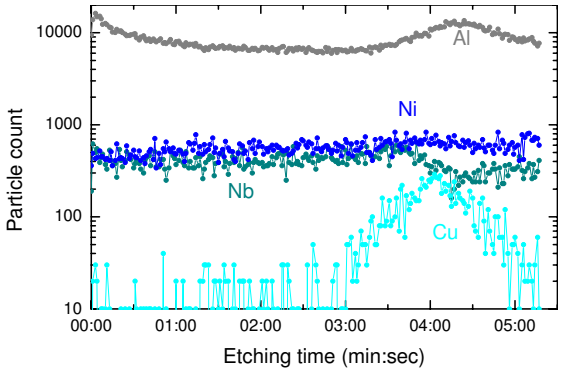


Figure 4.6: *Mass spectrometer graph: Etching of* Nb, NiCu, Cu *and* $Al_2O_3 - Al$ *layer of SINFS type stack down to S-layer. The wedgelike* NiCu*-layer provoked a smearing of peaks of the underlying* Al *and* Cu *layers. The* Ni *peak can hardly be distinguished from the background signal.*

•In the last photolithographic step the wiring layer was defined. After a short ion-beam etching to reduce the contact resistance, a 300 nm thick Nb wiring was deposited. Fig. 4.5(d) shows the schematic cross section of the fully patterned device.

It is interesting to note that the anodization was successful in presence of the NiCu layer. No problems with parallel currents through the NiCu layer during anodization were obtained. Probably the ferromagnetic layer was so thin that it was immediately overgrown by $Nb_2O_5$ shortly after starting the anodization procedure. At a rate of about 1 V/s the junction was anodized up to a voltage of 60 V (corresponding to 52 nm of anodized Niobium). The form factor of 2.3 for Niobium oxidation corresponds to 120nm of formed $Nb_2O_5$, providing a complete side coverage of the barrier and the ferromagnetic layer.

### 4.5.1 Idle region and capacitance

The formation of the junction area was done by leaving a window in the insulating region of $Nb_2O_5$ (dielectric constant $\epsilon \approx 30$). The $Al_2O_3$ tunnel barrier has a dielectric constant $\epsilon \approx 4 - 9$. The insulating area between bottom and top electrodes, which provided the passivation of the bottom electrode all around the tunnel area, is the so-called *idle region*, see Fig. 4.7. It was shown that the presence of the idle region changes the static [118] and the dynamic properties [119] of Josephson tunnel junctions.

The total specific capacitance of a Josephson junction is given by $C^*_{\text{total}} = C^*_{Al_2O_3} + C^*_{Nb_2O_5}$ with capacitance $C^* = \epsilon\,\epsilon_0\,w_{i,j}/d_I^{i,j}$, and the total specific self-inductance by $\overline{L}^{-1}_{\text{total}} = \overline{L}^{-1}_{Al_2O_3} + \overline{L}^{-1}_{Nb_2O_5}$ with self inductance per unit length $\overline{L}_{i,j} = \mu_0\; d'_{i,j}/w_{i,j}$, width $w_{i,j}$, dielectric constant $\epsilon_{i,j}$, insulator thickness $d_I^{i,j}$ and magnetic thickness $d'_{i,j} = d_I^{i,j} + \lambda_L \coth(t_1/\lambda_L) + \lambda_L \coth(t_2/\lambda_L)$. The indexes $i$ and $j$ refer to the idle and the junction region, respectively.

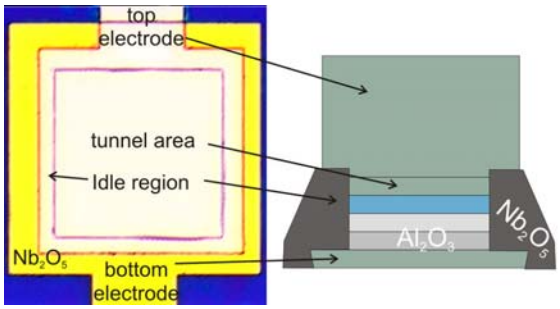


Figure 4.7: *Optical microscope picture (top view) and cross section of a window junction with idle region. The area of the junction is* $100 \times 100\ \mu\mathrm{m}^2$.

A junction with idle region is characterized by a larger capacitance $\overline{C}_{\mathrm{total}}$ and a smaller self-inductance $\overline{L}_{\mathrm{total}}$ per unit length, compared to the *naked* junction.[2] The capacitance and self-inductance of the junction are connected to the Swihart velocity $\bar{c}_0$ by

$$\frac{1}{\sqrt{C^*_{\mathrm{Al_2O_3}} \cdot \overline{L}_{\mathrm{Al_2O_3}}}} = c\sqrt{\frac{d^j_I}{\epsilon_j d'_j}} = \bar{c}_0$$

In the idle region I get

$$\frac{1}{\sqrt{C^*_{\mathrm{Nb_2O_5}} \cdot \overline{L}_{\mathrm{Nb_2O_5}}}} = c\sqrt{\frac{d^i_I}{\epsilon_i d'_i}} = c\sqrt{\frac{d^i_I \epsilon_j}{d^j_I \epsilon_i}\frac{d'_j}{d'_i}} > \bar{c}_0$$

Thus, the Swihart velocity is increased outside the window region, i.e. inside the idle region. The idle region plays a prominent role in the phase velocity of the electromagnetic wave and can influence the estimation of Swihart velocity, capacitance and magnetic thickness $d'$ of junction. Monaco *et al.* [119] reported for junctions with an idle region i) along the long junction dimension a *frequency dependent increase* and ii) along the end of junctions a *frequency independent decrease* of the phase velocity.

The focus of this thesis was on the static properties of Josephson junctions, i.e. the coupling of phase. This was done by measurements of the critical current $I_c$ when changing the magnetic field, the temperature or the F-layer thickness. For the sake of simplicity, the junction layout was not optimized for measurements in the dynamic region. Fiske step measured for junctions with different geometries, but same thickness of $Al_2O_3$ tunnel barrier, yielded different values for the capacitance. The estimated capacitance was decreasing with increasing ratio of the idle over the junction region. I calculated the capacitance using the junction with the smallest idle region. The aluminium oxide tunneling barrier formed at 0.015 mbar gave a specific capacitance $\overline{C}$ of $\approx 8\ \mu\mathrm{F/cm}^2$. The detailed study of dynamics in $\pi$ or 0–$\pi$ coupled junctions is subject of future work.

[2] Junctions with a neglectable idle region.

Table 4.2: *Final patterning and deposition/etching receipt for SIFS junctions with a step in the F-layer. 0 ($\pi$) JJ with the F-layer thickness $d_1$ ($d_2$) is denoted as* $SIF_0S$ *(*$SIF_\pi S$*) and the F-layer step height is* $\Delta d_F = d_2 - d_1$.

| receipt | assets and drawbacks |
|---|---|
| deposition of $SIF_\pi S$ | well defined ✓ |
| etching down to $SIF_0$ | etching of S (completely) and F (about $\Delta d_F$) ? |
| | roughness of $F_0$ ? |
| deposition of cap Nb | high transparent $F_0$/S interface ? |

## 4.6 SIFS junctions with step in the F-layer

Although some time was spent on the complex and sophisticated fabrication of SIFS junctions with a stepped F-layer, the description is brief, as just the successful attempt is described.

The 0 JJ with the F-layer thickness $d_1$ is denoted as $SIF_0S$, the $\pi$ JJ ($d_F = d_2$) as $SIF_\pi S$ and the F-layer step height between both coupling regimes is $\Delta d_F = d_2 - d_1$.

The SIFS junctions with step in the F-layer were based on the SIFS structures described in Section 4.5. The sign of the critical current and therefore the phase $\phi$ (0 or $\pi$) in the ground state depends on the thickness $d_F$ of the ferromagnetic layer. Rigorous control of *both* F-layer thicknesses was mandatory to achieve a *symmetric* 0–$\pi$ JJ with F-layer thicknesses $d_1, d_2$ and step-height $\Delta d_F$. Both parts (0, $\pi$) of the junction should have the same length $L_0 = L_\pi$. The proper chosen thicknesses of the F-layers should yield the same absolute critical current densities: $j_c(d_1) = -j_c(d_2)$.

### Accuracy of stepped F-layer

Magnetron sputtering is based on the combination of ion production and acceleration near the target. The isotropic deposition of the sputtered metal atoms leads to shadow effects ($\sim 10\ \mu$m) if using metal or Si shadow masks to define the 0–$\pi$ step. In addition, the inaccuracy of in situ mask handling sets a handicap for patterning of the 0–$\pi$ step. Using optical lithography the condition $L_0 = L_\pi$ could be fulfilled up to an accuracy of 1 $\mu$m. The shadow effect at the side of the photoresist was much reduced, as the resist had a height of $\sim 1\ \mu$m. Patterning of the structures by optical lithography is done ex situ by means of water, organic polymers, developers and solvents under thermal heating of the resist up to 120°C. Thus, the top surface of the sample was oxidized and had to be removed by short ion-beam etching to obtain similar interface transparencies in 0 and $\pi$ parts.

### Reactive dry etching

In the past two decades a lot of research was done on the use of selective etching in Nb/Al-$Al_2O_3$/Nb stack fabrication processes, such as wet etching, $CF_4$ and $SF_6$ reactive ion etching (RIE) or other techniques [120, and references herein]. In particular, it was shown that $SF_6$ provides an excellent RIE chemistry for low-voltage

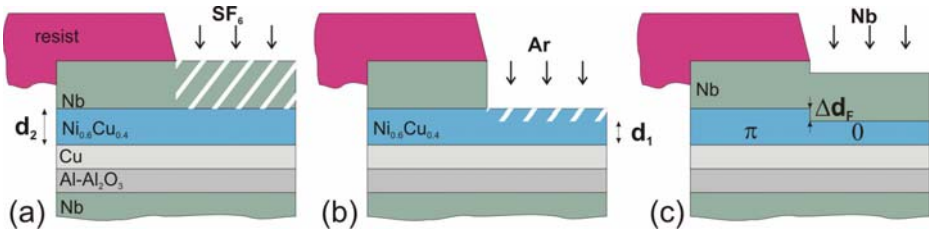


Figure 4.8: *The complete SIFS, i.e. the high quality SINFS, stack was protected in part by photoresist. The* Cu*-layer was necessary for uniform current transport (cf. Chap. 6.3.1): (a) reactive etching of* Nb *with* $SF_6$ *down to* NiCu *layer, (b) ion-etching of* NiCu *to set* 0 *coupling and (c) in situ deposition of cap* Nb *layer.*

anisotropic etching of Nb with high selectivity towards other metals [120]. I have chosen $SF_6$ to remove the Nb-layer.

The inert $SF_6$ dissociated in a rf-plasma and the fluor diffused to the surface of the substrate, where it reacted with niobium

$$5F + Nb \longrightarrow NbF_5.$$

The volatile $NbF_5$ was pumped out of the etching-chamber. For reactive dry etching the still existing shadow-effects by the photoresist at the side of junction could be neglected.

### 4.6.1 Patterning of step in the F-layer

The patterning of the 0–$\pi$ JJ can be done by several approaches. For this thesis the receipt from table 4.2 was chosen.
The deposition of a $\pi$ coupled JJ with subsequent in situ etching of the S and F-layers and deposition of the S-layer to define the 0 coupled parts was the most likely technique to yield functional 0–$\pi$ JJs with small variation of parameters. The 0–$\pi$ patterning was done after the complete deposition of the SIFS stack and before the definition of the junction mesa by argon-etching and $Nb_2O_5$ insulation. The actual junction was centered at a step in the F-layer, visible by the non-uniform Nb layer above (ramp of $\sim$ 20 nm height and $\sim$ 1 $\mu$m width). Hence, it took place between steps (a) and (b) as shown in Fig. 4.5.

#### Reactive and ion-etching

Simple ion-etching of both Nb and NiCu did not provide a good control over the final F-layer thickness, as this unselective long-timed etching has the disadvantages of non-stable etching rates and an non-uniform etching front. Thus, either the tunnel barrier was partly etched, or the etching was stopped before reaching the ferromagnetic layer. If reactive dry etching was used, the last part of etching still had to include an ion-etch to remove all non-metallic etching products such as fluorides and sulfides from the top-layer of the NiCu, in case that $SF_6$ was used as process gas.

**Etching/Deposition parameters**

The 0–$\pi$ patterning process is depicted in Fig. 4.8. The key points were i) *selective reactive etching* of the Nb, ii) *ion-etching* of the NiCu to define $SIF_0$ and iii) subsequent *in situ* deposition of Nb.

After deposition and lift-off of the complete $SIF_\pi S$ stack the junction was partly protected with photoresist to define the step location in the F-layer.
• The unprotected 40 nm Nb cap layer was removed by reactive dry etching with $SF_6$. The $SF_6$ gas pressure was $1.5{\cdot}10^{-2}$ mbar and the power density was 0.6 W/cm$^2$. The selective etching provided an etching rate[3] of Nb $\sim 1$ nm/s, whereas the NiCu served as an etching barrier due to the much lower etching rates of Cu and Ni. Nb was completely removed to avoid any (superconducting) short circuits at the side. At the same time the NiCu surface was still homogeneous and flat, as can be determined from the electric transport measurements (see Chapter 7).
• A few tens of nanometers of NiCu were Ar ion-etched at a very low rate: 0.008 nm/s. The argon pressure was $5 \cdot 10^{-3}$ mbar and the power density was 0.6 W/cm$^2$. The low power density of the etching-source reduced the damage of the NiCu film below the surface and at the same time gave a good control over the thickness.
• Finally a 40 nm Nb layer was deposited by magnetron sputtering.
The complete etching and subsequent deposition of 40 nm Nb cap layer was done in situ at a background pressure below $2 \cdot 10^{-6}$ mbar.

In Fig. 7.5 a centered 0–$\pi$ coupled SIFS junction is presented, although the 0–$\pi$ step could hardly be resolved by optical microscopy and is denoted by the black dashed line. To my knowledge, this was the first controlled patterning of 0–$\pi$ Josephson junctions based on a ferromagnetic interlayer.

### 4.6.2 Structural analysis of the step

On reference samples I structured multiple 0–$\pi$ steps with 2 $\mu$m gap and width for structural analysis after etching and Nb deposition. The topography was obtained by SEM (Hitachi-S4100) with a field-emission electron gun operating at 6.3 kV and AFM (S.I.S Picostation) in non-contact mode, as depicted in Fig. 4.9(a+b). For SEM the photoresist was left on the sample and for AFM it was removed by lift-off technique. While etching with $SF_6$ the NiCu-layer served as etching barrier. Thus it facilitated the over-etching of the Nb to ensure its complete removal. Just the short-timed argon-etched NiCu-layer was slightly non-uniform near the resist walls (resist height 1 $\mu$m) due to the anisotropic etching front. Since in real 0–$\pi$ JJs the 0 coupled part had dimensions about 10 $\mu$m or larger, the non-uniformity of the NiCu layer near the 0–$\pi$ boundary, created by shadow-effects of the resist, was averaged out in transport measurements and could be neglected.

However, the deposition of Nb after the reactive and ion-beam etching led to a non-uniform cap layer. The slight asymmetry in the wall gradients of the resist, as seen in SEM, caused a variation of the Nb deposition rates near the resist walls. This explains the difference in stack height (much larger than $\Delta d_F$), as can be seen at the AFM image of the SINFS stack shown Fig. 4.9(b).

[3]The etching rates were estimated from reference samples with thick films.

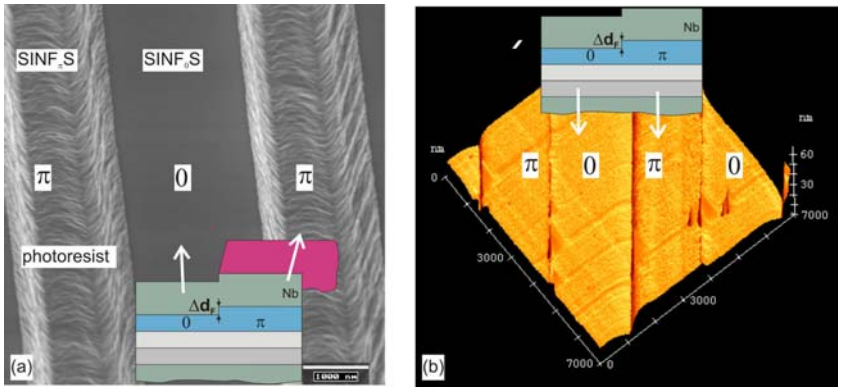


Figure 4.9: *Topography of* $(0\text{-}\pi)_n$ *reference sample with* 2 $\mu$m *wide gaps after etching and* Nb *deposition. (a) SEM image before removal of photoresist (protecting* $\pi$ *coupled parts). (b) AFM image* ($7 \times 7$ $\mu$m$^2$) *after removal of photoresist.*

# Chapter 5

# Ferromagnetic NiCu alloys

The magnetic properties of the F-layer in the SIFS stack are of great importance in the search for $\pi$ coupled Josephson junctions. The choice of the ferromagnetic layer has great impact on the current transport characteristics. All the essential parameters of $\pi$ coupled JJs, such as the critical current density and related parameters like damping of the plasma oscillations are determined by the F-layer. For this thesis I have chosen the $Ni_{60}Cu_{40}$ alloy, consisting of the strong ferromagnet Ni and diluted with diamagnetic Cu.

## 5.1 Theory of NiCu alloys

The saturated magnetic moments of the 3*d* transition atoms can be changed over a large range in binary alloys by changing the number of electrons per atom [122]. The well-known *Slater-Pauling curve* shows a linear correlation for the average moment $m_{at}$ and the number of electrons per atom for alloy atoms which differ only by one or two atom-numbers, such as $_{28}$Ni and $_{29}$Cu.

In fact, bulk NiCu alloys have been very intensively studied in the second decade of the 20$^{th}$ century as model systems for the onset of magnetism. They vary smoothly from paramagnetic to ferromagnetic order with increasing Ni content (see Fig. 5.1). For just a few Ni impurities in a Cu matrix some magnetic Ni clusters arise from

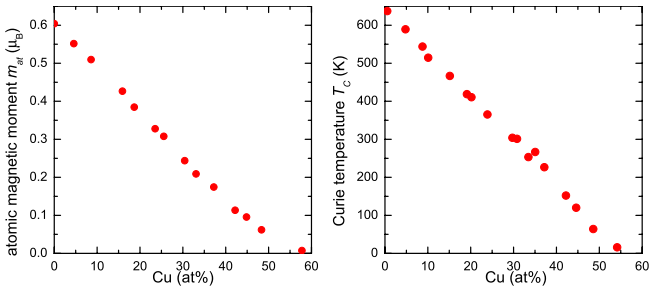


Figure 5.1: *Magnetic moment $m_{at}$ per atom and Curie temperature $T_C$ of bulk* NiCu *alloys. Measured by Ahern at al. [121] in 1958.*

statistical concentration fluctuations. If the impurity concentration increases further, the cluster spins begin to overlap with their nearest neighbors and a correlation develops, which leads to large but local ferromagnetic regions. Thus, the inhomogeneity is the onset of ferromagnetism in those disordered alloys. For Ni concentrations larger than $44 - 47.6\%$ [123] ferromagnetism arises. A recent publication by Rusanov *et al.* [124] on dc and rf magnetron sputtered thin films of $Ni_xCu_{1-x}$ alloys with $x = 0.60, 0.50$ and 0.45 at.% is in good agreement with the data from bulk alloys [121]. It should be mentioned that for a Ni concentration of up to 80% *clustering* was observed. However, the annealing temperatures (several 100°C) and times (several hours) for the observation of clustering in $Ni_{60}Cu_{40}$ samples were much larger than my standard parameters of 4 min photoresist baking at 120°C [125] during the patterning.

### 5.1.1 Very thin NiCu films

The magnetism in thin magnetic films is weaker than in bulk. Of particular interest is the so-called *dead magnetic layer* in which the ferromagnetism and even the magnetic moments are suppressed. For Co and Fe the first monolayers already show a magnetic moment at 10 K [126]. Ni films with less than two atomic layers possess no magnetic moment, but show an enhanced susceptibility at 10 K. Ni films thicker than three monolayers show a magnetic moment [126]. This sets the lower limit for the thickness of the dead magnetic layer in polycrystalline NiCu alloys.

For dc sputtered films from a $Ni_{60}Cu_{40}$ target onto a Nb film a change of the stoichiometry with decreasing film thickness was reported [127]. NiCu films with thickness below 4 nm display a change of the Ni content from 60% to 50%. The authors claim that the enhanced wetting of Cu of the bottom Nb layer is responsible for the compositional change. Hence, NiCu films pose a reduced exchange energy $E_{ex}$ at the lower interface of SFS stacks compared to the top interface. To my knowledge no work on the wetting of NiCu on a $Al_2O_3$ tunnel barrier (present in the SIFS multilayer presented in this thesis) has been published, yet.

## 5.2 Characterization of $Ni_{60}Cu_{40}$

I have chosen the diluted ferromagnetic alloy $Ni_{60}Cu_{40}$ as the ferromagnet in SIFS stacks to reduce both the strong magnetic scattering and the magnetic inhomogeneity observed in SFS junctions with F $=Ni_xCu_{1-x}$ alloys for $x$ up to 0.53 atomic percent [128, 129]. $Ni_{60}Cu_{40}$ is a weak itinerant ferromagnet and the magnetization of its thin films is in-plane [130].

### 5.2.1 Stoichiometry

Sputtering of NiCu alloys at room temperature is known to preferentially remove the Cu atoms to a degree which is consistent with the sputtering yield ratio of pure Cu and Ni [131]. The pre-sputtering time should be long enough to reach the equilibrium state with a constant Ni/Cu sputter ratio.

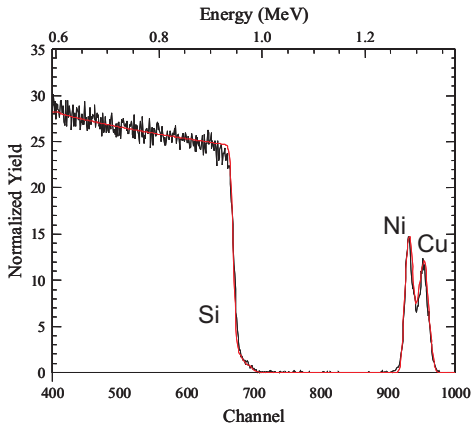


Figure 5.2: *Data and fit of RBS measurement of a* 10 nm $Ni_{60}Cu_{40}$ *film on* Si *substrate.*

The stoichiometry of the sputtered films was determined by Rutherford Backscattering (RBS) on a thin film sample. The detector determines the energy after backscattering of mono-energetic 1.7 MeV He-atoms on the NiCu alloy. The energy distribution of the backscattered atoms is a function of the adjacent atom numbers Z = 28 (Ni) and Z = 29 (Cu)and demands very thin films for separation of both peaks to avoid multiple scattering. Fig. 5.2 shows the obtained spectra of a 10 nm thin NiCu film on a Si substrate with 400 nm $SiO_2$ surface layer. The Si and its oxide peaks are at much lower energies. With a computer program [132] the spectra of the sample was simulated using the natural isotopic structure of both elements. The fitting yielded a composition of 60% Ni and 40% Cu.

### 5.2.2 Electric properties

The residual resistance $\rho_F = 53.97\ \mu\Omega$cm was measured by four-point probe on a bare NiCu film at 10 K. The large resistance reflects the disorder of the random positions of Ni and Cu atoms and is in good agreement with the experiments on similar NiCu alloys [123]. I calculated a mean free path

$$\ell = m_e/\rho_F n_e e^2 \approx 0.2\,\text{nm},$$

with electron mass $m_e$, carrier density $n_e$ and electron charge $e$. It was found for bulk samples that the Fermi level does not change significantly as the concentration of the Cu increases [133], thus the bulk value of Ni crystals ($v_F = 2.8 \cdot 10^5$ m/s [134]) is taken. The diffusion coefficient is calculated with the Fermi velocity $v_F$ as

$$D = \ell v_F/3 \approx 0.2\,\text{cm}^2/\text{s}.$$

The coherence length of the order parameter $\xi_{F1}$ is determined as 0.78 nm (see Chapter 6). The ratio $\ell/\xi_{F1} \approx 0.25 < 1$ indicates that the SIFS with F = $Ni_{60}Cu_{40}$ junction is in diffusive limit, see Sec. 2.3 for details.

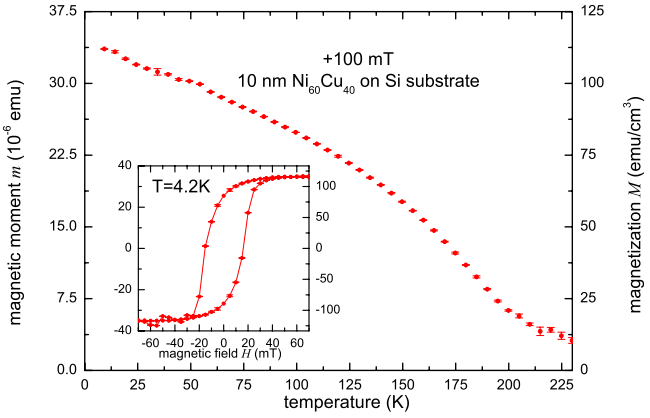


Figure 5.3: *Superconducting quantum interference device (SQUID) magnetometry on* 10 nm $Ni_{60}Cu_{40}$ *alloy yielded the temperature dependence of the saturation magnetization. The inset depicts the magnetic field dependence of the saturation magnetization at* 4.2 K.

### 5.2.3 Magnetic properties

The study of the volume magnetization of NiCu films with areas about 30 $mm^2$ and 10 nm thickness was done by a Quantum design Co. MPMS2 superconducting quantum interference device (SQUID) magnetometer (sensitivity about $10^{-7}$ emu).[1] A detailed overview on SQUID principles and applications can be found in [135] and partly in the first part of this thesis.

The magnetization as a function of the temperature and in-plane magnetic field of 100 mT is shown in Fig. 5.3. The Curie temperature $T_C$ was extrapolated to about 225 K. From the $M(H)$ loop in the inset of Fig. 5.3 an atomic saturation moment of $m_{at} = 0.15\,\mu_B/$ at a magnetic field of about 40 mT was calculated. It fits to the magnetic moment per atom $m_{at,NiCu}$ calculated by interpolation from reference data [65, 124, 133, 136]. Likewise, the Curie temperature $T_C$ was in good agreement with the values reported in literature [137].

The exchange energy (i.e. the splitting between spin-up and spin-down bands at the Fermi level) of bulk magnets had been calculated for NiCu alloys as a function of the concentration between 70% and 100% of Ni [133]. The linear extrapolation down to 60% (notice that both Curie temperature $T_C$ and the magnetic moment $m_{at}$ depend linearly on the Ni concentration too) indicated a value of roughly $E_{ex} \approx 100$ meV. However, the exact determination of $E_{ex}$ by extrapolation is problematic. There is a discrepancy between the results obtained from spin-resolved photoemission spectroscopy on bulk Ni crystals $E_{ex} = 100 - 175$ meV [138, 139] and higher theoretical predictions $E_{ex} = 300 - 425$ meV [140].

Considering the very low magnetic signal of a thin magnetic film on the thick

[1] In this Chapter the magnetic quantities and units are partly given in the CGS – emu system, as this system is used by the SQUID magnetometer set-up. Nevertheless, the author is aware of the fact that this is not consistent with the rational SI system.

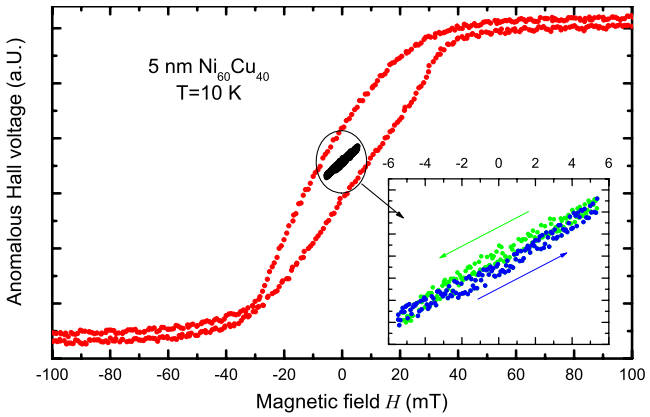


Figure 5.4: *Anomalous Hall effect on* 5 nm $Ni_{60}Cu_{40}$ *alloy. The inset shows the minor loop up to* 5 mT*, yielding a linear dependence of the saturation magnetization on magnetic field.*

diamagnetic Si substrate, the anomalous Hall effect [141] was used for hysteresis measurements on a 5 nm NiCu film as shown in Fig. 5.4. The Hall-resistance

$$R_H = R_{\text{Hall}} \cdot (\mu_0 [H + M]) + R_{\text{a}} \cdot \mu_0 M$$

is determined by the normal Hall-effect (Lorentz force on charge carrier) and the second term is proportional to the magnetization of sample. For magnetic alloys such as NiCu the first term $\sim |R_{\text{Hall}}|$ is much smaller than the anomalous Hall-coefficient $R_{\text{a}}$ [141]. Hence, the resistance signal detected in the crossbar structure corresponds to the total magnetization of the thin magnetic film.

The saturation field of the 5 nm sample was about 40 mT, too. The sample showed a moderate remanent magnetization of about 20% of the saturation magnetization. The coercive field for this sample was smaller than for the 10 nm sample from Fig. 5.3.

### Weak magnetic field and very thin F-layer

Hysteresis measurement of a demagnetized (by heating above $T_{\text{C}}$, followed by zero field cooling) sample of 5 nm thickness with the field amplitude sweeping between ±5 mT indicated a linear, reversible response of the magnetic moments, as presented in the inset of Fig. 5.4. For these *minor loops* no or a just very weak remanent magnetization of the NiCu layer was detectable.

This implied that for demagnetized samples the stray field of the magnetic domains in the NiCu film canceled out and no external magnetic flux appeared. If external magnetic fields were weak ($< 5$ mT) the total magnetization of sample was reversible.

The Josephson junctions were always cooled down in zero magnetic field. After zero field cooling the SIFS stack has a demagnetized ferromagnetic interlayer and

produces no net-magnetic flux.
To study the transport in SIFS junctions the maximum applied magnetic field was given by the oscillation length of the magnetic diffraction pattern $I_c(H)$. It was usually below 1 mT for standard sized ($\sim 100\ \mu$m) junctions. Usually, the F-layer in the sandwich should display no remanent magnetization on a macroscopic scale.

### 5.2.4 Calculation of remanent magnetization in NiCu films

The $\pi$ JJs fabricated for this thesis had a NiCu thickness of about 6 nm and the dead magnetic layer thickness is calculated as $\approx 3$ nm by $I_c(d_F)$ measurements on SIFS junctions, see Chapter 6.

I want to roughly estimate the shift of the Fraunhofer pattern $I_c(H)$ in case of a single domain state of the ferromagnetic layer. Therefore, the magnetization and the magnetic flux of a thin $Ni_{60}Cu_{40}$ film are calculated. The magnetic dipole moment of NiCu is given by

$$m = MV = m_{\mathrm{at}} \frac{N_{\mathrm{A}}\rho}{m_{\mathrm{mol}}} V,$$

where $m_{\mathrm{at}} = 0.15\mu_{\mathrm{B}}$, $N_{\mathrm{A}}\rho/m_{\mathrm{mol}}$ is the number of atoms per unit volume and $V$ is volume of the NiCu layer. 1 cm$^3$ contains $N_{\mathrm{A}}\rho/m_{\mathrm{mol}} = 8.8 \times 10^{22}$ atoms, if $\rho = \rho_{\mathrm{bulk}} = 8.92\ \mathrm{g/cm^3}$ and molar weight $m_{\mathrm{mol}} = 60.6$ g.

The total magnetic dipole moment is $m = 0.15\mu_{\mathrm{B}} \cdot 8.8 \times 10^{28} = 123.1\ \mathrm{kAm^2}$ and the magnetization $M = 123.1$ kA/m. Magnetic induction is $B = \mu_0 M = 0.153$ T.

A cross section of the length $L$ and the F-layer thickness $d_F$ encloses an intrinsic magnetic flux

$$\Phi_F = d_F \cdot L \cdot \mu_0 M$$

The total magnetic flux $\Phi$ through the F-layer is $\Phi_F$ plus the flux from external magnetic field $\Phi_H = (2\lambda_L + d_F) \cdot L \cdot \mu_0 H$. Inserting $\lambda_L = 90$ nm for Nb yields:

$$\Phi = \Phi_F + \Phi_H = 7.67 \times 10^{-14}\ \mathrm{Tm^2} + 1.85 \times 10^{-11}\ \mathrm{m^2} \cdot \mu_0 \mathrm{H}.$$

for a JJ of the length $L = 100\ \mu$m and the F-layer thickness $d_F = 5$ nm. In terms of magnetic flux quantum $\Phi_0$ this gives

$$\frac{\Phi}{\Phi_0} = 37.0 + 8.9 \frac{1}{\mathrm{mT}} \cdot \mu_0 H.$$

Note that the calculation does not include the dead magnetic layer and assumes a single domain ferromagnetic layer, which somehow contradicts the experimental results presented in this Chapter. With the assumptions above the $I_c(H)$ pattern would be shifted about 37 periods from the center. For the standard $I_c(H)$ measurements in this thesis the magnetic field $\mu_0 H$ was below 1 mT to trace out multiple oscillation periods. However, all junctions except with $d_F$ very close to the critical thickness of 0 to $\pi$ transition where the 0–$\pi$ JJ may occur by roughness of the F-layer (see Chapter 7), had a nearly symmetric Fraunhofer pattern with maximum critical current at zero field. This indicated a multiple domain state of the F-layer with zero net magnetic flux to the outside.

Nevertheless, sometimes the $I_c(H)$ pattern was shifted along the field axis, due to remanent magnetization or trapped vortices. Usually, short heating above the critical

superconducting transition temperature $T_c$ provided again a centered, symmetric magnetic field dependence of the critical current $I_c(H)$. The magnetic state of the F-layer should not change much, as the sample was still much below the Curie-temperature $T_C \gg T_c$ during the thermic cycle.

# Chapter 6

# 0 and $\pi$ coupled Josephson junctions

In this Chapter I report on the characterization of Josephson tunnel junctions with ferromagnetic interlayer.
A number of requirements concerning the manufacturing as well as electrical and magnetic issues had to be met to ensure the fabrication of high quality junctions.
• Regarding the fabrication, the patterning of samples should be reliable and provide a good insulation of the superconducting electrodes. The wedgelike F-layer in SIFS junctions enabled a fast patterning of nearly identical junctions with gradually increasing thickness of F-layer. The inevitable run-to-run variations when studying the F-layer thickness dependence of critical current were avoided.
•Proper electrical functioning requests that the tunnel barrier should be pinhole free, in order to have all the transport carried by tunneling and at the same time the barrier should be thin enough to allow direct tunneling of charge carriers.
• A magnetic requirement is that the F-layer provides a uniform coupling of phase of the two superconductors.

Motivated by the demand for high quality junctions I have developed an alternative fabrication process, leading to the so-called *SINFS*-type junctions, patterned by SNEAP (Sec. 4.5). Transport measurements on the SINFS junctions showed that the quality of the junctions was considerable improved by i) using $Nb_2O_5$ as insulator between the superconducting electrodes and ii) planarization of the ferromagnetic interlayer by an additional Cu layer.
Parts of this Chapter were published in Ref. [72, 142].

### Measurement technique

The Josephson tunnel junctions were cooled below the critical temperature $T_c$ of the superconductor. By immersing the sample directly into liquid helium temperatures of 4.2 K or lower could be reached. The sample was magnetically shielded in a cylindrical high permeability container, since the spatial distribution of its phase $\phi(x)$ depended on the magnetic field. Magnetic fields up to several 100 $\mu$T could be applied in-plane of the junction barrier by a cylindrical superconducting coil and bias currents up to 200 mA. The influence of the lead resistances onto the electric transport measurements was avoided by using a four-point probe set-up (see Fig.

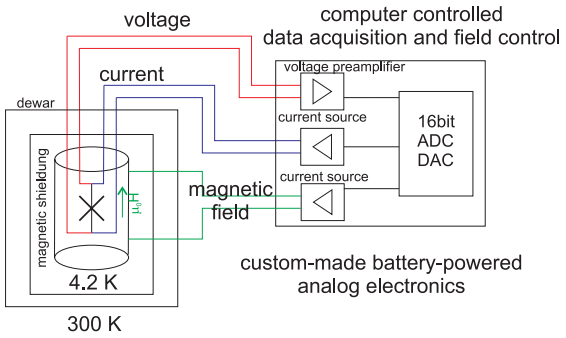


Figure 6.1: *Sketch of the basic measurement set-up containing analog and digital electronics and electromagnetic shielding inside the dewar filled with liquid helium. The Josephson junction is depicted by the cross.*

6.1).

The sample was current-biased by a current source with adjustable range between 200 mA and 100 nA and the voltage across the junction was measured by a room-temperature voltage amplifier with adjustable low-pass filters. Both current source and voltage amplifier were custom-made and battery-powered. The bias currents through the sample and magnet-coil were controlled and the voltage across the junction was monitored using 16-bit D/A–A/D converters. The data-acquisition was controlled using GoldExI [143] or LABVIEW software.

## 6.1 SIS junctions

Before fabricating Josephson tunnel junctions with a ferromagnetic interlayer (SIFS) the SIS stack consisting of a Nb/Al-$Al_2O_3$/Nb trilayer were optimized. The Nb/Al overlayer technique [108] and the easy control of the oxide formation in Al are essential to fabricate high quality Josephson junctions .

Besides a reliable patterning of junctions, the interlayer roughness was essential for high quality junctions. Using SIS-type junctions the roughness of the lower Nb/Al and upper $Al_2O_3$/Nb interfaces were optimized by anodization spectroscopy and atomic force microscopy (AFM) to achieve a uniform distribution of the tunnel current and low run-to-run spreads of $j_c$.

### 6.1.1 Anodization spectroscopy

The main challenge for the fabrication of tunnel junctions with low leakage current was the formation of a high quality tunnel barrier.

Anodization spectroscopy is helpful to monitor tunnel barrier properties before individual junctions are fabricated from a trilayer stack [116]. The bottom part of Fig. 6.2 depicts a typical anodization spectra of a high quality Nb/Al-$Al_2O_3$/Nb stack. The anodic oxide was moving from the surface (top Nb layer) to the inner

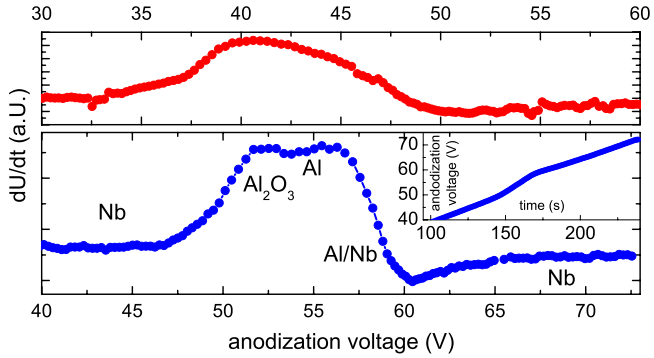


Figure 6.2: *Anodization profile of* Nb/Al-$Al_2O_3$/Nb *stack. Top: sample with rough interlayers. Bottom: sample with sharp interfaces. This sample was cooled during deposition and the deposition parameters (pressure, power) had been optimized. The anodization voltage versus time is depicted on the inset.*

part. The aluminium forms oxides with larger specific resistance than the niobium oxides. First, the Nb top-electrode was anodized at the constant rate $(\delta V/\delta t)_{\mathrm{Nb}}$. Subsequently when the oxide front was reaching the Nb-$Al_2O_3$ interface the voltage derivative increased to $(\delta V/\delta t)_{\mathrm{Al_2O_3}}$, then decreased to $(\delta V/\delta t)_{\mathrm{Al}}$ before reaching the Nb bottom-electrode with $(\delta V/\delta t)_{\mathrm{Nb}}$. At the $\mathrm{Al}-\mathrm{Nb}$ interface first another maximum and than a minimum were reached before $(\delta V/\delta t)$ was stabilizing again. The width and height of the Al induced peak in the spectra give information about the sharpness of the Al interfaces. Diffusion processes and other non-ideal interlayers led to a rounded anodization spectra with broadened crossovers (see Fig. 6.2, top).

However, one has to be cautious. A sharp anodization profile, as shown in the bottom part of Fig. 6.2, is necessary but not sufficient to obtain high quality junctions. It does not reveal information about the kind of oxidation process, i.e. oxidation in room ambient air or in pure oxygen atmosphere. Only niobium deposited on a tunnel barrier formed by pure oxygen yields a good quasiparticle I-V characteristic [115, 116]. Hence, transport measurements on SIS junctions at low temperatures (4.2 K) are necessary to finally judge the quality of junctions.

## 6.2 SIS junctions formed at various oxidation exposures

After optimizing the interlayer roughness of the trilayer by variation of the deposition parameters, the tunnel barrier thickness $d_I$ could be well controlled and reproduced. The critical current density depends exponentially on the tunnel barrier thickness $j_c \propto \exp(-d_I)$. The $Al_2O_3$ thickness was controlled by the oxidation conditions of the Al layer, i.e. the partial pressure of the oxygen, the oxidation time and temperature. The quasiparticle tunnel resistance $\propto \exp(d_I)$ per unit area and the specific capacitance $C^* \propto 1/d_I$ of the junction depend on the tunnel barrier thickness,

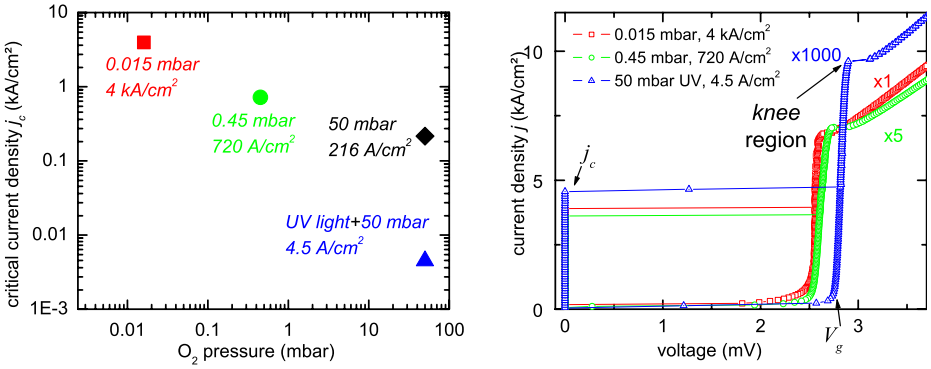


Figure 6.3: *Left: Dependence of $j_c$ on oxygen pressure $p_{O_2}$ (30 min) during $Al_2O_3$ formation. Right: I-V characteristics ($H = 0$) of the junctions illustrate the slight decrease in hysteresis and increase of quasiparticle current with decreasing $p_{O_2}$. Current axis of the* 0.45 mbar *and the* 50 mbar + UV *samples is scaled by* 5 *and* 1000*, respectively. The measurements were done at* 4.2 K.

too.

A classical work by Kleinsasser and coworkers summarizes the available data on critical current density $j_c$ in dependence on the oxidation parameters of the Al-layer on Nb/Al-$Al_2O_3$/Nb junctions [144]. They find a single, nearly universal dependence: $j_c$ is determined by the product of the oxidation pressure $p_{O_2}$ and the oxidation time.[1] Keeping the oxidation time constant, this dependence can be approximated by $j_c \propto (p_{O_2})^{-const}$. There are two distinct regimes in this dependence, corresponding to high and low critical current densities. The low-exposure regime of oxygen, yielding $j_c > 10$ kA/cm$^2$, reflects the completion of the initial Al oxide layer. The conductance is dominated by metallic-like pinhole defects, whose density decreases with increasing $O_2$ exposure. In contrast, the high-exposure (low $j_c$) regime reflects the further, slower oxide growth with continuing drop of $j_c$ with increasing tunnel barrier thickness [145]. For the low-exposure regime, the metallic pinholes lead to large leakage currents for voltages $V$ below $V_g$ (i.e. strong damping) and larger run-to-run and on-chip variation of $j_c$ than for the high-exposure regime. Hence, I fabricated JJs with $j_c$ below 5 kA/cm$^2$, unambiguously being in the high-exposure regime.

SIS junctions were fabricated with areas between 25 $\mu$m$^2$ and 10 000 $\mu$m$^2$, depending on the chosen conditions for the barrier formation and the resulting critical current density.

The Nb/Al-$Al_2O_3$/Nb stacks had an Al layer thickness before oxidation of about 5 nm, to ensure a closed Al overlayer and the formation of pure Al-oxides. In Fig. 6.3 the dependence of the critical current density $j_c$ on oxidation pressure $p_{O_2}$ and the current-voltage characteristics (IVC) are shown for some SIS junctions. The dependence of $j_c \propto (p_{O_2})^{-const}$ is visible for the non-UV oxidized samples. Changing

[1] For room-temperature oxidation, as used in this thesis.

Table 6.1: *Electrical parameters of representative* Nb/Al-$Al_2O_3$/Nb *junctions.*

| $p_{O_2}$ [mbar] | $j_c$ [A/cm$^2$] | $\lambda_J$ [$\mu$m] | $\beta_c$ | $2\Delta/e$ [mV] | $V_c$ [mV] |
|---|---|---|---|---|---|
| 0.015 | 4 000 | 6.1 | 700 | 2.57 | 1.60 |
| 0.45 | 720 | 14.1 | $\approx$5000 | 2.64 | 1.49 |
| 50 | 216 | 25.8 | $\approx$3000 | 2.67 | 1.64 |
| 50+UV | 4.5 | 179 | $\rightarrow \infty$ | 2.83 | 1.4 |

the partial oxygen pressure from 0.001 to 50 mbar the critical current density $j_c$ could be varied over a large range. To reach the regime of very low critical current densities UV-enhanced oxidation was used [112]. In the right part of Fig. 6.3 the hysteretic current-biased I-V characteristics of Nb/Al-$Al_2O_3$/Nb junctions are depicted. All three samples show hysteretic IVCs. The low subgap current is an indicator of high quality. The junctions are strongly underdamped.

The figures of merit, i.e. critical voltage $V_c = I_cR$, McCumber-Stewart parameter $\beta_c$ (Eq.(1.12)) and double gap of Nb $V_g = 2\Delta/e$ are summarized for the four junctions from the left part in Fig. 6.3 in table 6.1. The Josephson penetration depth, Eq.(1.14), was calculated for JJs with thick electrodes and $\lambda_L = 90$ nm. The $V_c = I_cR$ products were typically in the range of $1.4 - 1.64$ mV.

After reaching the critical Josephson current the junction switched into the voltage state. At the voltage $V \approx V_g$ the tunneling current was dominated by quasiparticles due to the overlap of the peaks in the densities of states for both superconductors. $V_g$ is defined as the midpoint of the steep current rise. In case of identical superconducting electrodes the gap can be estimated by the gap voltage $V_g = 2\Delta/e$. It varied from 2.83 mV for the UV-oxidized sample (4.5 A/cm$^2$) to about 2.57 mV for the 4 kA/cm$^2$ sample. The gap $\Delta$ varied between 1.41 meV to 1.28 meV, slightly dropping for larger values of $j_c$.

The data available in the literature [144–146] for Nb/Al-$Al_2O_3$/Nb with similar oxidation conditions is in good agreement with the data from table 6.1.

### 6.2.1 Proximity effect on aluminium

The proximity effect in non-oxidized aluminum under the barrier is of importance for the interpretation of the IVCs, as it causes the *knee* region for voltage $V > 2\Delta/e$ and before switching to the normal ohmic state [144]. The real configuration of the junction has to be described by an SNIS model and its microscopic treatment can be found in the references [87, 147]. The aluminum thickness can be minimized to have a less pronounced proximity effect. However, the formation of Nb-oxides at the upper $Al_2O_3$ interface may provoke a proximity knee, too. The oxide layers are formed due to the high affinity of niobium for oxygen.

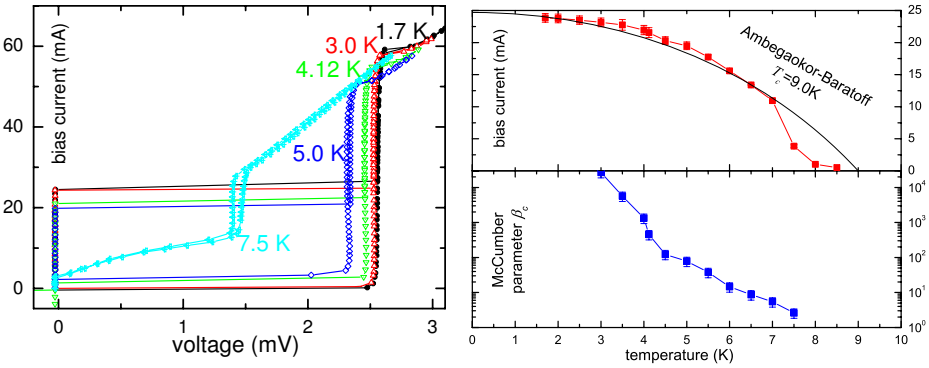


Figure 6.4: *SIS junctions. Left: Temperature dependence of the IVC. Right: Temperature dependence of the critical current $I_c$ and Stewart-McCumber damping parameter $\beta_c$. The $I_c(T)$ dependence for an ideal SIS junction is plotted. The JJ was oxidized at* 0.45 mbar.

### 6.2.2 Stewart-McCumber parameter $\beta_c$

As mentioned in the preceding Section the degradation of quality for SIS junctions with a higher $j_c$ is usually attributed to pin-holes in the thin oxide barrier. The formation of these pin-holes is related to the coverage of the Al surface with $Al_2O_3$ oxides. Usually, a higher oxygen exposure will reduce the formation of pin holes. Along with higher $j_c$ the more transparent tunnel barrier causes an increased subgap leakage current and a decreased energy gap (see table 6.1). A larger subgap current increases the damping of plasma oscillations. Hence, the Stewart-McCumber parameter $\beta_c$, which is related to the damping coefficient $\alpha = 1/\sqrt{\beta_c}$, changed from 700 to infinity when $j_c$ was decreasing from 4000 A/cm$^2$ to 4.5 A/cm$^2$. $\beta_c$ is determined using the approximation $\beta_c \approx (4/\pi)^2(I_c/I_r)^2$, with return current $I_r$.

The strong Cooper pair breaking in the F-layer yielded a low $j_c$ in SIFS-type junctions (see Section 6.5). The SIS-based JJs with the highest $j_c$, formed at $p_{O_2}$ = 0.015 mbar, still exhibited high quality properties. I used these conditions for the tunnel barrier oxidation of the SIFS stacks to counterbalance the strong reduction of $j_c$ in the F-layer.

### 6.2.3 Temperature dependence of IVC

Next I consider the temperature dependence of SIS junctions at zero magnetic field. The temperature dependence of the IVC, the critical current $I_c$ and the Stewart-McCumber parameter $\beta_c$ are shown in Fig. 6.4. According to Ambegaokar and Baratoff [36, 37] the temperature dependence of the critical current reduces to that of the gap in case of equal energy gaps. However, the gaps of the bottom and the top electrode in the Nb/Al-$Al_2O_3$/Nb stack may differ. This can be caused by the interaction of the top electrode with the oxide barrier, or by the unequal growth conditions, leading to different disorder in the near-barrier layers. In addition, the proximity effect in Al leads to a modification of the Ambegaokar-Baratoff tempera-

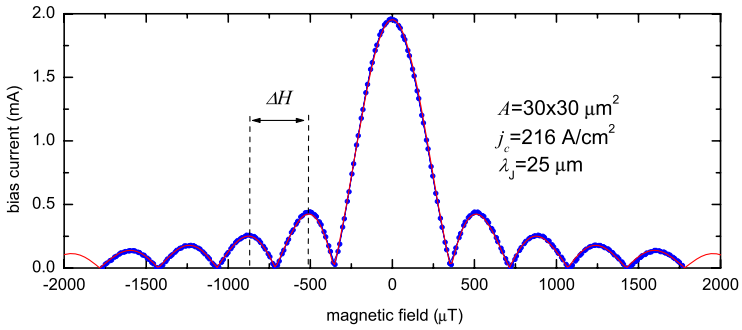


Figure 6.5: *Measured critical current diffraction pattern and fitting (red curve) for a short SIS junction. The period $\Delta H$ is determined by the junction length $L$.*

ture dependence towards a more linear one, described by Rowell and Smith [148].

At higher temperatures the gap $\Delta$ was reduced, provoking an increased subgap current, a vanishing proximity effect on Al and the overdamping of oscillations of phase. For temperatures below 4.2 K the IVC changed just a little, apart from the Stewart-McCumber parameter, which was difficult to determine for low temperatures, as the return current $I_r$ was approaching zero.

### 6.2.4 Magnetic field diffraction pattern

The uniformity of the tunnel current transport in a Josephson junction can be judged qualitatively from the magnetic field dependence of the critical current $I_c(H)$. The magnetic field was applied in-plane and parallel to the junction border. The magnetic diffraction pattern depends in a complex way on the *effective* junction length $\ell = L/\lambda_J$ and on the current distribution over the tunnel barrier. If the pattern of a short ($\ell \leq 1$) Josephson junction was i) symmetric with respect to both polarities of the critical current and the magnetic field and ii) the critical current $I_c$ was completely vanishing at the minima, the magnetic field penetrated symmetrically from both junction sides. When the pattern was not symmetric, irregular or has a current offset, the current transport over the barrier was non-uniform. This effect can be attributed to a non-uniform tunnel barrier, a defect in the junction insulation or a trapped magnetic flux in the superconducting banks.

The starting point for all Josephson junctions presented in this thesis was a symmetric, regular magnetic field dependence of the critical current with completely vanishing critical currents at the minima.

In Fig. 6.5 a textbook like critical current diffraction pattern of a Josephson junction of effective length $\ell = 1.2$ and its fitting are shown. The period $\Delta H$ is proportional to the reciprocal junction length $L$ in the direction perpendicular to the magnetic field. The interference pattern from this JJ is practically indistinguishable from the ideal one, indicating a high degree of tunnel current uniformity over the junction area. Thus, the still small $\ell = 1.2$ ensured a homogeneous distribution of supercurrent over the tunnel barrier. The critical currents were vanishing at integral

multiples of $H_{c1}$. The fitting yielded the critical current $I_c = 1.95$ mA and the oscillation period $\Delta H = \frac{2\pi}{\Phi_0}\Lambda\mu_0 H_{c1}$ with $\mu_0 H_{c1} = 356\ \mu$T.

The London penetration depth $\lambda_L$ for thick $\gg \lambda_L$ superconducting electrodes was found from the period $\Delta H$ of the $I_c(H)$ for junction of the length $L$, as $\lambda_L \approx \Lambda/2 = \Phi_0/(2L\Delta H)$. This estimation gave a London penetration depth of approximately $\lambda_L \approx 96$ nm, which is consistent with published data for sputtered polycrystalline Nb [149].
However, the thickness of bottom electrode $t_1 = 120$ nm (top electrode $t_2 = 400$ nm) could not be treated as large compared to $\lambda_L$. For very thin superconducting electrodes the effective magnetic thickness of the JJ $\Lambda$ is modified to $\Lambda = \lambda_L \tanh(t_1/2\lambda_L) + \lambda_L \tanh(t_2/2\lambda_L)$ [43] and, depending on geometry of the junctions, a geometry factor for magnetic field focussing has to be included. The London penetration depth $\lambda_L$ was then calculated as 159 nm. This value is much larger than the reported ones for Nb-based Josephson junctions in literature [149], i.e. $\lambda_L \approx 90$ nm. Using the value from literature $\lambda_L = 90$ nm together with the actual thicknesses of electrodes the first minimum of $I_c(H)$ was calculated as $\mu_0 H_{c1} = 489\ \mu$T. I attribute the difference to the measured minimum to a field focussing effect of the superconducting electrodes and the idle region.

The SIFS and SINFS junctions in this thesis were all patterned in overlap-geometry, and the current distribution was uniform. For a detailed discussion of the junction geometrical configuration, see Barone and Paterno [49].
The strong decay of the critical current density $j_c$ in the F-layer yielded a large Josephson penetration depth $\lambda_J \propto \sqrt{1/j_c}$, thus most of the SIFS or SINFS junctions were in the short junction limit.

## 6.3 SIFS junctions with $Ni_{60}Cu_{40}$ alloy

A great part of this thesis was devoted to the fabrication of high quality Josephson tunnel junctions with ferromagnetic interlayer. High quality means: homogeneous and uniform distribution of supercurrent over the tunnel barrier and the F-layer, low junction-to-junction deviation and reasonably electrical parameters, e.g. critical current density, damping and $I_cR$ product.

Both the short coherence length $\xi_{F1}$ of the Cooper pairs in the F-layer and the intrinsic ferromagnetism complicated the characterization of the SIFS junctions.
• In general, *interface roughness* at the barrier leads to an inhomogeneous current transport, which can cancel out the coherent Josephson coupling. The conditions for non-uniform supercurrent are given by the ratio of the NiCu interface roughness over the coherence length $\xi_{F1}$ and oscillation length $\xi_{F2}$ of the supercurrent. In $Ni_{60}Cu_{40}$ these values are about $0.5 - 1.5$ nm, as calculated in Sec. 6.5. An interface roughness of this order of magnitude provokes deviations from the standard symmetric magnetic diffraction pattern.
• If the sample was not demagnetized before cooldown (in case that the Curie temperature of F-layer is above 300 K) or a non sufficient magnetic shielding during cooldown prevents zero field cooling, the F-layer may have a non-vanishing *remanent magnetization*, which in the simplest case gives just a shift of the $I_c(H)$ pattern along the $H$ axis, see Sec. 6.6.

• In presence of a vanishing net magnetization but *multiple magnetic domains*, the domain walls modify the superconducting coherence length. Thus, a non-homogeneous supercurrent with a complicated, asymmetric $I_c(H)$ pattern might arise, see a publication by Bergeret and coworkers [64] for details.
• A multidomain F-layer with *antiparallel orientated magnetization* in the domains provokes a spatial modulation of the phase difference $\phi(x)$ along the junction length. Hence, the critical current $I_c$ may show oscillations as a function of the F-layer thickness, which are *independent* from the oscillations between 0 and $\pi$ of the coupling of phase [150].

As mentioned before, the starting point for all measurements was i) a central peak in $I_c(H)$ near zero magnetic field and ii) a symmetric $I_c(H)$ pattern for both polarities of current. This signifies that the superconducting phase difference did not change along the junction length for zero magnetic field, presumably due to a small-scale magnetic domain structure of the F-layer with zero net magnetization. When the sample was heated above $T_c$ (but below Curie temperature $T_C$) and a small field $\simeq 1$ mT was applied briefly, the $I_c(H)$ was found to be shifted in the opposing direction of the applied field.[2] Presumably this led to a finite magnetization in the F-layer, although anomalous Hall effect measurement (Sec. 5) on a NiCu-layer with similar thickness indicated a linear, paramagnetic response of the magnetization on the external magnetic field. However, the trapping of flux in or between the superconducting electrodes (e.g. an Abrikosov vortex) when applying magnetic fields can shift the $I_c(H)$ pattern, too. This flux was removed by heating the sample above $T_c$ and recooling it in zero field.

### 6.3.1 SIFS and SINFS junctions

The fabrication of junctions was optimized regarding the homogeneity of the current transport. From the F-layer thickness dependence on the critical current, i.e. the $I_c(d_F)$ curve reported by other groups [8, 9, 68], it is evident that a rigorous control of the F-layer thickness and spread of the junction parameters was mandatory to observe the 0 to $\pi$ crossover.

Care was taken to keep the roughness of the NiCu film low. Topological and electrical measurements indicated that the direct deposition of NiCu on the tunnel barrier led to an inhomogeneous current transport. An additional 2 nm thin Cu layer between the $Al_2O_3$ tunnel barrier and the ferromagnetic NiCu brought considerable benefits, as it ensured a homogeneous current transport. In this way a high yield of functional devices with $j_c$ spreads less than 2% was obtained.

The short coherence length of supercurrent $j_c \propto \exp(-d_F/\xi_{F1})$ in the F-layer demanded junctions with rather large areas to obtain a reasonable high $I_c$. Unless otherwise noted, the JJs with ferromagnetic interlayer were square shaped with an area of $100 \times 100\,\mu\text{m}^2$.

The Fraunhofer modulation of the critical current $I_c$ is shown in Fig. 6.6 for SIFS junctions with 2 nm (a) and 4 nm (b) NiCu layers and an SINFS junction with

[2] If measured in $I_c(H)$ mode the SIFS stack resembled a magneto-resistance (MR), i.e. Tunnel-MR (FIF-stack) or Giant-MR (FNF-stack) contact. These devices are based on the magnetic remanence of their F-layers.

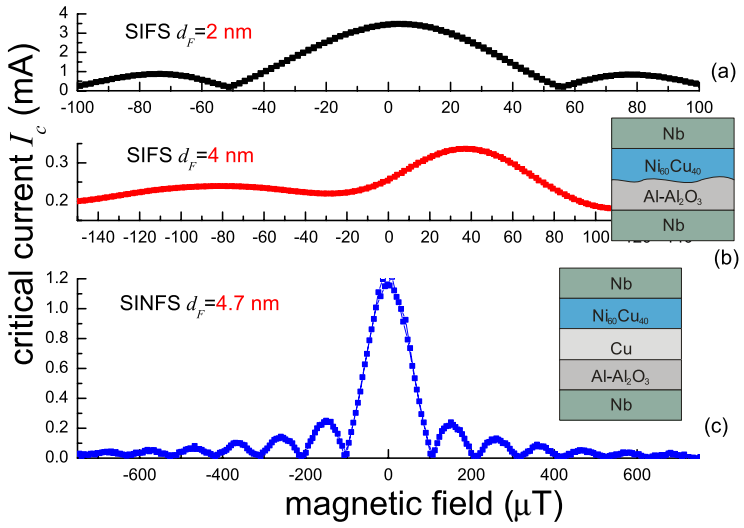


Figure 6.6: *$I_c(H)$ of (a) SIFS (2 nm* NiCu*), (b) SIFS (4 nm* NiCu*) and (c) SINFS (*Cu *2 nm,* NiCu *4.7 nm) stack. Oxygen pressure is 0.45 mbar for SIFS and 0.015 mbar for SINFS type.*

2 nm Cu and 4.7 nm NiCu(c). All these ferromagnetic junctions were still in the 0 coupled regime (see Sec. 6.5). The magnetic field was swept in both directions and no hysteresis can be seen, at least for these small fields.

### SIFS junctions

For thin (below 3 nm) NiCu layers I could measure a clear Fraunhofer-like modulation, cf. Fig. 6.6(a). The F-layer was thinner than the dead magnetic layer. For thicker NiCu layers the $I_c(H)$ deviated considerably from the ideal Fraunhofer pattern, Fig. 6.6(b). Although the electrical measurements on SIS junctions indicated a high quality barrier (right part of Fig. 6.3), this suggests some finite roughness of the $Al_2O_3$ tunnel barrier and/or of the NiCu layer. AFM-measurements (see below) indicated that the 2 nm NiCu layer on-top the $Al_2O_3$ formed similar roughness contours. Thus, the effective thickness of the NiCu-layer was constant and the supercurrent transport remained homogeneous, as shown in Fig. 6.6(a). When doubling the thickness of the NiCu-layer to 4 nm, its top roughness was about 0.9 nm and the effective NiCu layer thickness was not uniform, explaining the transport measurements depicted in Fig. 6.6(b).

### SINFS junctions

By including a 2 nm Cu layer under the NiCu I recovered the clean Fraunhofer pattern. I could even use a thinner $Al_2O_3$ barrier for SINFS, although this should slightly increase the roughness of $Al_2O_3$. The Cu-layer between $Al_2O_3$ and NiCu smoothed

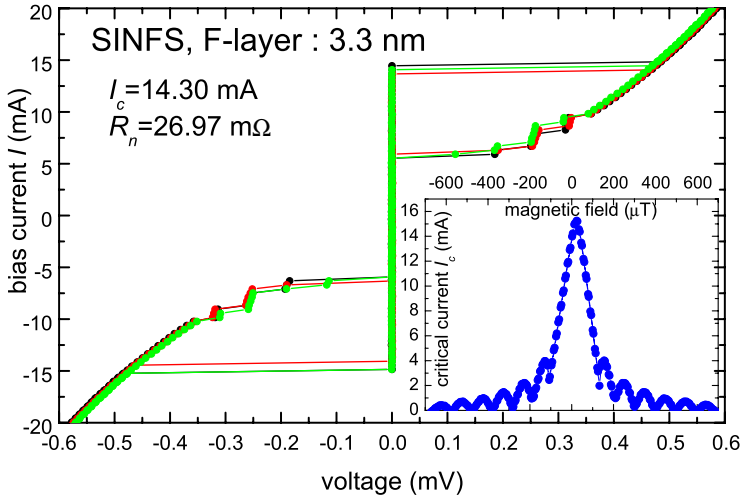


Figure 6.7: *I-V characteristics of three SINFS junctions, oxygen pressure for $Al_2O_3$ formation was 0.015 mbar. Variation of $I_c$ is $\delta I_c = 2\%$ and of $R_n$ is $\delta R_n = 0.5\%$.*

the lower NiCu-interface and provided a uniform ferromagnetic layer. Even for thicker (up to 8.5 nm) NiCu-layers I measured uniform supercurrents through such SINFS junctions as shown in Fig. 6.6(c).
The strong proximity effect of Cu yielded a very weak Cooper pair breaking in the 2 nm Cu-layer. SIS and SINS samples of identical oxidation conditions for the $Al_2O_3$ barrier showed similar critical current densities (not shown).

A low junction-to-junction deviation was obtained in SINFS-type junctions. In Fig. 6.7 the characteristics of three underdamped SINFS junctions with a 3.3 nm NiCu layer are shown. The parameter spread of the critical current and the normal resistance (and therefore $\beta_c$) was below 2% ($I_c = 14.3 \pm 0.3$mA, $R_n = 26.97 \pm 0.16$m$\Omega$ and $\beta_c = 10$). Even the very sensitive sub-gap characteristics were nearly identical for all junctions. These junctions exhibited a high quality $I_c(H)$ pattern (inset of Fig. 6.7), just like the Fraunhofer pattern of SINFS JJs with 4.7 nm NiCu layer in Fig. 6.6(c).

The voltage of the first step in the I-V characteristics was $V_{\text{step}} \approx 112\,\mu$V, depicted in Fig. 6.7. The capacitance was estimated from Fiske step measurements on junctions with similar oxide thickness as $C \approx 8.0\,\mu\text{F/cm}^2$, i.e. $\omega_p = 2\pi \times 37.1$ GHz. Assuming $\lambda_L = 90$ nm and superconducting electrode thicknesses $d_1 = 120$ nm, $d_2 = 400$ nm the Josephson penetration depth was calculated as $\lambda_J = 30.7\,\mu$m. The Swihart velocity was $\bar{c}_0 = \lambda_J \omega_p = 0.024 \cdot c$, where $c$ is the speed of light in vacuum. For the junction with $L = 100\,\mu$m, the position of the first Fiske step (FS) had to be at

$$V_{\text{FS}} = \frac{\Phi_0 \bar{c}_0}{2L} = 73\,\mu\text{V},$$

and the position of the first Zero Field step at $2V_{\text{FS}} = 147\,\mu$V. Actually, neither the Fiske nor the Zero Field Step were similar to the resonance-steps observed in

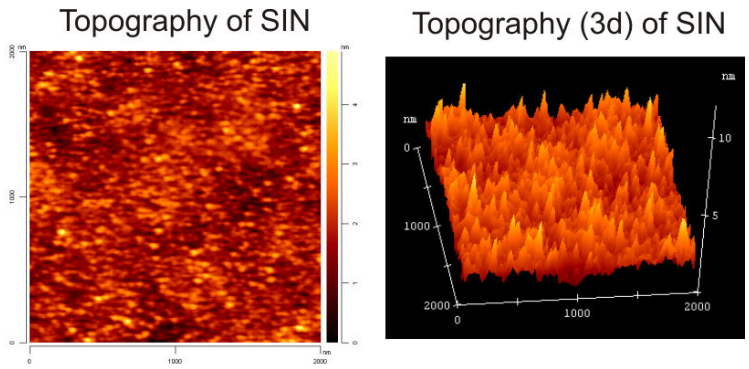


Figure 6.8: *AFM measurements of* Nb/Al-$Al_2O_3$/Cu *(SIN) stack. Measured area:* $2 \times 2$ $\mu m^2$. *left: 2d topography, right: 3d profile. Calculated roughness:* 0.50 nm *rms.*

experiment. The effective length $\ell$ of the junction was $\approx 3\lambda_J$, therefore these square shaped junctions were not in the strict 1d limit. This could explain the discrepancy of $V_{FS}$ and $V_{ZFS}$ with experiment.

### Atomic force microscopy on SIFS and SINFS

On reference samples I performed ex situ[3] atomic force microscopy (AFM) measurements. The measured roughness (rms) is shown in table 6.2. The roughness of the $SiO_2$ surface of the Si substrate was less than 0.3 nm. A 120 nm Nb film showed a roughness of 0.44 nm, which increased to 0.60 nm after deposition of 5 nm Al and even up to 0.90 nm after further 4 nm of NiCu. Insertion of a 2 nm Cu film after oxidation decreased the roughness of the SIN stack down to 0.50 nm, see Fig. 6.8. Now the top roughness of the SINF (F: 4.7 nm) stack was about 0.68 nm. The ferromagnetic interlayer in an SINFS stack exhibited at both interfaces of NiCu a lower roughness than in an SIFS stack. Non-uniform growth of the NiCu on top of $Al_2O_3$ may be caused by island-formation of the first monolayers when grown directly on $Al_2O_3$ (see the inset of Fig. 6.6). The wetting of Cu atoms on Nb, reported in [127], provoked a non-homogeneous growth of NiCu film too, as the stoichiometry varied with increasing thickness of the film.

Some more, alternative explanations for the appearance of non-uniform tunnel currents are possible, as the roughness of reference samples might be changed by ex

[3]Note that the formation of a native oxide layer on the surface of samples may notably change their topography.

Table 6.2: *Atomic force microscopy measurement done on reference stacks.*

| sample | Si-substrate | S | SI | SIF | SIN | SINF |
|---|---|---|---|---|---|---|
| roughness (rms) [nm] | $< 0.3$ | 0.44 | 0.60 | 0.90 | 0.50 | 0.68 |

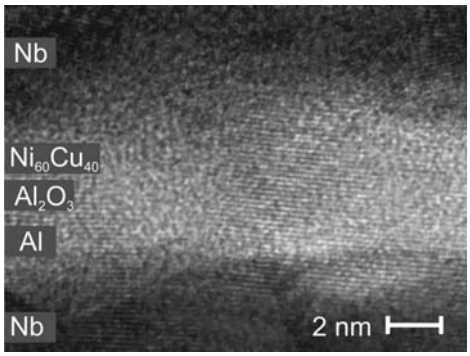


Figure 6.9: *Cross-sectional High-Resolution Transmission Electron Microscopy (HRTEM) image of a* Nb/Al-$Al_2O_3$/NiCu/Nb *(SIFS) stack.*

situ oxidation shortly before the AFM measurement and the obtained data could not be verified for thin films in vacuum.
• The diffusion of Ni atoms into the $Al_2O_3$ barrier for longer deposition times (stronger heating of sample) of NiCu might be possible. It can be stopped by a diffusion barrier made by the Cu layer.
• The 2 nm thick NiCu layer was well within the dead magnetic layer thickness $d_F^{\mathrm{dead}} \approx 3.09$ nm (Sec. 6.5), whereas the 4 nm thick NiCu layer should have some long-range order of magnetic moments. Even if both films have similar interface roughnesses, the longer proximity effect in the 2 nm NiCu layer might enable a still uniform current transport.
• The weakening of itinerant magnetism in the NiCu layer by the 2 nm Cu-layer could explain the symmetric Fraunhofer pattern for SINFS junctions with $d_F \approx$ 4.7 nm. However, even SINFS junctions with $d_F$ up to 8.5 nm gave no evidence for the recurrence of an inhomogeneous Josephson current transport, although the weakening effect of the Cu layer, when existing at all, should be very small for these F-layer thicknesses.

### Transmission electron microscopy

The characterization of samples with HRTEM (High-Resolution Transmission Electron Microscopy) provides an insight into the thin film crystal structure and yields extensive information on a variety of the sample properties, such as morphology, structures at and near the interfaces, density defects inside the sample and the lattice parameters. The sample substrate was cut into thin stripes and once a specimen has been mechanically thinned to a few microns, ion milling was used for thinning down to electron transparency.[4]

Fig. 6.9 displays a cross-sectional HRTEM image of an SIFS ($d_F \approx 5.0$ nm) stack which was taken under bright atom contrast conditions using a spherical-

[4]HRTEM measurements were conducted by Dr. K. Tillmann and D. Meertens of the Institut für Mikrostrukturforschung, Forschungszentrum Jülich.

aberration corrected electron microscope [151]. The polycrystalline structure of the room-temperature sputtered layers led to non-uniform orientation of the individual nanocrystallites with respect to the incident electron beam. Hence, only certain lattice planes were resolved at atomic plane distances. Moreover, the image contrast was slightly bleary, due to i) the formation of amorphous interlayers during the deposition and ii) the electron beam damage during operation of the HRTEM instrument.

However, the basic layer structure is clearly visible. The Al layer is undulated and does not appear like a potential two-dimensionally flat layer. The lower Nb/Al and the upper NiCu/Nb interfaces show the very same undulations, meaning that roughness and interdiffusion occurs on a short length scale. Nevertheless, the Al, $Al_2O_3$ and NiCu layers are not directly distinguishable from each other. This observation is attributed to the similar electron scattering amplitudes of these materials and to the interlayer roughness, which may give rise to projection artefacts.

## 6.4 IVC of JJs with thin F-layer

The behavior of Josephson tunnel junctions with a non-magnetic metallic interlayer, i.e. SINS or SNINS-types, cannot be described in the framework of standard tunnel theory of the Josephson effect. The tunnel current is extremely sensitive to the type of smearing of the superconducting gaps at $V \approx (\Delta_1 + \Delta_2)/e$. For instance, the expected quasiparticle curve of the I-V characteristic should exhibit:

- knee structures slightly above the sum gap voltage $V_g = (\Delta_1 + \Delta_2)/e$
- leakage current for low voltages $V < |(\Delta_1 + \Delta_2)/e|$
- supplementary singularities at $eV = \Delta_1, \Delta_2, |\Delta_1 - \Delta_2|$.

In case of SNIS-type junctions based on Nb/Al-$Al_2O_3$/Nb, the only deviation in I-V characteristic from the BCS-like SIS junction is the knee structure for $V_g = 2\Delta/e$, which can be described by the proximity effect [148].

The spatial inhomogeneities of the superconducting properties of the electrodes in $SN_1IN_2S$ tunnel junctions have been taken into account by Golubov and coworkers [87, 147, 152]. In these works the inhomogeneities stem from non-magnetic, diffusive layers $N_1$ and $N_2$ being much thinner than the coherence length.[5]

For SFS/SIFS junctions with very thin F-layers the magnetic moments are strongly suppressed. For $d_F < 3$ nm the F-layer is presumably non-magnetic on a macroscopic scale as no long range order of magnetic moments appears (cf. estimation of dead magnetic layer in Sec. 6.5). Although, due to inelastic spin scattering of Cooper pairs at the Ni sides the superconductivity may be strongly suppressed, providing an increased subgap conductance. In particular such a pair-breaking mechanism arises in thin films of weak ferromagnetic alloys as NiCu, which are close to the disappearance of magnetism and therefore quite favorable to large magnetic disorder. The spatial oscillations of the order parameter inside the ferromagnetic layer

[5]Note that in case of SIFS junctions the estimated coherence length $\xi_{F1}$ in $\approx 5$ nm thick F-layers is less than 1 nm, but it may be increased for thinner films.

can be neglected, as the magnetic phase of the JJ is nearly unchanged. The samples discussed in this Section were clearly within the 0 coupled region with F-layer thicknesses $d_F < d_F^{0\text{-}\pi}$, with $d_F^{0\text{-}\pi}$ the F-layer crossover thickness from 0 to $\pi$ coupling. From $I_c(d_F)$ measurements the magnetic dead layer thickness $d_F^{\text{dead}}$ was estimated as $\approx 3$ nm (see Section 6.5). Hence, the Nb/Al-$Al_2O_3$/Cu/NiCu/Nb ($SN_1IN_2FS$-like) junctions can be treated as SINFS or better $SN_1IN_2S$-type junctions if $d_F \lesssim d_F^{\text{dead}}$ as the NiCu-layer acts like a diffusive, non-magnetic metal with a very short coherence length $\xi_{F1}$.

Before discussing the IVCs of several SINFS JJs with different thicknesses of ferromagnetic layer a short review on the current-voltage and conductivity-voltage characteristics of SINS-type junctions is given.

### Theoretical review

The density of states for a F/S bilayer is zero at low energies up to the energy gap $\Omega$ ($\equiv \Delta_2$) in the spectrum of elementary excitations at the outer boundary of the F-layer, just as calculated by Golubov and coworkers for N/S bilayers. $\Omega$ is always below the energy gap of the bulk superconductor and depends on the temperature and the extent of the proximity effect, described by the dimensionless parameter:

$$\gamma_M = \frac{\rho_S}{\rho_F}\frac{\xi_S}{\xi_F}\frac{d_F}{d_S},$$

where $d_{S,F}$ are the thicknesses, $\xi_{S,F}$ the coherence lengths and $\rho_{S,F}$ the normal state resistance per unit length of the superconducting and ferromagnetic metals, respectively. In case of pure SIS ($d_F = 0$) junctions $\gamma_M$ vanishes and is linear increasing with $d_F/d_S$.

The gap of the superconducting counter-electrode (bottom superconductor) is treated as constant with $\Delta$ ($\equiv \Delta_1$). The proximity effect in the F-layer leads to a smearing of the singularity observed at voltages $V_g = (\Delta+\Omega)/e$. With increasing $\gamma_M$ the singularity shifts to regions of lower voltages, the height of the peak is reduced and its width is increased. For fixed $\gamma_M$ a rise in temperature leads to analogous changes.

In the region of low voltages $V < V_g = (\Delta + \Omega)/e$ the measured value of current is usually larger than the predicted one, even taking the reduced gap $\Omega$ into account. This *leakage* current appears if a significant number of low-energy density of states exists near the interface, i.e. the energy gap is zero. This situation takes place if the F-layer thickness is finite ($d_F \geq \xi_{F1}$). The coherence length $\xi_{F1}$ of the NiCu layer is below 1 nm (see Sec. 6.5), thus leakage current contributes for samples with $d_F > \xi_{F1}$.

For voltages $V > V_g$ the current-voltage characteristics approaches the straight line $I = V/R_n$. Note, that the conductance of a tunnel junction is voltage depended, but can be treated as constant for voltage $eV \ll \Phi_{Al_2O_3}$, with barrier height $\Phi_{Al_2O_3} \approx 1 - 2$ eV.

### Experiment

In the following I discuss the role of F-layer on the current-voltage characteristic of a Nb/Al-$Al_2O_3$/Cu/NiCu/Nb (SNINFS) junction. The lower normal metal layer

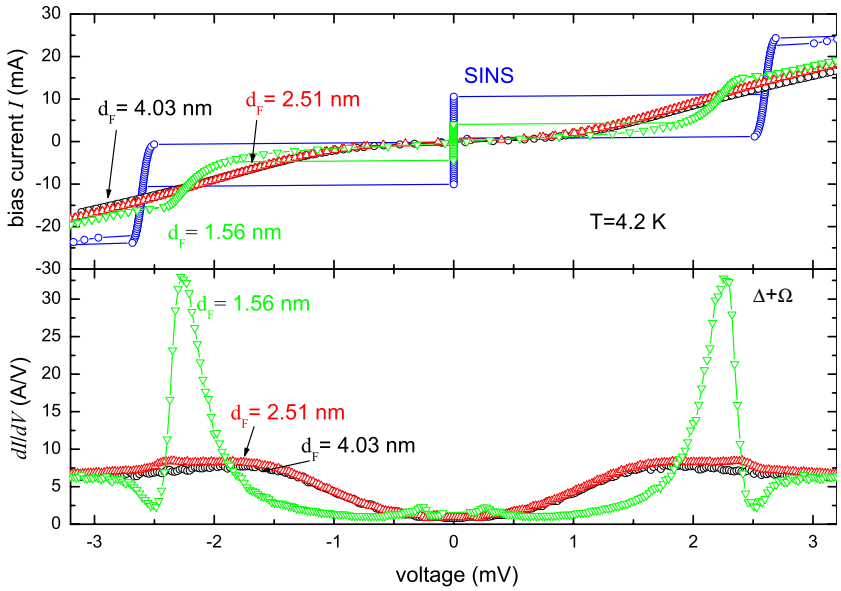


Figure 6.10: *Current voltage (top) and conductivity $dI(V)/dV$ (bottom) characteristics of SINS and SINFS junctions with various $d_F$. Thicker F-layer decreases the critical current and increases the leakage current.*

(Al) exists in the SIS junctions, too, and was discussed in Section 6.2. The upper normal metal layer (Cu), which ensures the uniform growth of F-layer, is very thin (2 nm). Both normal metals do not significantly change the I-V characteristics, apart from the proximity knee at $V = (\Delta + \Omega)/e$.

Fig. 6.10 depicts the IVCs of the SINFS[6] junctions for various $d_F$ (top) and the differential conductance $dI(V)/dV$ (bottom), measured at 4.2 K. The SINFS junctions were oxidized at 50 mbar.

The conductance $dI(V)/dV$ was calculated from the dc current-voltage characteristics shown in the upper part. The IVC for a SINS junction (same oxidation conditions) showed high quality tunneling, just like the SIS junctions in Sec. 6.2. The small hysteretic knee in the IVC for $V > (\Delta + \Omega)/e$ for this sample can be seen at the sample with $d_F = 1.56$ nm, too.

Increasing the F-layer thickness reduced the critical current $I_c$ and increased the subgap-conductance, i.e. a larger leakage current appeared and the voltage drop over the junction was reduced. The stronger dissipation in the system increased the damping of plasma oscillations. Hence, the width of the hysteresis was reduced. The peak conductivity $dI(V)/dV$ at $V = (\Delta + \Omega)/e$ is still visible for the sample with $d_F = 1.56$ nm, although it is much reduced compared to the SINS sample (not plotted). For the other samples the peak was smeared out and moved to lower

[6]To point of the high quality transport properties of these junction I will keep the notation SINFS.

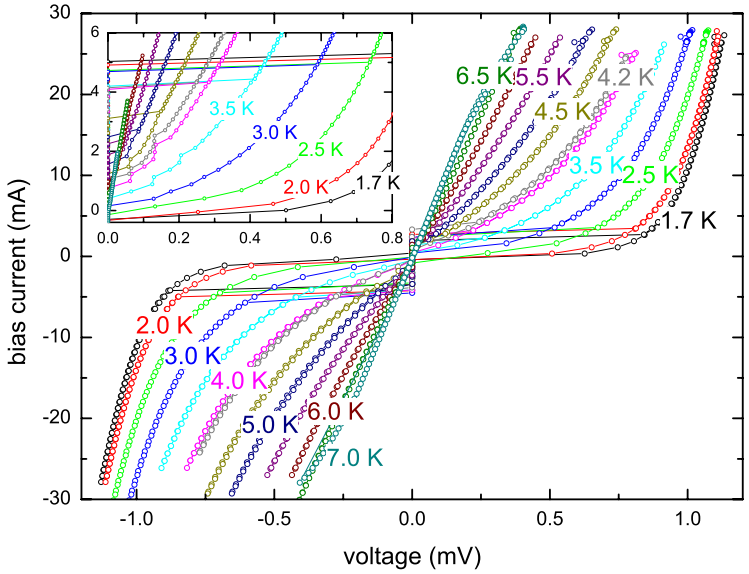


Figure 6.11: *Temperature dependence of IVC for SINFS junction with* $d_F = 4.28$ nm. *The voltage drop over the I/F double layer approaches asymptotically the gap of the bottom electrode for low temperatures and large bias currents. The* $Al_2O_3$ *tunnel barrier was formed at* 0.015 mbar.

voltages. The IVCs of samples with a thicker F-layer, i.e. 2.51 nm and 4.03 nm, were similar, apart from the critical current $I_c$, which was one order of magnitude smaller for the latter one. The supplementary singularities at $eV = \Delta, \Omega$ and $V = |\Delta_1 - \Omega|/e$ could not be detected at 4.2 K, probably due to the thermal smearing of the gaps $\Delta, \Omega$.

For detailed studies, the experiments have to be repeated at much lower temperatures, as done by Kontos and Aprili on their SINS/SIFS-type junctions at 300 mK [153].

### 6.4.1 Temperature dependence of IVC

Fig. 6.11 depicts the I-V characteristics of an SINFS junction ($d_F = 4.28$ nm) at temperatures between $T = 1.7$ K up to $T = 7.0$ K. The effect of increasing temperature for fixed $\gamma_M \propto d_F$ is similar to an increase of F-layer thickness at constant temperatures, as both reduce the superconducting gap. For higher temperatures the critical current vanished, and likewise the hysteresis disappeared due to an enhanced leakage current. The total I-V characteristic resembled that of an SNS (or SFS) junction, which is always overdamped. For very low temperatures the critical current increased, the sub-gap current was vanishing and the junction was strongly underdamped.
Unlike the SIS junctions, where the system jumps to a voltage that corresponds to

the double gap energy $2\Delta/e$, the voltage drop in SINFS junctions is reduced. Due to the very weak proximity effect in the F-layer the metallic conductance dominates at the boundary of the FS-bilayer. The maximum supercurrent density through the depicted SINFS junction was three orders of magnitude below the supercurrent through an SIS junction with similar oxide barrier thickness. Thus, the SINFS structure in voltage state resembles an SIN structure. For a current-biased system the maximum voltage drop after leaving the zero-voltage state is defined by the gap $\Delta_1$ of the bottom electrode, and is reduced by the appearance of leakage currents. For low temperatures, when the sub-gap conductance was notably reduced, the voltage approached asymptotically the gap $\Delta_1$, as shown in Fig. 6.11.

## 6.5 F-layer thickness dependence of SINFS junctions

I have investigated the thickness dependence of the critical current $I_c(d_F)$ of SINFS JJs for two samples with a thin and a thick tunnel barrier, respectively. To form the $Al_2O_3$ barrier the Al layer was oxidized at 0.015 or at 50 mbar to have $j_c^{(1)} \approx 4.0\,\mathrm{kA/cm^2}$ (sample 1) and $j_c^{(2)} \approx 0.19\,\mathrm{kA/cm^2}$ (sample 2) for the reference superconductor-insulator-superconductor (SIS) JJs. Due to a small magnetization the $I_c(H)$ of the junctions was sometimes slightly shifted along the $H$ axis.

### 6.5.1 Critical current

On sample 1 the JJs with very thin F-layer had such a high critical current that I could not reach it due to strong thermal heating. Moreover JJs with large $j_c$ had $\lambda_J \ll 100\,\mu$m so that the junctions were in the long 2d JJ limit. For sample 1 I show only JJs having normalized length less than $2\lambda_J$, so that I can treat them as SJJs. To investigate the limit of very thin F-layers, I had to use samples from sample 2 with thicker tunnel barrier. The nonmonotonic $I_c(d_F)$ dependence of both samples is shown in Fig. 6.12(a).

The Eq.(2.4) is modified to include the dead magnetic layer thickness $d_F^{\mathrm{dead}}$. It is clear that $I_c^{\mathrm{SINFS}} < I_c^{\mathrm{SIS}}$ for any thickness $d_F$ even if $d_F \leq d_F^{dead}$. The dead layer is taken into account as follows. If $d_F \leq d_F^{dead}$ the F-layer works as N-layer. And only for $d_F > d_F^{dead}$ there is an exponentially decaying oscillation given by Eq.(2.4), but with $d_F - d_F^{dead}$ substituted instead of $d_F$.

Thus, the estimation of $I_c(d_F)$ is modified by introducing as new fitting parameter the thickness of the dead layer $d_F^{dead}$. For $d_F > d_F^{dead}$ the formula reads

$$j_c(d_F) = j_c(0)\, e^{\frac{-d_F^{dead}}{\xi_{F1}^{dead}}}\, e^{\frac{-(d_F - d_F^{dead})}{\xi_{F1}}} \cos\left(\frac{d_F - d_F^{dead}}{\xi_{F2}}\right),$$

which is equivalent to

$$j_c(d_F) = j_c(d_F^{dead})\, e^{\frac{-(d_F - d_F^{dead})}{\xi_{F1}}}\, \cos\left(\frac{d_F - d_F^{dead}}{\xi_{F2}}\right) = j_c^{\mathrm{eff}}\, e^{\frac{-d_F}{\xi_{F1}}}\, \cos\left(\frac{d_F - d_F^{dead}}{\xi_{F2}}\right). \tag{6.1}$$

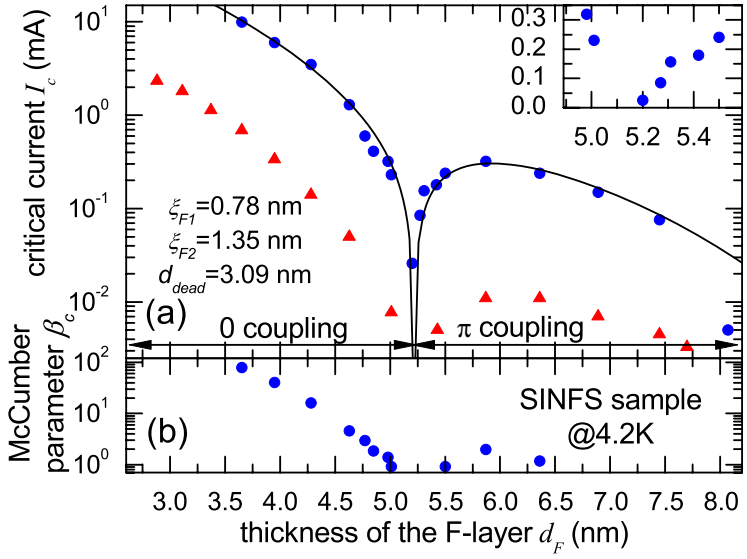


Figure 6.12: *$I_c(d_F)$ (a) and $\beta_c(d_F)$ (b) dependences (circles: sample 1, triangles: sample 2) and fitting curve for sample 1. The inset shows a magnification of* 0 *to* $\pi$ *transition region for sample 1 on a linear scale.*

As a result the parameters for fitting are $\xi_{F1}$, $\xi_{F2}$ and both $j_c^{\text{eff}}$ and $d_F^{dead}$.

The coupling changed from 0 to $\pi$ at the crossover thickness $d_F^{0-\pi} = \frac{\pi}{2}\xi_{F2} + d_F^{\text{dead}} = 5.21$ nm. However, the shape of the $I_c(d_F)$ curve did not change with the thickness of the tunnel barrier, but the amplitude of $I_c(d_F)$ was proportional to the reciprocal transparency parameter $\gamma_{B1}^{-1}$. In the interval of $d_F$ from 0 to 9 nm the value of $j_c$ changed over five orders of magnitude from $j_c = 4$ kA/cm$^2$ to below 0.05 A/cm$^2$ (sample 1). For larger $d_F$ the voltage drop at 4.2 K was very low (below 1 $\mu$V) and appeared at low bias currents (below 1 $\mu$A). Hence, it was of the same order of magnitude as the electric background noise of the system.

By fitting $I_c(d_F)$ for sample 1 using Eq. (6.1), I estimated $\xi_{F1} = 0.78$ nm and $\xi_{F2} = 1.35$ nm and dead F-layer thickness $d_F^{\text{dead}} \approx 3.09$ nm. For $d_F < d_F^{\text{dead}}$ the critical current density $j_c^{\text{SINFS}}(d_F)$ did not get higher than $j_c^{\text{SIS}}$. As can be seen, the inelastic magnetic scattering was strong ($\xi_{F1} < \xi_{F2}$) and $\xi_{F1} \ll d_F$, thus Eq. (2.4) was valid. Moreover, the samples were in the diffusive limit, as the mean free path $\ell = 0.2$ nm was shorter than the coherence length $\xi_{F1}$.

The maximum critical current density in the $\pi$ state was $j_c(\pi) = 3.8$ A/cm$^2$ (sample 1) and $j_c(\pi) = 90$ mA/cm$^2$ (sample 2) at $T = 4.2$ K. For sample 1 I estimated $\lambda_J \approx 190$ $\mu$m, which can be *increased* by increasing the thickness of the tunnel barrier. A further *decrease* of $\lambda_J$ by lowering the $Al_2O_3$ thickness was limited by appearance of microshorts in the barrier (see Sec. 6.9).

In the previous work by Ryazanov et al. [79] the $I_c(d_F)$ dependence was not traced down to $d_F = 0$. Indeed the 0 to $\pi$ crossover was later found to be in this not investigated window. In my case a crossover at 5.21 nm was found, thus the

previous crossover, if any, should be at about 2.5 nm. I have checked junctions with $d_F$ down to $d_F = 2$ nm with the step in $d_F$ about 0.2 nm and did not observe any other minimum. These data points are not shown in Fig. 6.12 and were not used for fitting because the critical current density was so high that the corresponding JJs were in the long 2d limit, so that the visible/measurable $I_c < j_c L w$.

**Comparison with literature**

The first F-layer thickness dependence of the critical current in SIFS junctions was measured by Kontos *et al.* [9] using a diluted PdNi alloys as ferromagnet. They observed the first 0 to $\pi$ transition by $I_c(d_F)$ measurements. In this alloys the role of magnetic scattering is weaker than in the NiCu alloys I used.
Recently, Ryazanov and coworkers reported on the observation of both 0 to $\pi$ and $\pi$ to $2\pi = 0$ transition [68] in SFS JJs using a magnetically weaker $Ni_{0.53}Cu_{0.47}$ alloy ($T_C = 60K$). Although the spin-flip scattering was taken into account too, the high interface transparency ($\gamma_B = 0.52$) provided a different $I_c(d_F)$ dependence than Eq. (2.4). The lower $E_{ex}$ led to larger $\xi_{F1} = 1.23$ nm and $\xi_{F2} = 3.70$ nm. The magnetic dead layer was 1.4 times larger than in the SINFS JJs of this thesis.

### 6.5.2 Stewart-McCumber parameter $\beta_c$

Fig. 6.12(b) shows the dependence of the McCumber parameter $\beta_c(d_F)$ for sample 1, which was estimated by $I_c$ and $I_r$, measured at $T = 4.2$ K. The capacitance $C \approx 800$ pF, determined from Fiske step spacing $V_{FS} = 73\mu$V was nearly independent from $d_F$. It depended on the thickness of the $Al_2O_3$ barrier, as expected from theory. The resistance $R \approx 55\,\mathrm{m}\Omega$ was likewise nearly independent from $d_F$ (deviation below 2%).

Since $\beta_c \propto I_c R^2 C$, for constant $R$ and $C$ the critical current $I_c$ determined the damping of the plasma oscillations. In addition, a thicker F-layer thickness ($d_F > \xi_{F1}$) increased the dissipation of the plasma oscillations due to the larger leakage current. As can be seen at Fig. 6.12 the $\beta_c(d_F)$ and the $I_c(d_F)$ dependences were similar. Near the 0–$\pi$ crossover and for thick F-layers the $I_c$ was very low and the junctions became overdamped, i.e. $\beta_c < 0.7$ (not shown). For the $\pi$ JJs with $d_F$ near the maximum of the $I_c(d_F)$ curve a hysteresis appeared on the $I$-$V$ characteristic.

### 6.5.3 Transparency parameters

The tunnel current has a cubic dependence on the bias voltage [154–156], which could be approximated by an ohmic dependence for small voltages $V \ll (\Phi_1 + \Phi_2)/2$, where $\Phi$ is the barrier height on each side of tunnel barrier. Thus, the normal resistance $R_n$ was extrapolated from the linear part in IVC after the junction jumped to the voltage state. Sample 1 had an ohmic resistance $R = R_n = 55\,\mathrm{m}\Omega$ and a specific resistance of $\rho_0 = 5.5\,\mu\Omega\,\mathrm{cm}^2$, whereas sample 2 had $R = 1.06\,\Omega$ and $\rho_0 = 106\,\mu\Omega\,\mathrm{cm}^2$. The transparency parameter (cf. Sec. 2.3.1) of the SINFS-interfaces was calculated using $\xi^* = 9.84$ K for sample 1: $\gamma_B^1 = 10.5$ and sample 2: $\gamma_B^2 = 203$. The ratio of the transparency parameters $\gamma_B^2/\gamma_B^1 = 19.33$ reflects the ratio of $j_c^1/j_c^2 = 21.05$ for the

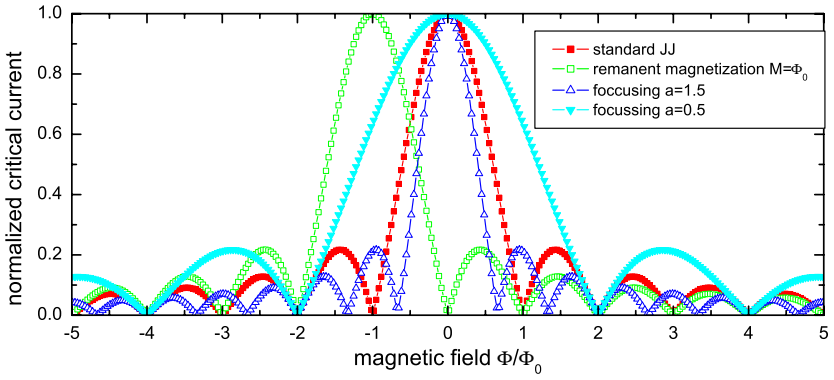


Figure 6.13: *Calculated magnetic diffraction pattern for remanent magnetization in single domain state and magnetic field focussing in short Josephson junction.*

critical current density $j_c$ of SIS junctions with same oxidation conditions as sample 1 and 2. As $\gamma_B > 1$ the SINFS junctions were indeed low transparency systems.

## 6.6 $I_c(H)$ of JJs with ferromagnetic interlayer

In this Section the effect of intrinsic magnetization of the F-layer onto the supercurrent transport will be calculated.

### Remanent magnetization and field focussing in F-layer

Lets assume that the Josephson phase $\phi$ is modified due to a remanent magnetization of the F-layer $M$ and a field focussing effect $a$ on the total magnetic field $H+M$. For simplification both $H$ and $M$ are treated as normalized dimensionless parameters. The focussing of the magnetic field might be caused by the generation of screening currents in the superconducting banks and the flux guidance of the magnetic field inside the F-layer. For a short Josephson junction the critical current is given by the first Josephson relation Eq.(1.5)

$$I_c = w \int_0^L j_0 \sin [\underbrace{\phi_0 + a \cdot x(H+M)}_{\phi}] dx,$$

with width of junction $w$ and an arbitrary initial phase $\phi_0$. Integration over the junction length yields ($I_{c0} = j_c L w$):

$$I_c(H) = I_{c0} \frac{\cos(\phi_0) - \cos(\phi_0 - aL(H+M))}{a(H+M)}.$$

The phase-field relation for maximum $I_c$ is calculated as:

$$\phi_0 = -\arctan\left(\frac{\sin(aL(H+M))}{2\sin^2\left(\frac{aL(H+M)}{2}\right)}\right).$$

In Fig. 6.13 the effect of finite $M$ and $a$ on the magnetic diffraction pattern is plotted. Variation of the focussing parameter changes the *effective* magnetic field through the junction and thus the oscillation period, whereas a remanent magnetization simply shifts the magnetic diffraction pattern along the field axis. In the next Section the magnetic diffraction pattern of two samples with different F-layer thicknesses are discussed.

### 6.6.1 $I_c(H)$ as function of $T$ and $d_F$

The influences of temperature and F-layer thickness on the $I_c(H)$ pattern were investigated for two samples. Both samples were fabricated in the same run, had junction length of 100 $\mu$m and thicknesses of the superconducting electrodes $t_1 = 120 \pm 10$nm and $t_2 = 400$ nm. The junction with lower critical current was 0 coupled ($d_F = 5.11$ nm), whereas the other sample was $\pi$ coupled ($d_F = 5.87$ nm). The $I_c(H)$ pattern is shown in Fig. 6.14 and the junction parameters are summarized in table 6.3. Two effects were notable for decreasing temperature. The peaks of $I_c(H)$ were i) more pronounced and ii) moved to larger magnetic fields.
At lower temperatures, the larger gap facilitated a jump to larger voltages if the bias current exceeds $I_c$. Hence, the voltage criterion for $I_c(H)$ measurements gave a better estimation of $I_c(H)$ for lower temperatures, explaining the first effect.
The temperature dependence of the oscillation period can be explained by the temperature dependence of the magnetic penetration depth [51]:

$$\lambda_L(T) \propto \lambda_L(0) \left[ 1 - \left( \frac{T}{T_c} \right)^4 \right]^{-1/2}.$$

Assuming a somehow reduced superconducting transition temperature of 8 K of the Nb near the F-layer (inverse proximity effect) the change of $\frac{\lambda_L(4.2\,\mathrm{K})}{\lambda_L(2\,\mathrm{K})}$ is about 4%, thus accounting for the change of the side-maxima and minima in $I_c(H)$.

Both samples were clearly inside the SJJ limit, but the effective junction length was slightly different, $L = 0.50\lambda_J$ for the 0 JJ and $L = 0.61\lambda_J$ for the $\pi$ JJ. The difference in the F-layer thicknesses could be neglected, thus

$$\Lambda = \lambda_L[\tanh(t_1/2\lambda_L) + \tanh(t_2/2\lambda_L)].$$

The oscillation length of the magnetic diffraction pattern is given by $\Phi = a\mu_0 H L \Lambda$, with field focussing parameter $a$. The first minimum of the Fraunhofer dependence

Table 6.3: *Parameters of SINFS junctions depicted in Fig. 6.14 for the lowest temperature.*

| $d_F$ [nm] | $I_c$ [$\mu$A] | $j_c$ [A/cm$^2$] | $\lambda_J$ [$\mu$m] | $d'$ [nm] | $\Lambda$ [nm] | $\mu_0 H_{c1}$ [$\mu$T] | $\mu_0 H_{c1}^{exp}$ [$\mu$T] |
|---|---|---|---|---|---|---|---|
| 5.11 | 335 | 3.35 | $200 \pm 13$ | $193 \pm 26$ | $140 \pm 11$ | $146 \pm 11$ | 134 |
| 5.87 | 505 | 5.05 | $163 \pm 11$ | $193 \pm 26$ | $140 \pm 11$ | $146 \pm 11$ | 121 |

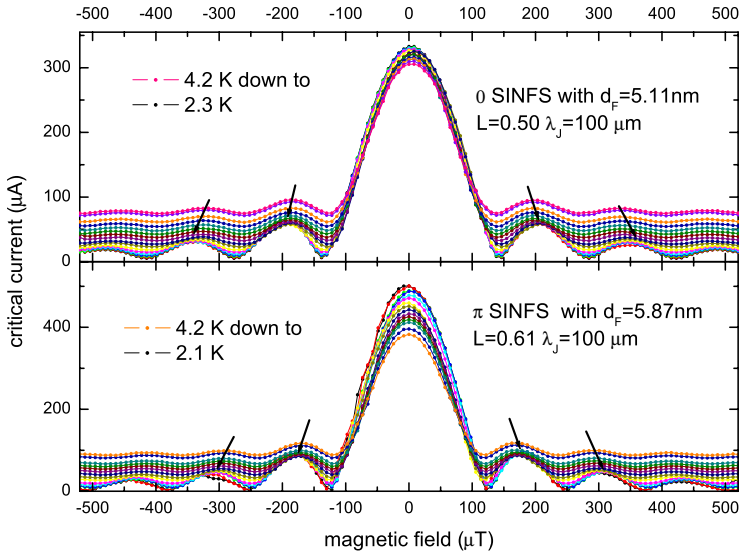


Figure 6.14: *Magnetic diffraction pattern of* 0 *and* $\pi$ *SINFS samples at different temperatures. The arrows denote the direction of change.*

should appeared for $a = 1$ at:

$$\mu_0 H_{c1} = \frac{\Phi_0}{L\Lambda} \approx 146 \pm 11\ \mu\mathrm{T}$$

The experimental value of 134 $\mu$T and 121 $\mu$T, respectively, can be explained by a field focussing effect. The difference in temperature, i.e. 2.3 K and 2.1 K can be excluded as the reason for the deviation in $H_{c1}$. Hence, the junction with thinner F-layer thickness reached $H_{c1}$ at higher magnetic fields. Thus, the magnetic flux density $\Phi/L\Lambda$ was decreased by 11% compared to the junction with thicker F-layer. This can be seen from Fig. 6.14 by comparing the minima of the diffraction pattern.

A larger set of data is necessary for a reasonable conclusion about field focussing effects on the $I_c(H)$ pattern in Josephson junctions with ferromagnetic interlayer, as the spontaneous formation and orientation of magnetic domains may influence the field focussing, too.

## 6.7 Fiske steps in SIFS JJs

I measured Fiske steps on two square shaped $100 \times 100\ \mu\mathrm{m}^2$ samples. The data is plotted in Fig. 6.15 and the voltages of the Fiske steps are summarized in table 6.4. Both junctions were 0 coupled and near the SJJ limit ($\ell = 1.06$ and 2.5). The measurements were done at 4.2 K.

Assuming a London penetration depth of 90 nm and superconducting electrode thicknesses $t_1, t_2$ of 120 nm and 400 nm the Swihart velocity $\bar{c}$ was calculated as

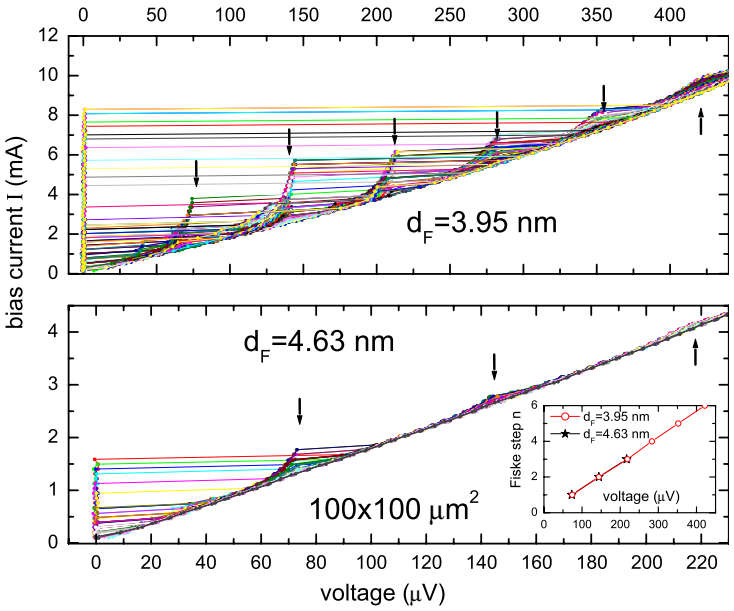


Figure 6.15: *Experimentally measured Fiske step on the IVCs of SINFS-type JJs, measured at* 4.2 K. *The arrows denote the Fiske steps.*

2.4% of speed of light and the $j_c$ dependent plasma frequency ($\omega_{p0} \propto \sqrt{j_c}$) as $\omega_{p0} = 2\pi \times 12.03$ GHz and $\omega_{p0} = 2\pi \times 28.6$ GHz, respectively. The capacitance was estimated as $C = 800$ pF, i.e. the specific capacitance was $\overline{C} = 8\ \mu\mathrm{F/cm^2}$. This value is nearly twice as large as reported in literature [149] for SIS junctions with similar barrier thicknesses. The idle region may increase the Swihart velocity and modify the calculated value of the capacitance, determined by Fiske resonances (see Chap. 4.5.1 for details).

Another method to calculate the capacitance is to estimate the McCumber-parameter by $I_c = 8.5\,\mathrm{mA}$, $I_r = 1.65\,\mathrm{mA}$, $V_r = 78\mu V$ for sample with $d_F = 3.95$ nm. This gave $\beta_c(V_r) \approx 47$. The capacitance can be estimated as $\overline{C} \approx 8.15\,\mu\mathrm{F/cm^2}$, i.e. $\omega_p = 2\pi \times 28.3\,\mathrm{GHz}$. The calculation for the sample with thicker F-layer gave an even larger capacitance of $\overline{C} \approx 9.35\,\mu\mathrm{F/cm^2}$. Note that this calculation is only strictly valid in case of linear damping term $\alpha\dot{\phi}$. The damping depends on the type

Table 6.4: *Fiske step voltages of the I-V characteristics plotted in Fig. 6.15.*

| $d_F$ [nm] | $I_c$ [mA] | $\lambda_J$ [$\mu$m] | 1st [$\mu$V] | 2th [$\mu$V] | 3th [$\mu$V] | 4th [$\mu$V] | 5th [$\mu$V] | 6th [$\mu$V] |
|---|---|---|---|---|---|---|---|---|
| 3.95 | 8.4 | 40 | 74 | 144 | 219 | 283 | 352 | 422 |
| 4.36 | 1.5 | 94 | 73 | 144 | 217 | - | - | - |

of subgap conductance [157], i.e. the back part of the IVC and varies strongly with temperature.

## 6.8 Temperature dependence of 0 and $\pi$ SINFS junctions

Here I discuss the effect of temperature on the coupling, the current-voltage characteristics and the damping of plasma oscillations for SINFS-type junctions. This is similar to the discussion in Section 6.4, where the IVCs of SINFS junctions was studied for variation of the F-layer thickness $d_F$ and temperature $T$. However, these junctions were in the limit of *thin* F-layer thickness and hence, all were 0 coupled. Moreover, those measurements have been performed in a not-highly shielded environment, which could decrease the hysteresis of junction and thus the Stewart-McCumber parameter $\beta_c$.

Several junctions from sample 1 were measured in a highly shielded dewar at the Universität Tübingen[7] using a SQUID-voltmeter or, in case of underdamped junctions, a room temperature voltage amplifier. These measurements were in good agreement with the results obtained at Forschungszentrum Jülich, although the amplitude of critical current in zero field seems to be increased by $20-30\%$. Subsequent cooldowns from room-temperature to 4.2 K in the same set-up did not give an indication for a change in critical current, although magnetic remanence may slightly shift the $I_c(H)$ pattern along the field axis. I attribute the increase of $I_c$ to the better set-up with less fluctuation sources for premature switching into the voltage state.

A structural change in the stack, e.g. in the tunnel barrier or F-layer, with time or temperature could be attributed for the increase of $j_c$, too. To my knowledge, there is no data about annealing properties of Josephson junctions with ferromagnetic barrier in the literature yet. However, it is well known that the $Al_2O_3$ tunnel barrier changes their properties under temperature-treatment of 100°C or higher, cf. [158], but not for samples kept always at room-temperature.

The I-V characteristics and $I_c(H)$ pattern of an SINFS $\pi$ JJs with highest $j_c$ are shown in Fig. 6.16, cf. the IVC of the SIS JJ shown in the inset. At lower temperature the leakage current decreased and the gap moved to higher voltages. In experiment due to heating effects at high bias currents, part of the sample was becoming normal before reaching the gap voltage. The magnetic diffraction pattern $I_c(H)$ was measured with a voltage criterion of 5 $\mu$V, which was better suited for lower temperatures when the voltage drop across the INF-interlayers was larger.

At $T \leq 2.61$ K a step at 149 $\mu$V is visible on the IVC in Fig. 6.16. I found that the Fiske steps have a spacing $V_{\mathrm{FS}} \approx 74\,\mu$V. Thus, I conclude that the observed step is the first zero field step and is not related to any magnetization of the F-layer.

### Temperature dependence of oscillation length $\xi_{F2}$

In general, the complex temperature dependence of the current-voltage characteristics depends on the individual temperature dependences of the gaps $\Delta, \Omega$, the leakage

[7] These measurements were conducted by M. Kemmler.

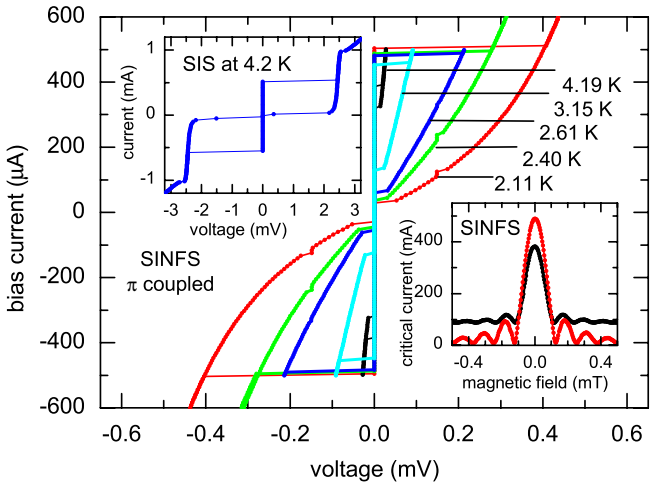


Figure 6.16: *I-V(T) dependence of $\pi$ SINFS ($d_F = 5.87$ nm) junction. The top inset shows IVC of SIS junction at* 4.2 K, *the bottom inset the $I_c(H)$ dependence of SINFS junction at* 4.2 and 2.11 K.

current (i.e. the sub-gap conductivity), the proximity effect in N and F-layers and the change of oscillation period $\xi_{F2}$ due to the thermal energy contribution to pair-breaking processes. The last contribution was neglected in Sec. 6.4, as all samples were in the limit of thin F-layer thicknesses.

The temperature dependence of the exchange field $E_{\rm ex}$ is a way how the temperature could interfere through variation of $\xi_{F1}$ and $\xi_{F2}$. But it is negligible if $T_c \ll T_{\rm C} = 225$ K, because the exchange field is then nearly constant for temperatures below the superconducting transition temperature [68]. The magnetic and spin-orbit scattering mix the up and down spin states. If the spin-flip scattering time $\tau_s$ is short $\hbar\tau_s^{-1} \gg k_B\, T_c$, like in NiCu alloys, the temperature dependence of scattering provides the dominant mechanism for $I_c(T)$.

In general the dissipation decreases for lower temperatures, thus the Stewart-McCumber parameter $\beta_c$ increases, the voltage drop across the barrier when reaching the resistive state becomes larger and the critical current increases (if changes of $\xi_{F2}$ can be neglected). The oscillation period $\xi_{F2}$ becomes shorter for decreasing temperature, thus the whole $I_c(d_F)$ dependence is shifted to thinner F-layer thicknesses. Hence, the temperature dependence of the critical current $I_c(T)$ is the interplay of an increasing component due to an increasing gap and a magnetic coupling dependent contribution which may de- or increasing $I_c$, see Sec. 6.8.2.

### 6.8.1 Temperature dependence of $I_c$ and $\beta_c$

As discussed before, the variation of temperature modifies $\xi_{F1}$ and $\xi_{F2}$ and can even change the ground state of junction [65, 79]. Since $E_{\rm ex}$ of $Ni_{60}Cu_{40}$ is relatively large, a change of $T$ affects the SINFS JJs much less than in the previous works on the

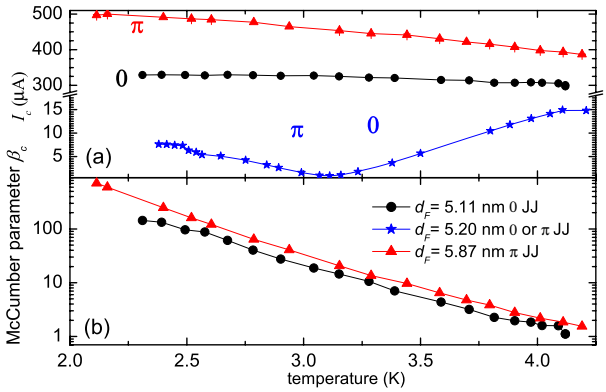


Figure 6.17: *$I_c(T)$ (top) and $\beta_c(T)$ (bottom) dependences of 0 and $\pi$ coupled SINFS junctions.*

stronger diluted ferromagnetic NiCu alloys [65, 79]. The $I_c(T)$ relations for three JJs from sample 1 are shown in Fig. 6.17(a).
At $d_F = 5.11$ nm the JJ was still 0 coupled, but one can attribute the nearly constant $I_c$ below 3.5 K to the interplay between an increasing gap $\Delta$ and a decreasing oscillation length $\xi_{F2}(T)$.
The JJ with $d_F = 5.20$ nm was 0 coupled at $T = 4.2$ K, but changed its coupling to $\pi$ below 3.11 K. For a detailed discussion, see next Section 6.8.2.
The $d_F = 5.87$ nm JJ (as well shown in Fig. 6.16) exhibited the highest critical current among the $\pi$ JJs ($j_c = 5\,\mathrm{A/cm^2}$ at 2.16 K). To my knowledge, the corresponding $\lambda_J = 160\,\mu$m is the shortest achieved for SIFS (or SINFS) JJs up to now.

The bottom part of Fig. 6.17 depicts the $\beta_c(T)$ dependence for the same JJs. The $\beta_c$ of the always overdamped JJ with $d_F = 5.20$ nm was not estimated. The value of $\beta_c$ increased exponentially below 4 K for both 0 and $\pi$ JJs. This indicates a very weak Cooper pair breaking in the F-layer for these temperatures.

A low damping for $\pi$ JJs is important for studying the junction dynamics in $\pi$ or 0–$\pi$ coupled JJs like eigenfrequency spectroscopy, observation of macroscopic quantum tunneling or semi-integer Zero Field Steps in 0–$\pi$ JJs.
In Appendix B.1 the IVC of a $\pi$ coupled JJ at 41 mK is depicted. At these extremely low temperature the junction was strongly underdamped.

### 6.8.2 Temperature induced 0 to $\pi$ transition

The sample with $d_F = 5.20$ nm changed by variation of temperature the coupling from 0 to $\pi$, as can be deduced from its $I_c(T)$ dependence plotted in the upper part of Fig. 6.17 at zero magnetic field and the $I_c(H,T)$ dependence depicted in Fig. 6.18. These measurements were performed using a highly sensitive SQUID-voltmeter with voltage criterion $V_c$ of 10 and 50 nV for detection of the critical current. For all temperatures the junction was overdamped, as the critical current was very low ($\beta_c \propto I_c$).

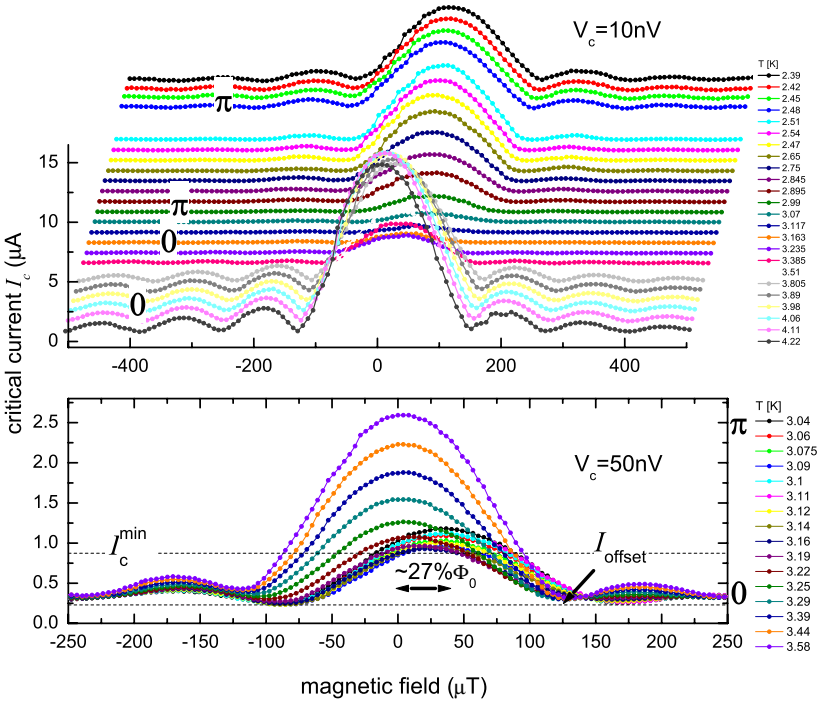


Figure 6.18: *Top: Temperature dependence of $I_c(H)$ of $d_F = 5.20$nm SINFS junction. Curves have been offset vertically and horizontally. Bottom: At 0 to $\pi$ transition the $I_c(H)$ became asymmetric, presumably due to roughness induced 0–$\pi$ phase boundary inside the junction.*

At the 0 to $\pi$ crossover point the critical current $I_c(T)$ should vanish and formally change its sign. Since only the magnitude of the critical current could be measured, the branch of the $\pi$ coupled regime (lower temperature) was reflected into the positive region. One can extract from the three samples in Fig. 6.17 that the possibility to detect a temperature induced 0 to $\pi$ crossover was lost by changing the F-layer thickness only by 0.1 nm.

During the 0 to $\pi$ transition of sample $d_F = 5.20$ nm its critical current was not vanishing completely ($I_c^{\min} \approx 0.87\,\mu$A) (Fig. 6.18 bottom) either due to roughness of the ferromagnet or the prominent $\sin(2\phi)$ component in the current-phase relation [89, 159], which can appear intrinsically or again due to roughness [160, 161]. Note the very small residual offset current $I_{\text{offset}} = 0.25\ \mu$A in the $I_c(H)$ pattern. At the crossover temperature $T_{0\text{-}\pi} = 3.11$ K the $I_c(H)$ could still be traced through several minima, so the roughness of the total junction area still had to be low. The center of the diffraction pattern $I_c(H)$ changed gradually from zero field by $\sim 27\%$ of a flux quantum $\Phi_0$ along the $H$-axis to the right, while changing the coupling phase from 0 to $\pi$. At the same time the amplitudes of the side-maxima became slightly

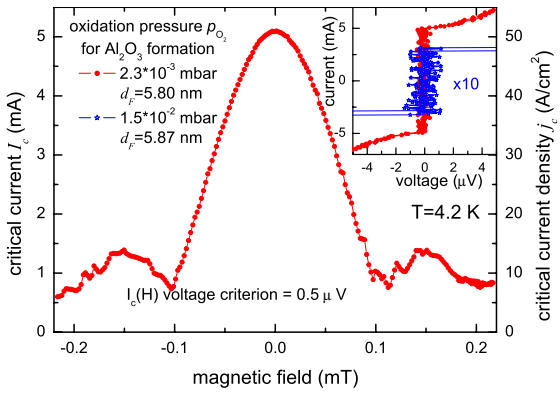


Figure 6.19: *Magnetic diffraction pattern of the $\pi$ JJ with $j_c = 50$ A/cm$^2$ and IVC (inset). Current axis of the reference $\pi$ JJ with thicker $Al_2O_3$ barrier is scaled by factor* 10.

asymmetric. Probably some roughness of the F-layer (e.g. at the junction border) provided 0 and $\pi$ coupled regions in the JJ, i.e. it became a very asymmetric 0–$\pi$ junction. This may explain the shift and asymmetry of $I_c(H)$. For even lower temperatures (2.4 K) the $I_c(H)$ patterns became symmetric, indicating a uniform coupling again.

## 6.9 Upper limit of $j_c$ for $\pi$ coupled JJs

I want to focus on the critical current density $j_c$ and Josephson penetration depth $\lambda_J \propto 1/\sqrt{j_c}$ in $\pi$ JJs. In SINFS junctions with NiCu alloys the highest critical current density $j_c$ for $\pi$ coupling was three orders of magnitude below the $j_c$ of SIS junctions with similar oxidation conditions. This was caused by the strong magnetic scattering of Cooper pairs in the diluted ferromagnets. The very short coherence length $\xi_{F1}$ for $Ni_{60}Cu_{40}$ alloys sets a limitation for higher critical current densities.

From the application point of view, a high critical current density and consequently a short Josephson penetration depth $\lambda_J$ are desirable for various purposes, for example to obtain a large $I_cR$ product or to reach the LJJ limit within reasonable dimensions.

The $d_F = 5.87$nm junction from sample 1 (shown in Fig. 6.16) showed the highest critical current density of the $\pi$ junctions from sample 1 with $j_c = 5\,\mathrm{A/cm^2}$ at 2.16 K. At this temperature the junction was highly underdamped with a Stewart-McCumber parameter $\beta_c = 700$.

A further increase of $j_c$ can be achieved by decreasing the $Al_2O_3$ barrier thickness. However, at the same time the specific tunneling resistance is reduced (i.e. $R$), hence $I_cR$ may even decrease. Miller and coworkers [145] reported on Nb/Al-$Al_2O_3$/Nb (SIS) JJs having $j_c$ up to 400 kA/cm$^2$, but of considerable lower quality. Their junctions had a large subgap current and a strong damping due to the appearance of microshorts in this very thin tunnel barrier.

One SINFS sample with an extremely thin $Al_2O_3$ barrier was fabricated at an oxygen pressure of $2.3 \cdot 10^{-3}$ mbar. This is one decade lower than the oxidation pressure used for my standard SINFS junctions and clearly belongs to the low-exposure regime, with the well-known disadvantages, see Sec. 6.2 for details. The magnetic diffraction pattern and the I-V characteristic of a $\pi$ coupled JJ with $d_F = 5.80$ nm, measured at 4.2 K, are shown in Fig. 6.19. The symmetric $I_c(H)$ modulation indicated a still homogeneous current transport through the junction, although the voltage drop in resistive state was much reduced due to leakage currents. This junction was as well measured at temperatures down to 1.7 K (not shown). It was always overdamped, therefore the leakage current was dominated by temperature-independent *microshorts* in the barrier instead of temperature-dependent *breaking* of Cooper pairs in the F-layer, like for the junction shown in Fig. 6.16.

However, the very high critical current density $j_c$ in $\pi$ state of about 50 A/cm$^2$ may be well suited for applications where the strong dissipation does not matter, or is even desired.

Some recent publication [8, 70, 83] about SFS and SIFS junctions in clean limit with $Ni_3Al$, Ni, Co as magnets indicate the possibility to obtain high $j_c$'s in $\pi$ JJs. Although, the very short oscillation length $\xi_{F2} < 0.5$ nm makes them very sensitive to interface roughness and the stronger magnetic remanence may complicate the $I_c(H)$ measurements.

# Chapter 7

# 0, $\pi$ and 0–$\pi$ SIFS JJs

This Chapter describes the experiments with SIFS 0–$\pi$ JJs, along with 0 and $\pi$ reference junctions. The calculations show that the 0–$\pi$ JJ has a magnetic flux in the ground state.
The $\pi$ and 0–$\pi$ junctions are of interest for several purposes. One can build *Rapid Single Flux Quantum* (RSFQ) devices with active $\pi$ junctions [162], using the double degenerated flux in 0–$\pi$ JJs for memory devices or in quantum limit as qubits [20], study semifluxons like in d-wave superconductors [22, 93, 99], investigate the physics of fractional vortices (like big spins) in various geometries [98] et cetera.

The idea of an SIFS[1] 0–$\pi$ JJs is presented in Chapter 3 and can be summarized as:

It was demonstrated both theoretically (Chapter 2) and experimentally (Chapter 6) that the critical current of SIFS JJ changes its sign (and the ground state from 0 to $\pi$) as a function of the F-layer thickness $d_F$, as shown in Fig. 6.12. By choosing two F-layer thicknesses $d_1 < d_2$ such that $I_c(d_1) \approx -I_c(d_2)$, an SIFS structure with a step like F-layer thickness is fabricated, see Fig. 7.1. If the F-layer has the thickness $d_1$ for one half of the junction and the thickness $d_2$ for the other half, a *symmetric* 0–$\pi$ JJ is obtained. The term symmetric refers both to amplitude of $j_c$ and length $L$ in 0 and $\pi$ coupled parts. In this case, a double degenerated spontaneous flux will be generated in vicinity of the phase boundary. The flux is created by supercurrents circulating around the step in the F-layer. It is equal to $|\Phi_0/2|$ in case of a LJJ.[2]

[1] Although the actual stack sequence for the junctions is SINFS, the N-layer is not relevant for the electric and magnetic properties discussed here and will be neglected in this Chapter. It was introduced to reduce the roughness of the interfaces.

[2] The results presented in this Chapter were obtained in cooperation with M. Kemmler and Dr.

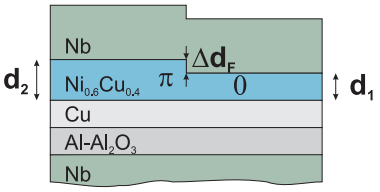


Figure 7.1: *Sketch of* 0–$\pi$ *SINFS JJ with stepped F-layer.*

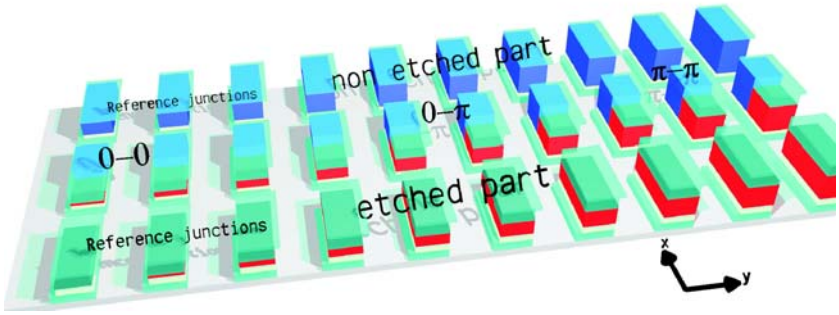


Figure 7.2: *Schematic layout of stepped JJ along with reference junctions. F-layers with thicknesses $d_1$ are denoted in red, and step $\Delta d_F$ and $d_2$ in blue. The F-layer thickness increases from left to right. The actual F-layer thickness is much smaller than depicted.*

Parts of this Chapter were published in Ref. [163].

## 7.1 JJ with step in the F-layer

The workout of a precise patterning and etching process to define JJs with the F-layer thicknesses $d_1, d_2$ on the *same* chip and even within the same JJ was an extremely demanding task. The difference in F-layer thickness was obtained by etching. The precise control of the uniformity of etching to obtain similar F/S interfaces for the etched $d_1$ and non-etched $d_2$ F-layers and a low junction-to-junction deviation were the biggest obstacles. For details on the deposition and the etching parameters for the stepped F-layer, see Sec. 4.6.1.

All the junctions had an area of 10 000 $\mu$m$^2$, but different sizes. Still all lateral sizes were comparable or shorter than the Josephson penetration depth $\lambda_J$.

### 7.1.1 Fabrication of step in the F-layer

To fabricate a stepped F-layer, I used a similar patterning process as for the junctions with uniform F-layer thickness. The layout of stepped junctions and the placement of reference junctions is depicted in Fig. 7.2. As in case for the simple SIFS junctions (Chap. 4), the F-layer was deposited with a gradient of thickness in $y$-direction on the S/I stack, see Fig. 7.2. After the deposition of 40 nm Nb as cap layer and lift-off I obtained the complete SIFS stack with F-layer thickness $d_F(y)$, but without steps in $d_F$ yet. The deposition parameters for the multilayer stack and especially the oxidation conditions of Al-layer were the same as for the sample 1 in Chap. 6. To produce the desired step-like variation in $d_F$, the parts of the JJ that were supposed to have a larger thickness $d_2$ were protected by photoresist, see Fig. 4.8. Then the Nb cap layer was removed by reactive dry etching using $SF_6$. A few tenth of nanometer

E. Goldobin, both from the University of Tübingen.

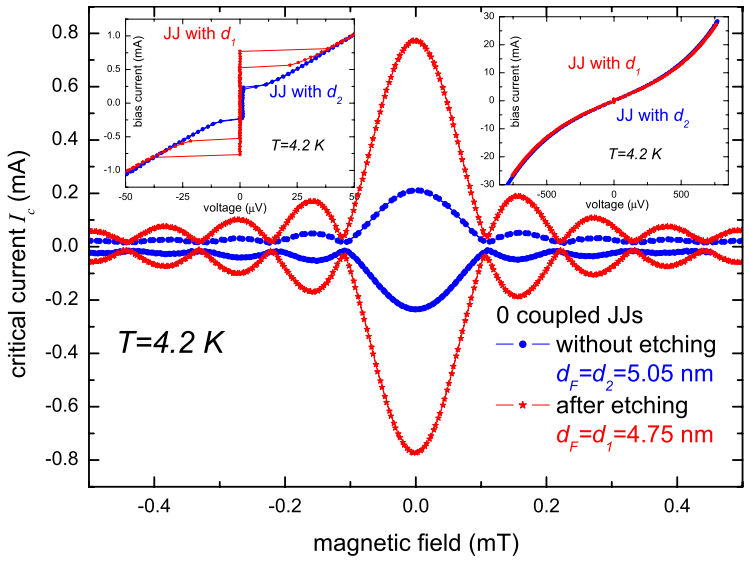


Figure 7.3: *$I_c(H)$ of etched (star) and non-etched (dots) JJs (4.2 K). The insets show IVCs for small and large bias current ranges in zero magnetic field.*

($\Delta d_F = d_2 - d_1$) of NiCu were Ar ion etched at a very low power and rate to avoid any damaging of the NiCu film under the surface and to keep a good control over the step height. When the F-layer thickness was reduced down to the thickness $d_1$ the etching was stopped and 40 nm of Nb were deposited in situ.

Various structures on the chip were placed within a narrow ribbon along the $x$-direction and replicated along $y$-direction. One ribbon contained references JJs with the F-layer thicknesses $d_1$ (uniformly etched) and $d_2$ (non-etched) and a JJ with step in the F-layer thickness from $d_1$ to $d_2$. The length $L_0$ and $L_\pi$ are within lithographic accuracy of $\approx 1$ $\mu$m. A set of structures for different $d_F(y)$ with an increase in $d_F$ for each row of about 0.05 nm was obtained. The increase of the F-layer thickness along $y$ axis was determined from reference films.

### 7.1.2 Quality of the etched junctions

Fig. 7.3 shows the results of experimental investigation of some reference JJs, i.e. the IVC and $I_c(H)$ dependence for a non-etched junction (dot) with the F-layer thickness $d_2$ and a uniformly etched junction (star) with thickness $d_1 = d_2 - \Delta d_F$ are depicted. The thickness of $\Delta d_F$ was estimated by comparison of $I_c$ of both samples with the data from Fig. 6.12 (sample 1). Both junctions were still in the 0 coupling regime. The insets show the I-V characteristics for small and large ranges of bias current. Besides the difference in $I_c$, the $I_c(H)$ dependence and the IVCs (right inset) showed no evidence for an inhomogeneous current transport for both samples. The larger $I_c$, but same resistance and capacitance led to a slightly hysteretic IVC of the etched sample, just as the samples with thinner $d_F$ (discussed in Chapter 6).

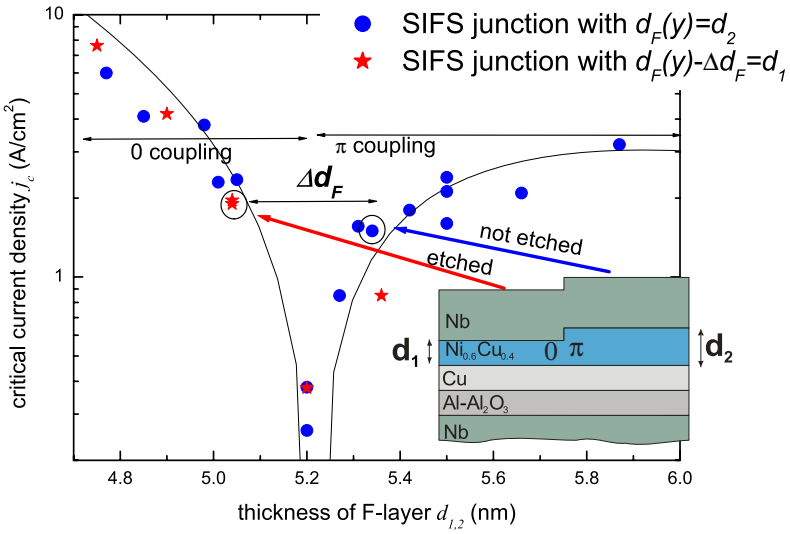


Figure 7.4: *Critical current $I_c$ of the uniformly etched (star) and non-etched (dot) SIFS junctions versus the F-layer thickness before etching $d_F$. The fit of the experimental data for non-etched samples using Eq.(7.1) is shown by the continuous line. The JJs were oxidized at* 0.015 mbar.

The scattering of the critical current $I_c$ and resistance $R$ on the etched junctions was, just like for the non etched SIFS junctions, of the order of 2%. For example, the scattering of $I_c$ can be seen at Fig. 7.4. At $d_F = 5.04$ nm two uniformly etched samples with same area have critical current densities $j_c$ of 1.90 A/cm$^2$ and 1.96 A/cm$^2$, respectively. The trapping of magnetic flux might cause a larger variation in critical current density than the interface asymmetry stemming from the etching process.

## 7.2 0–π SIFS JJs

In each ribbon in $y$-direction of the wafer there was a set consisting of the following three JJs:

- a JJ not affected by the etching with $d_2 \equiv d_F(y)$
- a JJ etched uniformly with $d_1 \equiv d_F(y) - \Delta d_F$
- a JJ etched to have an F-layer with the step from $d_1$ to $d_2$.

For the low transparent SIFS junctions the $I_c(d_F)$ dependence is given by Eq.(2.4):

$$I_c(d_F) \sim \exp\left(\frac{-d_F}{\xi_{F1}}\right) \cos\left(\frac{d_F - d_F^{\text{dead}}}{\xi_{F2}}\right), \tag{7.1}$$

where $\xi_{F1}$, $\xi_{F2}$ are the coherence and oscillation lengths as derived in Sec. 6.5. The data points from the SIFS junctions with the F-layer thickness $d_2$ are dots, star ones are from junctions after uniform etching of the F-layer down to a final thickness of $d_1$.

The coupling of junctions changes from 0 to $\pi$ at the crossover thickness $d_F^{0\text{-}\pi} = \frac{\pi}{2}\xi_{F2} + d_F^{\text{dead}} = 5.21$ nm. Fitting $I_c(d_F)$ to the non-etched junctions yielded $\xi_{F1} = 0.78$ nm, $\xi_{F2} = 1.35$ nm and $d_F^{\text{dead}} = 3.09$ nm (black line in Fig. 7.4). See Chapter 6 for details.
By comparison with the experimental $I_c(d_F)$ data for the etched samples I estimated the etched away F-layer thickness as $\Delta d_F \approx 0.3$ nm. The uniformly etched samples (star) were already shifted by this amount, see Fig. 7.4.

Now a set of junctions is chosen which had the thickness $d_2$ and critical current $I_c(d_2) < 0$ ($\pi$ junction) before etching and the thickness $d_1 = d_2 - \Delta d_F$ and critical current $I_c(d_1) \approx -I_c(d_2)$ after etching (0 junction). One of the possibilities to choose is the junction set denoted by circles around the data points in Fig. 7.4. In practice, I tried to choose $d_2$ so that $I_c(d_2)$ corresponds to the maximum absolute value of the supercurrent in the $\pi$ state. In this case the 0–$\pi$ JJ has the shortest $\lambda_J$ and lowest possible damping for the $\pi$ part, which is favorable for semifluxons and qubits. In any case, due to the rather steep slope of the $I_c(d_F)$ curve at $d_F \approx d_1$, $I_c(d_1)$ is very sensitive to $d_1$. Therefore, it was not so easy to fabricate 0–$\pi$ JJs with $|j_c(d_1)| = |j_c(d_2)|$.

### 7.2.1 0, $\pi$ and 0–$\pi$ Josephson junctions

In the next Sections only three JJs out of the selected set are discussed.

- a 0 JJ with F-layer thickness $d_1$ and the critical current density $j_0 \equiv j_c(d_1)$
- a $\pi$ JJ with F-layer thickness $d_2$ and the critical current $j_\pi \equiv j_c(d_2)$
- a 0–$\pi$ JJ with thicknesses $d_1$, $d_2$ and critical densities $j_0$, $j_\pi$ in 0 and $\pi$ halves

All these junctions had dimensions $330 \times 30$ $\mu$m$^2$, see Fig. 7.5. The 0–$\pi$ JJ consisted of one 0 and one $\pi$ region of equal lengths $L_0 = L_\pi = 165$ $\mu$m$^2$ (within lithographic accuracy). I assume that the critical current density in all 0 regions (and in all $\pi$ regions) was the same, as no indication for an inhomogeneous current transport was given.

The I-V characteristics and the magnetic field dependence of the critical current $I_c(H)$ was measured for all three junctions. The magnetic field $H$ was applied in-plane of the sample and along the $y$-direction, see Fig. 7.5, thus $H$ was parallel to the step discontinuity in the F-layer. The magnetic diffraction pattern of the 0–$\pi$ JJ and the 0 and $\pi$ reference JJs are plotted in Fig. 7.6. Due to a small net magnetization of the F-layers the $I_c(H)$ of references junctions were slightly shifted along the $H$ axis.[3] Nevertheless, both had the same oscillation period $\mu_0 H_{c1} \approx 36$ $\mu$T. At $T \approx 4.0$ K the I-V characteristics were non-hysteretic with $I_c^0 \approx 208$ $\mu$A, $I_c^\pi \approx 171$ $\mu$A, as can be seen in Fig. 7.6. The magnetic field dependence, top of Fig. 7.6, of the reference

[3]The influence of a finite magnetization on $I_c(H)$ pattern is estimated in Sec. 7.3.3.

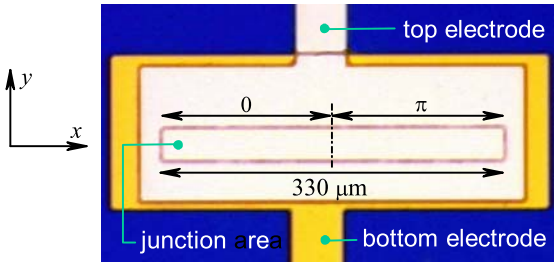


Figure 7.5: *Picture of the* $330 \times 30$ $\mu$m$^2$ *JJ (top view). The* 0–$\pi$ *boundary/step in the F-layer (if any) is indicated by a dashed line.*

junctions $I_c^0(H)$ and $I_c^\pi(H)$ look like almost perfect Fraunhofer patterns. The 0–$\pi$ junction was slightly asymmetric $\Delta = j_c^\pi / j_c^0 \neq 1$, but the magnetic field dependence $I_c^{0\text{-}\pi}(H)$ had a clear minimum near zero field, although it was somewhat asymmetric and shifted along the $H$ axis.

To achieve a more symmetric configuration, the bath temperature was varied from 4.2 K down to 2.3 K, because a decrease of the temperature should increase $I_c^\pi = I_c(d_2)$ stronger than $I_c^0 = I_c(d_1)$. The reason of this is the interplay between the increase of the gap $\Delta(T)$ and the shift of $I_c(d_F)$ curve towards lower $d_F$ due to a reduction of $\xi_{F2}(T)$ when temperature decreases, as already discussed in Chap. 6. The increase of gap yields a higher $j_c$. The half with thicker F-layer, i.e. the $\pi$ coupled part, has a slightly stronger suppression of the superconducting gap near the S/F interface and should have a faster increase of $I_c$. The change of $\xi_{F2}$ *decreases* $I_c^0$ and *increases* $I_c^\pi$. As a result, in experiment both $I_c^0(T)$ and $I_c^\pi(T)$ were increasing when decreasing the temperature, but with different rates. At $T \approx 2.65$ K the critical currents $I_c^0$ and $I_c^\pi$ became approximately equal.

The main experimental result of this Chapter is presented in the bottom part of Fig. 7.6. It shows the $I_c(H)$ dependences for all three junctions at $T \approx 2.65$ K. One can see that the $I_c^0(H)$ and $I_c^\pi(H)$ pattern almost coincide, having the form of a symmetric Fraunhofer pattern with the critical currents $I_c^0 \approx 220$ $\mu$A, $I_c^\pi \approx 217$ $\mu$A and the same period of modulation. The $I_c^{0\text{-}\pi}(H)$ dependence has a clear minimum near zero field and almost no asymmetry. The critical currents at the left and right maxima (146 $\mu$A and 141 $\mu$A) differ by less than 4 %. The magnetic diffraction pattern $I_c(H)$ was measured with the voltage criterion of $0.5\,\mu$V. This criterion gave an $\approx 1\%$ increase in $I_c^{0\text{-}\pi}(H)$ at the central minimum.

To ensure that the dip on $I_c^{0\text{-}\pi}(H)$ near zero field came from the stepped 0–$\pi$ boundary formed by a step-like F-layer, I measured $I_c^{0\text{-}\pi}(H_x)$ by applying the field along $x$-direction (perpendicular to the step discontinuity). In this case $I_c^{0\text{-}\pi}(H_x)$ pattern looks like a Fraunhofer pattern with maximum at zero field, as shown in the inset of Fig. 7.6. Probably the sample was slightly tilted against the magnetic field and the F-layer had a finite magnetization, thus the $I_c(H)$ was asymmetric in the side-maxima and $I_c(0) \approx 93$ $\mu$A was higher than for the measurements with magnetic field along the step $I_c^{0\text{-}\pi}(0)$. This measurement was done separately in a Helium bath set-up with more noise and less magnetic shielding. The larger voltage

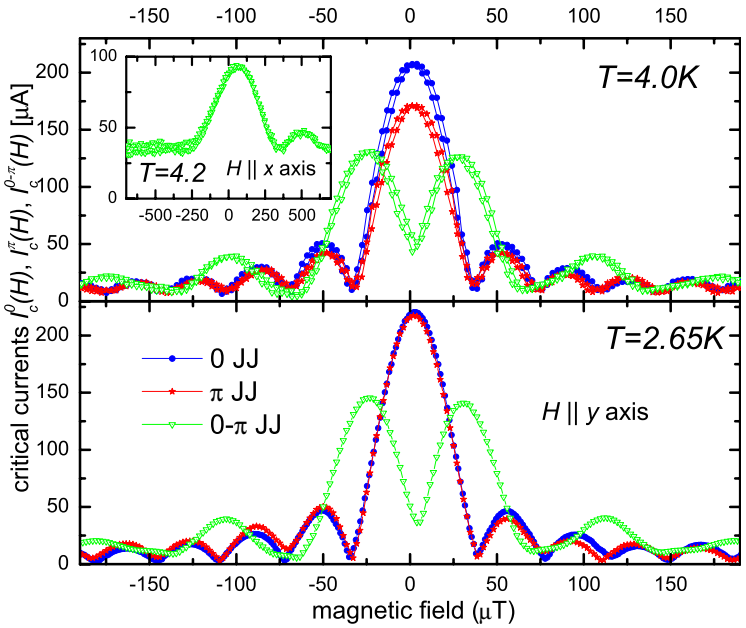


Figure 7.6: *Junction geometries* $330 \times 30$ $\mu$m$^2$. $I_c(H)$ *of* 0–$\pi$ *JJ (triangle) with* $H$ *applied parallel to short* ($y$) *axis and step in the F-layer, along with the non-etched (dot) and etched (star) reference SIFS junctions. Top:* $I_c(H)$ *at* 4.0 K, *Bottom:* $I_c(H)$ *at* $T \approx 2.65$ K, *symmetric* 0–$\pi$ *JJ. The inset shows the* $I_c(H)$ *pattern of* 0–$\pi$ *JJ with* $H$ *parallel to long* ($x$) *axis. The JJs were oxidized at* 0.015 mbar.

criterion ($1\,\mu$V) and the higher bath temperature (4.2 K) contributed to the current offset in $I_c(H)$, too.

## 7.3 Physics of 0–$\pi$ JJs

Let us review the conditions for appearance of a spontaneous vortex in an one-dimensional Josephson junction with symmetric or asymmetric 0–$\pi$ phase boundary.

### 7.3.1 Ground state diagram

As mentioned in Chapter 3, for junctions of finite normalized length $\ell$ the vortex (or the associated supercurrent) appears in the short junction limit only for almost symmetric junctions, that means with only low deviations from $|j_c^\pi| \approx |j_c^0|$ and $L_\pi \approx L_0 \approx L/2$. Below I want to determine quantitatively the maximal degree of the asymmetry $\Delta = j_c^\pi / j_c^0$ in case of the centered ($L_\pi = L_0 = L/2$) 0–$\pi$ boundary for a given total junction length $\ell$, which still allowed to have a ground state with spontaneous magnetic flux. From Ref. [92] the two boundaries between flat phase

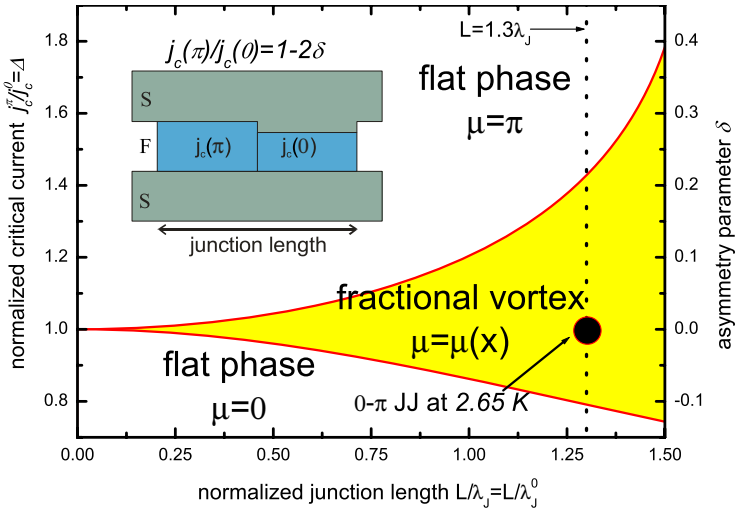


Figure 7.7: *Phase diagram of short 0–π Josephson junction. Vortex state exists in dashed region, outside is a homogeneous flat phase μ. The 0–π boundary is centered and the asymmetry stems from the difference in* $j_c^{\pi}/j_c^0 = \Delta = 1 - 2\delta$. *The vertical doted line indicates the length* $\ell = 1.3$.

states $\mu = 0$ or $\mu = \pi$ and the state with spontaneous fractional flux are given by the equations

$$\tan\left(\frac{L_0}{\lambda_J^0}\right) = \sqrt{\left|\frac{j_c^{\pi}}{j_c^0}\right|}\tanh\left(\frac{L_{\pi}}{\lambda_J^{\pi}}\right), \qquad \tanh\left(\frac{L_0}{\lambda_J^0}\right) = \sqrt{\left|\frac{j_c^{\pi}}{j_c^0}\right|}\tan\left(\frac{L_{\pi}}{\lambda_J^{\pi}}\right).$$

Normalizing the lengths to $\lambda_J \equiv \lambda_J^0$ and introducing $\Delta \equiv |j_c^{\pi}|/|j_c^0| = 1 - 2\delta$ with asymmetry parameter $\delta$ yields

$$\tan(\ell_0) = \sqrt{\Delta}\tanh\left(\ell_{\pi}\sqrt{\Delta}\right), \qquad \tanh(\ell_0) = \sqrt{\Delta}\tan\left(\ell_{\pi}\sqrt{\Delta}\right),$$

where $\ell_0 = L_0/\lambda_J$, and $\ell_{\pi} = L_{\pi}/\lambda_J$. Since the 0–π junction has equal length of 0 and π parts $L_0 = L_{\pi} = L/2$ ($L = 330$ μm), denoting $\ell_0 = \ell_{\pi} = \ell/2$, one gets two transcendental equations for $\Delta$, which define the boundaries between different ground states:

$$\tan(\frac{1}{2}\ell) = \sqrt{\Delta}\tanh\left(\frac{1}{2}\ell\sqrt{\Delta}\right), \qquad \tanh(\frac{1}{2}\ell) = \sqrt{\Delta}\tan\left(\frac{1}{2}\ell\sqrt{\Delta}\right).$$

For very short junctions $\ell \to 0$, both solutions give $\Delta \to 1$ [15]. By substituting $\Delta = 1 - 2\delta$ into Eqs. and Taylor-expanding them up to terms linear with $2\delta$ one can express $\delta$ as $\delta(\ell)$. Finally expanding with respect to $\ell$ up to quadratic terms $\ell^2$, one gets $\delta = \pm\ell^2/12$. Thus, for very short JJs ($\ell \to 0$) the range of $j_c^{\pi}$ with spontaneous

flux in the ground state is from $\Delta = j_c^\pi/j_c^0 = 1 - \ell^2/6$ to $1 + \ell^2/6$, i.e. may be extremely small, see Fig. 7.7.

For large $\ell$ one has to solve the transcended equations numerically. The results are present in Fig. 7.7, which depicts the phase diagram for the flux state depending on the normalized junction length $\ell$ and ratio $j_c^\pi/j_c^0$. If the 0–$\pi$ LJJ is asymmetric, i.e. $j_c^0 \neq j_c^\pi$ is out of the fractional vortex regime, the ground state corresponds to $\mu = 0$ or $\mu = \pi$. Note that the short JJs should be very symmetric to poses fractional flux in the ground state. JJ with large $\ell$ are very insensitive to the asymmetry.

For all junction length $\ell$ the appearance of a spontaneous magnetic flux is a second-order phase transition [92], that may be controlled by a temperature-induced variation of the asymmetry ratio $j_c^\pi/j_c^0$. This has been done in case of the 0–$\pi$ coupled junction presented in this Chapter.

### Symmetric short 0–$\pi$ JJ

I want to discuss the features of the $I_c^{0\text{-}\pi}(H)$ dependence and its meaning in case of the symmetric 0–$\pi$ junction, measured at 2.65 K. The Josephson penetration depth $\lambda_J = \sqrt{\Phi_0/2\pi\mu_0 j_c d'} \approx 259 \pm 17$ $\mu$m, was estimated taking the London penetration depth $\lambda_L = 90 \pm 10$ nm, the thicknesses of the superconducting electrodes $t_1 = 120 \pm 10$nm and $t_2 = 400$ nm, and $j_c = I_c^0/(Lw) = 2$ A/cm$^2$. The junction dimensions were the length $L = 330$ $\mu$m and the width $w = 30$ $\mu$m. The quantity $d'$ was given by $d' = d_I + d_F + \lambda_L \coth(t_1/\lambda_L) + \lambda_L \coth(t_2/\lambda_L)$. Thus, the normalized length $\ell = L/\lambda_J$ was $\approx 1.3$ (at $T = 2.65$K).

The ground state of the system in absence of a driving bias or magnetic field ($I = H = 0$) should be determined. The calculation of magnetic flux in the short junction limit was done in Section 3.3. For the symmetric 0–$\pi$ LJJ of the length $\ell = 1.3$ the ground state had a spontaneous flux

$$\pm\Phi = \Phi_0\ell^2/8\pi \approx 0.067 \cdot \Phi_0.$$

That means the spontaneous flux was 13% of $\Phi_0/2$. From the phase diagram and the junction length of $\ell = 1.3$, the ground state with spontaneous flux will still exist even for $j_c^\pi/j_c^0$ from 0.78 to 1.39 (see vertical dotted line corresponding to $\ell = 1.3$. Thus, *the junction was clearly inside the domain with spontaneous flux in the ground state* although one cannot see any striking indications of this on the $I_c^{0\text{-}\pi}(H)$ dependence. This JJ should even have some small spontaneous flux in the high temperature state of 4.0 K, as the asymmetry parameter $\Delta = 0.82$, i.e. $\delta = 0.09$, was still within the vortex state regime. The magnetic field profile corresponding to the spontaneous *vortex* at $T \approx 2.65$ K and $\ell = 1.3$ is shown in Fig. 7.8.

Note that even if $j_c^\pi/j_c^0$ was off the ground state with spontaneous flux, e.g. at higher temperature when the asymmetry was even larger and the ground state was flat ($\mu = 0$ in this case), by applying a bias current or a magnetic field one induced fractional flux in the system [17].

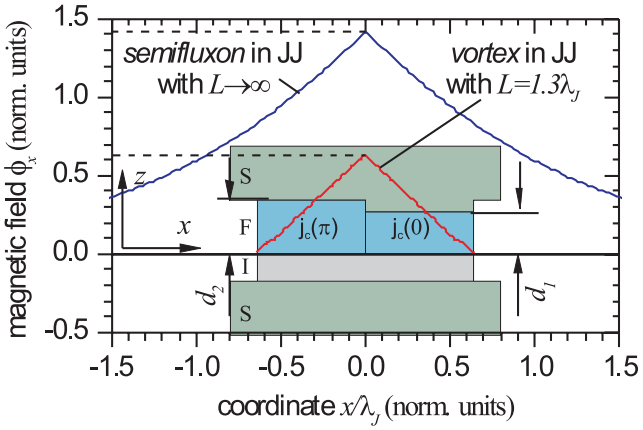


Figure 7.8: *Numerically calculated magnetic field of a spontaneous fractional flux in 0–π JJ of $\ell = 1.3$. The field of semifluxon in an infinite LJJ is shown for comparison.*

### 7.3.2 $I_c(H)$ dependences

#### $I_c(H)$ of reference JJs

Using a SJJ model, i.e. assuming that the phase $\mu(x)$ is a linear function of $x$ the first minimum of the Fraunhofer dependence for the reference 0 JJ or $\pi$ JJ can be calculated. It should appear at:

$$H_{c1} = \frac{\Phi_0}{\mu_0 L \Lambda} \approx 44.6 \pm 3.5 \ \mu\mathrm{T},$$

where the effective magnetic thickness of the junction

$$\Lambda = d_I + d_F + \lambda_L \tanh\left(\frac{t_1}{2\lambda_L}\right) + \lambda_L \tanh\left(\frac{t_2}{2\lambda_L}\right) \approx 140 \pm 11 \text{ nm}.$$

Therefore the experimental value of $34\mu$T was lower and can be explained by a weak field focusing effect of the geometry with the factor 1.3.

#### $I_c^{0\text{-}\pi}(H)$ for short ideal JJ

The magnetic diffraction pattern of $I_c^{0\text{-}\pi}$ for a symmetric, short 0–$\pi$ junction is given by Eq.(3.4):

$$I_c^{0\text{-}\pi}(H) = I_c^0 \frac{\sin^2\left(\frac{\pi}{2}\frac{\Phi}{\Phi_0}\right)}{\left|\frac{\pi}{2}\frac{\Phi}{\Phi_0}\right|},$$

where $\Phi/\Phi_0 = \mu_0 H L \Lambda/\Phi_0$ is the number of the applied flux quanta through the effective junction area. This dependence has a minimum at zero applied fields $I_c^{0\text{-}\pi}(0) = 0$, two symmetric maxima with critical current $I_c^{0\text{-}\pi}(H_m)/I_c^0 \approx 0.72$ at magnetic field $\mu_0 H_m = 2\Phi_0/L\Lambda$ and the first side minima appear at $\Phi_\Sigma/\Phi_0 = \pm 2$, which should

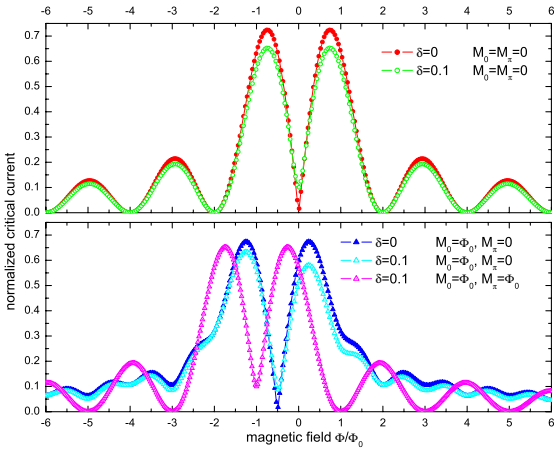


Figure 7.9: *Calculated magnetic diffraction pattern* $I_c^{0\text{-}\pi}(H)$ *for short* 0–$\pi$ *junction with asymmetry in* $j_c^{0,\pi}$ *and remanent magnetization (single domain)* $M_{0,\pi}$. *Only asymmetry in both* $j_c^{0,\pi}$ *and* $M_{0,\pi}$ *tilts the maxima.*

have a parabolic shape. A plot of $I_c^{0\text{-}\pi}(H)$ together with $I_c^{0,\pi}(H)$ patterns in the short junction limit is found in Fig. 1.7.

### 7.3.3 Remanent magnetization in short 0–$\pi$ JJ

The analytic solution for magnetic diffraction pattern in a short ($L < \lambda_J$) junction with different critical current density $j_c^0 \neq j_c^\pi$ and remanent magnetization $M_0 \neq M_\pi$ of F-layers in 0 and $\pi$ state can be found in analogy to the calculation for the flat phase junctions presented in Section 6.6. The 0–$\pi$ phase boundary is centered, i.e. $L_0 = L_\pi = L/2$. The magnetizations may be in a multidomain state $M_0, M_\pi \neq 0$, but the net magnetization may be very small, see Chapter 5. The random orientation of the net magnetization in each part (0, $\pi$) can provoke different magnetic states in both halves, i.e. $M_0 \neq M_\pi$. For simplification both $H$ and $M$ are treated as normalized, dimensionless parameters. It is assumed that $\phi^0(x) = \phi_0 + (M_0 + H)x$, $\phi^\pi(x) = \phi_\pi + (M_\pi + H)x$, $\phi^0(x) = \phi^\pi(x)$ with $-L_0 < x < L_\pi$ and $\phi_0 = \phi_\pi$. Then

$$I_c^{0\text{-}\pi}(H)\frac{1}{wL} = -j_0\frac{\cos(\phi_0) - \cos(\phi_0 - (H + M_0))}{2(H + M_0)} - j_\pi\frac{\cos(\phi_0 + (H + M_\pi)) - \cos(\phi_0)}{2(H + M_\pi)},$$

where $\phi_0$ is an arbitrary initial phase. The phase-field relation for maximum $I_c$ is reached for

$$\phi_0 = \arctan\left[\frac{j_\pi(H + M_0)\sin(H + M_\pi) - j_0(H + M_\pi)\sin(H + M_0)}{2(H + M_0)j_\pi\sin^2\left(\frac{H+M_\pi}{2}\right) + 2(H + M_\pi)j_0\sin^2\left(\frac{H+M_0}{2}\right)}\right].$$

Fig. 7.9 depicts the effect of non-zero, single domain magnetizations $M_0$, $M_\pi$ and different $j_c^0$, $j_c^\pi$ on the magnetic diffraction pattern $I_c^{0\text{-}\pi}(H)$ (asymmetry: $j_c^\pi/j_c^0 =$

$\Delta = 1 - 2\delta$).
• An asymmetry in critical current density $j_c^0 \neq j_c^\pi$ (dots) and $M_0 = M_\pi = 0$ lifts the central minimum upward and at the same time decreases (increases) the maxima, depending on $j_c^\pi / j_c^0 < (>) 1$.
• The effect of finite $M_0$, $M_\pi$ is depicted by the triangles. In case of the same magnetization $M_0 = M_\pi$ the $I_c(H)$ dependence is just shifted along the $H$-axis.
• If the remanent net magnetization differs in 0 and $\pi$ parts $M_0 \neq M_\pi$ and $j_c^\pi = j_c^0$, the $I_c^{0\text{-}\pi}(H)$ is shifted by $(M_0 + M_\pi)/2$, but the maxima are symmetric (have the same height). The first minima get *bumped* from the bottom and may even disappear for large difference in $M$.
• For $j_c^0 \neq j_c^\pi$ and $M_0 \neq M_\pi$ the diffraction pattern is not only shifted, the central minimum near zero field is lifted up, the side-minima lay about zero, but also the maxima become asymmetric.

During cooling down in one of the JJs sometimes some flux was trapped, which I associate with rearrangement of the domains in the F-layer. This events were quite rare, approximately 1 event in 10 hours. The $I_c(H)$ was suddenly shifting along $H$-axis by some value.

### 7.3.4 Discussion of experimental $I_c^{0\text{-}\pi}(H)$

All characteristic features of $I_c^{0\text{-}\pi}(H)$ dependence can be described by theory with the accuracy of few percent, although there are some discrepancies between simple SJJ theory and experiment, depicted in Fig. 7.6 and Fig. 7.10:

- In the experiment the minimum of $I_c^{0\text{-}\pi}(H)$ dependence was somewhat shifted along the field axis and the relative value of $I_c^{0\text{-}\pi}/I_c^0 \approx 0.16$. Thus, the minimum was not completely vanishing.

- The critical current at the side maxima $I_c^{0\text{-}\pi}(-H_m)/I_c^0 \approx 0.66$ and $I_c^{0\text{-}\pi}(+H_m)/I_c^0 \approx 0.64$ were below the theoretical value of 0.72 and were somewhat different.

- The first side minima of $I_c^{0\text{-}\pi}(H)$ were reached at the same magnetic field ($\Phi_\Sigma/\Phi_0 = \pm 2$) as the second minima of $I_c(H)$ for 0 or $\pi$ JJ, but it looked like bumped from the bottom and did not really reach zero.

All these effects can be explained and reproduced numerically by taking into account several deviations from the ideal short 0–$\pi$ Josephson junction model.

#### Asymmetry in critical current density

As shown in the preceding Section, for asymmetry in the critical current density $j_c^\pi = j_c^0(1 - 2\delta) \neq j_c^0$, instead of the curve (3.4), one will still get a symmetric magnetic diffraction pattern (SJJ model) for 0–$\pi$ JJ, but the minimum at zero field is $I_c^{0\text{-}\pi}(0)/I_c^0 = \delta$, and both maxima $I_c^{0\text{-}\pi}(\pm H_m)$ decrease below 0.72. In my experiments the asymmetry $\delta$ could be calculated from $I_c$ of 0 and $\pi$ reference junction as: $\delta \approx 1\%$. However, the *real* $j_c^{0,\pi}$ in the 0–$\pi$ JJ might differ a bit from the $j_c$ calculated from the reference junctions.

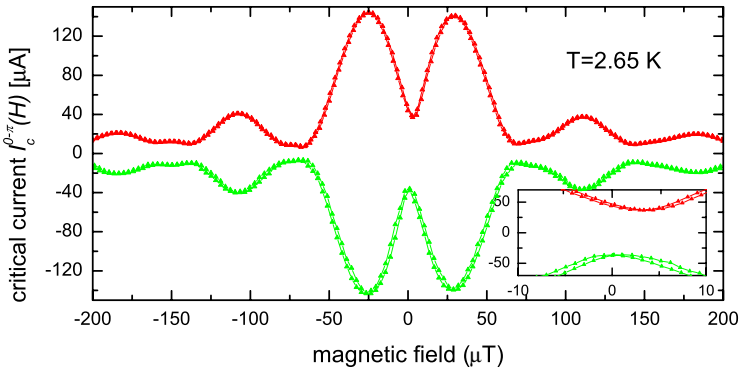


Figure 7.10: *$I_c(H)$ pattern of 0–$\pi$ JJ for both current polarities, measured at* 2.65 K. *The inset depicts the region around $H = 0$.*

#### Net magnetization of the F-layer

If in addition some weak net magnetization of the F-layer is assumed, such that $M_0$ is not equal to $M_\pi$, the $I_c^{0\text{-}\pi}(H)$ dependence is shifted along $H$ axis by $(M_0 + M_\pi)/2$.

Only if *both* components, i.e. the asymmetry in critical current density and a finite, but different magnetization in 0 and $\pi$ parts, are included at the same time, the $I_c^{0\text{-}\pi}(H)$ curve will get asymmetric maxima and characteristic bumps at the first side minima as observed in experiment.

### 7.3.5 Increase of minimum in $I_c^{0\text{-}\pi}(H)$

The value of $I_c^{0\text{-}\pi}(H)$ at the central minimum was also affected by the finite length of the junction $\ell \approx 1.3$. The deviations from the short junction model increased the critical current $I_c^{0\text{-}\pi}(H)$ at the central minimum, as plotted in Fig. 3.3 (b+c).

According to numerical simulation the minimum of $I_c^{0\text{-}\pi}(H)$ is formed by intersection of the two brunches (with positive and negative spontaneous flux) and should look like a cusp-like minimum. However, in experiment the minimum looked like parabolic, see the inset of Fig. 7.10. This can be due to noise in the magnetic field. Under the assumption of that the rounding at the bottom is caused by noise, the real value of $I_c^{0\text{-}\pi}(0)$ should be obtained by linearly extrapolating the $I_c^{0\text{-}\pi}(H)$ pattern near the minimum towards $H = 0$, which yields $I_c^{0\text{-}\pi}(0)/I_c^0 \approx 0.1$ instead of 0.16. However, carefully measurements using superconducting magnetic coils in persistent mode to exclude any magnetic field noise showed no further decrease of the minimum, see Fig. 7.10.

Another explanation is that the magnetic moments in the F-layer were re-orientated during $I_c(H)$ measurements, and the non-uniform intrinsic magnetization lifted the absolute minimum to the measured value of $I_c^{0\text{-}\pi}/I_c^0 \approx 0.16$.

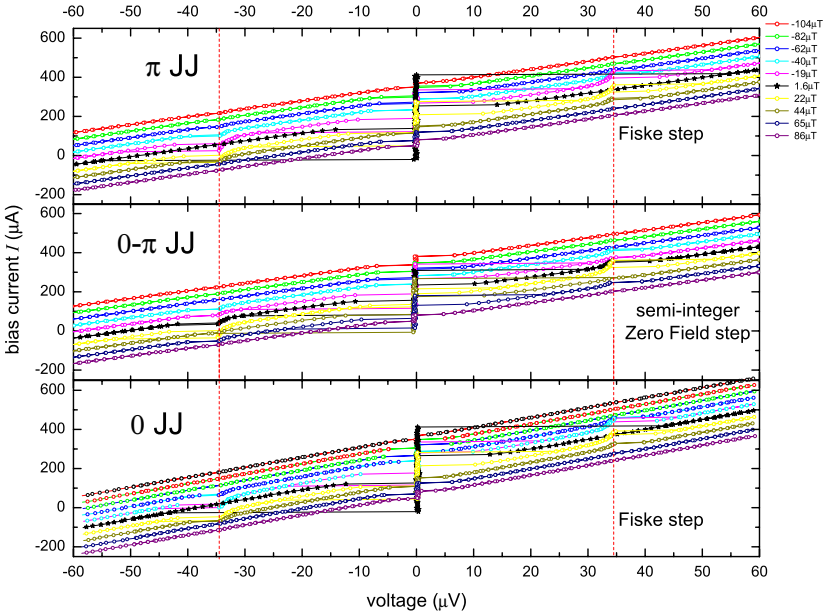


Figure 7.11: *Experimentally measured Fiske step (0,π JJs) and semi-integer ZFS (0–π JJ) on the IVCs, measured at* 2.6 K. *Curves have been offset vertically.*

## 7.4 Zero Field steps in 0–π and 0, π JJs

As pointed out in Chapter 3.4.1 one should observe semi-integer ZFS on the IVC of the 0–π JJ in case of not too strong damping and moderate length of junction, so that the fractional flux can still hop over this distance. Under the assumption that the flux in 0–π JJ is transferred with the same maximum velocity as in the reference 0 and π JJs, it should appear at the same voltages as the Fiske steps in magnetic field for the flat phase junctions.

In experiment, shown in Fig. 7.11, the 0 and π reference junctions showed resonance steps in the I-V characteristics at ±34 $\mu$V if a magnetic field was applied, but not in zero field (black line). The Zero Field Step appeared at 65 $\mu$V $\approx 2 \cdot V_{FS}$ for all three junctions (not depicted on the figure). The 0–π junctions even had in zero magnetic field a resonance step. I conclude that this is a semi-integer Zero Field Step, similar to those observed by Goldobin *et al.* [95]. The experimental confirmation of the existence of semi-integer ZFSs indicates the hopping of semifluxons. Thus, the presence of a magnetic vortex at the 0–π phase boundary was clearly indicated. Note, that the formation of *spontaneous* flux at $I = 0$ was not proved by the presence of semi-integer ZFSs, as the bias current could provoke a magnetic flux inside the asymmetric 0–π JJ. The voltage of the Fiske steps was in good agreement with Fiske step measurements on SINFS JJs with same junction geometry and oxide barrier.

# Part III

# Appendix

# Appendix A

# LTSEM measurements on SIFS junctions

Scanning electron microscopy (SEM) represents a powerful imaging tool for studying spatial structures in condensed matter [164]. A focused electron beam is scanned over the surface of an object and simultaneously an appropriate response signal (e.g. the emission of secondary electrons or a voltage change) generated by the electron beam irradiation is recorded. A 2d image of the surface topography is then obtained by synchronously displaying the response signal. It has become a standard technique for investigating objects kept at room temperature.

Low Temperature Scanning Electron Microscopy (LTSEM), designed at the University of Tübingen, allows one to investigate physical phenomena in superconducting thin film samples with a spatial resolution of about 2 $\mu$m. The low temperature stage used in this set-up is formed by a conventional He bath cryostat located outside of the specimen chamber of the SEM and surrounded by a liquid nitrogen tank for precooling and thermal shielding.

The basic elements of the LTSEM are shown in Fig. A.1. The sample (e.g. a Josephson junction) is mounted on a temperature controlled low-temperature stage

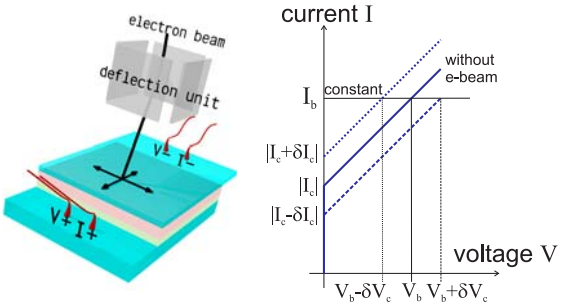


Figure A.1: *Left: Schematic overview of the Low Temperature Scanning Electron Microscopy (LTSEM) of Josephson tunnel junctions. The e-beam changes properties of the superconductors: origin of the spatial structures in resistively biased tunnel junctions. Right: change of IVC under e-beam radiation.*

of SEM in such a way that its surface can be directly scanned by the electron beam. The back of the sample is mounted in good thermal contact with a thermal reservoir kept at 4.2 K or lower. While scanning the sample surface with an electron beam, the junction is heated locally, resulting in a change of the local resistance. Simultaneously applying a constant bias current $I_b$ sets the junction to the voltage state with voltage $V_b$. This *local* change of resistance (proportional to the Josephson current) leads to a *global variation* of the voltage, which is detected by Lock-In technique at each point and plotted in a 2d picture. The electron beam induced change of the tunneling current can be expressed as [94]

$$\delta I_c(x,y) = \delta I_J(x,y) + \delta I_\phi(x,y)$$

where (x,y) is the position of the focused electron beam on the sample surface. $\delta I_J(x,y)$ is the local change of the maximum tunneling current density and $\delta I_\phi(x,y)$ is the change of tunneling current induced by the change of local phase difference, respectively. A positive change of the voltage $V_b + \delta V_c$, caused by a lower critical current $|I_c - \delta I_c|$ is depicted dark, whereas a reduction of voltage $V_b - \delta V_c$, i.e. a higher critical current $|I_c + \delta I_c|$, is depicted in white. The background (zero voltage change) signal is gray. A review of LTSEM was given by R. Gross and D. Kölle [94]. Details about the actual set-up and detection technique are given in the Ph.D. thesis of D. Doenitz [165].

LTSEM[1] was used twofold: for imaging of the current distributions over the tunnel barrier in SIFS and SINFS junctions and for studying the interaction between the local magnetic configuration and the external magnetic fields with respect to the current transport. As ferromagnetic interlayer $Ni_{60}Cu_{40}$ was used.

Unless otherwise noted, all junctions discussed in this Chapter are in the short Josephson limit, i.e. $\lambda_J \leq 1$.

## A.1 LTSEM on SIFS junctions

The first LTSEM measurements were performed on square shaped SIFS junctions ($d_F \approx 5.0$ nm, 0 coupled) with an area of $100 \times 100\,\mu\text{m}^2$. The junctions were cooled down in zero magnetic field. A SEM picture is shown in Fig. A.2(a). The cap electrode is light-colored and the bottom electrode dark. The junction (dashed line) was patterned in overlap geometry with idle region of $\approx 10\,\mu$m width.

The Fraunhofer pattern of sample A (cf. bottom of Fig. A.2(b)) was nearly symmetric, apart from the asymmetric side-maxima. Trapping of magnetic flux and/or roughness of the F-layer or tunnel barrier might be the reason. In the voltage image of the junction several inhomogeneities could be seen. Light-colored areas had a weaker voltage signal and thus less transport current. The dark colored areas had a concentration of supercurrent, probably due to a thinner F-layer in this region. The heating by the electron beam suppressed much of the total supercurrent and the voltage signal for this region was larger.

The sample B, see Fig. A.2(c), showed even larger inhomogeneities in the voltage image. Both samples were fabricated in the same run and were next to each other on

[1]LTSEM was performed in cooperation with D. Doenitz at the Universität Tübingen.

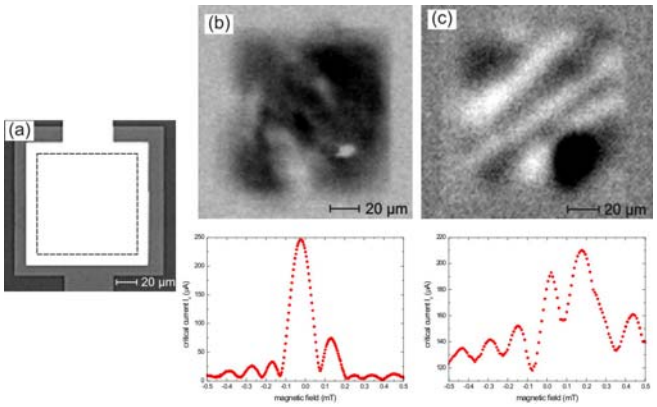


Figure A.2: *SIFS junctions: (a) SEM picture, dashed line denotes junction, (b) sample A: LTSEM voltage image of SIFS JJ in zero magnetic field, (c) sample B: black spot in bottom right corner denotes electric short. Bottom row:* $I_c(H)$ *pattern of the junction above. Sample A and B have F-layer thickness* $d_F \approx 5.0$ nm. *Data from [165].*

the chip. The magnetic diffraction pattern of the sample B deviated strongly from the ideal one, as a central peak and a clear minimum were absent.

The voltage image of sample B showed, apart from the electric short in the right corner, a diagonal pattern with alternating positive and negative voltage signal (lower or higher $I_c$), which corresponded to positive and negative directions of the current-flow. I assume that the effective magnetic field was not vanishing and the magnetic form anisotropy turns the remanent magnetization along the diagonal direction of the junction. Thus, the voltage picture showed the Josephson current under an internal magnetic field. The electric short was probably caused by some roughness of the F-layer, like the inhomogeneities in sample A. The location of the black spot was independent from the applied magnetic field, and probably caused the offset in $I_c(H)$ pattern of the sample B.

Interestingly, the sample A and B had the same order of magnitude of the critical current. SIS junctions with an electric short in the tunnel barrier had a strong asymmetric $I_c(H)$, similar to the one from sample B, but usually had much larger critical currents and large scattering of amplitudes.

In summary, the LTSEM voltage images from SIFS junctions showed an inhomogeneous current transport over the F/I double layer, which confirmed earlier results, see Chapter 6 for details. The diagonal pattern in one sample might be caused by a remanent magnetization along the diagonal direction.

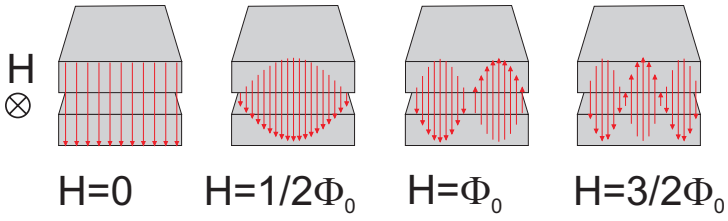


Figure A.3: *Modulation of* $j_c(x) = j_c \sin\left(\frac{2\pi}{\Phi_0}\Lambda\mu_0 Hx + \phi_0\right)$ *(red) for different magnetic fields (H) through JJ.*

## A.2 SIFS JJ with very thin F-layer in magnetic field

LTSEM imagines were obtained for a square shaped SIFS junction of 100 $\mu$m length, F-layer thickness $d_F = 2.8$ nm and Josephson penetration depth $\lambda_J = 66$ $\mu$m, too. The JJ was still of intermediate length $L/\lambda_J < 2$ and the magnetic field penetrated completely. This junction exhibited a symmetric magnetic field dependence of $I_c$ when measured in a liquid Helium dewar (depicted in Fig. A.4). The very thin F-layer (same order of magnitude as the dead magnetic layer thickness $d_F^{\text{dead}}$) ensured a homogeneous current transport despite the unfavorable SIFS stack.[2] However, when measured inside the LTSEM set-up a weak link in the Nb top-wiring near the junction edge appeared for bias currents larger than $I = 2$ mA. This prevented tracing out the complete magnetic field dependence, as the large critical current for small magnetic fields could not be measured correctly. I attribute the appearance of the weak link to the reduced thermal cooling power inside the LTSEM set-up. Thus, only voltage images taken at larger magnetic fields with bias currents below 2 mA were recorded, see Fig. A.4. The effect of an external magnetic field applied in-plane and along the junction axis is clearly seen.

The external magnetic field caused a constant gradient of the Josephson phase $\phi$ along the junction. This caused a sinusoidal modulation of the Josephson current density $j_c(x) = j_c \sin\left(\frac{2\pi}{\Phi_0}\Lambda\mu_0 Hx + \phi_0\right)$, resulting in the so-called vortex state of the junction. The evolution of the vortex state with increasing magnetic field is shown in Fig. A.3. The experimental results (Fig. A.4) agree well with theoretical expectations. A weak background field or a slight tilt of the sample versus the magnetic field caused the minor twist of the modulated voltage.

## A.3 Elliptical and circular SINFS JJs

The influence of the junction geometry onto the supercurrent transport was studied on the optimized SINFS-type junctions with $d_F \approx 5.1$ nm (still 0 coupled)

[2] Note that the $I_c(H)$ pattern of an SIFS junction with $d_F = 2.0$ nm is symmetric too, see Chap. 6.

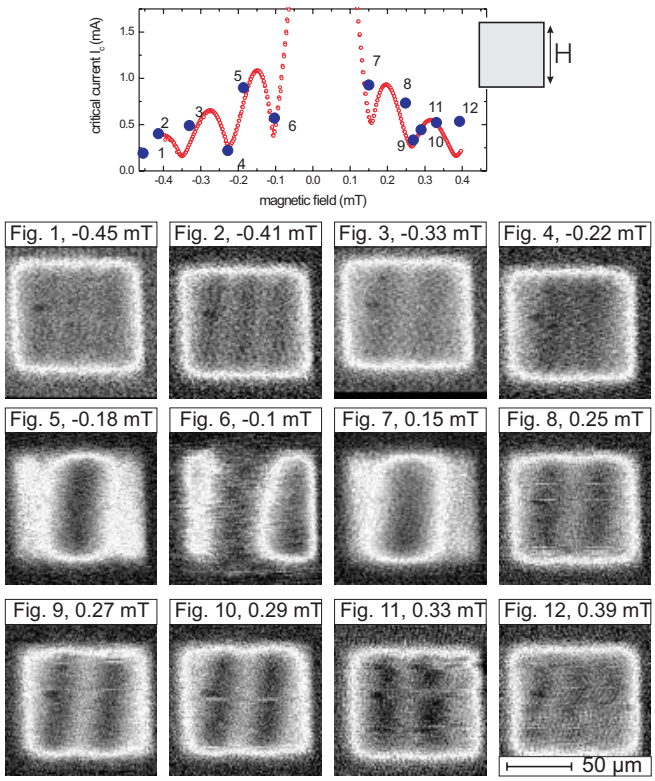


Figure A.4: *Imaging the spatial distribution of the Josephson current density in an SIFS tunnel junction with thin F-layer ($d_F$ = 2.8 nm) at different magnetic fields applied in-plane and along the vertical junction axis.*

The magnetization is in-plane for all thin ferromagnetic films due to the form-anisotropy [130]. An elliptical shaped JJ has two magnetic axis, a *hard* one (long axis) and a *weak* one (short axis). To minimize the stray fields the overall magnetization tends to be parallel to the magnetic hard axis. On the contrary a circular shaped JJ has no such magnetic hard or weak axis. Minimization of stray fields should lead to the formation of magnetic domains and domain walls, where the local magnetization is twisted from one domain state to another. The ideal magnetic circular junction with no net magnetic stray field tends to form a large domain wall in the middle of the junction, as was confirmed by simulations using OOMMF computer code [166] (not shown).

Both junctions (elliptical and circular) studied here were in the short Josephson limit. The Helium-dewar attached to the back of the sample was pumped during the experiments and the sample temperature was below 4.2 K, as can be determined from the I-V characteristic (not shown). Hence the voltage drop was larger and the signal to noise ratio of the measured differential voltage was increased compared to the measurements presented before, when the dewar was not-pumped and the bath

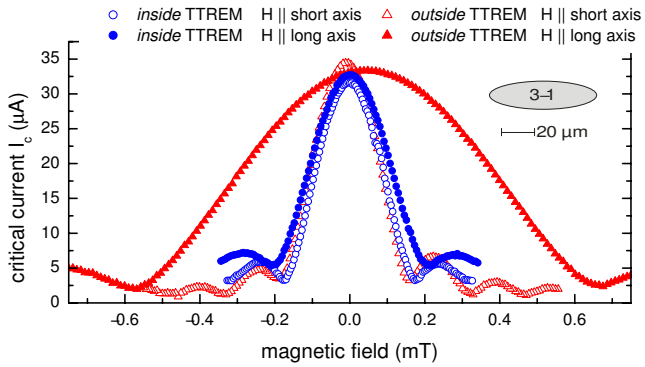


Figure A.5: *Magnetic field dependence of the elliptical shaped junction (sample 3-1) measured inside LTSEM (circle) and reference measurements in better shielded liquid* He *dewar (triangle). Full symbols represent $I_c(H)$ with $H$ parallel to long axis of the ellipse, open symbols $I_c(H)$ with $H$ parallel to short axis. The inset shows the scheme of the junction geometry. Data from [165].*

temperature was higher. More details can be found in [165].

### A.3.1 Elliptical junction

The elliptical SINFS junction, sample 3-1, had an area of 1000 $\mu$m$^2$ with 64 $\mu$m axis length for long and 20 $\mu$m for short axis.

The oscillation period of $I_c(H)$ should be reciprocally proportional to the junction length perpendicular to the magnetic field direction. Thus, one expects for the elliptical sample 3-1 an oscillation period for the magnetic field parallel to the long axis which is three times larger than for the magnetic field along the short axis. Measurements in a shielded liquid He dewar at Forschungszentrum Jülich, cf. Fig. A.5, of this junction showed indeed a clear correlation between period of $I_c(H)$ and the cross section of the junction normal to the magnetic field. However, inside the LTSEM set-up the $I_c(H)$ pattern for the magnetic field parallel to the long axis had just a 20% larger oscillation period than for the magnetic field along the short axis. Various reasons like magnetic background stray fields, remanent magnetization in the F-layer, field focussing effect by asymmetric superconducting electrodes and inhomogeneous magnetic fields or Abrikosov vortices could be attributed, see [165] for details. A tilt between the magnetic field and the samples could be excluded, as the electron beam, which is sensitive to the magnetic field via Lorentz force, indicated a good alignment of the sample and field.

• $H$ parallel short axis: The voltage images for the magnetic fields along the short axis are depicted in Fig. A.6. At zero field the voltage signal was nearly uniform and positive. Hence, the current transport was very homogeneous in these SINFS junctions, as pointed out earlier. Like the SIFS junction with thin F-layer (Fig. A.4) the experimental results of this sample were in good agreement with the theoretical expectations for short Josephson junctions. For example, at the first

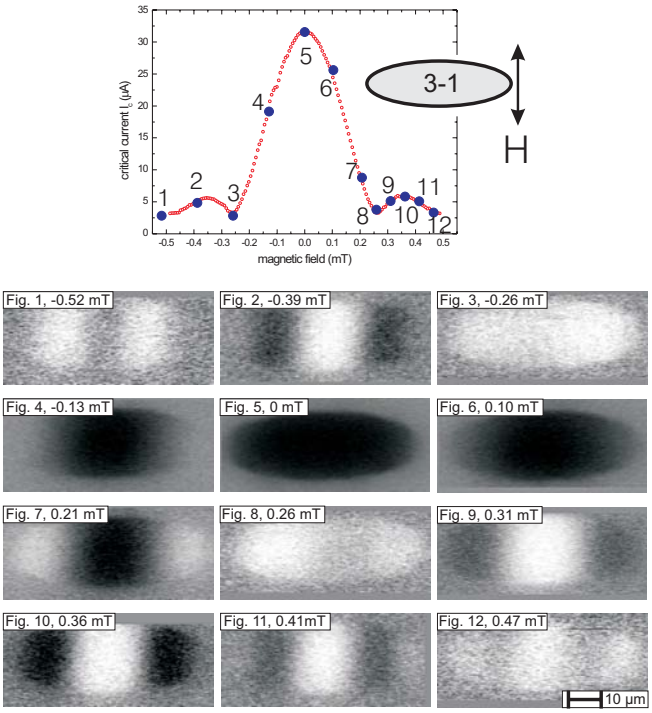


Figure A.6: *Elliptical shaped junction (sample 3-1) with magnetic field along the short axis of junction. Data from [165].*

side-maxima (Fig. 2, 10) three half-sine periods (positive change of voltage, negative change, positive change) are visible. Note that for the minima (Fig. 1, 3, 8, 12) exist several configurations of the phase. The system changed under the electron beam by reducing the voltage, as the beam was not a small change anymore and it moved to higher $I_c$.

• $H$ parallel long axis: The voltage images for magnetic fields along the long axis are shown in Fig. A.7. Like the results obtained for magnetic field parallel to the short axis (Fig. A.6) the modulation of the Josephson sine was perpendicular to the field axis, but the field was tilted. The direction of the tilt was not constant, but independent from the direction of the applied magnetic field. The tilt was consistent with the unexpected large oscillation period in the $I_c(H)$ pattern. If the magnetic field through the junction was perpendicular to the modulation of the Josephson sine, the *effective* length of the junction for the magnetic oscillation length was somewhat shorter than the length along the long axis. However, more experiments are necessary to explain this peculiar behavior of $I_c(H)$.

No indications for the presence of magnetic domains or domains walls can be determined for both directions of the magnetic field. Maybe the changes in local magnetization were smaller than the resolution size of 2 $\mu$m.

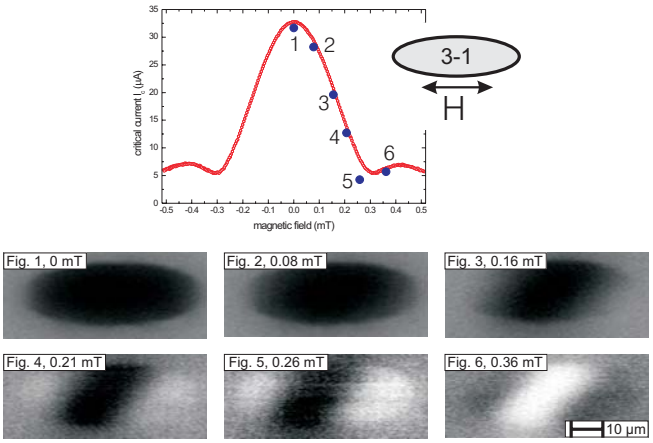


Figure A.7: *Elliptical shaped junction (sample 3-1) with magnetic field along the long axis. Data from [165].*

### A.3.2 Circular junction

The circular shaped SINFS junction, sample 3-3, had an area of 1000 $\mu$m$^2$ with a radius of 18 $\mu$m. It was located next to the elliptical junction (presented before) on the same chip.

• $H$ parallel vertical axis: The voltage images obtained for magnetic fields along vertical axis are depicted in Fig. A.8. The vertical axis corresponds to the short axis of the elliptical junction. The small diameter of the junction led to a rather large magnetic oscillation period, thus the $I_c(H)$ pattern could only be measured up to the first minimum, due to limitations of the current source for the generation of magnetic field. Analog to the elliptical sample 3-1 the voltage image was very uniform for zero field and showed modulations of the Josephson sine with increasing magnetic field. At the minima of $I_c(H)$, see Fig. 8, the electron beam reduced the negative current, hence the overall $I_c$ was increased and the voltage signal was negative for all parts of the junction.

• $H$ parallel horizontal axis: The voltage images for the magnetic fields along the horizontal axis are shown in Fig. A.9. Like for the elliptical junctions the magnetic oscillation period deviated from the expected one, although in this case the sample was even spatially isotropic. Reference measurements for both axis length in a shielded liquid He dewar at Forschungszentrum Jülich indicated the same oscillation period. The voltage images showed, like for the elliptical junction, a tilt of the Josephson sine. The tilt depended on the strength of the magnetic field. Again no indications for the presence of magnetic domains were found. More experiments are necessary to determine the origin of the tilt.

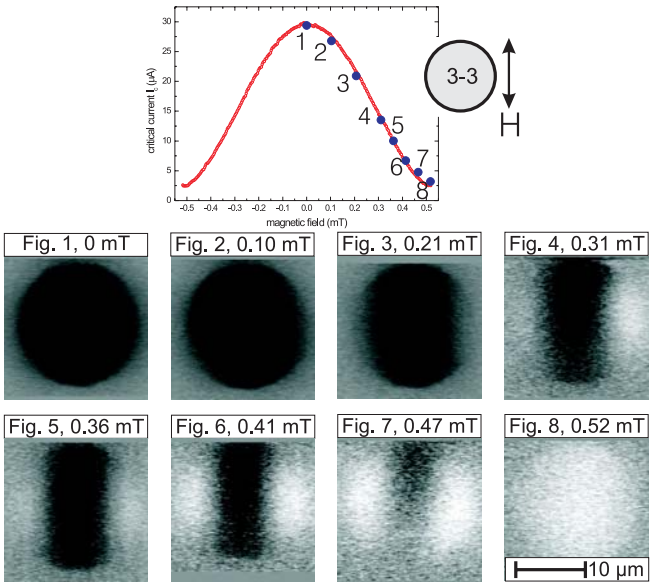


Figure A.8: *Circular junction (sample 3-3) with magnetic field along vertical axis. Data from [165].*

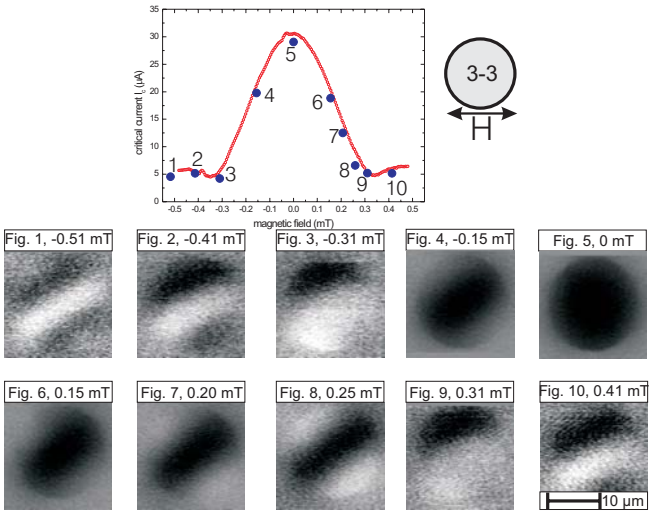


Figure A.9: *Circular shaped junction (sample 3-2) with magnetic field along the horizontal axis. Data from [165].*

# Appendix B

# Quantum states of $\pi$ junction

For more than two decades has been a growing interest in *macroscopic* quantum effects in Josephson junction. One of the motivations was to test if the laws of quantum mechanics also apply in macroscopic systems. In single junctions the degree of freedom is the phase difference of the superconducting order parameter across a junction. Several quantum phenomena, such as macroscopic quantum tunneling (MQT) [41, 167], microwave spectroscopy [42] and resonance tunneling [168] were demonstrated. For the use of Josephson junctions as qubits the experimental milestones are the observation of quantum superpositions of macroscopically distinct states, as done recently on a variety of Josephson junctions [12, 84, 169].

In this Chapter the escape rate and microwave spectroscopy measurements on a Josephson tunnel junction with a ferromagnetic layer are presented.[1] This $\pi$ coupled SIFS[2] Josephson junction was fabricated for this thesis and is from sample 2, presented in Chap. 6.5. To my knowledge, there are no reports about escape rate and spectroscopy measurements on a Josephson junction with a ferromagnetic interlayer up to now.

The thickness of the F-layer is $d_F = 5.43$ nm, the junction is square shaped with an area of $100 \times 100$ $\mu$m$^2$ and has a low very critical current density of (8.4 $\mu$A/cm$^2$ at 4.2 K) to avoid current heating effects. The Josephson penetration depth $\lambda_J$ is about 1000 $\mu$m, hence the junction is in the SJJ limit.

The experiments were done in a home made $^3$He/$^4$He dilution refrigerator, which provides a base temperature of about 40 mK. A description of the experimental set-up and the calculations is given in the recent Diploma thesis from S. Beutner [170, and references therein]. The data and results from the latest measurements after further improvement of the set-up were submitted recently [171].

## B.1 $\pi$ JJ in low temperature limit

The I-V characteristics of the junction measured at 41 mK and 4.2 K are plotted in Fig. B.1. At low temperatures the junction was strongly underdamped, $\beta_c \approx 15.000$, and exhibited a high quality factor $Q = \omega_p RC = 123$. For large bias currents

[1] The measurements have been performed by Karl Madek and Sven Beutner at Walther-Meissner-Institut, Garching.

[2] Actually it is SINFS-like, but the N-layer has just a structural function.

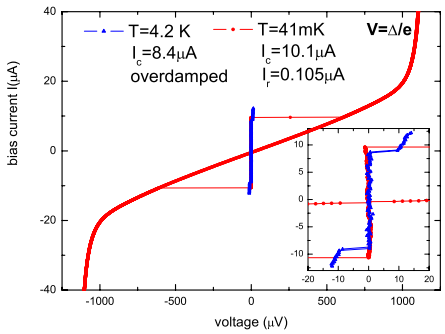


Figure B.1: *I-V characteristics of $\pi$ SIFS junctions ($d_F$ = 5.43 nm) at standard and millikelvin temperatures. The inset depicts the low leakage current for the* T = 41 mK *regime.*

($>$ 20 $\mu$A) the Cooper-pair density at the tunnel barrier, induced from the top-electrode through the F-layer can be neglected due to the strong leakage current in the F-layer. This means the stack was SIFN-type like for large currents. Thus, the voltage across the junction approached asymptotically the gap of the bottom Nb-layer: $\Delta \geq 1.1$ mV. The critical current changed slightly from 8.4 $\mu$A at 4.2K to 10.1 $\mu$A at 41 mK. Note that this IVC was measured after the escape measurements described below and with a different computer card. For these measurements the critical current was determined as $I_c \approx 13.9$ $\mu$A. A trapping of flux just before the measurement of IVC may explain the reduction of critical current. Up to now no magnetic field dependence could be measured, therefore the presence of some magnetic flux could not be detected. However, the high quality factor $Q$ and the asymptotic approach toward the gap-voltage for large bias currents hold independent of the presence of a trapped magnetic flux.

### B.1.1 Current ramp experiments

In a temperature range starting at 1.05 K down to 39 mK the distribution of the switching current $I_{sw}$ was determined. The important parameters were the mean switching current $\overline{I_{sw}}$ and the standard deviation $\sigma$, which are correlated with the position of the center and the width of the histogram. Fig. B.2 shows the switching current distribution for different temperatures. Premature switching to the voltage state led to a broadening of the peaks in the histogram and the position of the mean switching current decreased with increasing temperature. For the calculation of the escape rate and the fluctuation-free critical current $I_{c0}$ the plasma frequency $\omega_{p0}$, switching probability $P(I)$ and current ramping speed $dI/dt$ were necessary. Details of the calculation are explained in Ref. [170].

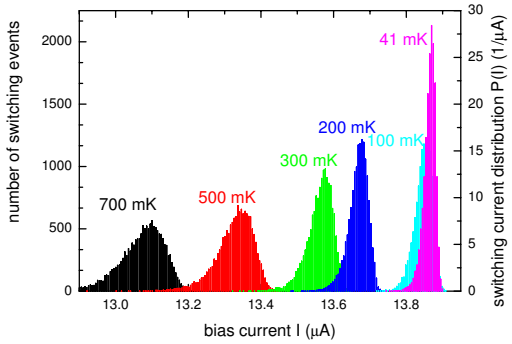


Figure B.2: *Evolution of the switching current distribution for different temperatures. Data from [170].*

## B.2 Escape temperature measurements

The escape temperature $T_{esc}$ was calculated for each temperature $T_{\mathrm{bath}}$, as described by Martinis *et al.* [41]. Similar to the temperature independence of the escape temperature below the crossover temperature $T^*$, the relative width $\sigma/\overline{I_{sw}}$ became minimal for $T < T^*$, when macroscopic quantum tunneling was the dominating escape process.

In the experiment neither the calculated escape temperature $T_{\mathrm{esc}}$ (Fig. B.3) became independent of the bath temperature, nor the standard deviation $\sigma$ set to a constant level (Fig. B.3) as the temperature $T_{\mathrm{bath}}$ dropped. Thus, macroscopic quantum tunneling was not assured in this junction. For temperatures below 250 mK the small change in the slope can be explained by an intermediate state which was observable for temperatures $1.4T^* < T < 3T^*$, cf. Ref. [41]. Indeed, the crossover temperature determined by microwave spectroscopy was calculated as $T^* = 31.0$ mK, which was 8 mK below the base temperature of the set-up. Future experiments will be performed in a cryostat with a lower base temperature to observe macroscopic quantum tunneling from the ground state and the first excited state.

## B.3 Microwave spectroscopy

In the Stewart-McCumber model [33, 34] the current-biased short Josephson junction is modeled as a particle of mass $m$ moving in an external, tilted washboard potential $U(\phi)$, as shown in Fig. 1.5 and in the top part of Fig. B.4. The phase difference $\phi$ across the junction represents the position of the particle.

The quantization of energy of the phase particle in the tilted washboard potential enables excitations to higher energy levels by applying microwaves with suitable frequencies $\nu_{rf}$ and powers $P_{rf}$ at the Josephson junction. Meanwhile the bias current is swept at a constant rate $dI/dt$ from zero until a voltage step occurred at the switching current $I_{sw}$. The bias current $I$ tilts the washboard potential, which causes a change of the energy level spacing. If the energy of the microwave photons

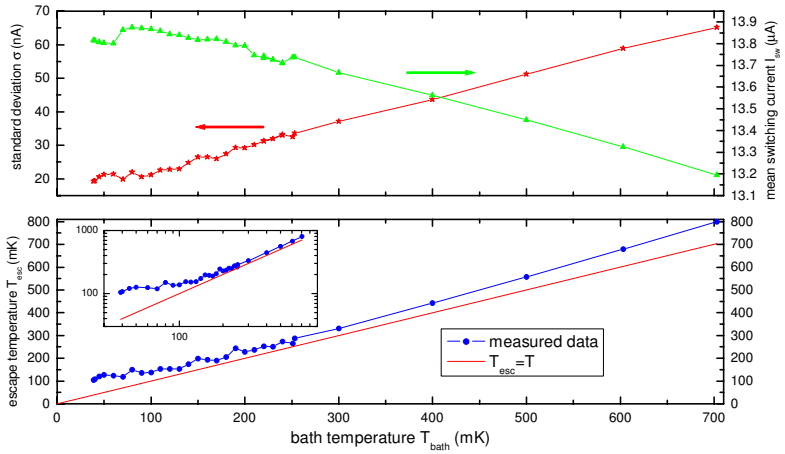


Figure B.3: *Top: Standard deviation $\sigma$ and $\overline{I_{sw}}$ versus the bath temperature. Bottom: Temperature dependence of the escape temperature $T_{esc}$ for $\pi$ SIFS junction. The inset has a log-log-scale. Data from [170].*

$E_{rf} = \hbar\omega_{rf} = \hbar 2\pi\nu_{rf}$ fits to an energy distance between two levels, the phase particle is excited to higher levels.
For suitable microwaves a double peak occurred in the switching current distribution, which was also observable in the time trace of the switching current, see the inset in the bottom part of Fig. B.4. This second peak occurred at a lower bias current and is designated as *resonance excited state*, i.e. the bias current is the *resonance current* $I_{res}$. The escape of a current-biased $\pi$ Josephson tunnel junction from the zero-voltage state in presence of a weak microwave radiation was investigated experimentally at 50 mK.

#### Multiphoton transition

In the parabolic approximation the energy level separation in a short Josephson junction is expected to scale with the applied bias current as $\Delta E = \hbar\omega_{p0}\left(1-(I/I_{c0})^2\right)^{1/4}$. Resonances with the externally applied microwaves appear for $n\nu_{rf} = \Delta E/(\hbar 2\pi)$, where $n$ is the number of photons absorbed in the transition between two energy levels.

### B.3.1 Spectroscopic determination of $\omega_{p0}$, $I_{c0}$ and $C$

The microwave spectroscopy was performed at very low temperatures of 50 mK. While applying microwaves in the frequency range between 1 and 10 GHz to the sample the switching current distribution was monitored. Meanwhile the microwave power was increased from low values up to higher values until the excited level became substantially populated and the switching current distribution became double peaked, as depicted on the inset of the bottom part of Fig. B.4.

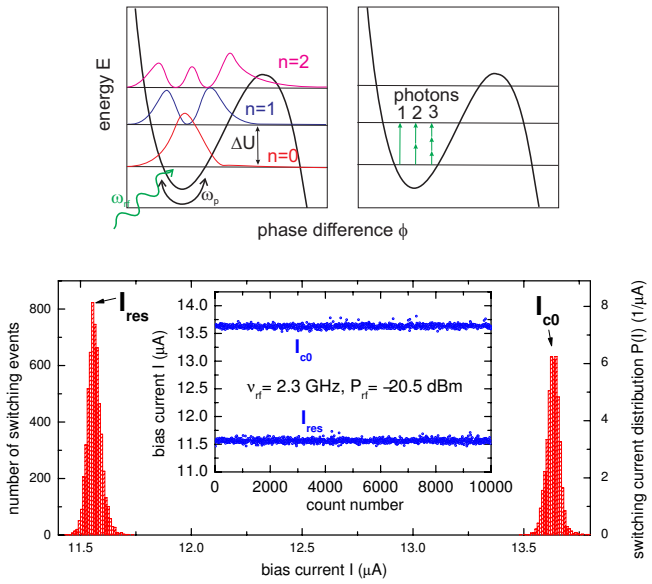


Figure B.4: *Top: Energy levels, squared wave functions and multiphoton transitions between ground state and the first excited state. Bottom: Double peak in switching current distribution and time trace of the switching current (inset), while microwave* $(\nu_{rf}, P_{rf})$ *was applied. Data from [170].*

The single branches at the top of Fig. B.5 designate the multi-photon transitions with $n$ photons from the ground state. It was clearly observed that the resonances fall into different groups as indicated by the lines, each line corresponded to resonances with a different number $n$ of photons. By multiplying the microwave frequencies with the number of photons $n$ one obtains the one photon curve, as shown on the lower part of Fig. B.5.
In the Fig. B.5 the fitting of all data to

$$\nu_{rf} = \frac{\omega_{p0}}{2\pi}\left(1 - \left(\frac{I}{I_{c0}}\right)^2\right)^{1/4},$$

yielded the plasma frequency $\omega_{p0}/2\pi = 8.31$ GHz, the critical current $I_{c0} = 14.2$ $\mu$A and the capacitance $C = 2\pi I_c/\Phi_0\omega_{p0}^2 = 14.11$ pF.

The critical current $I_{c0}$ estimated from microwave spectroscopy was in very good agreement with the $I_{c0} = 14.18$ $\mu$A, determined from the escape temperature measurements.

The capacitance was a factor of 10 smaller than the usual capacitance reported for SIS junction and similar $Al_2O_3$ barrier thicknesses [172, 173]. The additional normal and ferromagnetic metal layers should not change the capacitance $C$, as they simply form one part of the parallel plates in the condensator structure. The difference in capacitance can be attributed to the influence of the idle region, leading to a change in phase velocity in case of microwave spectroscopy, see Section 4.5.1 for details.

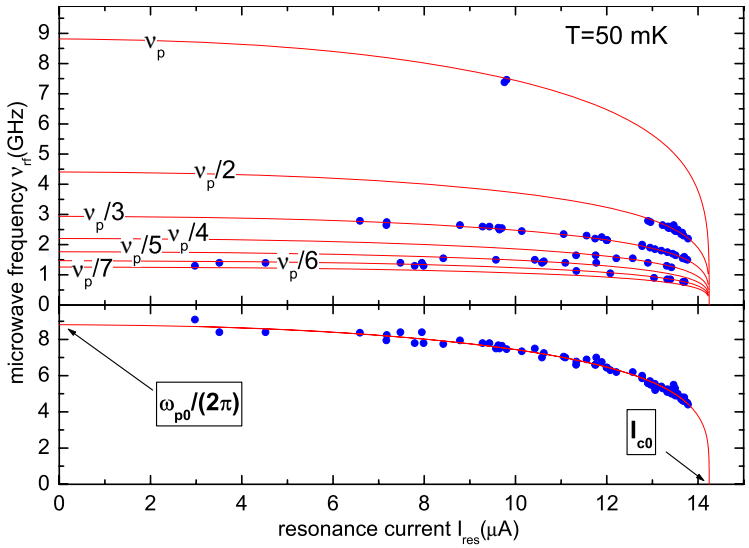


Figure B.5: *Top: Multi photon transition of the phase particle from the ground state to the first energy level. Bottom: multiplied by the number of photons n to obtain the one photon curve. Data from [170].*

# Appendix C

# List of symbols

| Symbol | Description |
|---|---|
| | **Physical constants** |
| $c$ | Speed of light |
| $e$ | Electron charge |
| $\epsilon_0$ | Vacuum permittivity |
| $\hbar$ | Planck constant |
| $k_B$ | Boltzmann constant |
| $m_e$ | Electron mass |
| $\mu_0$ | Vacuum permeability |
| $\mu_B$ | Bohr magnetron |
| $\Phi_0$ | Magnetic flux quantum |
| | **Greek letter symbols** |
| $\alpha$ | Normalized quasiparticle damping coefficient |
| $\beta_c$ | Stewart-McCumber parameter |
| $\gamma$ | Normalized bias current |
| $\gamma_B$ | Interface transparency |
| $\delta$ | degree of asymmetry |
| $\Delta$ | Superconducting energy gap |
| $\Delta d_F$ | Step height in F-layer |
| $\epsilon$ | Dielectric constant; energy of electron-like excitation |
| $\theta$ | Phase of superconductor |
| $\bar{\theta}(x)$ | Order-parameter related component of phase |
| $\lambda_J$ | Josephson penetration depth |
| $\lambda_L$ | London penetration depth |
| $\Lambda$ | Magnetic thickness |
| $\mu$ | Magnetic component of phase |
| $\xi_0$ | Coherence length in superconductor |
| $\xi_F$ | Complex coherence length in F-layer |
| $\xi_{F1}$ | Coherence length in F-layer |
| $\xi_{F2}$ | Oscillation length in F-layer |

| Symbol | Description |
|---|---|
| $\xi_N$ | Characteristic coherence length in N-metal |
| $\xi^*$ | Transparency parameter |
| $\rho$ | Junction resistance per unit length |
| $\rho_0$ | Specific resistance of junction per unit area |
| $\sigma$ | Standard deviation of switching-current distribution |
| $\tau_s$ | Inelastic magnetic scattering time |
| $\phi$ | Superconducting phase difference |
| $\phi_x$ | Magnetic field |
| $\phi_{xx}$ | Supercurrent |
| $\Phi$ | Magnetic flux |
| $\Psi$ | Superconducting macroscopic wave function |
| $\omega_{rf}$ | Microwave frequency |
| $\omega_{p0}$ | Josephson plasma frequency |
| $\Omega$ | Reduced superconducting gap |
| | **Arabic letter symbols** |
| $A$ | Junction area |
| $\overrightarrow{A}$ | Electromagnetic vector potential |
| $\bar{c}_0$ | Swihart velocity |
| $C$ | Total junction capacitance |
| $C^*$ | Specific capacitance of junction |
| $d_F^{\text{dead}}$ | Dead magnetic layer |
| $d_I$ | Tunnel barrier thickness |
| $d_F$ | F-layer thickness |
| $d_F^{0\text{-}\pi}$ | Critical crossover thickness |
| $d'$ | Magnetic thickness |
| $D^{\uparrow,\downarrow}$ | Density of states for electrons |
| $D$ | Diffusion constant |
| $e^*$ | Electron charge in superconductor |
| $E_F$ | Fermi energy |
| $\bar{E}_J$ | Josephson coupling energy |
| $E_{\text{ex}}$ | Exchange energy |
| $h$ | Normalized magnetic field |
| $H$ | Magnetic field |
| $H_{c1}$ | First critical field |
| $I$ | Bias current |
| $\widetilde{I}$ | Exchange integral |
| $I_c$ | Critical current |
| $I_d$ | Displacement current |
| $I_r$ | Return current |
| $I_q$ | Quasiparticle current |
| $I_J$ | Josephson-current |
| $I_{0,2}$ | Amplitude of first and second harmonic term |

| Symbol | Description |
|---|---|
| $dI/dt$ | Bias-current sweep rate |
| $I_{sw}$ | Switching current |
| $j$ | Bias current density |
| $j_c$ | Critical current density |
| $k$ | Complex wave vector |
| $k_F$ | Wave vector at Fermi level |
| $\ell$ | Electron mean free path; normalized junction length |
| $L$ | Length of junction |
| $m_{\mathrm{at}}$ | Magnetic saturation moment |
| $M$ | Magnetization |
| $n_e$ | Electron density |
| $n^{\mathrm{CP}}$ | Cooper pair density |
| $p_{\mathrm{O}_2}$ | Oxidation pressure |
| $P(I)$ | Switching-current probability distribution |
| $q$ | Wave vector of mass momentum |
| $Q$ | Quality factor |
| $R$ | Junction resistance |
| $R_n$ | Normal junction resistance |
| $R_s$ | Subgap junction resistance |
| $t$ | Time |
| $t_{1,2}$ | Bottom and top electrode thickness |
| $T$ | Temperature |
| $T_c$ | Critical temperature of superconductor |
| $T_{\mathrm{C}}$ | Curie temperature |
| $T^*$ | Crossover temperature |
| $T_{\mathrm{esc}}$ | Thermal escape temperature |
| $U$ | Potential for the phase |
| $V$ | Voltage |
| $V_c$ | Characteristic voltage |
| $V_g$ | Gap voltage |
| $V_{\mathrm{n,FS}}$ | Fiske step |
| $V_{\mathrm{n,ZFS}}$ | Zero Field step |
| $V_s$ | Shapiro step in current |
| $v_F$ | Fermi velocity |
| $w$ | Width of junction |
| $x, y, z$ | Spatial coordinates |

# Summary

The aim of this thesis was twofold. Based on the superconductor-insulator-ferromagnet-superconductor (SIFS) technology first $\pi$ coupled and second 0–$\pi$ coupled Josephson junctions have been fabricated and characterized. This involved both experimental and theoretical tasks.

From the experimental point of view, the main challenges were the realization of $\pi$ coupling in SIFS junctions and the precise integration of 0 and $\pi$ coupled parts in a single junction, i.e. a 0–$\pi$ junction. An appropriate material system based on a low $T_c$ superconductor with a relatively high transition temperature $T_c$, an insulating layer which forms a high quality tunnel barrier and a ferromagnetic layer to control the coupling of phase (0 or $\pi$) had to be selected.

The superconducting banks and the barrier were made by Nb and Al-$Al_2O_3$ technology and the ferromagnetic layer was realized by the diluted ferromagnetic NiCu alloy. The patterning was done by optical lithography. The coupling of the ferromagnetic Josephson tunnel junctions was investigated by means of transport measurements. The insertion of a Cu layer between the tunnel barrier and the ferromagnetic layer and a modified patterning process using the SNEAP technique yielded high quality Josephson junctions with low spread of parameters. Hence the multilayer stack became SINFS-type like, where the N-layer has a structural function.

Measurements of the maximum supercurrent of junctions as a function of the externally applied in-plane magnetic field indicated a highly uniform Cooper pair transport over the tunnel barrier and the ferromagnetic layer. The kind of coupling (0 or $\pi$) of the SIFS junctions was found from the dependence of the oscillating critical current density dependence on the F-layer thickness.

The main result was the fabrication of 0–$\pi$ coupled Josephson junctions by a stepped F-layer, where a spontaneously formed magnetic flux $\Phi$ is generated in case of a symmetric 0–$\pi$ SIFS junctions upon zero field cooling below $T_c$. The emergence of the spontaneous flux, which was calculated as 13% of half a flux quantum, was seen in the magnetic field dependence of the current-voltage characteristics of the 0–$\pi$ JJ and the 0 and $\pi$ reference junctions. The experimental data is in excellent quantitative agreement with theoretical expectations. To my knowledge, this is the first underdamped *tunnel* 0-$\pi$ junction based on low-$T_c$ superconductors. It can be measured directly due to its rather high $I_cR$ product.

# Outlook

Both $\pi$ (flat F-layer)and 0–$\pi$ (stepped F-layer) SIFS Josephson junctions offer interesting aspects for future research.

Generally speaking, the SIFS technology offers advantages over the existing $\pi$ and 0–$\pi$ junctions based on d-wave superconductors [22, 93] such as the low dissipation of plasma oscillations, no restrictions in topology and easy integration into the mature $Nb/Al\text{-}Al_2O_3/Nb$ technology.

### $\pi$ Josephson junction

It is highly desirable to use $\pi$ tunnel junctions to substantially improve the parameters of various classical and quantum electronic circuits.

For example, the use of $\pi$ junctions in rapid single flux quantum (RSFQ) logics may significantly reduce the size of the logic cells [11, 162]. The parameter which defines the speed of operation is the product of the critical current and resistance $I_cR$. If proceeding to the quantum regime, a $\pi$ junction may be used to construct a *quiet* flux qubit, which is self-biased and well decoupled from the environment [12]. Again one needs to use junctions with high resistance (to avoid decoherence) and reasonably high critical current density $j_c$ to have the Josephson energy $E_J \propto I_c = j_c \cdot A \gg k_BT$ for junction areas $A$ of a few square microns or below. Likewise, the Josephson plasma frequency $\omega_p \propto \sqrt{j_c}$, which plays the role of an attempt frequency in the quantum tunneling problem, has to be kept at the level of a few GHz.

For future studies of $\pi$ coupling in Josephson junctions the use of ferromagnets in the clean limit was suggested. Recently, some promising publications have appeared on the inversion of coupling realized by classical 3d magnets ($Co, Ni$) and alloys ($Ni_3Al$) in clean limit [70, 83]. However, the short oscillation period is still problematic for the exact determination of the coupling phase and the 0 to $\pi$ crossover thickness, but it may be possible with the precise F-layer wedge technique presented in this thesis.

The presence of domain walls and free magnetic moments in the F-layer may create a noise source for the current transport in SFS/SIFS-type junctions. Tracing out the magnetic field dependence of the critical current $I_c(H)$ rotates the magnetization or changes the size of magnetic domains, which should add some *Barkhausen* noise to the system. Up to now no measurement have been performed on the electric noise in SFS or SIFS junctions.

The 0 or $\pi$ coupled junctions fabricated in this thesis could be integrated into a superconducting ring with an odd number of junctions to prove the coupling by the magnetic field dependence of the critical current, as done in [75, 76].

The presence of higher harmonics in the current-phase relation could be determined. The first harmonic vanishes at the temperature-controlled inversion point of the coupling phase (0 to $\pi$) and the contribution of the second harmonic becomes predominant. An elegant method for the experimental investigation of the current-phase relation is based on the coupling of the junction of interest with an interferometer through a mutual inductance. Details can be found in [87].

Of interest are thermal escape or quantum tunneling and energy level quantization measurements of a single $\pi$ coupled Josephson junction. Such investigations have

already been started [170] and are described in part in Appendix B. The existence of quantized energy levels in the potential at an intermediate state were proved experimentally. The good agreement with the frequency-critical current relation indicates that the theoretical predictions for the Josephson junction potential can also be used to describe the behavior of the potential in SINFS junctions. It is suggested that quantum tunneling dominates the thermal escape at temperatures below 100 mK, if the critical current density is increased to 1 A/cm$^2$, which is a realistic order of magnitude for $\pi$ JJs with thin $Al_2O_3$ barrier.

Density of states (DOS) measurements in 0 and $\pi$ coupled NINFS-type Josephson tunnel junction with ferromagnetic NiCu alloys could be done in analogy to the experiments by Kontos *et al.* [174] using PdNi alloys. The 0 coupled junction should have a DOS with a maximum at the Nb gap edge and a minimum at the Fermi level, whereas for the $\pi$ coupled junctions the DOS is flipped with respect to the normal state.

The interplay of magnetic remanence, junction geometry and current transport through the F-layer could be studied. A remanence of the F-layer should give a hysteretic $I_c(H)$ pattern, and the formation of magnetic domains and walls should modify the coherence lengths of the superconducting order parameter. Details can be found in the theoretical publications [64, 150].

### 0–$\pi$ Josephson junction

There are many open questions concerning the 0–$\pi$ Josephson junctions. These structures allow to study the physics of fractional vortices with a good control of the ratio of symmetry between 0 and $\pi$ parts.

When going from the short to the long junction limit a change in the magnetic diffraction pattern should happen. The dip at zero field should decrease towards a plateau-like $I_c(H)$ pattern for the 0–$\pi$ LJJ. The spontaneous magnetic flux should approach half a flux quantum [15].

The formation of spontaneous flux in the ground state of multiple 0–$\pi$ phase boundaries in a long Josephson junction could be studied [18].

The 0–$\pi$ JJ could be included in a long annular junction and the polarization of the semifluxon could be read-out after the injection of integer fluxons and the appearance of zero-field steps for underdamped junction [98].

The fractional vortex could be studied by nearby dc or rf SQUIDs, scanning SQUID microscopy or LTSEM measurements, as done for flat phase junctions, see Appendix A. The shape of its magnetic field and the kind of coupling (ferromagnetic/antiferromagnetic) could be investigated for various lattice geometries.

Macroscopic quantum tunneling and microwave spectroscopy measurements should be performed on a 0–$\pi$ coupled junction, just as done on the flat phase $\pi$ junction described in Appendix B.

So-called $\varphi$ junctions could be constructed by periodic alternating short 0 and $\pi$ coupled junctions along the axis of a long linear junction. The current-phase relation has a very unusual shape with two maxima. In the short junction limit the field dependence of the critical current is very different from the standard Fraunhofer dependence [161].

$\pi$ and 0–$\pi$ are potential candidates for building flux-based qubits, also referred to as phase qubits. While the $\pi$ junction may serve a passive phase shifter in a *quite* qubit [12], the 0–$\pi$ junction may be used as the active part in the qubit, as was recently proposed [20]. When the energy barrier separating two degenerate classical fractional flux states becomes very small, the system may spontaneously switch between two states due to thermal excitation over the barrier or quantum tunneling through the barrier. Two semifluxons in a long 0–$\pi$–0 JJ at a distance slightly larger than the crossover distance from flat phase to flux state can be described by the dynamics of a single particle in a double-well potential, which may exhibit quantum tunneling at low temperatures. In a very short, symmetric 0–$\pi$ junction the low amplitude of its spontaneous flux lowers the potential barrier between the two degenerates states and quantum tunneling between the states may appear, too.

# Bibliography


[1] J. Bardeen, L. N. Cooper and J. R. Schrieffer, Phys. Rev. **108**, 1175 (1957).

[2] P. Fulde and R. A. Ferrell, Phys. Rev. **550**, 135A (1964).

[3] A. Larkin and Y. N. Ovchinnikov, Sov. Phys. JETP **20**, 762 (1965).

[4] B. D. Josephson, Phys. Lett. **1**, 251 (1962).

[5] L. Bulaevskiĭ, V. Kuziĭ and A. Sobyanin, JETP Lett. **25**, 7 (1977).

[6] A. I. Buzdin and M. Yu. Kupriyanov, JETP Lett. **53**, 321 (1991).

[7] A. V. Veretennikov, V. V. Ryazanov, V. A. Oboznov, A Yu. Rusanov, V. A. Larkin and J. Aarts, Physica B **284**, 495 (2000).

[8] Y. Blum, A. Tsukernik, M. Karpovski and A. Palevski, Phys. Rev. Lett. **89**, 187004 (2002).

[9] T. Kontos, M. Aprili, J. Lesueur and X. Grison, Phys. Rev. Lett. **89**, 137007 (2002).

[10] E. Terzioglu and M. R. Beasley, IEEE Trans. Appl. Supercond. **8**, 48 (1998).

[11] A. V. Ustinov and V. K. Kaplunenko, J. Appl. Phys. **94**, 5405 (2003).

[12] L. B. Ioffe, V. B. Geshkenbein, M. V. Feigel'man, A. L. Fauchère and G. Blatter, Nature (London) **398**, 679 (1999).

[13] J. H. Xu, J. H. Miller and C. S. Ting, Phys. Rev. B **51**, 11958 (1995).

[14] E. Goldobin, D. Koelle and R. Kleiner, Phys. Rev. B **66**, 100508 (2002).

[15] J. R. Kirtley, K. A. Moler and D. J. Scalapino, Phys. Rev. B **56**, 886 (1997).

[16] N. Stefanakis, Phys. Rev. B **66**, 214524 (2002).

[17] E. Goldobin, D. Koelle and R. Kleiner, Phys. Rev. B **67**, 224515 (2003).

[18] A. Zenchuk and E. Goldobin, Phys. Rev. B **69**, 024515 (2004).

[19] T. Gaber, E. Goldobin, A. Sterck, R. Kleiner, D. Koelle, M. Siegel and M. Neuhaus, Phys. Rev. B **72**, 054522 (2005).

[20] E. Goldobin, K. Vogel, O. Crasser, R. Walser, W. P. Schleich, D. Koelle and R. Kleiner, Phys. Rev. B **72**, 054527 (2005).

[21] C. C. Tsuei and J. R. Kirtley, Rev. Mod. Phys. **72**, 969 (2000).

[22] H. Hilgenkamp, Ariando, H. J. H. Smilde, D. H. A. Blank, G. Rijnders, H. Rogalla, J. R. Kirtley and C. C. Tsuei, Nature (London) **422**, 50 (2003).

[23] M. L. Della Rocca, M. Aprili, T. Kontos, A. Gomez and P. Spatkis, Phys. Rev. Lett. **94**, 197003 (2005).

[24] H. Kamerlingh-Onnes, Comm. Phys. Lab. Univ. Leiden **122**, 124 (1911).

[25] P. G. de Gennes, *Superconductivity of Metals and Alloys*, Addison-Wesley, New York (1999).

[26] V. L. Ginzburg and L. D. Landau, Zh. Eksp. Teor. Fiz. **20**, 1064 (1950).

[27] R. Doll and M. Näbauer, Phys. Rev. Lett. **7**, 51 (1961).

[28] B. S. Deaver and W. M. Fairbank, Phys. Rev. Lett. **7**, 43 (1961).

[29] R. Kleiner and D. Koelle, In J. Clarke and A. I. Braginksi, *SQUID Handbook*. Wiley-VCH (2004).

[30] P. W. Anderson and J. M. Rowell, Phys. Rev. Lett. **10**, 230 (1963).

[31] K. K. Likharev, *Dynamics ofJosephson Junctions and Circuits*, Gordon and Breach, New York (1986).

[32] H. Hilgenkamp and J. Mannhart, Rev. Mod. Phys. **74**, 485 (2002).

[33] W. C. Stewart, Appl. Phys. Lett. **12**, 277 (1968).

[34] D. E. McCumber, J. Appl. Phys. **39**, 3113 (1968).

[35] E. Goldobin, StkJJ-computer code.

[36] V. Ambegaokar and A. Baratoff, Phys. Rev. Lett. **10**, 486 (1963).

[37] V. Ambegaokar and A. Baratoff, Phys. Rev. Lett. **11**, 104 (1963).

[38] H. A. Kramers, Physica (Utrecht) **7**, 284 (1940).

[39] M. Büttiker, E. P. Harris and R. Landauer, Phys. Rev. B **28**, 1268 (1983).

[40] M. H. Devoret, J. M. Martinis and J. Clarke, Phys. Rev. Lett. **55**, 1908 (1985).

[41] J. M. Martinis, M. H. Devoret and J. Clarke, Phys. Rev. B **35**, 4682 (1987).

[42] A. Wallraff, T. Duty, A. Lukashenko and A. V. Ustinov, Phys. Rev. Lett. **90**, 37003 (2003).

[43] M. Weihnacht, Phys. Status Solidi **32**, K169 (1969).

[44] A. C. Scott, F. Y. F. Chu and D. W. McLaughlin, Proc. IEEE **61**, 1443 (1973).

[45] T. A. Fulton, In B. B. Schwartz and S. Foner, *Superconductor Applications: SQUIDs and Machines*, page 125. Plenum (1977).

[46] M. Cirillo, R. D. Parmentier B. and Savo, Physica D **3**, 565 (1981).

[47] R. D. Parmentier, In H. Weinstock and R. W. Ralston, *The New Superconducting Electronics*, page 221. Springer-Verlag (1993).

[48] J. C. Swihart, J. Appl. Phys. **32**, 461 (1961).

[49] A. Barone and G. Paterno, *Physics and Applications of the Josephson Effect*, John Wiley & Sons (1982).

[50] M. D. Fiske, Rev. Mod. Phys. **36**, 221 (1964).

[51] W. Buckel and R. Kleiner, *Supraleitung*, Wiley-VCH (2004).

[52] M. Faure and A. I. Buzdin, Phys. Rev. Lett. **94**, 187202 (2005).

[53] A. I. Buzdin, Rev. Mod. Phys. **77**, 935 (2005).

[54] E. A. Demler, G. B. Arnold and M. R. Beasley, Phys. Rev. B **55**, 15174 (1997).

[55] E. S. Stoner, Proc. Roy. Soc. A **165**, 372 (1938).

[56] A. F. Andreev, J. Exp. Theor. Phys. **19**, 1228 (1964).

[57] I. O. Kulik, Sov. Phys. JETP **30**, 944 (1970).

[58] S. V. Kuplevakhskii and I. I. Falko, JETP Lett. **52**, 340 (1990).

[59] A. I. Buzdin and V. V. Ryazanov, C. R. Physique **7**, 107 (2006).

[60] G. Eilenberger, Z. Phys. **214**, 195 (1968).

[61] K. L. Usadel, Phys. Rev. Lett. **25**, 507 (1970).

[62] Z. Radovic, M. Ledvij, L. Dobrosavljevic-Grujic, A. I. Buzdin and J. R. Clem, Phys. Rev. B **44**, 759 (1991).

[63] A. I. Buzdin, L. N. Bulaevskiĭ and S. V. Panyukov, JETP Lett. **35**, 178 (1982).

[64] F. A. Bergeret, A. F. Volkov and K. B. Efetov, Phys. Rev. B **65**, 134505 (2002).

[65] H. Sellier, C. Baraduc, F. Lefloch and R. Calemczuk, Phys. Rev. B **68**, 054531 (2003).

[66] C. Bell, R. Loloee, G. Burnell and M. G. Blamire, Phys. Rev. B **71**, 180501 (2005).

[67] V. Shelukhin, A. Tsukernik, M. Karpovski, Y. Blum, K. B. Efetov, A. F. Volkov, T. Champel, M. Eschrig, T. Lofwander, G. Schon and A. Palevski, Phys. Rev. B **73**, 174506 (2006).

[68] V. A. Oboznov, V. V. Bol'ginov, A. K. Feofanov, V. V. Ryazanov and A. I. Buzdin, Phys. Rev. Lett. **96**, 197003 (2006).

[69] A. Cottet and W. Belzig, Phys. Rev. B **72**, 180503 (2005).

[70] F. Born, M. Siegel, E. K. Hollmann, H. Braak, A. A. Golubov, D. Yu. Gusakova and M. Yu. Kupriyanov, Phys. Rev. B **74**, 140501 (2006).

[71] R. Latempa, L. Parlato, G. Peluso, G. P. Pepe, A. Ruotolo, A. Barone and A. A. Golubov, IEEE Trans. Appl. Supercond. **15**, 133 (2005).

[72] M. Weides, M. Kemmler, E. Goldobin, D. Koelle, R. Kleiner, H. Kohlstedt and A. Buzdin, Appl. Phys. Lett. **89**, 122511 (2006).

[73] S. M. Frolov, D. J. Van Harlingen, V. A. Oboznov, V. V. Bolginov and V. V. Ryazanov, Phys. Rev. B **70**, 144505 (2004).

[74] A. Bauer, J. Bentner, M. Aprili, M. L. Della Rocca, M. Reinwald, W. Wegscheider and C. Strunk, Phys. Rev. Lett. **92**, 217001 (2004).

[75] V. V. Ryazanov, V. A. Oboznov, A. V. Veretennikov and A. Yu. Rusanov, Phys. Rev. B **65**, 20501 (2001).

[76] W. Guichard, M. Aprili, O. Bourgeois, T. Kontos, J. Lesueur and P. Gandit, Phys. Rev. Lett. **90**, 167001 (2003).

[77] V. Zdravkov, A. Sidorenko, G. Obermeier, S. Gsell, M. Schreck, C. Müller, S. Horn, R. Tidecks and L. R. Tagirov, Phys. Rev. Lett. **97**, 57004 (2006).

[78] Ya. V. Fominov, N. M. Chtchelkachev and A. A. Golubov, Phys. Rev. B **66**, 14507 (2002).

[79] V. V. Ryazanov, V. A. Oboznov, A. Y. Rusanov, A. V. Veretennikov, A. A. Golubov and J. Aarts, Phys. Rev. Lett. **86**, 2427 (2001).

[80] L. Cretinon, A. K. Gupta, H. Sellier, F. Lefloch, M. Faure, A. Buzdin and H. Courtois, Phys. Rev. B **72**, 24511 (2005).

[81] A. Buzdin and I. Baladie, Phys. Rev. B **67**, 184519 (2003).

[82] Y. Blum, A. Tsukernik, M. Karpovski and A. Palevski, Phys. Rev. B **70**, 214501 (2004).

[83] J. W. A. Robinson, S. Piano, G. Burnell, C. Bell and M. G. Blamire, Phys. Rev. Lett. **97**, 177003 (2006).

[84] J. E. Mooij, T. P. Orlando, L. Levitov, L. Tian, C. H. van der Wal and S. Lloyd, Science **285**, 1036 (1999).

[85] T. P. Orlando, J. E. Mooij, Lin Tian, C. H. van der Wal, L. S. Levitov, S. Lloyd and J. J. Mazo, Phys. Rev. B **60**, 15398 (1999).

[86] J. J. A. Baselmans, T. T. Heikkila, B. J. van Wees and T. M. Klapwijk, Phys. Rev. Lett. **89**, 207002 (2002).

[87] A. A. Golubov, M. Yu. Kupriyanov and E. Il'ichev, Rev. Mod. Phys. **76**, 411 (2004).

[88] R. Melin, Europhys. Lett. **69**, 121 (2005).

[89] A. Buzdin, Phys. Rev. B **72**, 100501 (2005).

[90] H. Sellier, C. Baraduc, F. Lefloch and R. Calemczuk, Phys. Rev. Lett. **92**, 257005 (2004).

[91] S. M. Frolov, D. J. Van Harlingen, V. V. Bolginov, V. A. Oboznov and V. V. Ryazanov, Phys. Rev. B **74**, 020503 (2006).

[92] L. N. Bulaevskiĭ, V. V. Kuziĭ and A. A. Sobyanin, Solid State Commun. **25**, 1053 (1978).

[93] J. R. Kirtley, C. C. Tsuei, M. Rupp, J. Z. Sun, L. S. Yu-Jahnes, A. Gupta, M. B. Ketchen, K. A. Moler and M. Bhushan, Phys. Rev. Lett. **76**, 1336 (1996).

[94] R. Gross and D. Koelle, Rep. Prog. Phys. **57**, 651 (1994).

[95] E. Goldobin, A. Sterck, T. Gaber, D. Koelle and R. Kleiner, Phys. Rev. Lett. **92**, 057005 (2004).

[96] D. A. Wollman, D. J. Van Harlingen, J. Giapintzakis and D. M. Ginsberg, Phys. Rev. Lett. **74**, 797 (1995).

[97] N. Lazarides, Phys. Rev. B **69**, 212501 (2004).

[98] E. Goldobin, N. Stefanakis, D. Koelle and R. Kleiner, Phys. Rev. B **70**, 094520 (2004).

[99] J. R. Kirtley, C. C. Tsuei and K. A. Moler, Science **285**, 1373 (1999).

[100] A. Sugimoto, T. Yamaguchi and I. Iguchi, Physica C **367**, 28 (2002).

[101] A. V. Ustinov, Appl. Phys. Lett. **80**, 3153 (2002).

[102] B. A. Malomed and A. V. Ustinov, Phys. Rev. B **69**, 064502 (2004).

[103] C. Vanneste, C. C. Chi, W. J. Gallagher, A. W. Kleinsasser, S. I. Raider and R. L. Sandstrom, J. Appl. Phys. **64**, 242 (1988).

[104] H. Kroger, L. N. Smith and D. W. Jillie, Appl. Phys. Lett. **39**, 280 (1981).

[105] M. Gurvitch, M. A. Washington, H. A. Huggins and J. M. Rowell, IEEE Trans. Magn. **19**, 791 (1983).

[106] R. Berisch, *Sputtering by Particle Bombardment I*, Springer, Heidelberg (1981).

[107] J. Geerk, M. Gurvitch, D. B. McWhan and J. M. Rowell, ).

[108] H. Kohlstedt, F. König, P. Henne, N. Thyssen and P. Caputo, J. Appl. Phys. **80**, 5512 (1996).

[109] H. A. M. de Gronckel, H. Kohlstedt and C. Daniels, Appl. Phys. A **70**, 435 (2000).

[110] N. Cabrera, Phil. Mag. **40**, 175 (1949).

[111] N. Cabrera and N. F. Mott, Rep. Progr. Phys. **12**, 163 (1949).

[112] L. Fritzsch, H. J. Köhler, F. Thrum, G. Wende and H. G. Meyer, Physica C **296**, 319 (1998).

[113] P. Rottländer, H. Kohlstedt, P. Grünberg and E. Girgis, J. Appl. Phys. **87**, 6067 (2000).

[114] L. Young, *Anodic Oxide Films*, Academic, New York (1961).

[115] H. Kohlstedt, K. H. Gundlach and A. Schneider, IEEE Trans. Magn. **27**, 3149 (1991).

[116] T. Imamura and S. Hasuo, IEEE Trans. Magn. **25**, 1131 (1989).

[117] D. Nakada, K. K. Berggren, E. Macedo, V. Liberman and T. P. Orlando, IEEE Trans. Appl. Supercond. **13**, 111 (2003).

[118] J. G. Caputo, N. Flytzanis and M. Devoret, Phys. Rev. B **50**, 6471 (1994).

[119] R. Monaco, G. Costabile and N. Martucciello, J. Appl. Phys. **77**, 2073 (1995).

[120] A. W. Lichtenberger, D. M. Lea and F. L. Lloyd, IEEE Trans. Appl. Supercond. **3**, 2191 (1993).

[121] S. A. Ahern, M. J. C. Martin and W. Sucksmith, Proc. Roy. Soc. **248**, 145 (1958).

[122] G. Güntherodt and U. Rüdiger, In *30. Ferienkurs des Instituts für Festkörperforschung, Magnetische Schichtsystem.* Institut für Festkörperforschung, Forschungszentrum Jülich GmbH (1999).

[123] J. C. Ododo and B. R. Coles, J. Phys. F **7**, 2393 (1977).

[124] A. Rusanov, R. Boogaard, M. Hesselberth, H. Seiler and J. Aarts, Physica C **369**, 300 (2002).

[125] J. Vrijen and S. Radelaar, Phys. Rev. B **17**, 409 (1978).

[126] G. Bergmann, Phys. Rev. Lett. **41**, 264 (1978).

[127] J. Kim, J. H. Kwon, K. Char, H. Doh and H. Y. Choi, Phys. Rev. B **72**, 14518 (2005).

[128] K. Levin and D. L. Mills, Phys. Rev. B **9**, 2354 (1974).

[129] R. W. Houghton, M. P. Sarachik and J. S. Kouvel, Phys. Rev. Lett. **25**, 238 (1970).

[130] H. J. Elmers, In *30. Ferienkurs des Instituts für Festkörperforschung, Magnetische Schichtsystem.* Institut für Festkörperforschung, Forschungszentrum Jülich GmbH (1999).

[131] L. E. Rehn, S. Danyluk and H. Wiedersich, Phys. Rev. Lett. **43**, 1764 (1979).

[132] RUMP: Rutherford Backscattering Data Analysis Plotting and Simulation Package, http://www. genplot. com/.

[133] F. Brouers, A. V. Vedyayev and M. Giorgino, Phys. Rev. B **7**, 380 (1973).

[134] D. Y. Petrovykh, K. N. Altmann, H. Höchst, M. Laubscher, S. Maat, G. J. Mankey and F. J. Himpsel, Appl. Phys. Lett. **73**, 3459 (1998).

[135] A. Barone, *Principles and applications fo superconduncting quantum interference devices*, Word Scientific, Singapure (1992).

[136] V. V. Ryazanov, V. A. Oboznov, A. S. Prokofiev, V. V. Bolginov and A. K. Feofanov, J. Low Temp. Phys. **136**, 385 (2004).

[137] A. T. Hindmarch, C. H. Marrows and B. J. Hickey, Phys. Rev. B **72**, 100401 (2005).

[138] R. Raue, H. Hopster and R. Clauberg, Phys. Rev. Lett. **50**, 1623 (1983).

[139] A. Liebsch, Phys. Rev. Lett. **43**, 1431 (1979).

[140] E. Dietz, U. Gerhardt and C. J. Maetz, Phys. Rev. Lett. **40**, 892 (1978).

[141] R. Karplus and J. M. Luttinger, Phys. Rev. Lett. **95**, 1154 (1954).

[142] M. Weides, K. Tillmann and H. Kohlstedt, Physica C **437-438**, 349 (2006).

[143] E. Goldobin, GoldExI, http://www. geocities. com/goldexi.

[144] A. W. Kleinsasser, R. E. Miller and W. H. Mallison, IEEE Trans. Appl. Supercond. **5**, 26 (1995).

[145] R. E. Miller, W. H. Mallison, A. W. Kleinsasser, K. A. Delin and E. M. Macedo, Appl. Phys. Lett. **63**, 1424 (1993).

[146] H. Kohlstedt, G. Hallmanns, I. P. Nevirkovets, D. Guggi and C. Heiden, IEEE Trans. Appl. Supercond. **3**, 2197 (1992).

[147] A. A. Golubov, E. P. Houwman, J. G. Gijsbertsen, V. M. Krasnov, J. Flokstra, J. B. le Grand and P. A. J. de Korte, Phys. Rev. B **49**, 1073 (1995).

[148] N. L. Rowell and H. J. T. Smith, Can. J. Phys. **54**, 223 (1976).

[149] Hypres, Elmsford (NY), USA, http://www. hypres. com.

[150] A. F. Volkov and A. Anishchanka, Phys. Rev. B **71**, 24501 (2005).

[151] M. Lentzen, B. Jahnen, C. L. Jia, A. Thust, K. Tillmann and K. Urban, Ultramicroscopy **92**, 233 (2002).

[152] A. A. Golubov and M. Yu. Kupriyanov, J. Low Temp. Phys **70**, 83 (1988).

[153] T. Kontos, M. Aprili, J. Lesueur and X. Grison, Phys. Rev. Lett. **93**, 137001 (2004).

[154] J. G. Simmons, Appl. Phys. Lett. **34**, 1793 (1963).

[155] J. G. Simmons, Appl. Phys. Lett. **34**, 2581 (1963).

[156] W. F. Brinkman, R. C. Dynes and J. M. Rowell, Appl. Phys. Lett. **41**, 1915 (1963).

[157] W. C. Stewart, Appl. Phys. Lett. **45**, 452 (1974).

[158] S. Stein, Ph. D. thesis, Universität zu Köln, Germany (2004).

[159] M. Houzet, V. Vinokur and F. Pistolesi, Phys. Rev. B **72**, 220506 (2005).

[160] R. G. Mints, I. Papiashvili, J. R. Kirtley, H. Hilgenkamp, G. Hammerl and J. Mannhart, Phys. Rev. Lett. **89**, 67004 (2002).

[161] A. Buzdin and A. E. Koshelev, Phys. Rev. B **67**, 220504 (2003).

[162] T. Ortlepp, Ariando, O. Mielke, C. J. M. Verwijs, K. F. K. Foo, H. Rogalla, F. H. Uhlmann and H. Hilgenkamp, Science **319**, 1495 (2006).

[163] M. Weides, M. Kemmler, H. Kohlstedt, R. Waser, D. Koelle, R. Kleiner and E. Goldobin, Phys. Rev. Lett. **97**, 247001 (2006).

[164] L. Reimer, *Scanning Electron Microscopy*, Springer, Heidelberg (1985).

[165] D. Doenitz, Ph. D. thesis, Universität Tübingen, Germany (2006).

[166] M. J. Donahue and D. G. Porter, oommf-computer code, http://math.nist.gov/oommf.

[167] R. F. Voss and R. A. Webb, Phys. Rev. Lett. **47**, 265 (1981).

[168] R. Rouse, S. Han and J. E. Lukens, Phys. Rev. Lett. **75**, 1614 (1995).

[169] Y. Nakamura, Y. A. Pashkin and J. S. Tsai, Nature (London) **398**, 786 (1999).

[170] S. Beutner, Diploma thesis, Munich University of Technology (2006).

[171] K. Madek, S. Beutner, G. Wild, Ch. Probst, M. Weides, H. Kohlstedt, A. Marx and R. Gross, submitted to Phys. Rev. Lett. (2006).

[172] H. S. J. van der Zant, R. A. M. Receveur, T. P. Orlando and A. W. Kleinsasser, Appl. Phys. Lett. **65**, 2102 (1994).

[173] M. Maezawa, M. Aoyagi, H. Nakagawa and I. Kurosawa, Appl. Phys. Lett. **66**, 2134 (1995).

[174] T. Kontos, M. Aprili, J. Lesueur and X. Grison, Phys. Rev. Lett. **86**, 304 (2001).

# Publications

- M. Weides, M. Kemmler, H. Kohlstedt, R. Waser, D. Koelle, R. Kleiner and E. Goldobin
  0–$\pi$ *Josephson tunnel junctions with ferromagnetic barrier*
  Phys. Rev. Lett. **97**, 247001 (2006)

- M. Weides, M. Kemmler, E. Goldobin, D. Koelle, R. Kleiner, H. Kohlstedt and A. Buzdin
  *High quality ferromagnetic* 0 *and* $\pi$ *Josephson tunnel junctions*
  Appl. Phys. Lett. **89**, 122511 (2006)

- M. Weides, K. Tillmann and H. Kohlstedt
  *Fabrication of high quality ferromagnetic Josephson junctions*
  Physica C **437-438**, 349 (2006)

- K. Madek, S. Beutner, G. Wild, Ch. Probst, M. Weides, H. Kohlstedt, A. Marx and R. Gross
  *Observation of Macroscopic Quantum Behavior in* $\pi$ *Josephson Junctions with Ferromagnetic Interlayer*
  submitted to Phys. Rev. Lett. (2006)

# Conference contributions

- Combined ESF PiShift and Thiox Workshop, May 2006, Bordeaux, France
  *High quality ferromagnetic* 0*,* $\pi$ *and* 0–$\pi$ *Josephson tunnel junctions*
  M. Weides, H. Kohlstedt, R. Waser, M. Kemmler, E. Goldobin, D. Koelle and R. Kleiner

- DPG Frühjahrstagung, March 2006, Dresden, Germany
  *From* 0 *to* $\pi$ *coupled Josephson junctions*
  M. Weides, H. Kohlstedt, R. Waser, M. Kemmler, E. Goldobin, D. Koelle and R. Kleiner
  and *Current and phase distribution in Josephson junctions with ferromagnetic interlayer*
  M. Weides, H. Kohlstedt, R. Waser, D. Doenitz, D. Koelle and R. Kleiner

- E.U. - U.S. Workshop on Quantum Information and Coherence, December 2005, Munich, Germany
  0–$\pi$ *coupled Josephson junctions: a potential qubit system*
  M. Weides, H. Kohlstedt, R. Waser, E. Goldobin, D. Koelle and R. Kleiner

- Tagung Kryoelektronische Bauelemente, Oktober 2005, Bad Herrenalb, Germany
  *Fabrication of high quality ferromagnetic Josephson junctions -towards semifluxon qubits based on* 0–$\pi$ *SIFS junctions-*
  M. Weides, H. Kohlstedt, R. Waser, K. Tillmann, E. Goldobin, D. Koelle and R. Kleiner

- Joint JSPS and ESF Conference on Vortex Matter in Nanostructured Superconductors (VORTEX IV), September 2005, Crete, Greece
  *Fabrication of high quality ferromagnetic Josephson junctions -towards semifluxon qubits based on* 0–$\pi$ *SIFS junctions-*

M. Weides, H. Kohlstedt, R. Waser, K. Tillmann, E. Goldobin, D. Koelle and R. Kleiner

- 2nd International Workshop on Spin-FET Quantum Based Information Processing, March 2005 Research Centre Juelich
  *$\pi$ coupled SIFS junctions for Semifluxon Qubits*
  M. Weides, H. Kohlstedt, R. Waser, E. Goldobin, D. Koelle, R. Kleiner and V. Ryazanov

- DPG Frühjahrstagung, March 2005, Berlin, Germany
  *SIFS junctions for Semifluxon Qubits*
  M. Weides, H. Kohlstedt, R. Waser, E. Goldobin, D. Koelle, R. Kleiner and V. Ryazanov

- International Workshop on Solid State based Quantum Information Processing, September 2004, Herrsching, Munich, Germany
  *Towards semifluxon qubits based on 0–$\pi$ SIFS Josephson Junctions*
  M. Weides, E. Goldobin, H. Kohlstedt, D. Koelle, R. Waser and R. Kleiner

- Combined ESF Vortex and ESF PiShift Workshop, May 2004, Bad Münstereifel, Germany
  *Josephson coupling in SIFS tunnel junctions*
  M. Weides, E. Goldobin, H. Kohlstedt, D. Koelle, R. Waser and R. Kleiner

- DPG Frühjahrstagung, March 2004, Regensburg, Germany
  *Josephson coupling in* $Nb/Al_2O_3/Cu_{52}Ni_{48}/Nb$ *tunnel junctions*
  M. Weides, H. Kohlstedt, E. Goldobin, D. Koelle, R. Waser and R. Kleiner

Schriften des Forschungszentrums Jülich
Reihe Informationstechnik / Information Technology

1. **SAM - Untersuchung von Aushandlungen in Gruppen mittels Agentensimulation**
   von N. Lepperhoff (2002), VI, 278 Seiten
   ISBN: 978-3-89336-298-1

2. **Praxisbezogene IDL-Programmierung**
   von M. Busch, R. Bauer, H. Heer, M. Wagener (2002), XVI, 216 Seiten, 12 farb. Abb.
   ISBN: 978-3-89336-308-7

3. **Segmentierung von Volumendatensätzen mittels dreidimensionaler hierarchischer Inselstrukturen**
   von J.-F. Vogelbruch (2002), V, 191 Seiten, zahlr. farb. Abb.
   ISBN: 978-3-89336-309-4

4. **ComputerMathematik mit Maple**
   von J. Grotendorst (2003), VI, 274 Seiten mit beiliegender CD-ROM, zahlr. farb. Abb.
   ISBN: 978-3-89336-325-4

5. **ComputerMathematik mit Maple – Zweite überarbeitete und erweiterte Auflage**
   von J. Grotendorst (2004), VI, 294 Seiten mit beiliegender CD-ROM, zahlr. farb. Abb.
   ISBN: 978-3-89336-354-4

6. **The Internet in Germany: Atlas of Providers and Regions**
   by N. Lepperhoff, W. Fischer (2004), VIII, 103 pages, many coloured fig.
   ISBN: 978-3-89336-358-2

7. **Störstellen in Galliumnitrid-basierenden Transistoren**
   von M.J. Wolter (2004), V, 132 Seiten, 19 farb. Abb.
   ISBN: 978-3-89336-361-2

8. **Programming in C++: Audio-Visual Lecture of the course "Object-oriented programming in C++"**
   von B. Mohr, M. Boltes, R. Koschmieder (2004), DVD (18 hours, 22 minutes recorded in 15 sessions)
   ISBN: 978-3-89336-369-8

9. **Fabrication and characterization of planar Gunn diodes for Monolithic Microwave Integrated Circuits**
   by S. Montanari (2005), c. 150 pages, 26 col. fig.
   ISBN: 978-3-89336-396-4

10. **IDL Referenz der ICG-Daten-Struktur**
    von R. Bauer (2006), XIV, 130 Seiten
    ISBN: 978-3-89336-426-8

Schriften des Forschungszentrums Jülich
Reihe Informationstechnik / Information Technology

11. **Piezoresponse Force Microscopy and Surface Effects of Perovskite Ferroelectric Nanostructures**
by F. Peter (2006), 106 pages
ISBN: 978-3-89336-444-2

12. **Molecular Electronic Building Blocks Based on Self-Assembled Monolayers**
by B. Lüssem (2006), 138 pages
ISBN: 978-3-89336-454-1

13. **Josephson Tunnel Junctions with Ferromagnetic Interlayer**
by M. Weides (2007), IX, 144 pages
ISBN: 978-3-89336-472-5

High-quality Josephson tunnel junctions with ferromagnetic interlayers are presented. Depending on the thickness of the ferromagnetic $Ni_{0.6}Cu_{0.4}$ layer and on the ambient temperature, the junctions were in the 0 or $\pi$ coupled ground state. Using a step-like ferromagnetic layer, the first controllable 0-$\pi$ tunnel Josephson junction was obtained. The ground state of the 0-$\pi$ junction corresponds to a spontaneous vortex of supercurrent pinned at the 0-$\pi$ phase boundary, carrying a fractional vortex of 6.7 % of the magnetic flux quantum $\Phi_0$. The ability to fabricate 0, $\pi$ and 0-$\pi$ Josephson junctions within the same process opens up new prospects for applications in complementary logic circuits, quantum bits and also for the investigation of fractional vortices.

## Author

The author Dr. Martin P. Weides studied physics at the University of Cologne, Germany, and the Universidad Complutense de Madrid, Spain. After working on magnetic tunnel junctions at the Institute for Solid State Research, Research Centre Juelich, Germany, during his first degree he later focused on superconducting and magnetic thin films for his Ph.D. thesis and performed the experimental work at Juelich, and at the Institute of Solid State Physics of the Russian Academy of Sciences, Chernogolovka, Russia. This book is a slightly revised version of his Ph.D. thesis submitted to the University of Cologne in 2006.

Forschungszentrum Jülich
in der Helmholtz-Gemeinschaft

50 Jahre Zukunft

**Band/Volume 13**
**ISBN 978-3-89336-472-5**

**Informationstechnik**
**Information Technology**